Surface Science Reports 77 (2022) 100552

Contents lists available at ScienceDirect

Surface Science Reports

journal homepage: www.elsevier.com/locate/surfrep

Atom scattering as a probe of the surface electron-phonon interaction at conducting surfaces

J.R. Manson [a,b,*], G. Benedek [b,c], Salvador Miret-Artés [b,d]

[a] Department of Physics and Astronomy, Clemson University, Clemson, SC, 29634, USA
[b] Donostia International Physics Center (DIPC), Paseo Manuel de Lardizabal, 4, 20018, Donostia-San Sebastián, Spain
[c] Dipartimento di Scienza Dei Materiali, Università di Milano-Bicocca, Via Cozzi 55, 20 125, Milano, Italy
[d] Instituto de Física Fundamental, Consejo Superior de Investigaciones Científicas, Serrano 123, 28 006, Madrid, Spain

ARTICLE INFO

Article history:
Received 3 September 2021
Accepted 22 January 2022
Available online 31 January 2022

ABSTRACT

An atomic projectile colliding with a surface at kinetic energies in the thermal or hyperthermal range interacts with and is reflected by the electronic density well in front of the first layer of target atoms, and it is generally accepted that the repulsive interaction potential is proportional to the density of electrons extending outside the surface. This review develops a complete treatment of the elastic and inelastic scattering of atoms from a conducting surface in which the interaction with the electron density and its vibrations is treated using electron-phonon coupling theory. Starting from the basic principles of formal scattering theory, the elastic and inelastic scattering intensities are developed in a manner that identifies the small overlap region in the surface electron density where the projectile atom is repelled. The effective vibrational displacements of the electron gas, which lead to energy transfer through excitation of phonons, are directly related to the vibrational displacements of the atomic cores in the target crystal via electron-phonon coupling. The effective Debye-Waller factor for atom-surface scattering is developed and related to the mean square displacements of the atomic cores. The complex dependence of the Debye-Waller factor on momentum and energy of the projectile, including the effects of the attractive adsorption well in the interaction potential, are clearly defined. Applying the standard approximations of electron-phonon coupling theory for metals to the distorted wave Born approximation leads to expressions which relate the elastic and inelastic scattering intensities, as well as the Debye-Waller factor, to the well known electron-phonon coupling constant λ. This treatment reproduces the previously obtained result that the intensities for single phonon inelastic peaks in the scattered spectra are proportional to the mode specific mass correction components $\lambda_{\mathbf{Q},\nu}$ defined by the relationship $\lambda = \langle \lambda_{\mathbf{Q},\nu} \rangle$. The intensities of elastic diffraction peaks are shown to be a weighted sum over the $\lambda_{\mathbf{Q},\nu}$, and the Debye-Waller factor can also be expressed in terms of a similar weighted summation. In the simplest case the Debye-Waller exponent is shown to be proportional to λ and for simple metals, metal overlayers, and other kinds of conducting surfaces values of λ are extracted from available experimental data. This dependence of the elastic and inelastic scattering, and that of the Debye-Waller factor, on the electron-phonon coupling constant λ shows that measurements of elastic and inelastic spectra of atomic scattering are capable of revealing detailed information about the electron-phonon coupling mechanism in the surface electron density.

1. Introduction

The scattering of well defined beams of atoms and small molecules with energies in the thermal or hyperthermal range has a long history in the investigation of surfaces and surface properties and the extensive literature has been surveyed in a number of important review articles [1–15]. The seminal experimental work was carried out by Stern and his students, initially in laboratories in Frankfurt [16,16b] and later in Hamburg [17,17b]. Although they were using thermal beams, with a broad Maxwellian distribution of energies, they were able to confirm the existence of the de Broglie

---

[*] Corresponding author. Department of Physics and Astronomy, Clemson University, Clemson, SC, 29634, USA.
E-mail address: jmanson@clemson.edu (J.R. Manson).

https://doi.org/10.1016/j.surfrep.2022.100552

wavelength of an atom through demonstrations of diffraction of a He beam by a LiF(001) surface [18,18c]. Further work demonstrated the presence of the attractive van der Waals adsorption well in the atom-surface interaction potential via observations of resonance with its bound states [19,19b], a process later given the name selective adsorption [20,20c].

The development of the supersonic jet beam [21–23] provided an impetus to the field because this produced a nearly monoenergetic and highly angularly defined beam of projectile atoms. Also at roughly the same time ultra high vacuum techniques became highly developed and this provided new methods for maintaining the cleanliness of prepared surfaces for periods long enough to make well-controlled measurements. As a result, atom scattering, and in particular He atom scattering (HAS) has become a major tool in the arsenal of experimental techniques for surface analysis. Its particular attributes are that with typical kinetic energies in the meV range it is non-destructive, while the de Broglie wavelengths are comparable to crystal lattice spacing making diffraction a highly probable process. Similarly, the energies and wavelengths are comparable to those of phonons, making interactions with single phonons or small numbers of phonons a readily measurable process.

Since very early on it has been generally understood that low energy atoms are repelled from a crystal surface at distances well in front of the positions of the first layer of atomic cores, and that this repulsive force originated from the Pauli exclusion [24] of electrons in the two weakly overlapping electronic densities, that is to say the overlap of the electron cloud of the atom with the weak and decaying electronic density as it extends outward from the crystal surface. Because this repulsive force originates as the incoming atomic electron density attempts to embed itself in the rarefied density of surface electrons, it is a logical assumption that the interaction potential should be proportional to the surface electron density in the region of the classical turning point [25]. This electron density is to a good approximation exponentially decaying with distance far from the surface. In fact, the first mathematical treatment of the eigenfunctions of an exponential potential was developed by Mott and Jackson while investigating energy transfer at a gas-surface interface [26]. In that same paper their wavefunctions were used to calculate the Mott-Jackson matrix elements of an exponential perturbing potential, and those matrix elements were used to calculate what is now known as single phonon excitations in the distorted wave Born approximation (DWBA). However, the first quantitative theoretical verification of the proportionality between the repulsive force on an atom and the surface electron density was provided much later by Esbjerg and Nørskov in 1980 [27]. This question has subsequently been addressed by others and although there is significant disparity on the value of the proportionality constant, the basic concept of the potential being proportional to electron density appears to be well established [28,29].

Because of the small kinetic energies involved it is generally accepted that the dominant method of energy transfer in atom-surface collisions is through excitation of phonons. When specifically referring to conducting surfaces, there is also the question of whether an atom colliding with the surface will generate electronic excitations, and the most likely process at least for metals would be the creation of electron-hole (e-h) pairs. For the particular case of He atom scattering, there have been a number of theoretical studies of the possibility of electronic excitations and the results, with only very special exceptions, indicate that electron-hole pair creation is negligible under normal experimental conditions [30]. For heavier atoms, such as the other rare gases, the excitation of e-h pairs becomes somewhat more probable, but for the most part remains small and the dominant process for gas-surface energy transfer is through creation and annihilation of phonons.

The fact that incoming atomic projectiles are repelled by the weak electron cloud far outside the surface means that they do not directly sense the positions and vibrations of the target core atoms, but rather sense the target atoms only indirectly through electronic interactions. This has significant importance in the case of gas-surface energy exchange via phonons. Because of the distant interaction, atomic projectiles sense the vibrations of the surface electrons, and only indirectly those of the core atoms, and the latter may be quite different from the former in both amplitude and polarization. This was first realized experimentally in He atom scattering from the Cu(001) surface where it was observed that the scattering cross section for excitation of the longitudinal phonon resonance was seemingly anomalously large compared to the weak signal that would be predicted based on the polarization vectors of the crystal cores [31]. Many other such events have subsequently been observed in which the vibrations of the surface electron density produces He atom scattering intensities that behave quite differently than those that would be predicted upon considerations of the core vibrations alone [32–34]. This strong involvement of the electron density response makes atom scattering significantly different from other commonly used methods, such as electron, X-ray or neutron scattering, all of which directly measure the vibrations of the cores. In atom-surface scattering the atom senses an effective vibrational displacement, that of the surface electrons, and only indirectly the vibrations of the cores.

More recently the problem of how to determine the effective vibrational displacement for inelastic atom-surface scattering has been treated in a novel manner using electron-phonon interaction (e-ph) theory [35]. This treatment uses extensions, appropriate for the atom-surface interaction, of the theory of electron-phonon interaction adapted from that used in the theory of superconductivity [36,37]. Explicit calculations of single quantum annihilation and creation show that the intensities of scattering by single phonon events in metals are directly proportional to the mode selected components of the electron-phonon coupling constant λ introduced into the theory of superconductivity by Eliashberg [38] (note that λ is sometimes known as the electron mass correction factor). Quantitative theoretical agreement was demonstrated with experimental measurements of He atom scattering by the shear-vertical (SV) modes of thin, ordered multilayers of Pb on a Cu(111) substrate [35,39].

The purpose of this paper is to review and expand on the work of Sklyadneva et al. [35,39] and to present a more complete picture of the electron-phonon contribution to both elastic and inelastic scattering of atoms by surfaces. This work identifies and places into quantitative terms a number of features of the atom-surface interaction potential for both elastic and inelastic scattering. The electron-phonon interaction couples the motion of the electron density to that of the crystal cores and allows explicit determination of the effective vibrational displacements sensed by the colliding atomic projectiles. Hence the phonon vibrations giving rise to energy transfer to the atomic projectiles are directly related to the actual vibrations of the cores, i.e., to the same vibrational displacements measured by electron, X-ray or neutron scattering.

In the process the position and thickness of the thin region of the electron gas where the overwhelming majority of the repulsive interaction occurs is clearly and quantitatively delineated. This thin layer can be identified with the topology of the quasi-two-dimensional layer that is often called the locus of classical turning points, or region of closest approach. This identification arises naturally because the electron-phonon interaction with the incoming projectile atom occurs in the region of overlap between the surface electronic wave functions, as they decay away outside the last crystal layer, and the distorted wave functions of the atomic projectiles which decay extremely rapidly in the opposite direction into the surface.

Very important to any many body scattering system is a proper treatment of the Debye-Waller (D-W) factor. The Debye-Waller expression is usually written as $\exp\{-2W(\mathbf{k}_f, \mathbf{k}_i)\}$ and appears as a multiplicative factor in calculations of the intensity of any coherent quantum mechanical component of the observable scattered intensity, such as diffraction peaks, diffuse elastic intensity, or inelastic scattering. It is interpreted as a decrease in a particular quantum mechanically coherent intensity component due to increasing fractions of intensity directed into inelastic phonon transfer channels. As a part of this work we review the formal treatment of atom-surface scattering theory and demonstrate how the Debye-Waller factor arises naturally when starting from first principles. In particular, we show how the full Debye-Waller factor should appear in a proper treatment of the distorted wave Born approximation. This is important, because many theoretical treatments of single phonon inelastic scattering rely on the DWBA, and if approximations leading to the DWBA are invoked too early in such a theoretical analysis, the Debye-Waller factor does not appear or is incorrectly evaluated [40].

The process of determining the correct Debye-Waller factor for atom scattering leads to an identification of the effective mean square displacement sampled in the collision. To explain this more instructively, it is of interest to first discuss the argument $2W$ of the Debye-Waller factor as it usually appears in bulk neutron or X-ray diffraction, or in Low Energy Electron Diffraction (LEED). In its simplest form it is given in terms of the mean square displacement of a crystal atom

$$2W = \left\langle [\Delta\mathbf{k}\cdot\mathbf{u}_l]^2 \right\rangle \ , \tag{1}$$

where if all crystal atoms are identical l is the site label of any one of them, $\mathbf{u}_l$ is its displacement vector and $\hbar\Delta\mathbf{k} = \hbar(\mathbf{k}_f - \mathbf{k}_i)$ is the momentum transfer, or scattering vector. The simplest approximation is to use a Debye distribution of phonons at high temperature, i.e., for temperatures T greater than the Debye temperature Θ_D and for simple crystal lattices this leads to $2W \longrightarrow 3\hbar^2\Delta\mathbf{k}^2T/[k_BM_S\Theta_D^2]$ where k_B is the Boltzmann constant. For the case of atom-surface scattering, recognizing that momentum transfer parallel to the surface is usually small compared to the perpendicular direction, this expression is often simplified to that for specular scattering which is

$$2W \ \longrightarrow\ \frac{24\ m}{M_S}\,\frac{E_i\cos^2(\theta_i)T}{k_B\Theta_D^2}\ , \tag{2}$$

where E_i is the incident kinetic energy and θ_i is the incident angle measured with respect to the surface normal direction and m and M_S are the masses of the projectile and target, respectively. However, Eq. (2) presents some major problems of interpretation, because only the temperature T in that expression is clearly identified and well defined, as opposed to the situation of Eq. (1) for neutrons in which all quantities are unambiguously identified, with the displacement and mass M_S clearly being those of the crystal cores. For atom scattering from a conducting surface the mean square displacements which define the Debye-Waller exponent are those of the surface charge density that occur at the classical turning point as an effect of the thermal motion of the underlying atom cores. In this case the mass M_S appearing in Eq. (2) has to be viewed as an effective mass which may have little to do with the actual masses at the surface.

This unsatisfactory situation concerning the Debye-Waller exponent for atom scattering from a conducting surface has led to the new theoretical treatment of the scattering process presented here which invokes the electron-phonon interaction. In this treatment the Debye-Waller factor is still expressed in terms of an effective mean square displacement of the surface electrons, however, this effective mean square displacement is directly related to a weighted mean square displacement of the crystal core displacements. This means that all quantities appearing in the Debye-Waller argument $2W$ become well defined in terms of the readily calculable and well understood core vibrations.

Since this treatment relates the scattering intensities and Debye-Waller factor to the crystal cores via the electron-phonon interaction, it is shown that essentially all aspects of the scattering can be related to the electron-phonon coupling constant λ of superconductivity theory, or to its phonon mode specific components $\lambda_{\mathbf{Q},\nu}$ defined through the relation $\lambda = \langle\lambda_{\mathbf{Q},\nu}\rangle = \sum_{\mathbf{Q},\nu}\lambda_{\mathbf{Q},\nu}/(3N)$ where N is the number of atoms and $3N$ is the number of phonons, and where $\{\mathbf{Q},\nu\}$ is the set of quantum numbers that completely specifies a surface phonon mode, i.e., $\mathbf{Q}$ is its parallel wave vector and ν is the branch index [41]. These mode-specific components of λ are generally associated with the width of a phonon mode [42–44], but we will show below that they also define the intensity of phonon mode peaks in the energy resolved He atom scattering spectra from metal surfaces.

The impetus of this work was the earlier recognition that the measured intensities for single phonon transfer events can be expressed in terms of proportionality to $\lambda_{\mathbf{Q},\nu}$ [35,39,45,46]. In this review a detailed derivation of this earlier single phonon excitation theory is developed, and the theory is extended to include descriptions of other measurable properties of atom-surface scattering such as the intensities of elastic diffraction peaks and the Debye-Waller factor. This description begins in Section 2 with a formal treatment of atom-surface scattering theory which results in expressions giving the measurable scattering intensities for elastic (diffraction) and single phonon features, complete with the Debye-Waller factor describing thermal attenuation of all quantum features. The extension to other quantum features such as multiple phonon excitation are briefly discussed. Section 3 extracts from the formal scattering theory the distorted wave Born approximation. This is of importance because most treatments of single phonon excitation are carried out in the DWBA. After these presentations of formal scattering theory the electron-phonon approach to atom-surface scattering is developed in Section 4. The next section, Section 5, shows how the elastic and inelastic quantum features are related to the e-ph coupling constant λ and its mode components $\lambda_{\mathbf{Q},\nu}$. An important development in this section is the demonstration that the argument of the Debye-Waller factor $2W(\mathbf{k}_f, \mathbf{k}_i)$ under a wide range of conditions is proportional to λ. This property is exploited in Section 6 to extract values of λ at the surface of a large number of systems using available Debye-Waller attenuation data. Beginning with the simplest systems and experimental data, namely the thermal attenuation of He atom scattering from simple metals, a total of over 50 different systems are analyzed and the corresponding surface values of λ are determined and compared with known values of λ for the bulk materials. In addition to the simple metals, data is analyzed for Pb overlayers on Cu(111), chalcogenides and topological surfaces, graphite and single-layer graphene supported on ordered metal substrates. In all cases the values of λ obtained at the surface compare favorably with known bulk values available in the literature. Most of the experimental data analyzed were for the thermal attenuation of elastic and single phonon scattering of He atoms, but several examples of other projectiles such as Ne are examined. In addition to the temperature dependence of the Debye-Waller factor, some values of λ were obtained using the energy and angular dependence of the Debye-Waller exponent. Section 7 gives a presentation of the inelastic close coupling (ICC) formalism which is a formalism for calculating elastic and inelastic scattering intensities and which automatically includes the thermal attenuation of these quantum features. This section is included because it provides an independent method for calculating the thermal attenuation and, when combined with the e-ph theory developed here, provides an independent way of extracting λ from thermal attenuation data. Finally, in Section 8 some conclusions are drawn and possible extensions of this work are discussed.

2. Formal treatment of surface scattering

It is of interest to think of surface scattering geometry as one in which the target occupies half of all space, to which is assigned the region $z \lesssim 0$. The incident beam of particles is prepared as a very narrow wave packet traveling towards the surface, and the detector measures the flux of scattered particles in the asymptotic region $z \to +\infty$ after the collision with the surface. The primary difference when compared with scattering from a three dimensional target is the broken symmetry perpendicular to the surface which implies that momentum is not conserved in the z-direction. However, if there is a well defined periodicity parallel to the surface, a condition of momentum conservation will arise in those directions, which is denoted as the two dimensional vector $\mathbf{R}$, i.e., $\mathbf{r} = \{x, y, z\} = \{\mathbf{R}, z\}$. It is best to begin from elementary principles of formal scattering theory, and then later impose the broken symmetry presented by the surface target. In this manner, one is assured of retaining all remaining symmetry and quantum effects, and in particular, a correct analysis of the Debye-Waller factor is obtained.

An appropriate starting point is to begin from the Generalized Fermi Golden Rule, which gives the transition rate w_{fi} in terms of the transition matrix T_{fi} [47,48].

$$w_{fi} = \frac{2\pi}{\hbar} \left| T_{fi} \right|^2 \delta(\mathcal{E}_f - \mathcal{E}_i) , \tag{3}$$

where $\mathcal{E}_i$ and $\mathcal{E}_f$ are the initial and final total energies of the universe of interest, consisting of target and projectile described by the Hamiltonian

$$H = H_{phonons} + H_{projectile} + V , \tag{4}$$

where $H_{phonons}$ is the unperturbed Hamiltonian of the many-body target (not necessarily a periodic crystal), $H_{projectile}$ is the unperturbed Hamiltonian of the projectile atom and V is the interaction potential coupling the two systems. The state labels i and f denote the good quantum numbers of the initial and final states of the system when the target and projectile are well separated and not coupled by the interaction potential V. These states are defined by

$$H_{phonons} |n_i\rangle = \varepsilon_i |n_i\rangle , \tag{5}$$

and

$$H_{projectile} \Phi_i(\mathbf{r}) = E_i \Phi_i(\mathbf{r}) . \tag{6}$$

Under ideal experimental conditions for atom-surface scattering, an unperturbed projectile state of arbitrary momentum $\hbar\mathbf{k}_f$ is a plane wave

$$\Phi_f(\mathbf{r}) = \frac{1}{L^{3/2}} e^{i\mathbf{k}_f \cdot \mathbf{r}} , \tag{7}$$

where L is a quantization length. The transition matrix is then given by

$$T_{fi} = \left(\Phi_f \left| \langle n_f | \widehat{T} | n_i \rangle \right| \Phi_i \right) , \tag{8}$$

where $\widehat{T}$ is the transition operator.

In scattering from a many-body target the initial and final states of the target are usually not measurable, hence one must average over initial target states and sum over all possible final target states. The transition rate for a projectile initially prepared in the state Φ_i to make a transition to state Φ_f is given by

$$w(\mathbf{k}_f, \mathbf{k}_i) = \left\langle \frac{2\pi}{\hbar} \sum_{n_f} \left| T_{fi} \right|^2 \delta(\mathcal{E}_f - \mathcal{E}_i) \right\rangle , \tag{9}$$

where the large brackets $\langle \ldots \rangle$ signify the average over an equilibrium distribution of initial target states.

For completeness we note that the actual quantity measured in most atom-surface or molecule-surface scattering experiments is the differential reflection coefficient $d^3R/d\Omega_f dE_f$ which is the fraction of particles scattered into a small solid angle $d\Omega_f$ and into a small final energy interval dE_f. This is related to the transition rate in the following way:

$$\frac{d^3R}{d\Omega_f \, dE_f} = \frac{L^4}{(2\pi\hbar)^3} \frac{m^2 |\mathbf{k}_f|}{k_{iz}} \; w(\mathbf{k}_f, \mathbf{k}_i) , \tag{10}$$

where k_{iz}, which is proportional to the incident flux, is the component of $\mathbf{k}_i$ normal to the surface.

We can eliminate the sum over final target states in Eq. (9) via the Van Hove-Glauber-Weinstock [49–51] transformation to the interaction picture. Representing the δ-function in Eq. (9) by a Fourier expansion

$$w(\mathbf{k}_f, \mathbf{k}_i) = \frac{1}{\hbar^2} \int_{-\infty}^{+\infty} dt \left\langle \sum_{n_f} T_{if} T_{fi} \, e^{-i(\varepsilon_f - \varepsilon_i + E_f - E_i)t/\hbar} \right\rangle , \tag{11}$$

and transforming to the time-dependent transition operators in the interaction picture via

$$\widehat{T}(t) = e^{iH_{phonon} t/\hbar} \widehat{T} e^{-iH_{phonon} t/\hbar} , \tag{12}$$

the transition rate becomes

$$w(\mathbf{k}_f, \mathbf{k}_i) = \frac{1}{\hbar^2} \int_{-\infty}^{+\infty} dt e^{-i(E_f - E_i)t/\hbar} \tag{13}$$

$$\times \left\langle \sum_{n_f} \left(\Phi_i \left| \langle n_i | \widehat{T}(0) | n_f \rangle \right| \Phi_f \right) \left(\Phi_f \left| \langle n_f | \widehat{T}(t) | n_i \rangle \right| \Phi_i \right) \right\rangle .$$

The sum over final target states is eliminated via closure

$$\sum_{n_f} |n_f\rangle\langle n_f| = \widehat{\mathbf{1}}, \tag{14}$$

leading to

$$w(\mathbf{k}_f, \mathbf{k}_i) = \frac{1}{\hbar^2} \int_{-\infty}^{+\infty} dt \; e^{-i(E_f - E_i)t/\hbar}$$

$$\times \left\langle \left(\Phi_i \left| \widehat{T}(0) \right| \Phi_f \right) \left(\Phi_f \left| \widehat{T}(t) \right| \Phi_i \right) \right\rangle , \tag{15}$$

with a more compact notation being

$$w(\mathbf{k}_f, \mathbf{k}_i) = \frac{1}{\hbar^2} \int_{-\infty}^{+\infty} dt \; e^{-i(E_f - E_i)t/\hbar} \left\langle \widehat{T}(0)_{\mathbf{k}_i, \mathbf{k}_f} \; \widehat{T}(t)_{\mathbf{k}_f, \mathbf{k}_i} \right\rangle . \tag{16}$$

In the case of scattering from a bulk target, the classic example being neutron scattering from a crystal, the transition operator is usually written as a pairwise summation over all unit cells and over all atoms forming the basis within each cell

$$\widehat{T} = \sum_{\ell} \sum_{\kappa} \widehat{T}_{\ell,\kappa} , \tag{17}$$

where ℓ is a three-dimensional (3-D) integer denoting each cell and κ is an integer denoting basis elements within the unit cell.

The case of atom-surface scattering is somewhat different. The interaction consists of an attractive van der Waals potential in front of a strongly repulsive potential created by Pauli exclusion of the overlapping electron clouds of the projectile atom and the surface. The electron density in front of the terminal layer of surface atoms decays approximately exponentially, thus the repulsive scattering occurs over a very short region in the direction z normal to the surface, but well in front of the first layer of target atomic cores. As we will explicitly show in Sec. 4 below, the interactions involving inelastic exchange of energy occur over a very short range primarily with the repulsive part of the potential. The qualitative reasons for this are evident; the $1/z^3$ tail of the long-range attractive van der Waals force is an average arising from all the target atoms, hence it does not vibrate and cannot contribute to the exchange of phonon energy quanta, and the higher order corrections to the van der Waals forces are only weakly dependent on the vibrations of the target cores. The repulsive part of the potential is roughly exponentially decreasing with z outside the surface, while the wave functions of the incoming atomic projectiles are strongly decreasing functions of z inside this region of increasing surface electronic density. Hence, the region where inelastic interactions with the phonons of the target can occur is in the very narrow region of overlap between the outward-decaying electronic density and the inward-decaying atomic wave functions. This qualitative description of the quasi-two-dimensional nature of the atom-surface interaction will be demonstrated in a more rigorous manner below in Sec. 4. Effectively, the repulsive atom-surface collision occurs within a thin two-dimensional (2-D) layer in which energy transfer via phonons occurs over a very narrow region. Albeit, this is a region that may be corrugated by the underlying target core atoms, but nevertheless is a narrow region that can be viewed as a corrugated 2-D surface, essentially the surface of the locus of classical turning points.

Thus, for surface scattering of atoms the transition operator can be viewed as a 2-D summation over unit cells parallel to the surface. Formally, the transition operator looks the same as Eq. (17) but ℓ is now a 2-D integer that denotes all surface unit cells and κ is an integer that counts elements within the surface unit cell. In some instances, for example when considering ordered overlayers on top of a substrate, it is convenient to use κ as the label to count the atomic layers from the outermost down to the substrate.

For simplicity, and to avoid cluttering the notation, for the present it will be assumed that the surface consists of Bravais unit cells and the summation over κ is neglected. This assumption is merely for simplifying the notation in many of the equations to come below, and it should be stressed that the general case of a unit cell with a multiple core basis is a straightforward generalization that can be readily carried out. In fact, it is necessary in some instances to retain the possibility of summing over elements within a surface unit cell and one important example arises when taking the classical limit of large kinetic energies and high temperatures [52].

If it is further assumed that all unit cells are identical, the transition operator can be written as a pairwise summation

$$\widehat{T}(t) \;=\; \sum_{\ell} \widehat{T}_{\ell}(t) \;=\; \sum_{\ell} \widehat{T}^{0}(\mathbf{r}-\mathbf{r}_{\ell}-\mathbf{u}_{\ell}(t))\;, \tag{18}$$

where ℓ is now regarded as a 2-D integer. Note that $\mathbf{r}_{\ell}=(\mathbf{R}_{\ell},z_S)$ is actually a two-dimensional position vector because the z-component is a constant denoting the position of the surface plane. The displacement vector $\mathbf{u}_{\ell}=(\mathbf{U}_{\ell},u_{z,\ell})$ is three-dimensional and denotes vibrational displacement of the unit cell in all three directions, i.e., $\mathbf{U}_{\ell}(t)$ parallel to the surface and $u_{z,\ell}(t)$ perpendicular to the surface. However, it is important to reiterate that $\mathbf{u}_{\ell}$ is not, in general, the vibrational displacement vector of the atomic cores making up the target. As discussed above, atomic projectiles scatter from the electron density at a distance located well outside the positions of the cores, thus $\mathbf{u}_{\ell}$ is the effective displacement vector actually felt by the projectiles. One of the main objectives of this work is to relate this effective displacement to the true displacement vectors of the cores.

Recognizing that in general the displacement operator for a displacement $\mathbf{a}$ is $\exp\{-i\Delta\mathbf{k}\cdot\mathbf{a}\}$, the time-dependent transition operator becomes

$$\widehat{T} \;=\; \sum_{\ell} e^{-i\Delta\mathbf{k}\cdot(\mathbf{r}_{\ell}+\mathbf{u}_{\ell})}\;\widehat{T}^{0}(\mathbf{r})\;, \tag{19}$$

a result that can also be shown by direct evaluation of the transition matrix element for the operator of Eq. (18) using the atomic eigenstates of Eq. (7).

The transition operator of Eq. (19) allows the transition rate of Eq. (15) or (16) to be cast into the form

$$w(\mathbf{k}_f,\mathbf{k}_i) \;=\; \frac{1}{\hbar^2}\int_{-\infty}^{+\infty} dt\; e^{-i(E_f-E_i)t/\hbar}\sum_{\ell,\ell'} e^{-i\Delta\mathbf{K}\cdot(\mathbf{R}_{\ell}-\mathbf{R}_{\ell'})}$$
$$\times\left\langle\, e^{-i\Delta\mathbf{k}\cdot\mathbf{u}_{\ell}(0)}\; e^{i\Delta\mathbf{k}\cdot\mathbf{u}_{\ell'}(t)}\;\; T^{0}(0)_{\mathbf{k}_i,\mathbf{k}_f}\; T^{0}(t)_{\mathbf{k}_f,\mathbf{k}_i}\right\rangle\;, \tag{20}$$

where $\Delta\mathbf{K}$ is the two-dimensional component of $\Delta\mathbf{k}$ parallel to the surface. At this point, the expression still allows for the transition operator to retain t-dependence, i.e., we do not immediately make the standard assumption that all t-dependence is contained only in the displacement operator $\mathbf{u}_{\ell}(t)$. If the t-dependence in $T^{0}(t)_{\mathbf{k}_f,\mathbf{k}_i}$ is weak, one can make the decoupling approximation which consists of averaging both terms separately

$$w(\mathbf{k}_f,\mathbf{k}_i) \;=\; \frac{1}{\hbar^2}\int_{-\infty}^{+\infty} dt\; e^{-i(E_f-E_i)t/\hbar}\sum_{\ell,\ell'} e^{-i\Delta\mathbf{K}\cdot(\mathbf{R}_{\ell}-\mathbf{R}_{\ell'})}$$
$$\times\left\langle\, e^{-i\Delta\mathbf{k}\cdot\mathbf{u}_{\ell}(0)}\; e^{i\Delta\mathbf{k}\cdot\mathbf{u}_{\ell'}(t)}\right\rangle\left\langle\, T^{0}(0)_{\mathbf{k}_i,\mathbf{k}_f}\; T^{0}(t)_{\mathbf{k}_f,\mathbf{k}_i}\right\rangle. \tag{21}$$

This point becomes important later in the evaluation of the distorted wave Born approximation in atom-surface scattering, because when properly defined the DWBA is shown to retain a weak time-dependence in its approximation for the operator $T^{0}(t)_{\mathbf{k}_f,\mathbf{k}_i}$.

At this point, however, we will now make the standard assumption that the only time dependence is in the $\mathbf{u}_{\ell}(t)$, i.e., $T^{0}(t)_{\mathbf{k}_f,\mathbf{k}_i}=T^{0}_{\mathbf{k}_f,\mathbf{k}_i}$, thus the transition rate becomes

$$w(\mathbf{k}_f,\mathbf{k}_i) \;=\; \frac{1}{\hbar^2}\int_{-\infty}^{+\infty} dt\; e^{-i(E_f-E_i)t/\hbar}\sum_{\ell,\ell'} e^{-i\Delta\mathbf{K}\cdot(\mathbf{R}_{\ell}-\mathbf{R}_{\ell'})}\left|T^{0}_{\mathbf{k}_f,\mathbf{k}_i}\right|^2$$
$$\times\left\langle\; e^{-i\Delta\mathbf{k}\cdot\mathbf{u}_{\ell}(0)}\; e^{i\Delta\mathbf{k}\cdot\mathbf{u}_{\ell'}(t)}\right\rangle\;. \tag{22}$$

The average over vibrational displacement states is facilitated using two well-known theorems. First is the Baker-Campbell-Hausdorf theorem

$$e^{A}\;e^{B} \;=\; e^{A+B}\;e^{[A,B]/2}\;, \tag{23}$$

which is valid if both the operators A and B commute with the commutator $[A,B]$. The second is the theorem valid for any harmonic function u whose probability distribution is Gaussian:

$$\left\langle e^{au}\right\rangle \;=\; e^{a^2\langle u^2\rangle/2}\;, \tag{24}$$

with a an arbitrary constant which may be complex. Eq. (24) is clearly applicable to the average over phonons in the harmonic approximation.

The above theorems allow the following commutation and average-evaluation operations on Eq. (22)

$$w(\mathbf{k}_f,\mathbf{k}_i) = \;=\; \frac{1}{\hbar^2}\int_{-\infty}^{+\infty} dt\; e^{-i(E_f-E_i)t/\hbar}\sum_{\ell,\ell'} e^{-i\Delta\mathbf{K}\cdot(\mathbf{R}_{\ell}-\mathbf{R}_{\ell'})}\left|T^{0}_{\mathbf{k}_f,\mathbf{k}_i}\right|^2$$
$$\times\, e^{-\left\langle\left[\Delta\mathbf{k}\cdot\left(\mathbf{u}_{\ell}(0)-\mathbf{u}_{\ell'}(t)\right)\right]^2\right\rangle/2}\;\; e^{[\Delta\mathbf{k}\cdot\mathbf{u}_{\ell}(0),\;\Delta\mathbf{k}\cdot\mathbf{u}_{\ell'}(t)]/2}\;. \tag{25}$$

Since the commutator is a c-number, it can be combined with the cross terms arising from $\left\langle\left[\Delta\mathbf{k}\cdot\left(\mathbf{u}_{\ell}(0)-\mathbf{u}_{\ell'}(t)\right)\right]^2\right\rangle/2$. With the definition of the Debye-Waller exponent argument

$$W^{eff}(\mathbf{k}_f,\mathbf{k}_i) \;=\; \left\langle\left(\Delta\mathbf{k}\cdot\mathbf{u}_{\ell}(0)\right)^2\right\rangle/2 \;=\; \left\langle\left(\Delta\mathbf{k}\cdot\mathbf{u}_{\ell'}(t)\right)^2\right\rangle/2\;, \tag{26}$$

the mean square average being the same at all times t and for all unit cells ℓ, and the definition of the time-dependent displacement-displacement correlation function as

$$2\mathcal{W}^{eff}_{\ell,\ell'}(\mathbf{k}_f,\mathbf{k}_i,t) \;=\; \langle\Delta\mathbf{k}\cdot\mathbf{u}_{\ell}(0)\Delta\mathbf{k}\cdot\mathbf{u}_{\ell'}(t)\rangle\;, \tag{27}$$

the transition rate takes the following form

$$w(\mathbf{k}_f,\mathbf{k}_i) = \frac{1}{\hbar^2}\int_{-\infty}^{+\infty} dt e^{-i(E_f-E_i)t/\hbar}\sum_{\ell,\ell'} e^{-i\Delta\mathbf{K}\cdot(\mathbf{R}_\ell-\mathbf{R}_{\ell'})}\left|T^0_{\mathbf{k}_f,\mathbf{k}_i}\right|^2$$
$$\times\; e^{-2W^{eff}(\mathbf{k}_f,\mathbf{k}_i)} e^{2\mathcal{W}^{eff}_{\ell,\ell'}(\mathbf{k}_f,\mathbf{k}_i,t)} \tag{28}$$

One important point of this work is to recognize that the Debye-Waller factor (or its argument $2W^{eff}(\mathbf{k}_f,\mathbf{k}_i)$) is not the traditional D-W factor of, for example, neutron scattering. To paraphrase what was already stated in the Introduction, in neutron scattering the D-W factor is determined by the mean-square vibrations of the atomic cores of the bulk. In atom-surface scattering, the projectile atoms scatter from the electron density outside of the terminal atomic core layer of the sample. Thus, the vibrations "seen" by the projectile atom are those of the electron cloud, which are driven by the core vibrations via the electron-phonon interaction. This is the reason for labeling $2W^{eff}(\mathbf{k}_f,\mathbf{k}_i)$ as the "effective" D-W argument.

It is worthwhile noting that the Debye-Waller argument is given by the correlation function evaluated at equal positions and zero time (i.e., equal times). This means that in the integrand of Eq. (28), if $\ell = \ell'$ and $t = 0$, the Debye-Waller argument is exactly cancelled by the correlation function. This has consequences for the classical limit of large numbers of phonon transfers, when the most important contributions to the correlation function are at small times and equal positions, i.e., the classical limit corresponds to when quantum correlation lengths and times become very small. In the classical limit, the correlation function can be expanded, and the first order term exactly cancels $2W^{eff}(\mathbf{k}_f,\mathbf{k}_i)$, implying that all quantum features have been repressed and only broader, classical distributions are left behind in the scattered spectra [52,53].

In passing it is of interest to point out that the geometry of surface scattering is really that of a backscattering experiment, meaning that the projectile is reflected from the surface back into the same half-space from which it arrived. The implication is that for the scattering vector $\Delta\mathbf{k} = (\Delta\mathbf{K}, \Delta k_z)$, its normal component is typically large compared to the parallel components since $\Delta k_z = k_{fz} - k_{iz} = |k_{fz}| + |k_{iz}|$. This means, for example, that the more important contribution to the effective Debye-Waller exponent of Eq. (26) will, under most experimental conditions, come from the contributions due to normal momentum transfer.

For collisions in which the interactions with the surface vibrations are weak, in which $2\mathcal{W}^{eff}_{\ell,\ell'}(t) \ll 1$, which is essentially the same as having a small Debye-Waller argument, $2W^{eff} \ll 1$, the exponential of the correlation function in Eq. (28) can be expanded as

$$e^{2\mathcal{W}^{eff}_{\ell,\ell'}(t)} \approx 1 + 2\mathcal{W}^{eff}_{\ell,\ell'}(t) + 2\left[\mathcal{W}^{eff}_{\ell,\ell'}(t)\right]^2 + \dots . \tag{29}$$

The leading term in Eq. (29) is associated with elastic scattering in which no energy is transferred in the collision of the atom with the surface. The first order term gives the leading contribution to single quantum transfers of phonons. Double phonon transfers and larger are contained in the higher order terms in the expansion of Eq. (29).

2.1. Elastic scattering

Keeping only the lowest order term in the expansion of Eq. (29) leads to

$$w^{(0)}(\mathbf{k}_f,\mathbf{k}_i) = \frac{1}{\hbar^2}\int_{-\infty}^{+\infty} dt\; e^{-i(E_f-E_i)t/\hbar}\; e^{-2W^{eff}(\mathbf{k}_f,\mathbf{k}_i)} \tag{30}$$
$$\times \sum_{\ell,\ell'} e^{-i\Delta\mathbf{K}\cdot(\mathbf{R}_\ell-\mathbf{R}_{\ell'})}\left|T^0_{\mathbf{k}_f,\mathbf{k}_i}\right|^2 .$$

The integral over time is the Fourier transform of a Dirac δ-function which gives the conservation of energy. The summations over surface lattice cells produce the law of conservation of momentum parallel to the surface: $\sum_{\ell,\ell'} \exp\{-i\Delta\mathbf{K}\cdot(\mathbf{R}_\ell - \mathbf{R}_{\ell'})\} = N^2 \sum_{\mathbf{G}} \delta_{\Delta\mathbf{K},\mathbf{G}}$, where N is the number of surface unit cells and the Kronecker δ-function signifies that the final parallel momentum after collision can differ from the incident parallel momentum only by a surface reciprocal lattice vector $\mathbf{G}$, or $\mathbf{K}_f = \mathbf{K}_i + \mathbf{G}$ which is Bragg's law for diffraction in two dimensions.

The elastic transition rate then takes the form

$$w^{(0)}(\mathbf{k}_f,\mathbf{k}_i) = \frac{2\pi}{\hbar} N^2 \sum_{\mathbf{G}} e^{-2W^{eff}(\mathbf{k}_f,\mathbf{k}_i)} \left|T^0_{\mathbf{k}_f,\mathbf{k}_i}\right|^2 \delta_{\Delta\mathbf{K},\mathbf{G}}\; \delta\left(E_f - E_i\right) . \tag{31}$$

It is important to emphasize that this is an exact result, within the kinematic approximations of a rigidly vibrating Bravais surface unit cell and assuming vibrations within the harmonic approximation. The δ-functions insure that the only observable scattering intensities are diffraction beams occurring with $\mathbf{K}_f = \mathbf{K}_i \pm \mathbf{G}$ and the final wave vector perpendicular to the surface is dictated by energy conservation, i.e.,

$$k_{fz} = \sqrt{\mathbf{k}_i^2 - (\mathbf{K}+\mathbf{G})^2} . \tag{32}$$

The intensity of each diffracted beam is proportional to the squared transition matrix $\left|T^0_{\mathbf{k}_f,\mathbf{k}_i}\right|^2$. Each diffraction intensity is multiplied by a Debye-Waller factor which correctly includes momentum transfer in all three directions. This latter statement is important because if one begins from a theoretical approximation with initial restrictions that are too stringent, such as beginning with the distorted wave Born approximation, the correct form of the Debye-Waller factor is not always obtained [54,55]. However, the approach in this section, which starts from first principles, insures that the Debye-Waller factor is correctly included, furthermore, it shows that if we subsequently make further, more restrictive approximations on the transition matrix $T^0_{\mathbf{k}_f,\mathbf{k}_i}$ such as eventually evaluating it in the DWBA, the correct Debye-Waller factor will still be retained.

For large values of $\mathbf{G}$ the perpendicular momentum of Eq. (32) becomes imaginary, and in order to assure the boundary condition that the amplitudes of these waves remain finite, the sign of the square root in Eq. (32) must be chosen to give exponentially decaying behavior in the asymptotic region. These are the evanescent diffraction beams.

2.2. Single phonon inelastic scattering

The transition rate for inelastic scattering with transfer of a single phonon is obtained from the general expression of Eq. (28) upon replacing the exponentiated displacement correlation function by its first order term in the expansion of Eq. (29)

$$w^{(1)}(\mathbf{k}_f,\mathbf{k}_i) = \frac{1}{\hbar^2}\int_{-\infty}^{+\infty} dt\; e^{-i(E_f-E_i)t/\hbar}$$
$$\times \sum_{\ell,\ell'} e^{-i\Delta\mathbf{K}\cdot(\mathbf{R}_\ell-\mathbf{R}_{\ell'})}\left|T^0_{\mathbf{k}_f,\mathbf{k}_i}\right|^2$$
$$\times\; e^{-2W^{eff}(\mathbf{k}_f,\mathbf{k}_i)} \;\langle \Delta\mathbf{k}\cdot\mathbf{u}_\ell(0)\Delta\mathbf{k}\cdot\mathbf{u}_{\ell'}(t)\rangle\; . \tag{33}$$

A review of the development of the phonon displacement operator in terms of normal modes appears in Appendix A. This shows that in a quite general manner, the displacement function can be expanded in normal modes as

$$\begin{aligned}\langle \Delta\mathbf{k}\cdot\mathbf{u}_{\ell}(0)\Delta\mathbf{k}\cdot\mathbf{u}_{\ell'}(t)\rangle = &\sum_{\alpha,\alpha'=1}^{3}\Delta k_{\alpha}\Delta k_{\alpha'}\\ &\times\sum_{\mathbf{Q},\nu}\left[\frac{\hbar}{2\,NM_S\omega(\mathbf{Q},\nu)}\right]e_{\alpha}(\mathbf{Q},\nu)e^{*}_{\alpha'}(\mathbf{Q},\nu)\\ &\times\, e^{-i\mathbf{Q}\cdot(\mathbf{R}_{\ell'}-\mathbf{R}_{\ell})}\,\left\{\left[n_{BE}(\omega(\mathbf{Q},\nu))+1\right]e^{-i\omega(\mathbf{Q},\nu)t}\right.\\ &\left.+\,n_{BE}(\omega(\mathbf{Q},\nu))e^{i\omega(\mathbf{Q},\nu)t}\right\} \end{aligned} \tag{34}$$

where α, α' run over the three cartesian components of the displacement, $\sum_{\mathbf{Q},\nu}$ is a summation over the parallel wave vector $\mathbf{Q}$ and branch index ν of the phonon mode, M_S is the effective mass of the surface unit cell, $\omega(\mathbf{Q},\nu)$ is the mode frequency, $n_{BE}(\omega(\mathbf{Q},\nu))$ is the Bose-Einstein distribution function, and $e_{\alpha}(\mathbf{Q},\nu)$ is the α-th cartesian component of the mode polarization vector.

When the displacement correlation function of Eq. (34) is inserted into the transition rate of Eq. (33) the sums over lattice positions ℓ and the integral over time can be carried out as before in the case of elastic scattering. The results are δ-functions giving energy and momentum conservation relations that include the transfer of a phonon, and the transition rate becomes

$$\begin{aligned} w^{(1)}(\mathbf{k}_f,\mathbf{k}_i) \;=\; &\frac{2\pi}{\hbar}\,N^2\sum_{\mathbf{Q},\;\nu}\;\sum_{\mathbf{G}}\delta_{\Delta\mathbf{K}-\mathbf{Q},\;\mathbf{G}}\;e^{-2W(\mathbf{k}_f,\mathbf{k}_i)}\left|T^{0}_{\mathbf{k}_f,\mathbf{k}_i}\right|^2\\ &\times\sum_{\alpha,\;\alpha'=1}^{3}\Delta k_{\alpha}\Delta k_{\alpha'}\frac{\hbar}{2\,NM_S\omega(\mathbf{Q},\nu)}\;e_{\alpha}(\mathbf{Q},\nu)\;e^{*}_{\alpha'}(\mathbf{Q},\nu)\\ &\times\left\{\left[n_{BE}(\omega(\mathbf{Q},\nu))+1\right]\delta\left(E_f-E_i+\hbar\omega(\mathbf{Q},\nu)\right)+\right.\\ &\left.+\,n_{BE}(\omega(\mathbf{Q},\nu))\delta\left(E_f-E_i-\hbar\omega(\mathbf{Q},\nu)\right)\right\}. \end{aligned} \tag{35}$$

In Eq. (35) the term proportional to $n_{BE}(\omega(\mathbf{Q},\nu)) + 1$ describes single phonon creation with the additional constant of $+1$ arising from zero point motion, while that term proportional to $n_{BE}(\omega(\mathbf{Q},\nu))$ gives phonon annihilation. The delta functions in parallel wave vector insure that $\Delta\mathbf{K} = \mathbf{Q} + \mathbf{G}$ or $\mathbf{K}_f = \mathbf{K}_i + \mathbf{Q} + \mathbf{G}$, i.e., the parallel momentum conservation law includes the momentum transferred by the phonon as well as a possible reciprocal lattice vector. The energy conservation delta function then fixes the value of k_{fz}, for example, in the case of phonon annihilation $k^2_{fz} = 2\,m[\,E_i + \hbar\omega(\mathbf{Q},\nu))]/\hbar^2 - (\mathbf{K}_i + \mathbf{Q} + \mathbf{G})^2$.

Eq. (35) can be written in the slightly simpler form after evaluating the summation using the momentum conservation δ-function

$$\begin{aligned} w^{(1)}(\mathbf{k}_f,\mathbf{k}_i) = &\frac{2\pi}{\hbar}\,N^2\sum_{\nu}\,e^{-2W^{eff}(\mathbf{k}_f,\mathbf{k}_i)}\left|T^{0}_{\mathbf{k}_f,\mathbf{k}_i}\right|^2\\ &\times\sum_{\alpha,\;\alpha'=1}^{3}\Delta k_{\alpha}\Delta k_{\alpha'}\frac{\hbar}{2\,NM_S\omega(\Delta\mathbf{K},\nu)}\\ &\times e_{\alpha}(\Delta\mathbf{K},\nu)\;e^{*}_{\alpha'}(\Delta\mathbf{K},\nu)\\ &\times|\;n_{BE}(\omega(\Delta\mathbf{K},\nu))\;|\delta(E_f-E_i-\hbar\omega(\Delta\mathbf{K},\nu)), \end{aligned} \tag{36}$$

where it is understood that $\omega(\Delta\mathbf{K},\nu) = \omega(\Delta\mathbf{K} + \mathbf{G},\nu)$ and similarly for the polarization vector, and we have used the fact that $-\,n_{BE}(-\omega(\Delta\mathbf{K},\nu)) = n_{BE}(\omega(\Delta\mathbf{K},\nu)) + 1$.

3. Distorted wave Born approximation

A formal treatment of the distorted wave Born approximation is perhaps best couched in terms of the two-potential formalism of scattering theory, as developed by Gell-Mann and Goldberger [47,48,56]. In this formalism the total Hamiltonian under consideration, consisting of the projectile and the many-body target, is written with the interaction potential V expressed as consisting of two parts, as follows:

$$H \;=\; H_0 \;+\; V \;=\; H_0 \;+\; \mathcal{U} \;+\; \mathcal{V}\,, \tag{37}$$

with eigenstates of each of these Hamiltonians defined as

$$\begin{aligned} &H_0\;\Phi_i = \mathcal{E}_i\;\Phi_i,\\ &H\;\Psi_i^{(\pm)} = (H_0\;+\;V)\;\Psi_i^{(\pm)}\\ &\qquad = (H_0\;+\;\mathcal{U}\;+\;\mathcal{V})\;\Psi_i^{(\pm)}\;=\;\mathcal{E}_i\;\;\Psi_i^{(\pm)}, \end{aligned} \tag{38}$$

where $\mathcal{U}$ is the distorting potential and $\mathcal{V}$ is the interaction potential, and the interaction, or distorted state given by

$$(H_0\;+\;\mathcal{U})\;\chi_i^{(\pm)}\;=\;\mathcal{E}_i\;\;\chi_i^{(\pm)}\,, \tag{39}$$

where the notation is such that $\Psi_i^{(+)}$ is an outgoing state, i.e., a state satisfying boundary conditions with the projectile initially in an incident incoming plane wave state with outgoing scattered waves. The index i denotes the good quantum numbers of the unperturbed state Φ_i, which are not necessarily good quantum numbers of the full state Ψ_i. The state $\Psi_i^{(-)}$ is the corresponding solution satisfying incoming wave boundary conditions.

A bit of explanation as to why the two-potential formalism is used is perhaps in order. Unlike some other scattering experiments, such as neutron or X-ray scattering. The surface scattering of atoms (and molecules) is a backscattering configuration. That is to say, while neutrons or X-rays are scattered predominantly in the forward direction and can be described by a cross section, in atom scattering all projectiles are scattered backwards into the half-space from which they came, i.e., the total cross section is infinite. For this reason in developing a theory it is convenient to use the two-potential formalism, sometimes called the distorted wave formalism, in which the potential $\mathcal{U}$ describes the very strong backscattering potential (whose eigenfunctions are the distorted waves) and the remainder (which contains most of the interesting physics) is contained in the potential $\mathcal{V}$.

In this formalism, the transition matrix elements can be written in several ways, among them are

$$T_{fi}\;=\;\left(\Phi_f\,|V|\,\Psi_i^{(+)}\right)\;=\;\left(\Phi_f\,|\mathcal{U}|\,\chi_i^{(+)}\right)\;+\;\left(\chi_f^{(-)}\,|\mathcal{V}|\,\Psi_i^{(+)}\right)\,. \tag{40}$$

The distorted wave Born approximation is obtained by solving for T_{fi} to lowest order by iteration on Eq. (40) with the first order correction to the full wave function, $\Psi_i^{(+)} \longrightarrow \chi_i^{(+)}$:

$$T_{fi}\;\approx\;\left(\Phi_f\,|\mathcal{U}|\,\chi_i^{(+)}\right)\;+\;\left(\chi_f^{(-)}\,|\mathcal{V}|\,\chi_i^{(+)}\right)\,. \tag{41}$$

In the treatment of atom-surface scattering it has often been convenient to treat $\mathcal{U}$ as a static potential whose repulsive part scatters incoming particles back into the half-space in front of the surface, and usually it is even taken to be a flat surface depending only on the normal position component z, i.e., $\mathcal{U}(\mathbf{r}) = \mathcal{U}(z)$. All corrugation of the surface and dynamics such as vibrations are then contained only in the potential $\mathcal{V}$. For present purposes, we will soon make this latter assumption, in which case the eigenstates are of the form

$$\Phi_i = \frac{1}{L^{3/2}}e^{i\mathbf{k}_i\cdot\mathbf{r}}|n_i\rangle, \tag{42}$$

and

$$\chi_i^{(\pm)} = \frac{1}{L}e^{i\mathbf{K}_i\cdot\mathbf{R}}\chi^{(\pm)}_{k_{iz}}(z)|n_i\rangle. \tag{43}$$

In the case of a flat distorting potential the $\chi^{(\pm)}_{k_{iz}}(z)$ in the asymptotic region far from the surface are sinusoidal functions, i.e., there they consist of a summation of two plane waves, one traveling towards the surface and the other traveling away. In this case the difference between incoming and outgoing wave functions is a trivial phase, which disappears from the scattering intensity, i.e.,

$$\chi^{(+)}_{k_{iz}}(z) \;=\; e^{i\delta_i}\chi^{(-)}_{k_{iz}}(z), \tag{44}$$

where δ_i depends only on k_{iz}.

With this division, the potential $\mathcal{U}$ contributes only to elastic scattering, and since it is a function only of z it describes only total specular reflection of the incident beam. Thus, the DWBA that will produce the lowest order single phonon transition rates and diffraction peak intensities comes from using the first order perturbation matrix element

$$T_{fi} \;\approx\; \left(\chi^{(-)}_f \left|\langle n_f|\mathcal{V}|n_i\rangle\right| \chi^{(+)}_i\right) \;, \tag{45}$$

in the Fermi Golden Rule of Eq. (3).

After application of the Glauber-Van Hove transformation to the interaction picture as in Sec. 2 above, the transition rate becomes

$$w(\mathbf{k}_f,\mathbf{k}_i) = \frac{1}{\hbar^2}\int_{-\infty}^{+\infty} dt e^{-i(E_f-E_i)t/\hbar}\left\langle\left(\chi^{(+)}_i(\mathbf{r})\,|\mathcal{V}(\mathbf{r},0)|\,\chi^{(-)}_f(\mathbf{r})\right)\right.$$
$$\left.\times\left(\chi^{(-)}_f(\mathbf{r})\,|\mathcal{V}(\mathbf{r},t)|\,\chi^{(+)}_i(\mathbf{r})\right)\right\rangle \;. \tag{46}$$

We note again that if the approximation of a flat-surface distorting potential is invoked, Eq. (44) allows the neglect of the $(\pm)$ notation on the wave functions. However, in the interest of generality we retain the $(\pm)$ notation through this Section.

As before, we choose the interaction potential to be a pairwise summation over unit cells $\{uc\}$ of the surface:

$$\mathcal{V}(\mathbf{r},t) \;=\; \sum_{\ell} v^{uc}(\mathbf{r}-\mathbf{r}_\ell-\mathbf{u}_\ell(t)) \;, \tag{47}$$

where ℓ is a 2-D integer that counts surface unit cells. In directions parallel to the surface, the matrix elements simplify as before:

$$\left(\chi^{(-)}_f(\mathbf{r})\,|\mathcal{V}(\mathbf{r},t)|\,\chi^{(+)}_i(\mathbf{r})\right) = \frac{1}{L^2}\sum_\ell e^{-i\Delta\mathbf{K}\cdot(\mathbf{R}_\ell+\mathbf{U}_\ell(t))}$$
$$\times\int_{-\infty}^{+\infty} dz\chi^{(-)*}_{k_{fz}}(z)v_{\Delta\mathbf{K}}(z-u_{z,\ell_z}(t))\chi^{(+)}_{k_{iz}}(z), \tag{48}$$

where $\Delta\mathbf{K} = \mathbf{K}_f - \mathbf{K}_i$ and the Fourier transform of the unit cell potential is given by

$$v_{\Delta\mathbf{K}}(z) \;=\; \int d\mathbf{R}\; e^{-i\Delta\mathbf{K}\cdot\mathbf{R}}\; v^{uc}(\mathbf{r}) \;. \tag{49}$$

In order to make further progress we need to Fourier transform the z-dependent potential.

$$v_{\Delta\mathbf{K}}(z-u_{z,\ell_z}(t)) \;=\; \frac{1}{2\pi}\int_{-\infty}^{+\infty} dq\; e^{iq\left(z-u_{z,\ell_z}(t)\right)}\; v_{\Delta\mathbf{K},q} \;, \tag{50}$$

which casts the matrix element into the form

$$\left(\chi^{(-)}_f(\mathbf{r})\,|\mathcal{V}(\mathbf{r},t)|\,\chi^{(+)}_i(\mathbf{r})\right) = \frac{1}{L^2}\sum_\ell e^{-i\Delta\mathbf{K}\cdot(\mathbf{R}_\ell+\mathbf{U}_\ell(t))}$$
$$\times\int_{-\infty}^{+\infty} dz\chi^{(-)*}_{k_{fz}}(z)\frac{1}{2\pi}\int_{-\infty}^{+\infty} dq e^{iq\left(z-u_{z,\ell_z}(t)\right)}$$
$$\times\, v_{\Delta\mathbf{K},q}\chi^{(+)}_{k_{iz}}(z). \tag{51}$$

At the mathematical expense of having to introduce the Fourier transform of the potential in the perpendicular direction, we now have placed all of the time-dependent phonon displacement operators into arguments of exponentials, which will allow a means to treat the thermal average. The transition rate now becomes

$$w(\mathbf{k}_f,\mathbf{k}_i) = \frac{1}{L^4}\,\frac{1}{\hbar^2}\left(\frac{1}{2\pi}\right)^2\int_{-\infty}^{+\infty} dt e^{-i(E_f-E_i)t/\hbar}$$
$$\times\sum_{\ell,\ell'} e^{-i\Delta\mathbf{K}\cdot(\mathbf{R}_\ell-\mathbf{R}_{\ell'})}\int_{-\infty}^{+\infty} dz\int_{-\infty}^{+\infty} dz'$$
$$\times\int_{-\infty}^{+\infty} dq e^{iqz}\int_{-\infty}^{+\infty} dq' e^{-iq'z'}\;\chi^{(+)*}_{k_{iz}}(z)\; v_{\Delta\mathbf{K},q}\;\; \chi^{(-)}_{k_{fz}}(z)$$
$$\times\chi^{(-)*}_{k_{fz}}(z')\; v_{\Delta\mathbf{K},q'}\;\; \chi^{(+)}_{k_{iz}}(z')$$
$$\times\left\langle\; e^{i\Delta\mathbf{K}\cdot\mathbf{U}_\ell(0)}\; e^{iqu_{z,\ell}(0)}\; e^{-i\Delta\mathbf{K}\cdot\mathbf{U}_{\ell'}(t)}\; e^{-iq'u_{z,\ell'}(t)}\right\rangle . \tag{52}$$

The thermal average over initial crystal states is handled just as before with the result

$$\left\langle e^{i\Delta\mathbf{K}\cdot\mathbf{U}_\ell(0)}e^{iqu_{z,\ell}(0)}e^{-i\Delta\mathbf{K}\cdot\mathbf{U}_{\ell'}(t)}e^{-iq'u_{z,\ell'}(t)}\right\rangle$$
$$= e^{-W^{eff}(\mathbf{q})}\; e^{-W^{eff}(\mathbf{q}')}\; e^{2\mathcal{W}^{eff}_{\ell,\ell'}(\mathbf{q},\mathbf{q}',t)}. \tag{53}$$

with the vector $\mathbf{q}$ defined as $\mathbf{q} = (\Delta\mathbf{K}, q)$ and similarly for $\mathbf{q}' = (\Delta\mathbf{K}, q')$. The arguments of the Debye-Waller exponents are

$$W^{eff}(\mathbf{q}) \;=\; W^{eff}(\mathbf{K}_f,\mathbf{K}_i,q) \;=\; \frac{1}{2}\left\langle\left(\;\Delta\mathbf{K}\cdot\mathbf{U}_\ell(0) \;+\; qu_{z,\ell}(0)\;\right)^2\right\rangle \;, \tag{54}$$

and similarly for $W^{eff}(\mathbf{K}_f,\mathbf{K}_i,q')$, and as usual these are independent of ℓ or t. These are labeled W^{eff} because they are effective Debye-Waller exponents arising from the vibrations of the electron density in the region where the incoming atomic projectiles collide, and are only indirectly connected to the vibrations of the cores. The meaning of W^{eff} will become evident when it is explicitly evaluated within the electron-phonon coupling theory of Sec. 4 below. The correlation function is

$$2\mathcal{W}^{eff}_{\ell,\ell'}(\mathbf{q},\mathbf{q}',t) = 2\mathcal{W}^{eff}_{\ell,\ell'}(\mathbf{K}_f,\mathbf{K}_i,q,q',t)$$
$$= \left\langle\;\left(\Delta\mathbf{K}\cdot\mathbf{U}_\ell(0)+qu_{z,\ell}(0)\right)\right.$$
$$\left.\times\;\left(\Delta\mathbf{K}\cdot\mathbf{U}_{\ell'}(t)+q'u_{z,\ell'}(t)\right)\right\rangle . \tag{55}$$

Note that both of the above can be separated out into terms depending only on parallel displacement $\Delta\mathbf{K}\cdot\mathbf{U}_\ell(0)$, terms depending only on $qu_{z,\ell}(0)$ or $q'u_{z,\ell'}(t)$, and cross terms involving both. In the direction parallel to the surface, things work out similarly as they do for the exact T-matrix formalism as in Sec. 2 above, and this is because of the symmetry in these directions. It will be useful to make this separation explicit in the notation for the Debye-Waller factors by writing

$$W^{eff}(\mathbf{K}_f,\mathbf{K}_i,q) \;=\; W_{\|}(\Delta\mathbf{K})+\widetilde{W}(\Delta\mathbf{K},q)\;, \tag{56}$$

where $W_{\|}(\Delta\mathbf{K})$ is the Debye-Waller argument for parallel motion, and all terms in q are contained in $\widetilde{W}(\Delta\mathbf{K},q)$. For completeness we write out the full form of the transition rate, using the above definitions.

$$w(\mathbf{k}_f,\mathbf{k}_i) = \frac{1}{L^4}\frac{1}{\hbar^2}\left(\frac{1}{2\pi}\right)^2\int_{-\infty}^{+\infty} dt e^{-i(E_f-E_i)t/\hbar}$$
$$\times\sum_{\ell,\ell'} e^{-i\Delta\mathbf{K}\cdot(\mathbf{R}_\ell-\mathbf{R}_{\ell'})}\int_{-\infty}^{+\infty} dz\int_{-\infty}^{+\infty} dz'$$
$$\times\int_{-\infty}^{+\infty} dq e^{iqz}\int_{-\infty}^{+\infty} dq' e^{-iq'z'}\;\chi^{(+)*}_{k_{iz}}(z)v_{\Delta\mathbf{K},q}\chi^{(-)}_{k_{fz}}(z)$$
$$\times\;\chi^{(-)*}_{k_{fz}}(z')v_{\Delta\mathbf{K},q'}\chi^{(+)}_{k_{iz}}(z')$$
$$\times\, e^{-2W_{\|}(\mathbf{K}_f,\mathbf{K}_i)-\widetilde{W}(\mathbf{K}_f,\mathbf{K}_i,q)-\widetilde{W}(\mathbf{K}_f,\mathbf{K}_i,q')}$$
$$\times\, e^{2\mathcal{W}^{eff}_{\ell,\ell'}(\mathbf{K}_f,\mathbf{K}_i,q,q',t)}. \tag{57}$$

3.1. Elastic scattering in the DWBA

As before, the elastic scattering contribution arises from the zeroth order expansion of the correlation function in Eq. (57).

$$
\begin{aligned}
w^{(0)}_{DWBA}(\mathbf{k}_f,\mathbf{k}_i) = {} & \frac{1}{L^4}\frac{1}{\hbar^2}\left(\frac{1}{2\pi}\right)^2\int_{-\infty}^{+\infty} dt e^{-i(E_f-E_i)t/\hbar} \\
& \times \sum_{\ell,\ell'} e^{-i\Delta\mathbf{K}\cdot(\mathbf{R}_\ell-\mathbf{R}_{\ell'})}\int_{-\infty}^{+\infty} dz \int_{-\infty}^{+\infty} dz' \\
& \times \int_{-\infty}^{+\infty} dq e^{iqz}\int_{-\infty}^{+\infty} dq' e^{-iq'z'}\,\chi^{(+)*}_{k_{iz}}(z) v_{\Delta\mathbf{K},q}\chi^{(-)}_{k_{fz}}(z) \\
& \times \chi^{(-)*}_{k_{fz}}(z') v_{\Delta\mathbf{K},q'}\chi^{(+)}_{k_{iz}}(z') \\
& \times e^{-2W_{\|}(\mathbf{K}_f,\mathbf{K}_i)-\widetilde{W}(\mathbf{K}_f,\mathbf{K}_i,q)-\widetilde{W}(\mathbf{K}_f,\mathbf{K}_i,q')}. \qquad (58)
\end{aligned}
$$

It now becomes clear that the averaging has resulted in a temperature-dependent potential in the z-direction, defined by

$$
\begin{aligned}
v^{eff}_{\Delta\mathbf{K}}(T,z) &= \frac{1}{2\pi}\int_{-\infty}^{+\infty} dq e^{iqz} v_{\Delta\mathbf{K},q} e^{-\widetilde{W}(\mathbf{K}_f,\mathbf{K}_i,q)} \\
&= \frac{1}{2\pi}\int_{-\infty}^{+\infty} dq e^{iqz} v_{\Delta\mathbf{K},q} e^{[-q^2\langle u_z^2\rangle-2q\Delta K_x\langle u_z u_x\rangle-2q\Delta K_y\langle u_z u_y\rangle]/2}. \qquad (59)
\end{aligned}
$$

The sum over lattice sites parallel to the surface and the time integral are done as before, and indicate conservation of parallel momentum and energy. The final form is

$$
\begin{aligned}
w^{(0)}_{DWBA}(\mathbf{k}_f,\mathbf{k}_i) = {} & \frac{2\pi}{\hbar}\frac{N^2}{L^4}\sum_{\mathbf{G}} e^{-2W_{\|}(\Delta\mathbf{K})}\left|\left(\chi^{(+)}_{k_{iz}}(z)\left|v^{eff}_{\Delta\mathbf{K}}(T,z)\right|\chi^{(-)}_{k_{fz}}(z)\right)\right|^2 \\
& \times \delta_{\Delta\mathbf{K},\mathbf{G}}\delta\left(E_f-E_i\right), \qquad (60)
\end{aligned}
$$

where the matrix element is

$$
\left(\chi^{(+)}_{k_{iz}}(z)\left|v^{eff}_{\Delta\mathbf{K}}(T,z)\right|\chi^{(-)}_{k_{fz}}(z)\right) = \int_{-\infty}^{+\infty} dz\ \chi^{(+)*}_{k_{iz}}(z)\ v^{eff}_{\Delta\mathbf{K}}(T,z)\ \chi^{(-)}_{k_{fz}}(z). \qquad (61)
$$

The elastic transition rate in this treatment of the DWBA has many of the characteristics discussed above in connection with the general case of Sec. 2. However, it has two important differences. First, only the parallel effective Debye-Waller factor $\exp\{-2W_{\|}(\Delta\mathbf{K})\}$ appears. This is because of the symmetry properties of the crystal parallel to the surface, i.e., exactly the same reason why only parallel momentum is conserved modulo a reciprocal lattice vector $\mathbf{G}$. Second, the matrix element has become modified by that part of the Debye-Waller-like factor associated with motion perpendicular to the surface, and this modification makes the effective potential dependent on the surface temperature T. The nature of the modification on the potential is evident from Eq. (59): the Gaussian term in q^2 insures convergence of the integral, and the exponentials with arguments linear in q give rise to a complex coordinate displacement. It should also be noted that these arguments linear in q are proportional to the cross-correlations such as $\langle u_x u_z\rangle$. For bulk phonons in crystals with a high degree of symmetry (e.g., all forms of cubic crystals) such averages vanish, but not necessarily so in the case of a surface because of the broken symmetry in the normal direction. The effect of the Gaussian term in q^2 is to smooth out any sharper features of the unmodified potential $v_{\Delta\mathbf{K}}(z)$, and this smoothing effect will increase with temperature as the mean square displacement increases. However, at all reasonable temperatures the effect on the potential is weak, and it is important to note that the temperature dependence introduced in this manner does not at all behave like the Debye-Waller factor associated with normal momentum transfer. Examples showing how the effective potential $v^{eff}_{\Delta\mathbf{K}}(T,z)$ differs from the original unmodified potential $v_{\Delta\mathbf{K}}(z)$ are discussed in Appendix B, where it is seen that a sharp feature in the unmodified potential is simply rounded, or if the unmodified potential is a repulsive exponential the temperature dependent modification merely shifts the position of the origin, i.e., it has virtually no effect on the nature of the scattering.

The origin of the temperature dependence introduced into the effective potential of Eq. (59) lies in the decoupling approximation for the transition operator exhibited in Eq. (21) above. The distorted wave Born approximation, derived properly in this treatment, has introduced a weak time-dependence in the transition operator, and upon averaging over vibrational states of the crystal, this time dependence of the transition operator is converted to a temperature dependence of the DWBA matrix element.

It is important to note that Eq. (60) does not contain the part of the Debye-Waller factor dependent on vibrational motion perpendicular to the surface which arises naturally in the general treatment of Eq. (31), i.e., Eq. (60) contains only the parallel part of the D-W factor. Thus, comparison with the general treatment of Eq. (31) shows that the correct way to introduce the distorted wave Born approximation into the general treatment for elastic scattering is through the transformation

$$
T^0_{\mathbf{k}_f,\mathbf{k}_i} \longrightarrow i\ \frac{\hbar^2 k_{iz}}{mL}\ e^{i\delta_0}\ \delta_{\Delta\mathbf{K},\mathbf{0}}\ +\ \left(\chi^{(+)}_{k_{iz}}(z)\left|v^{eff}_{\Delta\mathbf{K}}(T,z)\right|\chi^{(-)}_{k_{fz}}(z)\right). \qquad (62)
$$

where the first term introduced on the left hand side of Eq. (62) is the contribution coming from the flat-surface distorting potential $\boldsymbol{\mathcal{V}}$, as shown in Eq. (41), that contributes only to specular scattering as discussed above in connection with Eq. (45). The phase δ_0 is that accumulated by a projectile as it scatters specularly from $\boldsymbol{\mathcal{V}}$. This leads to the final expression for elastic scattering with the correct Debye-Waller factor

$$
\begin{aligned}
w^{(0)}_{DWBA}(\mathbf{k}_f,\mathbf{k}_i) = {} & \frac{2\pi}{\hbar}\frac{1}{a_c^2}\sum_{\mathbf{G}} e^{-2W^{eff}(\mathbf{k}_f,\mathbf{k}_i)} \\
& \times \left| i\frac{\hbar^2 k_{iz}}{mL} e^{i\delta_0}\delta_{\Delta\mathbf{K},\mathbf{0}} + \left(\chi^{(+)}_{k_{iz}}(z)\left|v^{eff}_{\Delta\mathbf{K}}(T,z)\right|\chi^{(-)}_{k_{fz}}(z)\right)\right|^2 \\
& \times \delta_{\Delta\mathbf{K},\mathbf{G}}\delta\left(E_f-E_i\right), \qquad (63)
\end{aligned}
$$

where a_c is the area of a surface unit cell. We note again that $2W^{eff}(\mathbf{k}_f,\mathbf{k}_i)$ may contain mixed cross-correlations between vibrational displacements in different Cartesian directions, because these cross-correlation averages do not necessarily vanish in the presence of the symmetry-breaking surface. Furthermore, the vibrational correlation functions found in $2W^{eff}(\mathbf{k}_f,\mathbf{k}_i)$ arise from the effective vibrational amplitudes encountered in the collision which are not as yet specified. These effective vibrational amplitudes will in general depend on the momentum vectors of the projectile collision and consequently $2W^{eff}(\mathbf{k}_f,\mathbf{k}_i)$ will depend on $\mathbf{k}_f$ and $\mathbf{k}_i$ independently in a more complicated manner, and not simply on the momentum vector $\mathbf{k}_f - \mathbf{k}_i$.

3.2. Inelastic, single-phonon scattering in the DWBA

The single phonon inelastic transition rate comes from the first order term in the expansion of $\exp\{2\mathcal{W}^{eff}\}$ in Eq. (57). The process of carrying out the various sums and integrals is quite similar to that of the elastic case in the above subsection, so we can simply write down the final result. Since some terms in $2\mathcal{W}^{eff}$ are linear in q or q', two related effective temperature-dependent potentials arise. One is the same as Eq. (59) above, and the other is its derivative

$$\begin{aligned}\widetilde{v}^{eff}_{\Delta\mathbf{K}}(T,z) &= \frac{1}{2\pi}\int_{-\infty}^{+\infty} dqqe^{iqz}v_{\Delta\mathbf{K},q}e^{-\widetilde{W}(\Delta\mathbf{K},q)}\\ &= \frac{-i}{2\pi}\frac{d}{dz}\int_{-\infty}^{+\infty} dqe^{iqz}v_{\Delta\mathbf{K},q}e^{-\widetilde{W}(\Delta\mathbf{K},q)}\\ &= -i\frac{d}{dz}v^{eff}_{\Delta\mathbf{K}}(T,z).\end{aligned}\tag{64}$$

Defining a vector operator as $\widehat{\mathbf{q}} = \{\Delta\mathbf{K}, -id/dz\}$ the single phonon inelastic scattering transition rate becomes

$$\begin{aligned}w^{(1)}_{DWBA}(\mathbf{k}_f,\mathbf{k}_i) = \frac{2\pi}{\hbar}\frac{1}{a_c^2}\sum_\nu e^{-2W_\parallel(\Delta\mathbf{K})}\frac{\hbar}{2NM_S\omega(\Delta\mathbf{K},\nu)}\\ \times\left|\left(\chi^{(+)}_{k_{iz}}(z)\left|\widehat{\mathbf{q}}v^{eff}_{\Delta\mathbf{K}}(T,z)\right|\chi^{(-)}_{k_{fz}}(z)\right)\cdot\mathbf{e}(\Delta\mathbf{K},\nu)\right|^2\\ \times\left\{\left[n_{BE}(\omega(\Delta\mathbf{K},\nu))+1\right]\delta\left(E_f-E_i+\hbar\omega(\Delta\mathbf{K},\nu)\right)\right.\\ \left.+\,n_{BE}(\omega(\Delta\mathbf{K},\nu))\delta\left(E_f-E_i-\hbar\omega(\Delta\mathbf{K},\nu)\right)\right\}.\end{aligned}\tag{65}$$

Comparing with the general, formal treatment of scattering in Eq. (36) shows that to obtain the correct Debye-Waller factor in the DWBA we need to do the following operation on Eq. (35) or (36)

$$T^0_{\mathbf{k}_f,\mathbf{k}_i}\ \Delta k_\alpha \longrightarrow \left(\chi^{(+)}_{k_{iz}}(z)\,\middle|\,\widehat{q}_\alpha\ v^{eff}_{\Delta\mathbf{K}}(T,z)\middle|\,\chi^{(-)}_{k_{fz}}(z)\right)\ .\tag{66}$$

As above in the case for the elastic transition rate, the presence of a weak temperature dependence in the effective potential arises from the fact that the DWBA includes additional dependences via the time dependent vibrations that are accounted for in the decoupling approximation of Eq. (21).

The final form for the transition rate in the DWBA, including the correct Debye-Waller factor is then

$$\begin{aligned}w^{(1)}_{DWBA}(\mathbf{k}_f,\mathbf{k}_i) = \frac{2\pi}{\hbar}\frac{1}{a_c^2}\sum_\nu e^{-2W^{eff}(\mathbf{k}_f,\mathbf{k}_i)}\frac{\hbar}{2NM_S\omega(\Delta\mathbf{K},\nu)}\\ \times\left|\left(\chi^{(+)}_{k_{iz}}(z)\left|\widehat{\mathbf{q}}v^{eff}_{\Delta\mathbf{K}}(T,z)\right|\chi^{(-)}_{k_{fz}}(z)\right)\cdot\mathbf{e}(\Delta\mathbf{K},\nu)\right|^2\\ \times|n_{BE}(\omega(\Delta\mathbf{K},\nu))|\delta(E_f-E_i-\hbar\omega(\Delta\mathbf{K},\nu)).\end{aligned}\tag{67}$$

We emphasize again that the mass M_S is not the mass of the crystal core atoms, it is the effective mass associated with the vibrational modes of the electron gas sampled by the colliding projectile, and similarly for the mode polarization vectors $\mathbf{e}(\Delta\mathbf{K},\nu)$.

4. The electron-phonon coupling approach to atom-surface scattering

4.1. Evaluation of the interaction potential

We wish to develop the theory of elastic diffraction and inelastic scattering of an atom colliding with the electron gas that extends outward from the terminal layer of atomic cores of the surface. The electron density vibrates due to the vibrations of the underlying crystal atomic cores, via the electron-phonon coupling. The basic theory has been developed by Sklyadneva et al. [35,39] who demonstrated that within a reasonable set of approximations the scattering intensity due to creation or annihilation of single phonon modes is proportional to the mode-dependent components $\lambda_{\mathbf{Q},\nu}$ of the electron-phonon coupling constant λ [38], defined as discussed above by the relationship due originally to Allen [41], $\lambda = \langle\lambda_{\mathbf{Q},\nu}\rangle$. The treatment presented here extends this earlier work to include the electron-phonon coupling contributions to elastic diffraction and to include a complete description of the Debye-Waller attenuation together with their relationships to the electron-phonon coupling constants.

The starting point is the distorted wave Born approximation developed in Sec. 3 above, with the repulsive part of the atom-surface interaction potential given by the Esbjerg-Nørskov approximation $A_N n(\mathbf{r},t)$ [27] where $n(\mathbf{r},t)$ is the electronic density and A_N is a constant typically, for He on metals, chosen to be about 340 eV/a_0^3, with a_0 the Bohr atomic length.

The total electronic density can be written as a sum over the density contributions of all occupied electron states as

$$n(\mathbf{r}) \;=\; \sum_{\mathbf{K},n}^{occ.} n_{\mathbf{K},n}(\mathbf{r}) \;=\; \sum_{\mathbf{K},n}^{occ.}\left|\widetilde{\psi}_{\mathbf{K},n}\right|^2\ ,\tag{68}$$

where the summation implicitly includes a factor of 2 for spin, the electron wave function state is identified by the parallel wave vector $\mathbf{K}$ and branch number n, and satisfies the Schrödinger equation

$$\left(H^{el}\ +\ V^{el}\right)\ \widetilde{\psi}_{\mathbf{K},n} = \widetilde{E}^{el}_{\mathbf{K},n}\ \widetilde{\psi}_{\mathbf{K},n}\ .\tag{69}$$

Hereafter it will be assumed that summations over the electron states designated by $\mathbf{K},n$ run only over occupied states. The normal momentum of the electronic wave function is no longer a good quantum number due to the broken symmetry in the perpendicular direction, so in this notation it is included in the branch number n.

V^{el} is the electron-phonon interaction potential coupling the electron states to the cores, and we will choose it in the usual manner to be a pairwise summation over core pseudopotentials

$$V^{el}\ =\ \sum_j v^{el}(\mathbf{r}-\mathbf{r}_j-\mathbf{u}_j)\ .\tag{70}$$

where, as opposed to the effective atom-surface potential of Eq. (47), the vibrational displacements $\mathbf{u}_j$ are now those of the cores and j is a 3-D integer that counts all cores in the half-space containing the crystal.

The unperturbed electronic eigenstates are solutions of

$$H^{el}\ \psi_{\mathbf{K},n} = E^{el}_{\mathbf{K},n}\ \psi_{\mathbf{K},n}\ ,\tag{71}$$

and through lowest order in perturbation theory $\widetilde{\psi}_{\mathbf{K},n}$ can be expressed in terms of $\psi_{\mathbf{K},n}$ as

$$\widetilde{\psi}_{\mathbf{K},n} = \psi_{\mathbf{K},n} + {\sum_{\mathbf{K}',n'}}' \psi_{\mathbf{K}',n'}\frac{1}{E^{el}_{\mathbf{K},n}-E^{el}_{\mathbf{K}',n'}}\left(\psi_{\mathbf{K}',n'}\left|V^{el}\right|\psi_{\mathbf{K},n}\right),\tag{72}$$

where the prime symbol on the summation indicates that the state $\{\mathbf{K},n\}$ is not included in the sum.

The perturbing potential, which includes electron-phonon coupling contributions to both elastic and inelastic interactions with colliding atomic projectiles, is proportional to the variation of the electronic density and can be expressed as a summation over $\{\mathbf{K},n\}$ components

$$\begin{aligned}\delta\mathcal{V}(\mathbf{r}) \cong A_N\delta n(\mathbf{r}) &= A_N\sum_{\mathbf{K},n}\delta n_{\mathbf{K},n}(\mathbf{r})\\ &= A_N\sum_{\mathbf{K},n}\left\{\left|\widetilde{\psi}_{\mathbf{K},n}\right|^2-\left|\psi_{\mathbf{K},n}\right|^2\right\}\\ &= A_N\Re\sum_{\mathbf{K},n}\left(\widetilde{\psi}_{\mathbf{K},n}-\psi_{\mathbf{K},n}\right)\left(\widetilde{\psi}^*_{\mathbf{K},n}+\psi^*_{\mathbf{K},n}\right).\end{aligned}\tag{73}$$

where the symbol $\Re$ signifies the real part is to be taken. Using Eq. (72) together with the pairwise summation form for the potential of Eq. (70) the variation $\delta n_{\mathbf{K},n}(\mathbf{r})$ to first order in perturbation theory becomes

$$\begin{aligned}\delta n_{\mathbf{K},n}(\mathbf{r}) \cong 2\Re\sum_j{\sum_{\mathbf{K}',n'}}'\psi^*_{\mathbf{K},n}\psi_{\mathbf{K}',n'}\frac{1}{E^{el}_{\mathbf{K},n}-E^{el}_{\mathbf{K}',n'}}\\ \times\left(\psi_{\mathbf{K}',n'}\left|v^{el}(\mathbf{r}-\mathbf{r}_j-\mathbf{u}_j)\right|\psi_{\mathbf{K},n}\right).\end{aligned}\tag{74}$$

Since each electron state contributes independently, the $\{\mathbf{K}, n\}$ contribution to the transition rate evaluated in the DWBA of Eq. (46) is then

$$w_{\mathbf{K},n}(\mathbf{k}_f, \mathbf{k}_i) = \frac{1}{\hbar^2} \int_{-\infty}^{+\infty} dt e^{-i(E_f - E_i)t/\hbar} \times \left\langle \left(\chi_i^{(+)} \left| \delta \mathcal{V}_{\mathbf{K},n}(\mathbf{r}, 0) \right| \chi_f^{(-)} \right) \left(\chi_f^{(-)} \left| \delta \mathcal{V}_{\mathbf{K},n}(\mathbf{r}, t) \right| \chi_i^{(+)} \right) \right\rangle, \tag{75}$$

Although the above is written with the proper notation for outgoing and incoming projectile wave functions, we now make the assumption that the distorting potential $\mathcal{U}(z)$ is a function only of the z component making this notation superfluous. When written more explicitly Eq. (75) gives

$$\begin{aligned} w_{\mathbf{K},n}(\mathbf{k}_f, \mathbf{k}_i) = {} & 4A_N^2 \frac{1}{\hbar^2} \int_{-\infty}^{+\infty} dt e^{-i(E_f - E_i)t/\hbar} \\ & \times \Re \sum_j \sideset{}{'}\sum_{\mathbf{K}',n'} \left(\chi_i \left| \psi^*_{\mathbf{K},n} \psi_{\mathbf{K}',n'} \right| \chi_f \right) \frac{1}{E^{el}_{\mathbf{K},n} - E^{el}_{\mathbf{K}',n'}} \\ & \times \Re \sum_{j'} \sideset{}{'}\sum_{\mathbf{K}'',n''} \left(\chi_f \left| \psi^*_{\mathbf{K},n} \psi_{\mathbf{K}'',n''} \right| \chi_i \right) \frac{1}{E^{el}_{\mathbf{K},n} - E^{el}_{\mathbf{K}'',n''}} \\ & \times \Big\langle \left(\psi_{\mathbf{K}',n'} \left| v^{el}(\mathbf{r} - \mathbf{r}_j - \mathbf{u}_j(0)) \right| \psi_{\mathbf{K},n} \right) \\ & \times \left(\psi_{\mathbf{K}'',n''} \left| v^{el}(\mathbf{r} - \mathbf{r}_{j'} - \mathbf{u}_{j'}(t)) \right| \psi_{\mathbf{K},n} \right) \Big\rangle . \end{aligned} \tag{76}$$

The above Eq. (76) contains two distinctly different types of matrix elements, the electron-phonon coupling matrix elements such as $\left(\psi_{\mathbf{K}',n'} \left| v^{el}(\mathbf{r} - \mathbf{r}_j - \mathbf{u}_j(t)) \right| \psi_{\mathbf{K},n} \right)$ which are subject to the thermal average, and the overlap matrix elements between electronic and projectile states such as $\left(\chi_i \left| \psi^*_{\mathbf{K},n} \psi_{\mathbf{K}',n'} \right| \chi_f \right)$.

The next logical step is to examine these, starting with the electron-phonon matrix element. The zero-order electronic wave functions $\psi_{\mathbf{K},n}$, in the region where the repulsive scattering takes place (≈3 Å from the first layer of core ions) can be regarded as approximately unperturbed plane waves in the directions parallel to the surface, but must be distorted wave functions in the normal direction due to the broken symmetry introduced by the presence of the surface, i.e.,

$$\psi_{\mathbf{K},n}(\mathbf{r}) \; = \; \frac{1}{L} e^{i\mathbf{K}\cdot\mathbf{R}} \varphi_{\mathbf{K},n}(z) \; . \tag{77}$$

This means that these matrix elements are a Fourier transform of the potential in the parallel directions, and we further introduce a Fourier transform in the z-coordinate

$$v^{el}_{\mathbf{K}-\mathbf{K}'} \left(z - z_{j_\perp} - u_{j_\perp}(t) \right) \; = \; \frac{1}{2\pi} \int_{-\infty}^{+\infty} dq \; e^{iq\left(z - z_{j_\perp} - u_{j_\perp}(t)\right)} \; v^{el}_{\mathbf{K}-\mathbf{K}',q} \; , \tag{78}$$

where the 3-D counting index j is divided into a 2-D parallel index $j_{\|}$ that counts unit cells in a plane parallel to the surface and a perpendicular 1-D index $j_\perp$ that counts planes within the half-space of the target crystal. Rewriting in detail the electron-phonon matrix element:

$$\begin{aligned} & \left(\psi_{\mathbf{K}',n'} \left| v^{el}(\mathbf{r} - \mathbf{r}_j - \mathbf{u}_j(t)) \right| \psi_{\mathbf{K},n} \right) \\ & = \frac{1}{L^2} \sum_{j_\perp} \sum_{j_{\|}} e^{i(\mathbf{K}-\mathbf{K}')\cdot\mathbf{R}_{j_{\|}}} \int_{-\infty}^{+\infty} dz \varphi^*_{\mathbf{K}',n'}(z) \varphi_{\mathbf{K},n}(z) \\ & \quad \times \frac{1}{2\pi} \int_{-\infty}^{+\infty} dq e^{iqz} v^{el}_{\mathbf{K}-\mathbf{K}',q} e^{-iqz_{j\perp}(t)} e^{i(\mathbf{K}-\mathbf{K}')\cdot\mathbf{U}_{j_{\|}}(t)} e^{-iqu_{j_\perp}(t)} . \end{aligned} \tag{79}$$

This is immediately recognized as a very convenient form for carrying out the thermal average over crystal vibrational state, because it places all phonon displacement operators in the exponent and the average can be carried out in a manner quite similar to that done in connection with Eq. (22) above.

The overlap matrix simplifies, because of the form of the electronic wave function of Eq. (77), and provides a relation between momenta parallel to the surface:

$$\begin{aligned} \left(\chi_i \left| \psi^*_{\mathbf{K},n} \psi_{\mathbf{K}',n'} \right| \chi_f \right) & = \frac{1}{L^4} \int d\mathbf{R} e^{-i\mathbf{K}_i\cdot\mathbf{R}} e^{-i\mathbf{K}\cdot\mathbf{R}} e^{i\mathbf{K}'\cdot\mathbf{R}} e^{i\mathbf{K}_f\cdot\mathbf{R}} \\ & \quad \times \left(\chi_{k_{iz}}(z) \left| \varphi^*_{\mathbf{K},n}(z) \varphi_{\mathbf{K}',n'}(z) \right| \chi_{k_{fz}}(z) \right) \\ & = \left(\chi_{k_{iz}}(z) \left| \varphi^*_{\mathbf{K},n}(z) \varphi_{\mathbf{K}',n'}(z) \right| \chi_{k_{fz}}(z) \right) \delta_{\mathbf{K}_f - \mathbf{K}_i, \mathbf{K}-\mathbf{K}'} . \end{aligned} \tag{80}$$

The overlap matrix element of Eq. (80) clearly illustrates the definition of the classical turning point. Appearing in that equation are products of the initial and final distorted waves $\chi_{i,f}$ and the electronic wave functions such as $\psi_{\mathbf{K},n}$. The electron wave functions decay outside the surface, to a close approximation as exponential functions of the normal variable z. The distorted waves decay in the opposite direction into the region of this electron cloud decay very rapidly, much more rapidly than exponential behavior [26]. Thus the contributions to the overlap matrix elements come from this very thin manifold layer of the overlap of the two different wave functions, and this layer is the definition of the locus of classical turning points.

Given the above forms of the overlap and electron-phonon matrix elements, the thermal average over crystal states can be effected and many of the summations can be carried out using the δ-functions. The process is quite similar to that of Sec. 2 above, and the final result using as before the notation $\Delta\mathbf{K} = \mathbf{K}_f - \mathbf{K}_i$ is

$$\begin{aligned} w_{\mathbf{K},n}(\mathbf{k}_f, \mathbf{k}_i) = {} & 4A_N^2 \frac{1}{L^4} \frac{1}{\hbar^2} \int_{-\infty}^{+\infty} dt e^{-i(E_f - E_i)t/\hbar} \\ & \times \frac{1}{2\pi} \int_{-\infty}^{+\infty} dq e^{iqz} \frac{1}{2\pi} \int_{-\infty}^{+\infty} dq' e^{-iq'z'} \\ & \times \sum_{j\equiv(j_{\|}, j_\perp)} \sum_{j'\equiv(j'_{\|}, j'_\perp)} e^{2\mathcal{W}_{j,j'}(\mathbf{K}_f, \mathbf{K}_i, q, q', t)} \\ & \times A_j(\mathbf{K}, n, \Delta\mathbf{K}, q) A^*_{j'}(\mathbf{K}, n, \Delta\mathbf{K}, q'), \end{aligned} \tag{81}$$

where

$$\begin{aligned} A_j(\mathbf{K}, n, \Delta\mathbf{K}, q) = {} & \sideset{}{'}\sum_{n'} \int_{-\infty}^{+\infty} dz \varphi^*_{\mathbf{K}-\Delta\mathbf{K},n'}(z) \varphi_{\mathbf{K},n}(z) \\ & \times e^{-W_{\|}(\mathbf{K}_f, \mathbf{K}_i) - \widetilde{W}(\mathbf{K}_f, \mathbf{K}_i, q)} \\ & \times e^{-iqz_{j_\perp}} e^{i\Delta\mathbf{K}\cdot\mathbf{R}_{j_{\|}}} \\ & \times \Re \left(\chi_{k_{iz}}(z) \left| \varphi^*_{\mathbf{K},n}(z) \varphi_{\mathbf{K}-\Delta\mathbf{K},n'}(z) \right| \chi_{k_{fz}}(z) \right) \\ & \times \frac{1}{E^{el}_{\mathbf{K},n} - E^{el}_{\mathbf{K}-\Delta\mathbf{K},n'}} v^{el}_{\Delta\mathbf{K},q} . \end{aligned} \tag{82}$$

The forms of the Debye-Waller-like arguments are similar to those found in Eqs. (54) and (56),

$$\begin{aligned} W(\mathbf{K}_f,\mathbf{K}_i,q) &= \frac{1}{2}\left\langle\left(\left(\Delta\mathbf{K}\cdot\mathbf{U}_{j_\parallel}(0)+qu_{z,j_\perp}(0)\right)^2\right\rangle\right. \\ &= \frac{1}{2}\left\langle\left(\left(\Delta\mathbf{K}\cdot\mathbf{U}_{j_\parallel}(0)\right)^2\right\rangle\right.+q\Delta\mathbf{K}\cdot\left\langle\mathbf{U}_{j_\parallel}(0)u_{z,j_\perp}(0)\right\rangle \\ &\quad +\frac{1}{2}q^2\left\langle u^2_{z,j_\perp}(0)\right\rangle \\ &= W_\parallel(\mathbf{K}_f,\mathbf{K}_i)+\widetilde{W}(\mathbf{K}_f,\mathbf{K}_i,q), \end{aligned} \tag{83}$$

and the time dependent displacement correlation function is similar to Eq. (55)

$$\begin{aligned} 2\mathcal{W}_{j,j'}(\mathbf{K}_f,\mathbf{K}_i,q,q',t) = &\left\langle\left(\Delta\mathbf{K}\cdot\mathbf{U}_{j_\parallel}(0)+qu_{z,j_\perp}(0)\right)\right. \\ &\times\left.\left(\Delta\mathbf{K}\cdot\mathbf{U}_{j'_\parallel}(t)+q'u_{z,j'_\perp}(t)\right)\right\rangle. \end{aligned} \tag{84}$$

As before, the cross terms in the averaged displacement correlations do not necessarily vanish because of the broken symmetry provided by the surface, however, we would expect them to be small, and in many cases it may be a good approximation to neglect those cross terms, in which case $\widetilde{W}(\mathbf{K}_f,\mathbf{K}_i,q)\approx\widetilde{W}(q)=\frac{1}{2}q^2\langle u^2_{z,j_\perp}(0)\rangle$ and depends only on the value eventually taken by q. The correlation functions of Eqs. (83) and (84) are called "Debye-Waller-like" because they involve the vibrational displacement of the target cores, and they are not the same as the effective Debye-Waller arguments sampled by the projectile atoms during the collision. This distinction will become clear in Sec. 4.4 below where the effective Debye-Waller factor will be explicitly determined in terms of the core vibrational amplitudes.

4.2. Electron-phonon coupling contribution to elastic scattering

As before, the elastic scattering transition rate is given by expanding the exponentiated displacement correlation function in Eq. (81) to zeroth order. It is also convenient to define, similar to before, an effective, temperature-dependent, electron-phonon potential

$$v^{el,eff}_{\mathbf{K}-\mathbf{K}'}(T,z) \;=\; \frac{1}{2\pi}\int_{-\infty}^{+\infty} dq\; e^{iqz}\; v^{el}_{\mathbf{K}-\mathbf{K}',q}\; e^{-\widetilde{W}(\mathbf{K}-\mathbf{K}',\ q)} \quad . \tag{85}$$

Note that $v^{el,eff}$ contains the "electron Debye-Waller-like factor" through its folding-in with the perpendicular part of $2W$, i.e., through the weighting of the Fourier transform integral by $\exp\{-\widetilde{W}(\mathbf{K}-\mathbf{K}',\ q)\}$. However, this includes only the parts of the Debye-Waller factor associated with perpendicular motion. The purely parallel part of the Debye Waller factor remains similar to the general treatment of Sec. 2.

With the above definitions, many summations become trivial, and the elastic transition rate components take the form

$$\begin{aligned} w^{(0)}_{\mathbf{K},n}(\mathbf{k}_f,\mathbf{k}_i) = \frac{4A_N^2}{a_c^2}\frac{2\pi}{\hbar}\sum_{\mathbf{G}} e^{-2W_\parallel(\mathbf{G})} &\\ \times\Bigg[\Re\sum_{n'}{}^{'}\left(\chi_{k_{iz}}(z)\left|\varphi^*_{\mathbf{K},n}(z)\varphi_{\mathbf{K}+\mathbf{G},n'}(z)\right|\chi_{k_{fz}}(z)\right) &\\ \times\quad\frac{1}{E^{el}_{\mathbf{K},n}-E^{el}_{\mathbf{K}+\mathbf{G},n'}} &\\ \times\sum_{j_\perp}\left(\varphi_{\mathbf{K}+\mathbf{G},n'}(z)\left|v^{el,eff}_{\mathbf{G}}(T,z-z_{j_\perp})\right|\varphi_{\mathbf{K},n}(z)\right)\Bigg]^2 &\\ \times\;\delta_{\mathbf{K}_f-\mathbf{K}_i,\mathbf{G}}\delta(E_f-E_i). \end{aligned} \tag{86}$$

The total transition rate is the summation over all electronic states

$$w^{(0)}_{DWBA}(\mathbf{k}_f,\mathbf{k}_i) \;=\; \sum_{\mathbf{K},n} w^{(0)}_{\mathbf{K},n}(\mathbf{k}_f,\mathbf{k}_i)\ . \tag{87}$$

This shows that the total transition rate in the DWBA differs from the form of the exact expression for elastic scattering of Eq. (31) in that it contains an incorrect form of the Debye-Waller factor. Thus the correct form of the transition rate in the DWBA which includes the total effective Debye-Waller factor is obtained by applying the following transformation to the exact expression of Eq. (31) above:

$$\begin{aligned} \left|T^0_{\mathbf{k}_f,\mathbf{k}_i}\right|^2 \longrightarrow \sum_{\mathbf{K},n}\Bigg| & i\frac{\hbar^2 k_{iz}}{mL}e^{i\delta_0}\delta_{\mathbf{K}_f-\mathbf{K}_i,\mathbf{0}} \\ & +\Re\sum_{n'}{}^{'}\left(\chi_{k_{iz}}(z)\left|\varphi^*_{\mathbf{K},n}(z)\varphi_{\mathbf{K}+\mathbf{G},n'}(z)\right|\chi_{k_{fz}}(z)\right) \\ & \times\frac{1}{E^{el}_{\mathbf{K},n}-E^{el}_{\mathbf{K}+\mathbf{G},n'}} \\ & \times\sum_{j_\perp}\left(\varphi_{\mathbf{K}+\mathbf{G},n'}(z)\left|v^{el,eff}_{\mathbf{G}}(T,z-z_{j_\perp})\right|\varphi_{\mathbf{K},n}(z)\right)\Bigg|^2. \end{aligned} \tag{88}$$

As in Eq. (62) above, the term proportional to $\delta_{\Delta\mathbf{K},\mathbf{0}}$ contributes only to specular scattering and comes from the distorting potential.

Below, we write out the full elastic transition rate in the DWBA for the non-specular diffraction peaks.

$$\begin{aligned} w^{(0)}_{DWBA}(\mathbf{k}_f,\mathbf{k}_i) = \frac{A_N^2}{a_c^2}\frac{8\pi}{\hbar}\sum_{\mathbf{G}} e^{-2W^{eff}(\mathbf{k}_f,\mathbf{k}_i)} &\\ \times\sum_{\mathbf{K},n}\Bigg[\Re\sum_{n'}{}^{'}\left(\chi_{k_{iz}}(z)\left|\varphi^*_{\mathbf{K},n}(z)\varphi_{\mathbf{K}+\mathbf{G},n'}(z)\right|\chi_{k_{fz}}(z)\right) &\\ \times\;\frac{1}{E^{el}_{\mathbf{K},n}-E^{el}_{\mathbf{K}+\mathbf{G},n'}} &\\ \times\sum_{j_\perp}\left(\varphi_{\mathbf{K}+\mathbf{G},n'}(z)\left|v^{el,eff}_{\mathbf{G}}(T,z-z_{j_\perp})\right|\varphi_{\mathbf{K},n}(z)\right)\Bigg]^2 &\\ \times\delta_{\mathbf{K}_f-\mathbf{K}_i,\mathbf{G}}\delta(E_f-E_i). \end{aligned} \tag{89}$$

Note that the effective meam-square displacements $<u^2>$ appearing in the effective Debye-Waller factor remain yet to be specified. They are the effective mean-square displacements of the electron density in the neighborhood of the classical turning point, which is in turn defined by the overlap integral matrix element. We will identify the effective mean-square displacements, and hence the effective Debye-Waller factor, below in Subsection 4.4, after the following discussion of the single-phonon inelastic scattering.

4.3. Electron-phonon contribution to single-phonon inelastic scattering

The single phonon contribution to the inelastic scattering intensity is obtained by expanding the correlation function $\exp\left\{2\mathcal{W}_{j,j'}(\mathbf{K}_f,\mathbf{K}_i,q,q',t)\right\}$ in Eq. (81) and keeping the first order term. It is convenient to define the effective, temperature-dependent, electron-phonon potential exactly the same way it was defined for the elastic case above in Eq. (85), but now we must also use its derivative:

$$\sum_{j_\perp}\int_{-\infty}^{+\infty} dq q_\alpha e^{iqz} e^{-iqz_{j\perp}} v^{el}_{\mathbf{K}-\mathbf{K}',q} e^{-\widetilde{W}(\mathbf{K}-\mathbf{K}',q)} = \sum_{j_\perp}\widehat{q}_\alpha v^{el,eff}_{\mathbf{K}-\mathbf{K}'}(T,z-z_{j\perp}), \tag{90}$$

where the vector operator is again as in Sec. 3.2 above $\widehat{\mathbf{q}} = (\Delta\mathbf{K}, -id/dz)$.

As previously, many of the summations can be carried out trivially. The summations in the surface-parallel directions define the momentum conservation relation, which is that the final projectile parallel momentum must equal that of the incident projectile, plus that contributed by the transferred phonon with a possible **G** vector. The result gives the transition rate components as

$$\begin{aligned} w^{(1)}_{\mathbf{K},n}(\mathbf{k}_f,\mathbf{k}_i) = \frac{A_N^2}{a_c^2}\frac{8\pi}{\hbar}\sum_\nu \frac{\hbar}{2NM\omega(\Delta\mathbf{K},\nu)} e^{-2W_\parallel(\mathbf{K}_f,\mathbf{K}_i)} \\ \times |\mathbf{B}(\mathbf{K},n,\Delta\mathbf{K})\cdot\mathbf{e}(\Delta\mathbf{K},\nu)|^2 \\ \times\left\{\left[n_{BE}(\omega(\Delta\mathbf{K},\nu))+1\right]\delta\left(E_f-E_i+\hbar\omega(\Delta\mathbf{K},\nu)\right)\right. \\ \left. + n_{BE}(\omega(\Delta\mathbf{K},\nu))\delta\left(E_f-E_i-\hbar\omega(\Delta\mathbf{K},\nu)\right)\right\}, \end{aligned} \tag{91}$$

where

$$\begin{aligned} \mathbf{B}(\mathbf{K},n,\Delta\mathbf{K}) = \Re\sum_{j_\perp}\sum_{n'}{}' \frac{\left(\chi_{k_{iz}}(z)\left|\varphi^*_{\mathbf{K},n}(z)\varphi_{\mathbf{K}-\Delta\mathbf{K},n'}(z)\right|\chi_{k_{fz}}(z)\right)}{E^{el}_{\mathbf{K},n}-E^{el}_{\mathbf{K}-\Delta\mathbf{K},n'}} \\ \times\left(\varphi_{\mathbf{K}-\Delta\mathbf{K},n'}(z)\left|\widehat{\mathbf{q}}v^{el,eff}_{\Delta\mathbf{K}}(T,z-z_{j\perp})\right|\varphi_{\mathbf{K},n}(z)\right). \end{aligned} \tag{92}$$

The total transition rate is the summation over all electronic modes

$$w^{(1)}_{DWBA}(\mathbf{k}_f,\mathbf{k}_i) = \sum_{\mathbf{K},n} w^{(1)}_{\mathbf{K},n}(\mathbf{k}_f,\mathbf{k}_i). \tag{93}$$

We also recall that the proper way to introduce the full and correct Debye-Waller factor is through comparison with the general result of Eq. (35) above that indicates the following transformation to be applied to Eq. (35)

$$\left|T^0_{\mathbf{k}_f,\mathbf{k}_i}\right|^2 \Delta k_\alpha\Delta k_{\alpha'} \longrightarrow \frac{4A_N^2}{a_c^2}\sum_{\mathbf{K},n}^{occ.} B_\alpha(\mathbf{K},n,\Delta\mathbf{K})\, B_{\alpha'}(\mathbf{K},n,\Delta\mathbf{K}). \tag{94}$$

The total transition rate can be put into a more compact and recognizable form, and with the correct effective D-W factor the final result for the single phonon transition rate in the DWBA is

$$\begin{aligned} w^{(1)}_{DWBA}(\mathbf{k}_f,\mathbf{k}_i) = \frac{A_N^2}{a_c^2}\frac{8\pi}{\hbar}e^{-2W^{eff}(\mathbf{k}_f,\mathbf{k}_i)}\sum_\nu\sum_{\mathbf{K},n}^{occ.}\frac{\hbar}{2NM\omega(\Delta\mathbf{K},\nu)} \\ \times|\mathbf{B}(\mathbf{K},n,\Delta\mathbf{K})\cdot\mathbf{e}(\Delta\mathbf{K},\nu)|^2 \\ \times|n_{BE}(\omega(\Delta\mathbf{K},\nu))|\delta\left(E_f-E_i-\hbar\omega(\Delta\mathbf{K},\nu)\right). \end{aligned} \tag{95}$$

It is important to note that the mass M and polarization vectors $\mathbf{e}(\Delta\mathbf{K},\nu)$ are those of the crystal core atoms. Scattering configurations for which $\Delta\mathbf{K}$ is larger than the distance to the Brillouin zone boundary are handled by the periodicity in the reciprocal lattice vectors, i.e., $\omega(\Delta\mathbf{K}+\mathbf{G},\nu) = \omega(\Delta\mathbf{K},\nu)$, with similar periodicity for the polarization vectors.

4.4. Determining the Debye-Waller factor, effective correlation functions and displacement operators of the electron density

The effective displacement correlation functions and displacement operators can be identified by comparing Eq. (95) to the corresponding DWBA result of Eq. (67) that we obtained from a general treatment, which for convenience is rewritten here:

$$\begin{aligned} w^{(1)}_{DWBA}(\mathbf{k}_f,\mathbf{k}_i) = \frac{2\pi}{\hbar}\frac{1}{a_c^2}\sum_\nu e^{-2W^{eff}(\mathbf{k}_f,\mathbf{k}_i)}\frac{\hbar}{2NM_S\omega(\Delta\mathbf{K},\nu)} \\ \times\left|\left(\chi_{k_{iz}}(z)\left|\widehat{\mathbf{q}}v^{eff}_{\Delta\mathbf{K}}(T,z)\right|\chi_{k_{fz}}(z)\right)\cdot\mathbf{e}^{eff}(\Delta\mathbf{K},\nu)\right|^2 \\ \times|n_{BE}(\omega(\Delta\mathbf{K},\nu))|\delta\left(E_f-E_i-\hbar\omega(\Delta\mathbf{K},\nu)\right), \end{aligned} \tag{96}$$

An important difference compared to Eq. (95) above is that the mass M_S is the effective mass and $\mathbf{e}^{eff}(\Delta\mathbf{K},\nu)$ is the effective phonon polarization vector of the electron gas. This result was obtained from an atom-surface interaction potential of pairwise summation form

$$\mathcal{V} = \sum_j v(\mathbf{r}-\mathbf{r}_j-\mathbf{u}_j), \tag{97}$$

Choosing the interaction potential according to the Esbjerg-Nørskov relation [27].

$$\mathcal{V}(\mathbf{r},t) = A_N\, n(\mathbf{r}), \tag{98}$$

and recognizing that since $n(\mathbf{r})$ is periodic parallel to the surface and thus is actually of the form of the summation of Eq. (97), identifies the DWBA matrix element as

$$\left(\chi_{k_{iz}}(z)\left|\widehat{q}_\alpha v^{eff}_{\Delta\mathbf{K}}(T,z)\right|\chi_{k_{fz}}(z)\right) = A_N\left(\chi_{k_{iz}}(z)\left|\widehat{q}_\alpha n^{eff}_{\Delta\mathbf{K}}(T,z)\right|\chi_{k_{fz}}(z)\right), \tag{99}$$

with

$$n^{eff}_{\Delta\mathbf{K}}(T,z) = \frac{1}{2\pi}\int_{-\infty}^{+\infty} dq\, e^{iqz}\, n_{\Delta\mathbf{K},\,q}\, e^{-\widetilde{W}(\Delta\mathbf{K},\,q)}. \tag{100}$$

It is important to emphasize here that the dispersion (van der Waals) part of the interaction potential can, in principle, be included in the distorted wave functions $\chi_{k_{iz}}(z)$. However, the choice of the interaction potential in the form of Eq. (98) implies that the attractive part of the potential due to dispersion forces is partially neglected. This is equivalent to saying that the atoms start interacting with the surface and exchange energy only during deceleration before contacting the surface and acceleration after the collision, the initial and final kinetic energies being therefore those at the bottom of the potential well. Thus, these disregarded effects of the attractive forces can be empirically compensated for by adding the depth of the potential well D to that part of the atom kinetic energy associated with normal motion [60]. Further discussion on this point appears in Subsections 5.3 and 5.5.

The identification of the effective displacement functions becomes evident upon introducing the matrix element of Eq. (99) into the electron-phonon DWBA of Eq. (95) above

$$\begin{aligned} w^{(1)}_{DWBA}(\mathbf{k}_f,\mathbf{k}_i) = \frac{4\pi}{a_c^2}e^{-2W^{eff}(\mathbf{k}_f,\mathbf{k}_i)} \\ \sum_\nu\sum_{\mathbf{K},n}\left|\left(\chi_{k_{iz}}(z)\left|\widehat{\mathbf{q}}v^{eff}_{\Delta\mathbf{K}}(T,z)\right|\chi_{k_{fz}}(z)\right)\cdot\mathbf{C}(\mathbf{K},n,\Delta\mathbf{K})\right|^2 \\ \times\left|n_{BE}(\omega(\Delta\mathbf{K},\nu))\right|\delta\left(E_f-E_i-\hbar\omega(\Delta\mathbf{K},\nu)\right), \end{aligned} \tag{101}$$

where the α cartesian component of the vector $\mathbf{C}(\mathbf{K},n,\Delta\mathbf{K})$ is

$$C_\alpha(\mathbf{K},n,\Delta\mathbf{K}) = \sqrt{\frac{1}{NM\omega(\Delta\mathbf{K},\nu)}}\,\frac{e_\alpha(\Delta\mathbf{K},\nu)\,B_\alpha(\mathbf{K},n,\Delta\mathbf{K})}{\left(\chi_{k_{iz}}(z)\left|\,\widehat{q}_\alpha\, n^{eff}_{\Delta\mathbf{K}}(T,z)\right|\chi_{k_{fz}}(z)\right)}. \tag{102}$$

Comparing the above to the general DWBA expression of Eq. (96), or Eq. (67), allows us to pick off the effective time and position dependent displacement correlation function in its dyadic form:

$$\left\langle u^{eff}_{\alpha,j}(0)u^{eff}_{\alpha',j'}(t)\right\rangle = 2\hbar\sum_{\mathbf{Q},\,\nu}\sum_{\mathbf{K},\,n} C_\alpha(\mathbf{K},n,\mathbf{Q})C^*_{\alpha'}(\mathbf{K},n,\mathbf{Q})e^{i\mathbf{Q}\cdot\left(\mathbf{R}_j-\mathbf{R}_{j'}\right)}$$
$$\times\left\{\left[n_{BE}(\omega(\mathbf{Q},\nu))+1\right]e^{-i\omega(\mathbf{Q},\nu)t}\right.$$
$$\left.+\,n_{BE}(\omega(\mathbf{Q},\nu))e^{i\omega(\mathbf{Q},\nu)t}\right\}, \tag{103}$$

where the summation $\sum_{\mathbf{Q},\,\nu}$ is restricted to the first surface Brillouin zone, $-\mathbf{G}/2<\mathbf{Q}<\mathbf{G}/2$.

Taking the limits $j=j'$ and $t\to 0$ the above becomes independent of lattice position and reduces to the mean square displacement

$$\left\langle u^{eff}_{\alpha,j}(t)u^{eff}_{\alpha',j}(t)\right\rangle = \left\langle u^{eff}_{\alpha,0}(0)u^{eff}_{\alpha',0}(0)\right\rangle$$
$$= 4\hbar\sum_{\mathbf{Q},\nu}\sum_{\mathbf{K},n} C_\alpha(\mathbf{K},n,\mathbf{Q})C^*_{\alpha'}(\mathbf{K},n,\mathbf{Q})$$
$$\times\left\{n_{BE}(\omega(\mathbf{Q},\nu))+\frac{1}{2}\right\}. \tag{104}$$

Eq. (104) is the effective mean square displacement seen by an atom in its collision with the surface. The relationship of the effective mean square displacement to the vibrations of the cores is determined via the electron-phonon interaction, thus we note again that in Eq. (104) the polarization vectors and the mass M are those of the cores, i.e. in particular the mass M is well defined and is not an effective mass. This effective mean square displacement is the same as appears in the Debye-Waller factor.

Both the mean square correlation function and the displacement correlation function above can be generated from the appropriate averaging using the following effective displacement operator $u^{eff}_{\alpha,\,j}(t)$ for the vibrational displacement of the j-th atom as a function of time t. For making correlation functions of the same cartesian direction (i.e., the diagonal terms of the dyadic) such as $\left\langle u^{eff}_{\alpha,\,j}(0)u^{eff}_{\alpha,\,j'}(t)\right\rangle$ the displacement operator is given by

$$u^{eff}_{\alpha,j}(t) = \sqrt{2\hbar}\sum_{\mathbf{Q},\,\nu}\left[\sum_{\mathbf{K},\,n}\left|C_\alpha(\mathbf{K},n,\mathbf{Q})\right|^2\right]^{1/2}$$
$$\times\; e^{i\mathbf{Q}\cdot\mathbf{R}_j}\left[\hat{a}^\dagger(\mathbf{Q},\nu)e^{-i\omega(\mathbf{Q},\nu)t}+\hat{a}(\mathbf{Q},\nu)e^{i\omega(\mathbf{Q},\nu)t}\right]. \tag{105}$$

Having the actual form of the displacement operator is useful for many other types of calculations and an example is the inelastic close coupling formalism discussed in Sec. 7 below. Other examples of the potential use of these displacement operators would be in the study of polarons or plasmons at the surface. For polarons in insulators, the polarization vector is proportional to the effective displacement and the charge density is the gradient of this polarization vector [57]. Using the phonon displacement of Eq. (105) would allow evaluation of the energy and effective mass of polarons including the effects of electron-phonon coupling. For the case of plasmons in metals, one could obtain a better estimate of the plasmon frequency upon taking account of the vibrational oscillations of the charge density, including electron-phonon interactions, via the phonon displacement vectors of Eq. (105). Even though the theory developed here is primarily for metals, the phonon displacements of Eq. (105) could be used in calculations for any of the many types of excitations of quasiparticles and collective excitations that are dependent on phonon displacements near the surface, thus including electron phonon coupling effects, and can also be extended to materials other than simple metals.

Finally, and for completeness, using the mean-square displacements of Eq. (104) above, we write out in full the argument of the effective D-W factor. This is the Debye-Waller factor that appears in both the elastic and the single phonon inelastic transition rates.

$$2W^{eff}(\mathbf{k}_f,\mathbf{k}_i) = \sum_{\alpha,\;\alpha'=1}^{3}\;\Delta k_\alpha\;\Delta k_{\alpha'}\;\left\langle u^{eff}_{\alpha,\,j}(t)\;u^{eff}_{\alpha',\,j}(t)\right\rangle$$
$$= 4\hbar\sum_{\mathbf{Q},\nu}\;\sum_{\mathbf{K},n}\left|\Delta\mathbf{k}\;\cdot\;\mathbf{C}(\mathbf{K},n,\mathbf{Q})\right|^2$$
$$\times\;\left\{n_{BE}(\omega(\mathbf{Q},\nu))+\frac{1}{2}\right\}. \tag{106}$$

A notable observation is that the Esbjerg-Nørskov constant A_N has cancelled out of the D-W factor. This is an important observation because it means that the effective Debye-Waller factor is based only on the very general principle that the atom-surface potential that causes energy transfer is proportional to the surface electron density, but does not depend on the value of the proportionality constant.

Notable also is the fact that the dependence on initial and final projectile momenta is substantially more complex than the simple dependence on $\Delta\mathbf{k}=\mathbf{k}_f-\mathbf{k}_i$ encountered in simpler theoretical treatments. This more complex momentum dependence, as well as dependence on the attractive adsorption well in the interaction potential, is introduced through the presence of the distorted atomic wave functions. The polarization vectors as well as the mass M in the above equation are those of the crystal cores, e.g., the same ones encountered in bulk neutron scattering. It is the electron-phonon coupling, via the e-ph matrix elements, that produces the actual effective vibrational mean-square displacements experienced by the colliding projectile interacting with the electron gas in front of the surface.

As an added comment, we note that the correlation functions of Eqs. (103) and (104) contain additional dependence on the temperature T apart from that expected from the Bose-Einstein functions appearing explicitly. Consequently, the same is true for the Debye-Waller factor of Eq. (106). This additional temperature dependence arises directly from the electron-phonon coupling matrix elements and can be viewed as additional temperature dependence arising from electronic Debye-Waller effects.

It is useful to note that the matrix elements $A(\mathbf{K},n,\mathbf{Q},q)$, $\mathbf{B}(\mathbf{K},n,\mathbf{Q})$ and $\mathbf{C}(\mathbf{K},n,\mathbf{Q})$ are essentially products of the perturbed potential multiplied by the electronic response function in the Lindhard [58] form at $T=0$ K (otherwise, at $T>0$ K the electronic Fermi occupation probabilities $f_{\mathbf{K},n}$ should appear through the product $f_{\mathbf{K},n}(1-f_{\mathbf{K}-\Delta\mathbf{K},n'})$. This form readily permits the extension of the theory to incorporate the response of low-energy acoustic surface plasmons (ASP) by replacing the Lindhard response function for free electrons with the one for interacting electrons in the random-phase approximation. The recent demonstration that HAS can detect ASPs in the THz regime calls for such an extension [59].

5. Relating scattered intensities to the electron-phonon coupling constant

In this section a series of well tested approximations of electron-phonon interaction theory is applied to the general expressions for scattering spectra and correlation functions derived in Sec. 4 above. We will begin with the intensity for single phonon inelastic scattering because that case illustrates the approximations in a clear manner and actually leads to the simplest and most easily interpreted results.

5.1. Single phonon spectrum and the mode-dependent electron-phonon coupling constant

We start by repeating the result of Eq. (95) for the transition rate of the single-phonon intensity spectrum, here written out in fully expanded form:

$$
\begin{aligned}
w^{(1)}_{DWBA}(\mathbf{k}_f,\mathbf{k}_i) = {} & \frac{A_N^2}{a_c^2}\frac{8\pi}{\hbar}e^{-2W^{eff}(\mathbf{k}_f,\mathbf{k}_i)}\sum_{\nu}\left[\frac{\hbar}{2NM\omega(\Delta\mathbf{K},\nu)}\right] \\
& \times\sum_{\mathbf{K},n}\Bigg[\Re\sum_{j_\perp}{\sum_{n'}}'\left(\chi_{k_{iz}}(z)\left|\varphi^*_{\mathbf{K},n}(z)\varphi_{\mathbf{K}-\Delta\mathbf{K},n'}(z)\right|\chi_{k_{fz}}(z)\right) \\
& \times\frac{1}{E^{el}_{\mathbf{K},n}-E^{el}_{\mathbf{K}-\Delta\mathbf{K},n'}} \\
& \times\left(\varphi_{\mathbf{K}-\Delta\mathbf{K},n'}(z)\left|\hat{\mathbf{q}}v^{el,eff}_{\Delta\mathbf{K}}(T,z-z_{j_\perp})\right|\varphi_{\mathbf{K},n}(z)\right) \\
& \cdot\mathbf{e}(\Delta\mathbf{K},\nu)\nu\Bigg]^2\left|n_{BE}(\omega(\Delta\mathbf{K},\nu))\right| \\
& \times\delta\left(E_f-E_i-\hbar\omega(\Delta\mathbf{K},\nu)\right). \qquad (107)
\end{aligned}
$$

A standard approximation often applied is to replace the energy denominators by the phonon energy [36], $E^{el}_{\mathbf{K},n}-E^{el}_{\mathbf{K}-\Delta\mathbf{K},n'}=\hbar\omega(\Delta\mathbf{K},\nu)$, an approximation that is quite appropriate to this treatment of single phonon transfers at metal surfaces [37]. This operation simplifies the above equation to

$$
\begin{aligned}
w^{(1)}_{DWBA}(\mathbf{k}_f,\mathbf{k}_i) = {} & \frac{A_N^2}{a_c^2}\frac{8\pi}{\hbar}e^{-2W^{eff}(\mathbf{k}_f,\mathbf{k}_i)}\sum_{\nu}\left[\frac{\hbar}{2NM\omega(\Delta\mathbf{K},\nu)}\right] \\
& \times\sum_{\mathbf{K},n}\frac{1}{\left[\hbar\omega(\Delta\mathbf{K},\nu)\right]^2}\Bigg[\Re\sum_{j_\perp}{\sum_{n'}}'\Big(\chi_{k_{iz}}(z)\Big|\varphi^*_{\mathbf{K},n}(z) \\
& \times\quad\varphi_{\mathbf{K}-\Delta\mathbf{K},n'}(z)\Big|\chi_{k_{fz}}(z)\Big) \\
& \times\left(\varphi_{\mathbf{K}-\Delta\mathbf{K},n'}(z)\left|\hat{\mathbf{q}}v^{el,eff}_{\Delta\mathbf{K}}(T,z-z_{j_\perp})\right|\varphi_{\mathbf{K},n}(z)\right) \\
& \cdot\mathbf{e}(\Delta\mathbf{K},\nu)\nu\Bigg]^2\left|n_{BE}(\omega(\Delta\mathbf{K},\nu))\right| \\
& \times\delta\left(E_f-E_i-\hbar\omega(\Delta\mathbf{K},\nu)\right). \qquad (108)
\end{aligned}
$$

We now cast the above into a more compact form using standard definitions. The overlap integral is usually defined by

$$
I_{n,n'}(\mathbf{K},\ \Delta\mathbf{K})\ \equiv\ \left(\chi_{k_{iz}}(z)\left|\varphi^*_{\mathbf{K},n}(z)\varphi_{\mathbf{K}-\Delta\mathbf{K},n'}(z)\right|\chi_{k_{fz}}(z)\right)\ . \qquad (109)
$$

It is a matrix element of the non-diagonal electron density function. The electron-phonon coupling matrix is notated as

$$
\begin{aligned}
g_{n,n'}(\mathbf{K},\ \Delta\mathbf{K},\nu)\equiv{} & \sum_{j_\perp}\left[\frac{\hbar}{2\ NM\omega(\Delta\mathbf{K},\nu)}\right]^{1/2} \\
& \times\left(\varphi_{\mathbf{K}-\Delta\mathbf{K},n'}(z)\ \left|\hat{\mathbf{q}}\ v^{el,eff}_{\Delta\mathbf{K}}(T,z-z_{j_\perp})\ \right|\ \varphi_{\mathbf{K},n}(z)\right) \\
& \cdot\mathbf{e}(\Delta\mathbf{K},\nu). \qquad (110)
\end{aligned}
$$

The definition for $g_{n,n'}(\mathbf{K},\Delta\mathbf{K},\nu)$ differs slightly from the standard definitions [36,41] in that an effective, temperature-dependent electron-phonon potential now appears in the matrix element in our treatment. This arises from the Debye-Waller considerations on the electrons that we have introduced into this treatment.

Using the above two definitions of Eqs. (109) and (110) puts the single-phonon transition rate into the form

$$
\begin{aligned}
w^{(1)}_{DWBA}(\mathbf{k}_f,\mathbf{k}_i) = {} & \frac{A_N^2}{a_c^2}\frac{8\pi}{\hbar}e^{-2W^{eff}(\mathbf{k}_f,\mathbf{k}_i)}\sum_{\nu}\frac{1}{\left[\hbar\omega(\Delta\mathbf{K},\nu)\right]^2} \\
& \times\sum_{\mathbf{K},n}\left[\Re{\sum_{n'}}'I_{n,n'}(\mathbf{K},\Delta\mathbf{K})g_{n,n'}(\mathbf{K},\Delta\mathbf{K},\nu)\right]^2 \\
& \times\left|n_{BE}(\omega(\Delta\mathbf{K},\nu))\right|\delta\left(E_f-E_i+\hbar\omega(\Delta\mathbf{K},\nu)\right). \qquad (111)
\end{aligned}
$$

We wish to put the above in terms of the mode-specific components of the electron-phonon coupling constant, which were first recognized by Allen [36,41,42] and are expressed as

$$
\lambda_{\mathbf{Q},\nu}=\frac{2}{\mathcal{N}(E_F)[\hbar\omega(\mathbf{Q},\nu)]^3}\sum_{\mathbf{K},n}\left|\sum_{n'}g_{n,n'}(\mathbf{K},\mathbf{Q},\nu)\delta_{\{\mathbf{K}-\mathbf{Q},n'\};\,k_F}\right|^2\delta_{\{\mathbf{K},n\};\,k_F}, \qquad (112)
$$

and their relation to the e-ph coupling constant is $\lambda=\langle\lambda_{\mathbf{Q},\nu}\rangle$. The Kronecker δ-functions signify that both electron states, denoted by $\mathbf{K},n$ and $\mathbf{K}-\mathbf{Q},n'$, must lie close to the Fermi energy and $\mathcal{N}(E_F)$ is the density of electronic states (DOS) at the Fermi energy.

Before casting the single phonon transition rate in terms of the $\lambda_{\mathbf{Q},\nu}$ it is necessary to show that the Kronecker δ-functions in the definition of Eq. (112) are implicitly present in Eq. (111). This is made evident by recognizing that the dominant contributions to the overlap matrix element $I_{n,n'}(\mathbf{K},\Delta\mathbf{K})$ come only from electron states very near the Fermi surface, i.e., we can write

$$
\begin{aligned}
I_{n,n'}(\mathbf{K},\Delta\mathbf{K}) & \equiv\left(\chi_{k_{iz}}(z)\left|\varphi^*_{\mathbf{K},n}(z)\varphi_{\mathbf{K}-\Delta\mathbf{K},n'}(z)\right|\chi_{k_{fz}}(z)\right) \\
& \approx\left(\chi_{k_{iz}}(z)\left|\varphi^*_{\mathbf{K},n}(z)\varphi_{\mathbf{K}-\Delta\mathbf{K},n'}(z)\right|\chi_{k_{fz}}(z)\right) \\
& \quad\times\delta_{\{\mathbf{K},n\};\,k_F}\delta_{\{\mathbf{K}-\Delta\mathbf{K},n'\};\,k_F} \qquad (113) \\
& =I_F(\Delta\mathbf{K})\delta_{\{\mathbf{K},n\};\,k_F}\delta_{\{\mathbf{K}-\Delta\mathbf{K},n'\};\,k_F}.
\end{aligned}
$$

The δ-functions indicate that the important contributions arise only when both electron wave functions have energies very near the Fermi energy, and this is also signified by the subscript F on the overlap integral $I_F(\Delta\mathbf{K})$. This result is understood by recognizing that outside the surface the electron wave functions are exponentially decaying with a length constant depending on the work function ϕ, i.e., for electrons at the Fermi energy

$$
\varphi_{\mathbf{K},n}(z)\ \approx\ e^{-\kappa_F z}\ , \qquad (114)
$$

with

$$
\kappa_F\ =\ \frac{\sqrt{2\ m_e^*\phi}}{\hbar}\ , \qquad (115)
$$

where m_e^* is the electronic effective mass. All other overlap matrix elements for electron energies deeper into the Fermi sea are much smaller. To make this explicitly clear, note that for electron states close to the Fermi energy the overlap integral is of the form

$$
I_F(\Delta\mathbf{K})\ \approx\ \left(\chi_{k_{iz}}(z)\left|e^{-2\kappa_F z}\right|\chi_{k_{fz}}(z)\right)\ , \qquad (116)
$$

and the projectile distorted wave functions $\chi_{k_{iz}}(z)$ and $\chi_{k_{fz}}(z)$ decay extremely rapidly towards the surface. All other electron wave functions would have energies with respect to the vacuum that result in decay constants $\kappa>\kappa_F$, thus their corresponding overlap integrals would be much smaller because of the rapid decay of the projectile wave functions. This justifies writing the overlap integral restricted to states near the Fermi surface with the electron wave vector δ-functions as we have done above in Eq. (113).

Combining the above definitions casts the transition rate of Eq. (111) into the following form:

$$
\begin{aligned}
w^{(1)}_{DWBA}(\mathbf{k}_f,\mathbf{k}_i) = {} & \frac{A_N^2}{a_c^2}\frac{4\pi}{\hbar}\mathcal{N}(E_F)e^{-2W^{eff}(\mathbf{k}_f,\mathbf{k}_i)} \\
& \times\sum_{\nu}\hbar\omega(\Delta\mathbf{K},\nu)\left|I_F(\Delta\mathbf{K})\right|^2\lambda_{\Delta\mathbf{K},\nu} \\
& \times\left|n_{BE}(\omega(\Delta\mathbf{K},\nu))\right|\delta\left(E_f-E_i+\hbar\omega(\Delta\mathbf{K},\nu)\right). \qquad (117)
\end{aligned}
$$

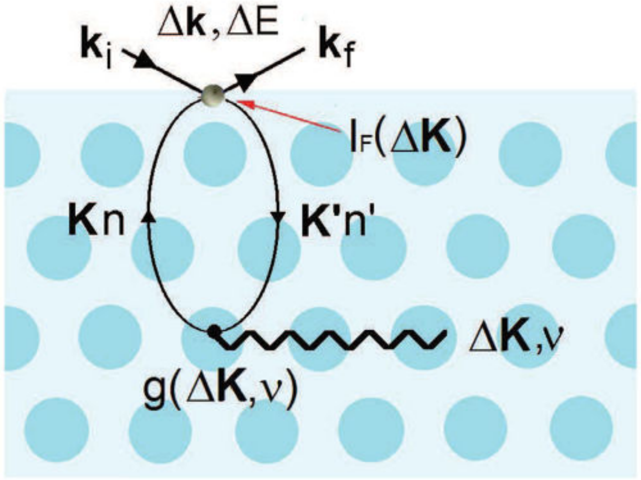

Fig. 1. An incident atom in a state of wavevector $\mathbf{k}_i$ is inelastically scattered into a final state of wavevector $\mathbf{k}_f$ by the overlap vertex $I_F(\Delta\mathbf{K})$ and creates a phonon of wavevector $\Delta\mathbf{K}$ and branch index ν via a virtual electron-hole pair of states and the electron-phonon vertex term g. (Reprinted with permission from Ref. [46]. Copyright [2016] American Chemical Society).

The above is similar to the important result of Sklyadneva et al. [35,39] It shows that the probability of creating (or annihilating) a phonon mode $\{\mathbf{Q},\nu\}$ with frequency $\omega(\mathbf{Q},\nu)$ is proportional to the respective electron-phonon coupling constant $\lambda_{\mathbf{Q},\nu}$. However, Eq. (117) contains an important difference, and that is it appears with the correct Debye-Waller factor $\exp\{-2W^{eff}(\mathbf{k}_f,\mathbf{k}_i)\}$. Furthermore, this Debye-Waller factor is the effective D-W factor of the electron density, via the electron-phonon coupling interaction, evaluated at the position of the overlap of the electronic wave functions and the wave functions of the colliding atomic projectile. This effective D-W factor has been identified and evaluated in Eq. (106) of Subsection 4.4 above.

The inelastic He-atom scattering process is illustrated by the diagram of Fig. 1, in which an incident projectile atom in a state of wavevector $\mathbf{k}_i$ is inelastically scattered into a final state of wavevector $\mathbf{k}_f$, eventually creating a phonon of wavevector $\Delta\mathbf{K}$ and branch index ν via the mediation of a virtual electron-hole pair involving the electronic states at the Fermi level of parallel wavevectors $\mathbf{K}$ and $\mathbf{K}'$ and band indices n and n'. The non-diagonal electron density matrix element $I_F(\Delta\mathbf{K})$ acts as an effective scattering potential, whose matrix element between the initial and final atom states provides the upper vertex term, whereas the lower vertex term is expressed by the electron-phonon matrix element $g_{n,n'}(\mathbf{K},\Delta\mathbf{K},\nu)$. It is important to remark that the phonon can be generated near the surface or, as depicted in Fig. 1, at several atomic planes beneath the surface, the maximum depth being determined by the range of the e-ph interaction. Since in some cases this maximum depth can be larger than might otherwise be expected the effect has been dubbed the quantum sonar effect (QSE) [35,39].

5.2. Elastic scattering and its relation to electron-phonon coupling

The elastic diffraction intensity was developed above in Subsection 4.2. The overlap integral is similar to that of Eq. (109) above for the inelastic case, its evaluation again shows that only electron states near the Fermi surface will contribute, but since the parallel momentum transfers are limited to surface reciprocal lattice vectors Eq. (113) simplifies to

$$I_{n,n'}(\mathbf{K},\ \mathbf{G}) \ = \ I_F(\mathbf{G})\ \delta_{\{\mathbf{K},n\};\,k_F}\ \delta_{\{\mathbf{K+G},n'\};\,k_F}\ . \tag{118}$$

Applying the electron-phonon approximation on the energy denominators of Eq. (89) must be specified more carefully in the elastic case. In setting $E^{el}_{\mathbf{K},n} - E^{el}_{\mathbf{K+G},n'} \approx \hbar\overline{\omega}(\mathbf{K},\nu)$ the energy $\hbar\overline{\omega}(\mathbf{K},\nu)$ must be regarded as an average phonon energy transferred in the electron-phonon interaction, because no net energy is exchanged between the final and initial state of the atomic projectile. The above two approximations transform the elastic transition rate into

$$w^{(0)}_{DWBA}(\mathbf{k}_f,\mathbf{k}_i) = \frac{A_N^2}{a_c^2}\frac{8\pi}{\hbar}\sum_{\mathbf{G}} e^{-2W^{eff}(\mathbf{k}_f,\mathbf{k}_i)}\big|I_F(\mathbf{G})\big|^2 \sum_{\mathbf{K},n}\frac{\delta_{\{\mathbf{K},n\};\,k_F}}{[\hbar\overline{\omega}(\mathbf{K},\nu)]^2}$$
$$\times\left|{\sum_{n'}}'\sum_{j_\perp}\Big(\varphi_{\mathbf{K+G},n'}(z)\,\Big|v^{el,eff}_{\mathbf{G}}(T,z-z_{j_\perp})\Big|\,\varphi_{\mathbf{K},n}(z)\Big)\right.$$
$$\left.\times\,\delta_{\{\mathbf{K+G},n'\};\,k_F}\right|^2\delta_{\mathbf{K}_f-\mathbf{K}_i,\mathbf{G}}\,\delta(E_f-E_i)\ . \tag{119}$$

In order to make Eq. (119) appear in a simpler form we can define a component containing the e-ph coupling information, similar to the $\lambda_{\mathbf{Q},\nu}$ of Eq. (112) arising for the inelastic case, as follows:

$$\Lambda(\mathbf{G}) = \sum_{\mathbf{K},n}\frac{\delta_{\{\mathbf{K},n\};\,k_F}}{[\hbar\overline{\omega}(\mathbf{K},\nu)]^2}\left|{\sum_{n'}}'\sum_{j_\perp}\Big(\varphi_{\mathbf{K+G},n'}(z)\,\Big|v^{el,eff}_{\mathbf{G}}(T,z-z_{j_\perp})\Big|\right.$$
$$\left.\times\,\varphi_{\mathbf{K},n}(z)\Big)\,\delta_{\{\mathbf{K+G},n'\};\,k_F}\right|^2\ . \tag{120}$$

Then the form of the elastic scattering intensity, after applying the standard electron-phonon approximations becomes

$$w^{(0)}_{DWBA}(\mathbf{k}_f,\mathbf{k}_i) = \frac{A_N^2}{a_c^2}\ \frac{8\pi}{\hbar}\ \sum_{\mathbf{G}}\ e^{-2W^{eff}(\mathbf{k}_f,\mathbf{k}_i)}\ \big|I_F(\mathbf{G})\big|^2$$
$$\times\ \Lambda(\mathbf{G})\ \delta_{\mathbf{K}_f-\mathbf{K}_i,\ \mathbf{G}}\ \delta(E_f-E_i)\ . \tag{121}$$

This is of the expected general form of Eq. (63) for elastic scattering in the DWBA where it is seen that the matrix element consists of the overlap integral factor $\big|I_F(\mathbf{G})\big|^2$ multiplied by the electron-phonon interaction factor $\Lambda(\mathbf{G})$. This latter factor, like the closely related electron-phonon coupling constant components $\lambda_{\mathbf{Q},\nu}$, is proportional to the mod-squared electron-phonon matrix elements, but it is defined only at the diffraction peak positions. The effective Debye-Waller exponent appearing in the elastic intensity is specified by Eq. (106).

5.3. Relating the Debye-Waller factor to the electron-phonon coupling constant

The argument of the exponential in the effective Debye-Waller factor is given above in Eq. (106). This is the general form which shows that the Debye-Waller exponent has a much more complicated energy dependence than the simple dependence on $\Delta\mathbf{k} = \mathbf{k}_f - \mathbf{k}_i$ often assumed based on approximations more suited for neutron scattering or X-ray diffraction. This additional energy dependence arises from the appearance of the matrix elements involving the distorted projectile states. This also indicates that effects of the adsorption well are included, since the distorted states will in general be solutions of a potential that contains an attractive well.

Further simplifications will, however, require additional approximations. One step is to recognize that to a good approximation the electron density will be approximately exponential, i.e., $n^{eff}_{\mathbf{Q}}(T,z) \propto \exp(-2\kappa_F z)$ and consequently its derivative will be approximately a multiplicative factor of $-2\kappa_F$. This permits combining the vector operator components $\widehat{q}_\alpha$ into a new momentum transfer vector operator that depends on momentum transfer, the electronic effective mass m_e^* and the work function ϕ

$$\hat{\hat{\mathbf{q}}} = \left(\Delta k_x, \Delta k_y, -i\frac{\Delta k_z}{2\kappa_F}\frac{d}{dz}\right) = \left(\Delta k_x, \Delta k_y, -i\frac{\hbar\Delta k_z}{2\sqrt{2\, m_e^*\phi}}\frac{d}{dz}\right), \tag{122}$$

allowing $2W^{eff}(\mathbf{k}_f, \mathbf{k}_i)$ to be expressed as

$$\begin{aligned} &2W^{eff}(\mathbf{k}_f, \mathbf{k}_i) \\ &= 8\sum_{\mathbf{Q},\nu}\sum_{\mathbf{K},n}\left[\Re\sum_{j_\perp}\sum_{n'}{}' \frac{\left(\chi_{k_{iz}}(z)\middle|\varphi^*_{\mathbf{K},n}(z)\varphi_{\mathbf{K-Q},n'}(z)\middle|\chi_{k_{fz}}(z)\right)}{\left(\chi_{k_{iz}}(z)\middle|n^{eff}_{\mathbf{Q}}(T,z)\middle|\chi_{k_{fz}}(z)\right)}\right. \\ &\quad\times\frac{1}{E^{el}_{\mathbf{K},n}-E^{el}_{\mathbf{K-Q},n'}}\left(\varphi_{\mathbf{K-Q},n'}(z)\middle|\hat{\hat{\mathbf{q}}}\, v^{el,eff}_{\mathbf{Q}}(T,z-z_{j_\perp})\middle|\varphi_{\mathbf{K},n}(z)\right) \\ &\quad\left.\cdot\mathbf{e}(\mathbf{Q},\nu)\sqrt{\frac{\hbar}{2NM\omega(\mathbf{Q},\nu)}}\right]^2\left\{n_{BE}(\omega(\mathbf{Q},\nu))+\frac{1}{2}\right\}. \end{aligned} \tag{123}$$

Applying the electron-phonon approximations of replacing the energy denominators by the phonon energy, and recognizing that the overlap integral restrains all electronic summations to the region of the Fermi surface as shown in Eq. (113) puts the exponent into the form

$$\begin{aligned} 2W^{eff}(\mathbf{k}_f, \mathbf{k}_i) &= 4\mathcal{N}(E_F)\sum_{\mathbf{Q},\nu}\hbar\omega(\mathbf{Q},\nu) \\ &\quad\times\left[\frac{I_F(\mathbf{Q})}{\left(\chi_{k_{iz}}(z)\middle|n^{eff}_{\mathbf{Q}}(T,z)\middle|\chi_{k_{fz}}(z)\right)}\right]^2 \\ &\quad\times\left\{n_{BE}(\omega(\mathbf{Q},\nu))+\frac{1}{2}\right\}\overline{\lambda}_{\mathbf{Q},\nu}, \end{aligned} \tag{124}$$

but because of the new definition of the vector operator $\hat{\hat{\mathbf{q}}}$ in Eq. (122) the electron-phonon matrix element, and hence the mode selected $\overline{\lambda}_{\mathbf{Q},\nu}$ are redefined slightly differently from the standard form of Eq. (112) as follows:

$$\begin{aligned} \overline{g}_{n,n'}(\mathbf{K},\mathbf{Q},\nu) \equiv{} &\sum_{j_\perp}\left[\frac{\hbar}{2NM\omega(\mathbf{Q},\nu)}\right]^{1/2} \\ &\times\left(\varphi_{\mathbf{K-Q},n'}(z)\middle|\hat{\hat{\mathbf{q}}}\, v^{el,eff}_{\mathbf{Q}}(T,z-z_{j_\perp})\middle|\varphi_{\mathbf{K},n}(z)\right)\cdot\mathbf{e}(\mathbf{Q},\nu), \end{aligned} \tag{125}$$

and

$$\begin{aligned} \overline{\lambda}_{\mathbf{Q},\nu} = {}&\frac{2}{\mathcal{N}(E_F)[\hbar\omega(\mathbf{Q},\nu)]^3}\sum_{\mathbf{K},n}\delta_{\{\mathbf{K},n\};k_F} \\ &\times\left|\sum_{n'}{}'\delta_{\{\mathbf{K-Q},n'\};k_F}\overline{g}_{n,n'}(\mathbf{K},\mathbf{Q},\nu)\right|^2. \end{aligned} \tag{126}$$

The high temperature limit, obtained by expanding the Bose-Einstein distribution function for $k_BT > \hbar\omega(\mathbf{Q},\nu)$, is

$$2W^{eff}(\mathbf{k}_f, \mathbf{k}_i) = 4\mathcal{N}(E_F)k_BT\sum_{\mathbf{Q},\nu}\left[\frac{I_F(\mathbf{Q})}{\left(\chi_{k_{iz}}(z)\middle|n^{eff}_{\mathbf{Q}}(T,z)\middle|\chi_{k_{fz}}(z)\right)}\right]^2\overline{\lambda}_{\mathbf{Q},\nu}. \tag{127}$$

The above forms show the dependence of the Debye-Waller exponent on the electron-phonon matrix elements, but expresses this dependence as a weighted summation over a slightly altered definition of the mode selective mass correction components $\lambda_{\mathbf{Q},\nu}$.

There is one interesting case in which the form of the Debye-Waller argument can be put in terms of a summation over the standard definition of Eq. (112) for $\lambda_{\mathbf{Q},\nu}$ and this is for the specular diffraction peak, where the parallel momentum transfer is zero. This is also a good approximation for when the transfer of momentum normal to the surface is large compared to the parallel momentum, for which $\Delta\mathbf{K}^2 \ll \Delta k_z^2$ and $\Delta\mathbf{K}$ can be ignored. In this case we have

$$\begin{aligned} 2W^{eff}(\mathbf{k}_f, \mathbf{k}_i) &= 4\mathcal{N}(E_F)\frac{m}{m_e^*}\frac{E_i\cos^2(\theta_i)}{\phi}\sum_{\mathbf{Q},\nu}[\hbar\omega(\mathbf{Q},\nu)] \\ &\quad\times\left[\frac{I_F(\mathbf{Q})}{\left(\chi_{k_{iz}}(z)\middle|n^{eff}_{\mathbf{Q}}(T,z)\middle|\chi_{k_{fz}}(z)\right)}\right]^2 \\ &\quad\times\left\{n_{BE}(\omega(\mathbf{Q},\nu))+\frac{1}{2}\right\}\lambda_{\mathbf{Q},\nu}, \end{aligned} \tag{128}$$

where $E_i\cos^2(\theta_i)$ is the incident energy associated with motion perpendicular to the surface. The corresponding high temperature limit is

$$\begin{aligned} 2W^{eff}(\mathbf{k}_f, \mathbf{k}_i) &= 4\mathcal{N}(E_F)\,\frac{m}{m_e^*}\,\frac{E_i\cos^2(\theta_i)}{\phi}k_BT \\ &\quad\times\sum_{\mathbf{Q},\nu}\left[\frac{I_F(\mathbf{Q})}{\left(\chi_{k_{iz}}(z)\middle|n^{eff}_{\mathbf{Q}}(T,z)\middle|\chi_{k_{fz}}(z)\right)}\right]^2\lambda_{\mathbf{Q},\nu}. \end{aligned} \tag{129}$$

The weighting coefficients are quantities that can be readily evaluated, i.e., the squared ratio of the overlap integral and the distorted wave matrix elements of the repulsive potential, and in many cases such as for a flat, weakly corrugated surface this ratio is nearly unity. Thus the simplest approximation is

$$\begin{aligned} 2W^{eff}(\mathbf{k}_f, \mathbf{k}_i) &= 4\mathcal{N}(E_F)\frac{m}{m_e^*}\frac{E_i\cos^2(\theta_i)}{\phi}k_BT\sum_{\mathbf{Q},\nu}\lambda_{\mathbf{Q},\nu} \\ &= 4\mathcal{N}(E_F)\frac{m}{m_e^*}E_i\cos^2(\theta_i)\left[\frac{k_BT}{\phi}\right]\lambda, \end{aligned} \tag{130}$$

which shows that the simplest form of the Debye-Waller argument for the specular diffraction beam is proportional to the electron-phonon coupling constant. This allows extraction of λ directly from the temperature dependence of the D-W exponent. Hereafter the symbol λ_{HAS} shall be used to indicate the e-ph coupling constant obtained from Eq. (130) and expressed as a function of the measured specular HAS intensity as

$$\lambda_{HAS} = \frac{-1}{2\mathcal{N}(E_F)}\,\frac{\partial\ln I_{00}(T)}{k_B\,\partial T}\,\frac{m_e^*\phi}{\hbar^2k_{iz}^2}. \tag{131}$$

Values of λ can also be extracted from the Debye-Waller behavior of diffraction peaks using a modified form of Eq. (130) for conditions in which the perpendicular momentum transfer is much larger than that in the directions parallel to the surface, and in fact this is the configuration most often encountered in experiments. Specifically, if $\Delta k_z^2 \gg |\mathbf{G}|^2$ then the Debye-Waller exponent associated with the $\mathbf{G}$ diffraction peak is obtained by making the following replacement in Eq. (130) above:

$$E_i\cos^2(\theta_i) = E_{iz} = \frac{\hbar^2k_{iz}^2}{2\,m} \longrightarrow \frac{\hbar^2|\Delta\mathbf{k}|^2}{8\,m}. \tag{132}$$

where for the diffraction peak the scattering vector is given by $|\Delta\mathbf{k}|^2 = \Delta k_z^2 + \mathbf{G}^2$.

At this point a word of caution should be introduced concerning the use of the so-called Beeby correction. This is an approximation that has been historically important in evaluating atom-surface scattering intensities and consists in adding the well depth D to the energy associated with motion normal to the surface. For the simplest case of specular scattering such as in Eq. (130) this implies

$$E_{iz} \;=\; E_i \cos^2(\theta_i) \;\longrightarrow\; E_{iz} + D \;, \tag{133}$$

whereas for a diffraction peak, such as the case of Eq. (132), the correction must be applied separately to both the incident and final normal momentum according to

$$E_{fz} \;=\; E_f \cos^2(\theta_f) \;\longrightarrow\; E_{fz} + D \;, \tag{134}$$

The Beeby approximation, as originally formulated [60], strictly applies to the use of hard wall repulsive potentials where it is valid only in the case of adsorption well depths that are small compared to the He atom energy associated with motion normal to the surface. In the formalism developed here the attractive well of the physisorption potential is naturally incorporated into the distorted wave Born approximation through the distorted wave functions such as $\chi_{k_{iz}}(z)$ and $\chi_{k_{fz}}(z)$. Thus, particularly for atomic projectiles interacting with metal surfaces, where the interactions involve soft, more slowly varying interaction potentials the attractive physisorption well is already partially accounted for in the distorted wave functions and the use of the Beeby correction is not needed. Also, in the case of flat and weakly corrugated surfaces such as most metals, the approximations leading to Eq. (130) show that the matrix elements taken with respect to these distorted wave functions cancel. Here, however, the inelastic processes have been assumed to mostly occur through the phonon-induced modulation of only the repulsive part of the potential, written in the Esbjerg-Nørskov form of Eq. (98). At surfaces with a fairly hard repulsive potential and a corresponding deep attracting well, as in semiconductors and conducting layered materials (e.g., graphite and transition metal chalcogenides), the role of the long-range attractive potential may not be negligible in inelastic scattering, especially for comparatively low incident energy of the atom projectiles, and the Beeby correction is in order. Clearly, if one uses approximate distorted wave functions $\chi_{k_{iz}}(z)$ and $\chi_{k_{fz}}(z)$ that do not account for the van der Waals attractive potential, then the Beeby correction should be used, with the caveat that its use is valid only if the well depth D is small compared to the energy associated with normal motion. Experimental groups often analyze their atom-scattering data using the Beeby correction. For this reason, we have reported some of the results shown below in Table 5 both with and without the Beeby correction.

5.4. Relationship between λ and the Debye effective force constant

It is of interest to relate the current interpretation of the Debye-Waller factor in terms of the electron-phonon interaction and the widely accepted interpretation in terms of the crystal core masses and Debye temperatures, i.e., the interpretation that is used in many other types of scattering such as neutron, electron or X-ray scattering and also for Mössbauer spectroscopy. The following equation expresses, for the simplest possible case of the specular beam, the two ways of writing the Debye-Waller exponent

$$2W^{\mathit{eff}}(\mathbf{k}_f, \mathbf{k}_i, T) \;=\; \frac{24\, m}{M_S}\,\frac{E_{iz} T}{k_B \Theta_D^2} \;=\; 4\mathcal{N}(E_F)\,\frac{m E_{iz}}{m_e^* \phi}\,\lambda\, k_B T \;. \tag{135}$$

The middle expression of Eq. (135) is the standard result of Eq. (2), often used for determination of the surface Debye temperature Θ_D from the thermal attenuation, while the final term on the right hand side is the result of the electron-phonon interpretation of Eq. (130) developed here. However, as explained above in connection with Eq. (2), for the case of atom scattering the meaning of Θ_D as well as the crystal mass M_S is ambiguous at best. The first problem is that these two parameters appear as the inseparable product $M_S\Theta_D^2$, the second problem is that the mass M_S is related to the true mass of the surface atomic cores only indirectly because the atomic projectiles interact with the electron cloud in front of the surface, and hence only indirectly with the cores. Thus, both M_S and Θ_D^2 are not necessarily those of the crystal core atoms, but are effective values as measured from the electron cloud. This ambiguity helps to explain why in many cases the values of Θ_D as determined from Debye-Waller analysis of He atom scattering experiments often are seen to vary widely from values determined by other types of experiments such as low energy electron diffraction or neutron scattering.

Eq. (135) provides an interesting link between the present e-ph theory and the conventional approach

$$\lambda_{HAS} \;=\; \frac{6 m_e^* \phi}{\mathcal{N}(E_F)}\;\frac{1}{\hbar^2 f_{Ds}} \;, \tag{136}$$

with $f_{Ds} = M_S \Theta_D^2 k_B^2/\hbar^2 = M_S \omega_D^2$ the effective Debye force constant. It is important to note that in Eq. (136) M_S and ω_D are the effective mass and frequency of a mode with the largest e-ph coupling, representing alone the entire spectrum, and cannot in general be interpreted as the surface atom mass and the usual surface Debye frequency ($\hbar\omega_D = k_B\Theta_D$) as derived, for example, from the analysis of LEED spectra, where the interaction between the probe and the atom cores is direct and not mediated by the free electron gas. Eq. (136) connects the e-ph interaction λ to the binding energy of Fermi-level electrons via ϕ, their density of states $\mathcal{N}(E_F)$ and the effective surface Debye force constant which is expressed as f_{Ds}.

5.5. The role of free-electron gas dimensionality

The surface charge density oscillations produced by the phonon thermal motion which are probed by the reflected atoms at a certain distance from the first atomic layer generally involve all electron states at the Fermi level. In the absence of surface states at the Fermi level only the continuum of bulk states contribute to the surface charge oscillations, whereas in the presence of surface localized states, the latter are supposed to contribute most, possibly due to their longer extension outside the crystal. In the former case the use in Eqs. (130) and (135) of the standard density of states $\mathcal{N}_F$ for the 3DEG can be used, whereas in the latter case the expression of $\mathcal{N}_F$ for the 2DEG should be more appropriate. Note that in a first application of this theory to metal surfaces [46] the 3-D $\mathcal{N}_F$ was used also for systems with surface localized states at the Fermi level, by heuristically using the surface-state Fermi wavevector instead of the bulk k_F, which proved satisfactory for a first estimation of λ from the temperature dependence of the D-W exponent.

In order to make the present theory applicable also to surface quasi-1D systems, like, e.g., Bi(114) [61–63], (see Subsection 6.4.1) as well as to quasi-crystalline surfaces which can be viewed as 2-D projections of periodic crystals with dimension $d > 3$ [64–66], it is convenient to introduce the Fermi-level DOS per unit energy and unit d-dimensional hypervolume

$$\mathcal{N}_F^{(d)} \;=\; \frac{k_F^d}{\gamma_d E_F} \;, \tag{137}$$

where

$$\gamma_d \;\equiv\; 2^{d-1}\,\pi^{d/2}\,\Gamma\!\left(\frac{d}{2}\right) \;, \tag{138}$$

d being the dimension, and Γ the Riemann gamma-function defined for integer d as

$$\begin{aligned}\Gamma\left(\frac{d}{2}\right) &= \left(\frac{d}{2}-1\right)! , \qquad \text{d even;}\\ &= \frac{(d-2)!!\sqrt{\pi}}{2^{(d-1)/2}} , \qquad \text{d odd.}\end{aligned} \tag{139}$$

For $d = 2$ ($\gamma_2 = 2\pi$) and $d = 3$ ($\gamma_3 = 2\pi^2$) the usual two-dimensional electron gas (2DEG) and three-dimensional electron gas (3DEG) expressions, $\mathcal{N}_F^{(2)} = m_e^*/\pi\hbar^2$ and $\mathcal{N}_F^{(3)} = m_e^* k_F/\pi^2\hbar^2$, respectively, are readily obtained with m^* the effective mass and $k_F = (2m_e^* E_F)^{1/2}/\hbar$ the Fermi wavevector. $\mathcal{N}_F^{(d)}$ is related to the d-dimensional DOS at the Fermi level $N^{(d)}$ by $\mathcal{N}_F^{(d)} = N^{(d)}(E_F)/r_0^d$, where r_0 is a length defining the lattice unit-cell hypervolume as $v^{(d)} \equiv r_0^d$.

From these definitions, the HAS electron-phonon coupling constant for a general d-dimensional free-electron system is given by

$$\lambda_{HAS}^{(d)} = -\frac{\phi\gamma_d}{(k_F r_0)^d}\,\frac{k_F^2}{(\Delta k_z)^2}\,\frac{\partial \ln\{I(T)\}}{k_B\,\partial T} . \tag{140}$$

In the case that the HAS reflectivity is available as a function of the incident wavevector $\mathbf{k}_i$, the electron-phonon coupling constant is obtained from

$$\lambda_{HAS}^{(d)} = -\frac{\phi\gamma_d}{4(k_F r_0)^d}\,\frac{k_F^2}{k_B T}\,\frac{\partial \ln\left\{I(T)/k_i\right\}}{\partial\left(k_{iz}^2\right)} , \tag{141}$$

where the factor k_i dividing the intensity is the energy-dependent correction to the incident beam intensity.

It is important to remark that the surface charge density, whose modulation scatters the probe atoms, receives comparable contributions from both the Fermi-level free electron bands of the bulk and the electronic surface states, either localized or in the form of surface resonances. The range of the electron-phonon interaction, which allows HAS to detect atomic vibrations several layers beneath the surface (quantum sonar effect, or QSE) is basically that of surface Friedel oscillations in the normal direction beneath the surface (Lang-Kohn (LK) oscillations) [67]. In the semi-infinite jellium they behave for $z \to \infty$ as $\cos[2(k_F z - \gamma_K)]/(k_F z)^2$, where γ_K is a phase shift, and the oscillation period π/k_F provides the length scale of the free-electron gas. First-principle calculations by Li et al. [68] for real metals such as aluminum low-index surfaces actually indicate a slower and less regular decay than predicted by a semi-infinite jellium with the k_F value for aluminum. The addition of the periodic lattice potential and of the corresponding periodicity of the surface potential, introduce further Fermi surface nestings, in addition to the one for $2k_F$ in the direction normal to the surface. Further nestings can occur between Fermi-surface states in equivalent symmetry directions, ($k_{F\parallel}$) and ($k_{F\perp}$). These reflections, as well as the associated diffraction (umklapp) processes, contribute LK oscillation components of periods ($\pi/k_{F\perp}$), which is generally longer than that of the single component for the semi-infinite jellium, (π/k_F). Surface states at the Fermi level with a wavevector k_{Fs} can also contribute additional components of LK oscillations. The simplest approximation to account for the considerable depth of the surface free-electron gas, including the complexity arising from the projection of the 3-D band structure on the surface space, and the prominent role of surface states is to treat the free-electron gas in the extended surface region as an ideal 3DEG with the surface-state Fermi wavevector k_{Fs} replacing the bulk k_F. The actual range c^* of the electron-phonon interaction responsible for the quantum-sonar effect and the phonon-induced surface charge density oscillations may be taken to be of the order of the surface-state length scale: $c^* \approx \pi/k_{Fs}$ [66]. With this in mind, the Fermi-level DOS of the 3DEG contained in the effective unit-cell volume $c^* a_c$ of the surface region probed by HAS can be expressed as

$$\mathcal{N}(E_F) = c^* a_c \mathcal{N}_F^{(3)} = n_s \mathcal{N}^{(2)}(E_F) ; \qquad n_s \equiv \frac{c^* k_F}{\pi} = \frac{k_F}{k_{Fs}} . \tag{142}$$

With this definition of the number n_s, essentially the number of surface layers contributing to the e-ph coupling constant, the surface 3DEG probed by HAS can be viewed as a stack of n_s 2DEGs, and the HAS electron-phonon coupling constant is then written as

$$\lambda_{HAS} = -\frac{2\pi\phi}{n_s a_c (\Delta k_z)^2}\,\frac{\partial \ln[I(T)]}{k_B T} . \tag{143}$$

It is noted that for a first guess of λ_{HAS} the simple approximation $N(E_F) \approx v_c \mathcal{N}_F^{(3)}$ with $v_c \equiv c_0 a_c$ equal to the crystallographic cell volume and k_{Fs} replacing k_F can be made, as in Ref. [46], provided $\pi/c_0 k_F$ is close to unity. The limits of this approximation can be appreciated from the comparison with the values of λ_{HAS} derived from Eq. (143) and presented in the next section.

It is of interest to note that the e-ph theory approach in this work provides an alternative view of the Beeby correction, namely it can be seen as a a way to account for the neglected effects of the long-range dispersion forces through a small extension to the depth over which He atom scattering samples the e-ph constant λ. As appears in the denominator of Eq. (143), for specular scattering where $\Delta k_z^2 = 4k_{iz}^2 = 8mE_{iz}/\hbar^2$ the normal component of the incident energy appears multiplied by the number n_s. This leads to the following interpretation of the Beeby correction

$$n_s E_{iz} \longrightarrow n_s(E_{iz} + D) \equiv \overline{n_s} E_{iz} , \tag{144}$$

where $\overline{n_s} = n_s(1 + D/E_{iz})$. Eq. (144) shows that the Beeby correction may be regarded as a small increase in the extension of the e-ph interaction depth n_s.

6. Numerical evaluations of λ from experimental data

In this section we determine values of λ_{HAS} as measured by atom scattering experiments for a number of different systems. The simplest and most readily available data are for the thermal attenuation of elastic diffraction intensities, notably the specular beam, but the dependence of the Debye-Waller factor on incident energy and other experimentally controlled variables such as incident and final angles is also considered.

6.1. Normal metals using thermal attenuation

When dealing with normal metal surfaces the simplest, though qualitative, approach is to use for $\mathcal{N}(E_F)$ in Eq. (131) the 3DEG expression

$$\mathcal{N}(E_F) = 3Zm_e^*/\hbar^2 k_F^2 , \tag{145}$$

where Z is the number of free electrons per atom. This gives

$$\lambda_{HAS} = \frac{1}{4\mathcal{N}(E_F)}\,\frac{-\partial \ln I_{00}(T)}{k_B\,\partial T}\,\frac{m_e^*\phi}{mE_{iz}} \approx \frac{-\partial \ln I_{00}(T)}{k_B\,\partial T}\,\frac{\phi\, k_F^2}{6\, Z\, k_{iz}^2} . \tag{146}$$

Examples of the thermal attenuation for the cases of Sb(111) and Bi(111) are shown in Fig. 2. Values of λ_{HAS} for several metals calculated with this 3DEG approximation appear in Table 1. The values for Sb(111) and Bi(111), $\lambda_{HAS} = 0.28$ and 0.57, respectively, compare favorably with the respective previously reported values of $\lambda = 0.27$ as calculated ab-initio by Campi et al. [88], and $\lambda = 0.60$ by Hofmann [86].

When a knowledge of the Fermi wavevectors of both bulk, k_F, and surface, k_{Fs}, is available, a reasonable guess of the e-ph interaction

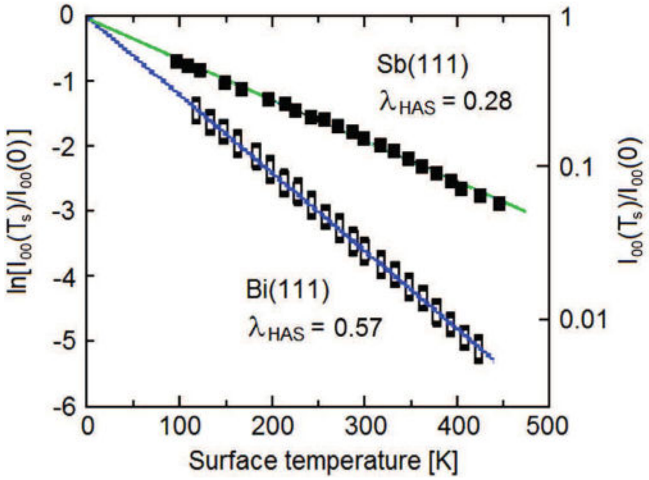

Fig. 2. Debye-Waller plots of the specular intensity vs. T for He atom scattering from Sb(111) and Bi(111). Data for Sb(111) from Ref. [69] and for Bi(111) from Ref. [70].(Reprinted with permission from Ref. [46]. Copyright [2016] American Chemical Society).

depth, represented by the number $n_s = k_F/k_{Fs}$ of Eq. (142) can be made and λ_{HAS} obtained in this way from Eq. (143). Examples for various surfaces are given in Table 2. Note that for Sb(111) and Bi(111) the same values of λ_{HAS} reported in Table 1 are obtained with k_{Fs} corresponding to that of the surface hole pockets [81,83]. The limited number n_s of surface layers probed by the surface e-ph interaction, suggests to model the conducting surface as a stack of 2DEGs, so as to deal with a Fermi level DOS independent of the actual value of the Fermi wavevector, the only information needed being the effective electron mass at the Fermi level. This approach originated from a HAS study of the e-ph interaction in ultrathin films as a function of the layer number, discussed in the next subsection, Sec. 6.2.

For Bi(111) a third independent method of determining λ_{HAS} arises from fitting the individual diffraction peak intensities using inelastic close coupling calculations, as discussed in detail below in Subsection 7.3. Briefly, the calculated fit to the helium scattering diffraction peaks gives a value $f_{Ds} = 4.2 \times 10^4$ erg/cm^2 for the Debye coupling constant appearing in Eq. (136). Combining with the 3-D free electron DOS of Subsection 5.5 leads to $\lambda_{HAS} = 6\pi^2\phi/(v_c k_F f_{Ds})$ where v_c is the unit cell volume. With values of ϕ and k_F taken from Table 2 the value $\lambda_{HAS} = 0.62$ is obtained, which is close to the other values quoted above, and is also listed in Tables 1 and 2.

Some additional comments about the data presented in Tables 1 and 2 are in order. The experimental HAS data for Pb(111) taken from Refs. [71,75] are for the specific case of seven monolayers of Pb on a Cu(111) substrate. It is also evident from the list of measured values of λ from other sources that there can be significant variations in reported bulk values, a situation that is illustrated by the cases of Bi(111) and Cu(110) as well as Pb(111) appearing in Table 2. The critical parameter in Eq. (146) is the Fermi wavevector appropriate for the surface electron gas which mostly contributes to the He-surface potential at the turning point. For the surfaces of Bi, Sb, Cu and W considered in Table 2, the values of k_F associated with relevant surface bands cutting the Fermi level have been extracted from the quoted literature. Ultrathin films such as 7 ML-Pb(111)/Cu(111), whose thickness is less than the range of electron-phonon interaction, present the interesting case that all the electronic states of the quantum well are involved and therefore the use of the bulk k_F appears to be more appropriate. In the case of copper, measurements on epitaxial nanometric films yield λ of the order of 0.1 [98], whereas photoemission data from the Cu(110) surface [95,96] yield $\lambda = 0.23 \pm 0.02$ for the surface states at $\overline{\mathrm{Y}}$. The value derived from HAS data with $k_F = 0.25$ Å^{-1} for the surface band at $\overline{\mathrm{Y}}$ [82] is $\lambda = 0.15$, intermediate to the above experimental values but closer to the Cu bulk value reported in Allen's review ($\lambda = 0.14 \pm 0.02$) [89]. Because of the quantum sonar effect [35,39], the information carried by HAS may not exclusively come from surface states. For weakly bound (van der Waals) layered crystals the surface electronic and dynamical properties differ little from the bulk ones. Moreover, for isoelectronic materials, such as Sb(111) and Bi(111), measured

Table 1
The e-ph coupling constant λ_{HAS} as derived from the temperature dependence of the HAS specular intensity Eq. (146) with the free-electron DOS assumption for selected conducting surfaces and compared with values of λ from other sources as cited. For Pb(111) the experimental data are from Ref. [71] and the value given for λ_{HAS} is for seven monolayers of Pb on a Cu(111) substrate. For the Cu data of Refs. [72,73] there were several incident angles measured and the ones chosen are denoted, and the slope of the D-W plot was taken in the region of room temperature.

Surface	$\Delta \ln \mathrm{I}(T)/\Delta T$ [10^{-3}K^{-1}]	k_{iz}^2 [Å^{-2}]	ϕ [eV]	k_F [Å^{-1}]	Z	λ_{HAS}	λ (other sources)
Cu(111) [73]	4.2 $\theta_i = 56.9°$	30.36 [73]	4.94 [77]	0.25 [82]	1	0.083	0.093 [98] 0.13 [99] 0.15 [36]
Cu(110) [73]	1.7 $\theta_i = 67°$	6.20 [73]	4.48 [77]	0.25 [82]	1	0.148	0.17 [87] 0.23 [95,96]
Cu(001) [72]	6.61 $\theta_i = 19°$	108.2 [72]	4.59 [77]	~ 0.6 [93]	1	0.195	0.15 ± 0.03 [36] 0.13 [99]
W (001)1 × 1 [74]	4.1	26.3 [74]	4.32 [80]	1.19 [84,85]	6	0.31	0.28 [89]
Pb(111) [71] [a]	5.0	5.65 [71,75]	4.25 [78]	0.65 [39]	4	0.769	0.95 [39] 0.7–0.9 [97]
Ag (111) [34] (1,0) peak	3.4	16.82 [34]	4.74 [90]	0.22 [92]	1	0.082	0.059 [91] 0.12 [99] 0.13 ± 0.04 [36]
K (110) [100] [b]	8.07	16.29 [100]	2.30 [78]	0.27 [101]	1	0.16	0.13 ± 0.03 [36] 0.11 [99]
Cs(110) [100] [c]	17.8	26.9 [100]	2.1 [78]	0.26 [101]	1	0.18	0.15 ± 0.03 [36] 0.16 [99]
Sb(111) [69]	5.6	22.8 [69]	4.56 [79]	0.80 [83]	5	0.28	0.27 [88]
Bi(111) [70]	11.5	16.79 [70]	4.23 [76]	0.72 [81]	5	0.57	0.60 [86] 0.45 [94]

[a] For a 7-ML film of Pb on Cu(111).
[b] For a 10-ML film of K on Ni(111).
[c] For a 10-ML film of Cs on Cu(111).

Table 2
The e-ph coupling constant λ_{HAS} as derived from the temperature dependence of the HAS specular intensity using the multiple layer free electron DOS of Eqs. (142) and (143) for selected conducting surfaces, compared with values of λ from other sources as cited. As in Table 1, for the Cu data of Refs. [72,73] there were several incident angles measured and the ones chosen are denoted, and the slope of the D-W plot was taken in the region of room temperature. Note that the values of λ_{HAS} for Sb(111) and Bi(111) are identical with those of Table 1, but here are calculated with a different form of the DOS.

Surface	$-\partial \ln[I(T)]/\partial k_B T$ $[eV^{-1}]$	k_{iz}^2 $[\text{Å}^{-2}]$	ϕ [eV]	k_F $[\text{Å}^{-1}]$	k_{Fs} $[\text{Å}^{-1}]$	n_s	λ_{HAS}	λ (other sources)
Cu(111) [73]	73.64 $\theta_i = 45°$	60.5	4.94 [77]	1.36 [102]	0.16 [105]	8.5	0.19	0.093 [98] 0.13 [99] 0.15 [36]
Cu(110) [73]	27.6 $\theta_i = 20°$	35.6	4.48 [77]	1.36 [102]	0.20 [103,104]	6.8	0.09	0.17 [87] 0.23 [95,96]
Cu(001) [72]	76.86 $\theta_i = 19°$	108.2	4.59 [77]	1.36 [102]	0.20 [109]	6.8	0.12	0.15 ± 0.03 [36] 0.13 [99]
Ag (111) [40]	20.40 $\theta_i = 45°$	60.5	4.74 [90]	1.20 [102]	0.22 [92]	5.5	0.07	0.059 [91] 0.12 [99] 0.13 ± 0.04 [36]
Al (111) [111]	16.1 $\theta_i = 45°$	34.6	4.28 [78]	1.75 [102]	1.10 [108]	1.6	0.30	0.39 [110], 0.38 [113] 0.43 ± 0.05 [36]
Pt (111) [40]	20.0 $\theta_i = 45°$	60.5	5.65 [78]	0.99 [107]	0.90 [112]	1.1	0.39	0.66, 0.31 [110] 0.40 ± 0.01 [36]
W (001)1 × 1 [74]	47.67 $\theta_i = 45°$	26.3	4.32 [80]	1.19 [84,85]	0.40 [106]	1.0	0.39	0.29 [89]
Sb(111) [69]	65.0	22.8	4.56 [79]	0.80 [83]	0.17[a] [83]	4.7	0.28	0.27 [88]
Bi(111) [70]	133.5	16.79	4.23 [76]	0.72 [81]	0.16[a] [81]	4.5	0.57	0.60 [86]
from ICC							0.62	0.45 [94]

[a] Hole pockets.

under similar conditions, the difference in λ_{HAS} is essentially due to that between the respective slopes of $2W(T)$ (Fig. 2 and Table 1). This provides a qualitative direct way to assess the e-ph coupling strengths by comparing the temperature dependence of the respective D-W exponents.

Recently, a value of $\lambda = 1.3$ for Bi(111) has been reported [45]. This value, which was obtained by comparing energy-resolved inelastic HAS scattering spectra for Bi(111) with those of Pb(111), is larger than that reported here obtained from Debye-Waller factor measurements on the specular diffraction peak, and also larger than the values reported from other sources. However, inelastic HAS spectra sample only a limited number of phonon modes, namely only those modes that can be accessed along the He atom scan curve. The scan curve, which results from energy conservation and conservation of momentum parallel to the surface, appears in a plot of energy transfer versus $\Delta\mathbf{K}$ as a parabolic function whose shape is determined by the incident He atom beam energy and angles, and the angular position of the detector. For example, a specific scan curve equation for the most commonly used in-plane scattering experimental configuration is given below in Eq. (177). Only those phonons with both energy $\hbar\omega_{\Delta\mathbf{K},\nu}$ and parallel momentum $\Delta\mathbf{K}$ lying on the scan curve are accessible in an inelastic HAS spectrum for a given set of experimental conditions. However, as is evident from its definition in the form due to Allen [41], $\lambda = \langle\lambda_{\mathbf{Q},\nu}\rangle$, the coupling constant λ is an average over all phonons. When, as a trial estimate of λ, the average over $\{\mathbf{Q},\nu\}$ is restricted to a selected set of phonons, e.g., those sampled by HAS along a single scan curve, trial values of λ dispersed over a fairly large range may be found. This is illustrated by the interesting example of Bi(111) vs. Pb(111) in Ref. [45], where a ratio of $\lambda_{Pb}/\lambda_{Bi} = 1.35$ was obtained from similar HAS scan curves for each of the two metals. This is in contrast with the ratio of 0.75, about a factor 2 smaller, from the Debye-Waller factors reported in Table 2, and means that under the kinematic conditions of Ref. [45] the phonons sampled in Bi(111) make a larger contribution to e-ph interaction than in the 7 ML-Pb(111) film. The comparison is interesting because Pb is a bulk superconductor with transition temperature decreasing from bulk to ultrathin films, whereas bulk Bi is not a superconductor, but it becomes so in reduced dimensionality [114], possibly because of some specific surface-localized phonons with particularly strong e-ph coupling. Thus, sampling different segments of the phonon spectrum with inelastic HAS may help in pinpointing which phonons are actually important for electron pairing in low-dimensional superconductors. The Debye-Waller factor, on the other hand, is not similarly limited by the scan curve, and hence is able to produce the true and correctly averaged λ for a given surface.

6.2. Metallic overlayers

The simple expression of Eq. (135) shows that in the temperature region where the D-W exponent is linear in temperature T it is also proportional to λ, and in the proportionality relation $\mathcal{N}(E_F)$ is the effective electron density of states at the Fermi level referred to the surface unit cell and includes only those states which cause a vibration of the surface charge density as a consequence of the thermal vibrational motion of the cores.

Bulk electronic properties of alkali metals can often be approximated as those of a free electron gas, and He atom scattering gives evidence that near the surface the electrons may also be approximated by a free electron gas. The evidence is that He atom scattering from all alkali surfaces thus studied exhibits only a specular diffraction peak and all other diffraction peaks have negligible intensity. This implies that the electronic density near the surface is very smooth, and justifies the use here of a free electron gas DOS for the region near the surface of alkali metals. Alkali metal crystals have body centered cubic (BCC) structure, and this holds true in the layer-by-layer growth. For all of the alkali metals studied here the layer-by-layer growth builds up also with a BCC structure regardless of the crystal structure or crystalline face orientation of the growth substrate.

An example of the alkali atom experiments is exhibited in Fig. 3a) which shows, for potassium overlayers on Ni(001), the specular He atom scattering Debye-Waller exponent $\ln[I(T)/I_0]$ is a nearly linear function of T at small monolayer (ML) numbers [115]. Interestingly, the slope of these D-W plots increases nearly linearly with ML number n for small ML numbers as shown in Fig. 3b) in terms of the dimensionless quantity α defined below in Eq. (148), but eventually

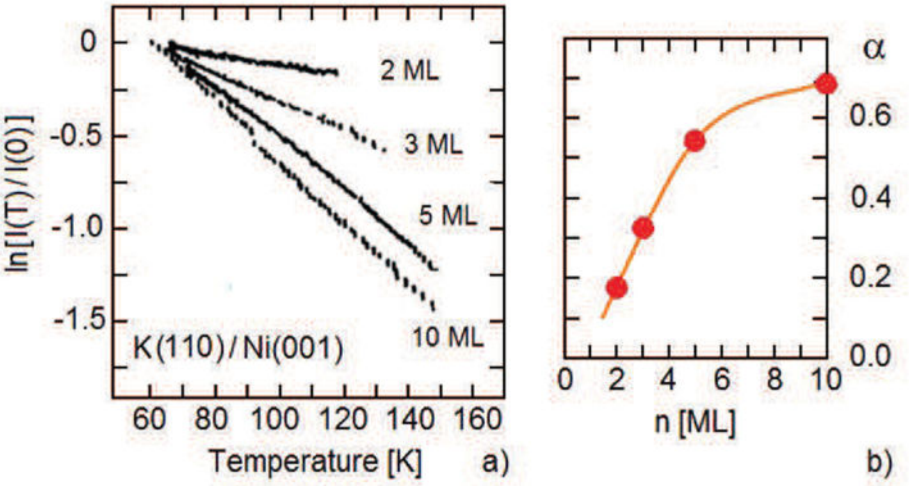

Fig. 3. a) The HAS reflectivity as a function of the surface temperature, normalized to the extrapolated $T = 0$ value, for 2, 3, 5 and 10 ML films of K (110) on Ni(111) (adapted from Ref. [100]). This is plotted on a logarithmic scale in order to show the approximate linearity of the Debye-Waller exponent with temperature. b) The average logarithmic slope of $I(T)/I_0$, expressed in terms of the dimensionless constant α of Eq. (148), increases linearly with the film thickness up to saturation at a thickness of 5 ML. (Reprinted with permission from Ref. [115]. Copyright [2018] American Chemical Society).

the slope saturates for ML numbers greater than $n = n_{sat}$. In this case saturation occurs for ML number $n_{sat} = 5$. For thicker films, which for K (110)/Ni(111) were measured up to $n > 10$ [100], the slope remains the same and may be regarded as that of semi-infinite K (110). In this case the number n_s of Eq. (142) is identified with n_{sat}.

The density of states for a two-dimensional nearly free electron gas is given by

$$\mathcal{N}^{(2D)}(E_F) = m_e^*/\pi\hbar^2 \ . \tag{147}$$

The experimentally observed linear behavior exhibited by successive layers of K in Fig. 3b) at small ML numbers strongly suggests that in this region each monolayer contributes independently to the density of states at the Fermi surface. Theoretical support for this supposition comes from recent calculations of the band structure of free-standing thin films of alkali metals [116]. The DOS can be calculated readily from the band structure. As an example, for a free standing film of up to 11 layers of Cs the band structure shows one parabolic quasi-free electron band per layer, each one contributing the same Fermi level DOS per unit surface area equal to $m_e^*/\pi\hbar^2$ [116]. As seen in Fig. 4, the band structure calculated ab-initio for a self-standing 11 ML Cs(110) film shows 11 parabolic quasi-free electron bands (disregarding the zone-boundary foldings and the small avoided crossings), corresponding to the same number of 2-dimensional electron gases (2DEG), each one contributing the same Fermi level DOS per unit surface area.

This linear increase of the D-W slopes shown in Fig. 3b) implies that in Eq. (135) for $n < n_{sat}$ one should use $\mathcal{N}(E_F) = nm_e^* a_c/\pi\hbar^2$ where a_c is the area of a unit cell. Then λ derived from Eq. (135) becomes

$$\lambda_{HAS} = \frac{\pi}{2n}\alpha \quad ; \quad \alpha \equiv \frac{\phi \ \ln[I(T_1)/I(T_2)]}{a_c k_{iz}^2 k_B (T_2 - T_1)} \ , \quad \text{for} \ \ n \le n_{sat} \ , \tag{148}$$

where T_1 and T_2 are any two temperatures in the region where $2W^{eff}(\mathbf{k}_f, \mathbf{k}_i; T)$ is linear in T. Since the dimensionless function α, derived from the HAS data and plotted in Fig. 3b), initially grows linearly with n, λ consequently has about the same value for $n < n_{sat}$. The first four layers produce the value $\lambda = 0.16$.

After saturation, i.e., for $n > 5$, the slope of the Debye-Waller plot no longer depends on the number of monolayers so it is appropriate to use in Eq. (135) the DOS for a free electron gas, $\mathcal{N}(E_F) = 3Zm_e^*/\hbar^2 k_F^2$, where Z is the number of electrons provided by each substrate metal atom. Using $Z = 1$ and 0.27 Å^{-1} for k_F [101] one actually obtains the same value as found above for $n < n_{sat}$, i.e., $\lambda_{HAS} = 0.16$ as shown in Table 1, which compares favorably with the known tabulated bulk values which range from 0.11 [99] to 0.13 ± 0.04 [36].

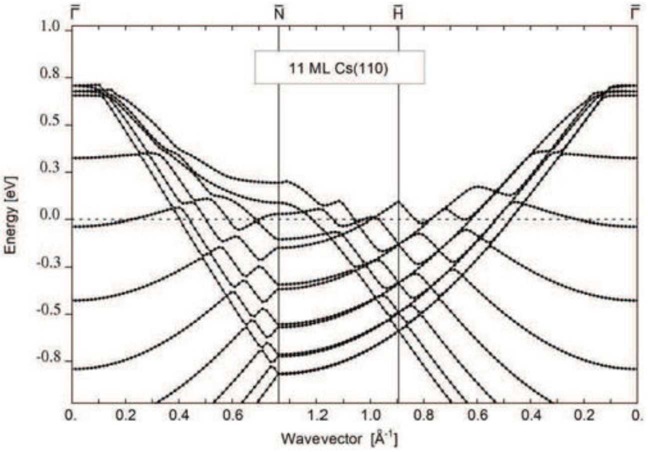

Fig. 4. DFT calculation of the band structure near the Fermi level ($E_F = 0$) of a self-standing 11 ML Cs(110) film, from Ref. [116].

Similar measurements have been made for Cs(110)/Cu(111) as shown in Fig. 5 [100]. It is seen that for this system saturation also begins after $n_{sat} = 5$. In this case the value of λ_{HAS} produced by the first three layers turns out to be 0.18. At saturation for $n > 5$, again using the three-dimensional free electron DOS in Eq. (135), the value produced is also 0.18 which compares favorably with the tabulated bulk values of 0.15 [36] and 0.16 [99]. The values of λ_{HAS} for $n < n_{sat}$ for these and all the other alkali metal systems studied here, together with more details, are contained in Table 3. The ability to study Cs with He atom scattering is interesting as it is one of the few elements that is difficult to study in the bulk with neutron scattering because of the very high neutron capture cross section of the Cs nucleus. He atom scattering at a Cs surface is not hampered by such problems.

With the identification of n_s of Eq. (142) as n_{sat}, Eq. (148) can be used for any conducting surface, provided a convenient value of n_s can be guessed from the crystallographic and electronic structure of the surface. From the few examples reported in Table 4, it is learned that for close-packed fcc metal surfaces with a short Thomas-Fermi

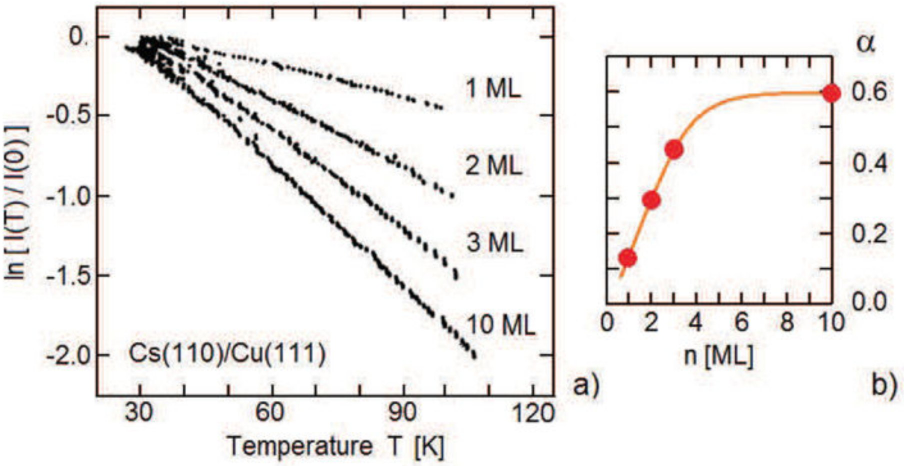

Fig. 5. Similar to Fig. 3, but for Cs(110) films on Cu(111). Data from Ref. [100]. (Reprinted with permission from Ref. [115]. Copyright [2018] American Chemical Society).

Table 3
The e-ph coupling constant λ_{HAS} derived from the specular intensities of helium atom scattering experiments on alkali metal and Pb layers deposited on various close packed metal substrates. Also shown are the relevant experimental parameters as well as values of λ for the bulk alkali metals taken from other sources as cited. The brackets $\langle\cdots\rangle$ signify an average taken over all n in the layer-by-layer growth spectra subject to $n \leq n_{sat}$.

Growing layers	$\langle \ln [I_n/I_{n+1}] \rangle$	T [K]	k_{iz}^2 [Å^{-2}]	ϕ [eV]	n $n \leq n_{sat}$	λ_{HAS}	λ (other sources)
Li (110)/ W (110) [117]	0.261	80	34.9	2.32 [118]	2–5	0.47 ± 0.11	0.40 [36] 0.35 [99]
Na (110)/ Cu(001) [120]	0.119	80	35.9	2.75 [78]	2–4	0.17 ± 0.03	0.16 [36] 0.24 [119]
K (110)/ Ni(001) [100]	0.206	100	27.1	2.30 [78]	2–5	0.16 ± 0.05	0.13 [36] 0.11 [99]
Rb (110)/ Ni(001) [100]	0.296	90	29.7	2.16 [78]	2–5	0.19 ± 0.06	0.16 [36] 0.15 [99]
Cs(110)/ Cu(111) [100]	0.346	75	26.9	2.14 [78]	1–5	0.18 ± 0.03	0.15 [36] 0.16 [99]
Pb(111)/ Cu(111) [75]	0.098 ± 0.016	140	5.65	4.25 [78]	$n \geq 3$	0.9–1.15	0.95 [39] 0.7–1.05 [97] 1.12–1.68 [36,99]

screening length, such as the (111) surfaces of Al, Ir and Pt, just one atomic layer ($n_s = 1$) accounts for the e-ph interaction. On the other hand the isostructural Ni(111) surface, having a shallow majority-spin surface state with k_{Fs} about one third of k_F requires $n_s = 3$ (see Eq. (142)) [132]. For the close-packed hexagonal Ru (0001) surface $n_s = 2$, corresponding to the periodicity in the z-axis, is a good choice, while for the less packed (110) surfaces of fcc Ag and of bcc Fe and Ba metals three atomic layers ($n_s = 3$) needs to be considered. As seen in Table 3, for bcc alkali (110) surfaces, providing just one conduction electron per atom, saturation is reached with 4–5 layers. On the other hand, Pb(111) ultra-thin films on Cu(111), also isostructural to Ni(111), reach saturation, as discussed in the next subsection, at a comparatively large value of n_s, presumably also related to a very shallow S2 surface state predicted at the K point of the surface Brillouin zone [133].

In addition to Debye-Waller plots such as Figs. 3a) and 5a) another important type of measurement which is often carried out is the monitoring of layer-by-layer growth from oscillations in the specular intensity as a function of deposition time, taken at a fixed temperature. An example of Li (110) monolayers deposited on a W (110) substrate at $T = 80$ K and $E_i = 37$ meV is shown in Fig. 6. Such measurements provide another method for obtaining the λ value for $n < n_{sat}$ by comparing intensities of the oscillation maxima (which occur at full ML coverage) for different ML numbers. Again, this possibility depends on the known linear behavior in temperature of the logarithmic Debye-Waller plots. To show this consider comparing the intensity maxima for the n and $n + \ell$ monolayers (with both n and $n + \ell < n_{sat}$) denoted by $I_n(T)$ and $I_{n+\ell}(T)$, respectively. In general, if layer-by-layer growth plots such as Fig. 6 are carried out at two different temperatures T_1 and T_2, with both of these temperatures within the range over which the D-W plots are linear in T, Eq. (148) can be expanded to produce a value of λ from the following combination

$$\begin{aligned}\lambda_{HAS} &= \frac{(n+\ell)\lambda - n\lambda}{\ell} \\ &= \frac{\pi\phi}{2\ell a_c k_{iz}^2 k_B (T_2 - T_1)} \left[\ln\left(\frac{I_{n+\ell}(T_1)}{I_{n+\ell}(T_2)}\right) - \ln\left(\frac{I_n(T_1)}{I_n(T_2)}\right) \right] \\ &= \frac{\pi\phi}{2\ell a_c k_{iz}^2 k_B (T_2 - T_1)} \left[\ln\left(\frac{I_{n+\ell}(T_1)}{I_n(T_1)}\right) - \ln\left(\frac{I_{n+\ell}(T_2)}{I_n(T_2)}\right) \right],\end{aligned} \tag{149}$$

provided that $n + 1 \leq n_{sat}$ and $\ell + n \leq n_{sat}$.

An even simpler expression can be obtained upon recognizing that the extrapolation of the specular intensity to $T = 0$ becomes independent of layer number, or can be normalized to the same value as shown in Figs. 2, 3 and 5. Thus, if the intensity at T_1 is taken to be that obtained by extrapolation to $T \to 0$, Eq. (149) simplifies to

$$\lambda_{HAS} = \frac{\pi\phi}{2\ell a_c k_{iz}^2 k_B T} \ln\left(\frac{I_n(T)}{I_{n+\ell}(T)}\right), \tag{150}$$

Table 4
Table giving λ_{HAS} for selected metals, calculated using methods similar to those used for determining λ_{HAS} for metallic layers with the 2-D free electron density of states.

Surface	T range [K]	E_i [meV]	ϕ [eV]	α	n_s	λ_{HAS}	λ (other sources)
Al (111) [111]	120–300	36	4.28 [78]	0.28	1	0.44	0.39 [110], 0.38 [113] 0.43 ± 0.05 [36]
Ir (111) [129]	250–700	64	5.27 [78]	0.19	1	0.30	0.41 [110], 0.34 [113] 0.50 [110]
Pt (111) [40]	275–800	63	5.65 [78]	0.27	1	0.48	0.66, 0.31 [110] 0.4 ± 0.1 [36]
Ru (0001) [127]	250–650	64	4.71 [78]	0.56	2	0.44	0.45 [99]
(Energy Dependence) [128]	200	10–97		0.42	2	0.33	0.4 ± 0.1 [36]
(Neon atoms) [128]	90–200	64		0.50	2	0.39	
Fe (110) [122] (diffuse elastic)	150–820	45.5	4.5 [78]	0.50	3	0.26	0.24 [123] 0.27 ± 0.01 [91]
Ag (110) [130] (diffuse elastic)	300–672	17.5	4.26 [78]	0.212	3	0.12	0.12, 0.04 [110]
Ba (110) [124]	145–480	~ 24	2.7 [78]	0.40	3	0.21	0.14 [121,125] < 0.15 [126] 0.27 [89]
Ni(111) [129]	250–600	66	5.15 [78]	1.16	3	0.60	0.3, 0.7 [110]
(^{3}He atoms) [131]	250–600	8		1.19	3	0.62	

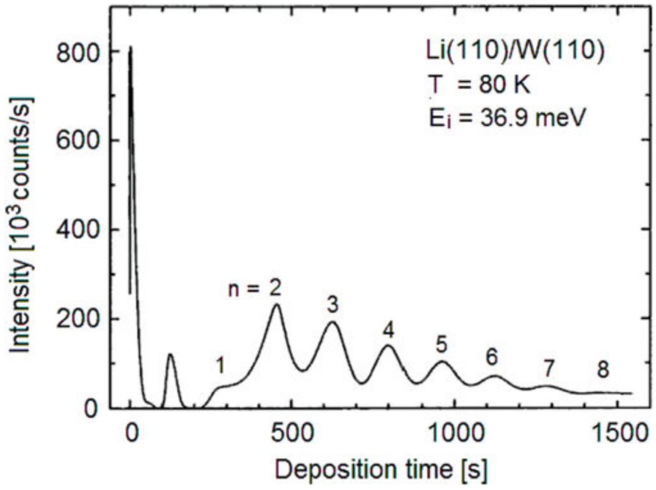

Fig. 6. The specular He atom scattering intensity as a function of deposition time (proportional to coverage) for Li (110) deposited on a W (110) substrate (from Ref. [117]). The ML numbers are indicated. The specular intensity saturates above $n = 8$. In this system there is a small maximum at 0.5 coverage, while the monolayer at $n = 1$ is rather disordered due to the conflicting periodicities of W (110) and the Li (110) layer. (Reprinted with permission from Ref. [115]. Copyright [2018] American Chemical Society).

as long as the temperature T is within the region for which $2W$ is linear in T. A distinct advantage of using the layer-by-layer growth methods of either Eq. (149) or (150) is that even if the growth curve is measured at only a single temperature, such as the case for Li (110) in Fig. 6, all combinations of two different peaks provide distinct values of λ, and this gives sufficient numbers of values for which a standard deviation of error can be evaluated. If the growth plots are carried out at two or more different temperatures, such as the case for Rb (110)/Ni(001) in Fig. 7b), Eq. (149) can be used and this provides even greater numbers of distinct values for λ.

The HAS specular intensity patterns for Li (110) on a W (110) substrate of Fig. 6 and Na (110)/Cu(001) in Fig. 7a), both deposited at a temperature of 80 K, show saturation behavior. For Li (110)/W (110) the saturation occurs after $n = 8$ and using Eq. (150) the average over $n = 2 \rightarrow 8$ gives $\lambda_{HAS} = 0.54 \pm 0.08$, while the more restricted average over $n = 2 \rightarrow 5$ gives $\lambda_{HAS} = 0.47 \pm 0.11$. By comparison the bulk value ranges from $\lambda = 0.30$ [99] to 0.40 [36]. The pattern of Na (110) growth in Fig. 7 suggests a very regular growth, and the average over $n = 2 \rightarrow 4$ gives $\lambda_{HAS} = 0.17 \pm 0.03$ as compared to 0.16 for bulk Na [36] and 0.24 for the surface of an Na quantum well [119].

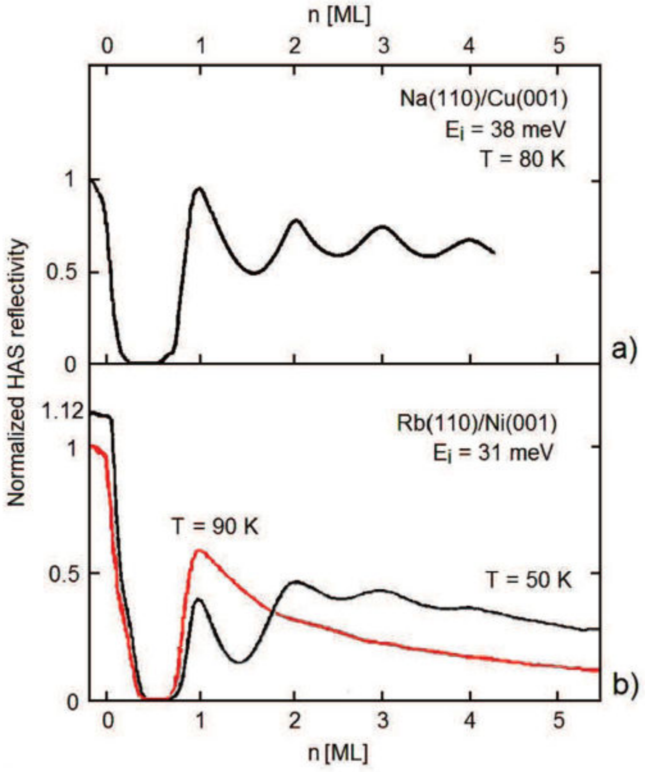

Fig. 7. a) Similar to Fig. 6 but for Na (110) monolayers on a Cu(001) substrate at $T = 80$ K, showing clear saturation behavior. From Ref. [120]. b) For Rb (110) monolayers on a Ni(001) substrate, showing measurements at two different temperatures of 50 and 90 K as marked. From Ref. [134]. (Reprinted with permission from Ref. [115]. Copyright [2018] American Chemical Society).

With regards to Rb (110)/Ni(001) in Fig. 7b) λ_{HAS} can be derived from the D-W temperature dependence over the range of $n = 2$–5 and for the two different temperatures of 50 and 90 K using both Eqs. (149) and (150). The average is $\lambda_{HAS} = 0.19 \pm 0.06$ as compared with the standard bulk value of 0.16 [36]. This bulk value is smaller, and also smaller than the values extracted via Eq. (149) from the D-W plot slopes [134] for $n > 2$ which are 0.19 at 50 K and 0.22 at 90 K.

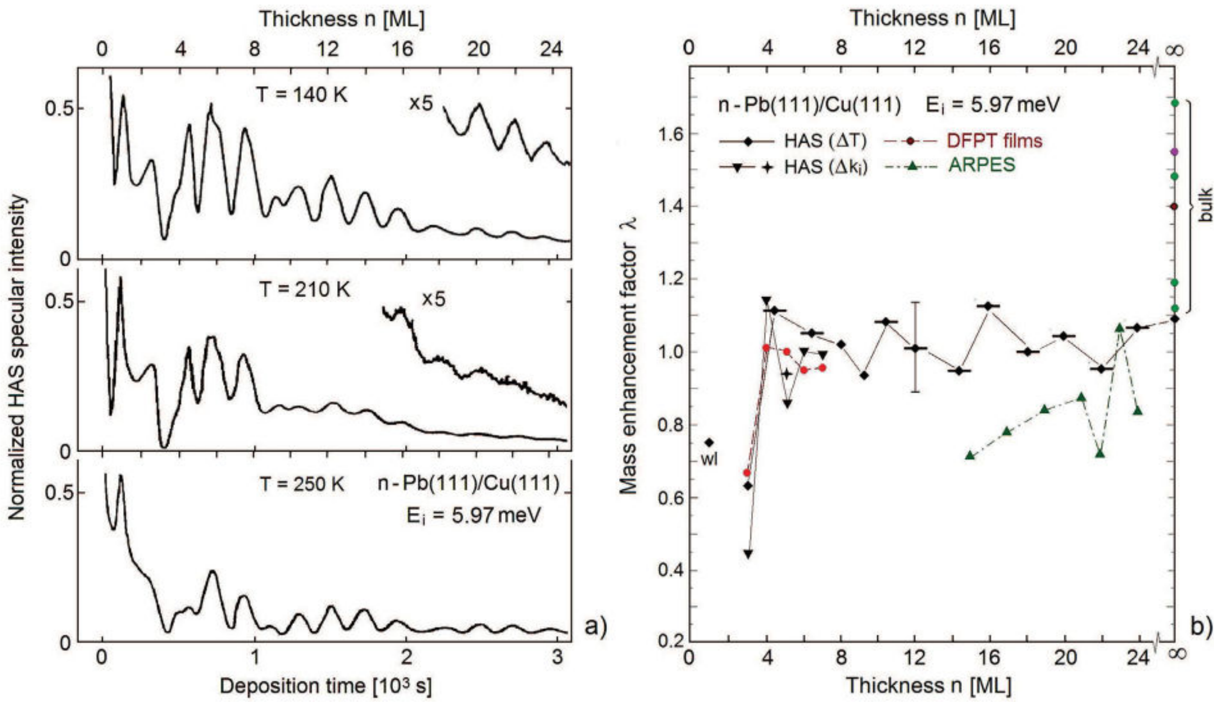

Fig. 8. a) Bilayer-by-bilayer growth curves for Pb(111) deposited on Cu(111) at temperatures of 140, 210 and 250 K as measured with HAS at the incident energy of 5.97 meV [75,137]. b) Values of λ_{HAS} extracted from the growth curves shown in a) (filled diamonds connected by a solid line). The isolated diamond at $n = 1$ marked "wl" is from the wetting layer. The downward-pointed filled triangles at small n are values of λ_{HAS} extracted from the energy dependence of the Debye-Waller factor as discussed below in Sec. 6.3 [138]. The point marked by a cross (+) is from energy dependent measurements made at $n = 5$ taken in conjunction with the temperature-dependent data [137]. Values of λ calculated with density functional perturbation theory for thin films are shown as filled circles connected by a dashed line [35]. The upward-pointing triangles connected by dash-dotted lines are angle resolved photoemission spectroscopy (ARPES) measurements [97]. A collection of values for bulk lead taken from the literature [36,99] (filled circles at $n \to \infty$) are shown for comparison. (Reprinted with permission from Ref. [115]. Copyright [2018] American Chemical Society).

This suggests that a non-negligible contribution to the decrease of the specular intensity comes from the increase of defects with temperature, as indicated also by the small layer-by-layer oscillations. On the other hand the lack of large oscillations, ostensibly due to defects, does not seem to strongly affect the value of λ_{HAS} which encompasses the electron-phonon interaction of the whole film as probed by HAS.

It is important to point out another advantage of obtaining λ from the layer-by-layer growth plots and this is that effects due to disorder and defects tend to cancel. This can be seen from the first line of Eq. (149); if at T_1 and T_2 the additional attenuation of the n-th (and similarly for the $n + \ell$-th) peak due to static disorder is identical, then it cancels out of the intensity ratio. This is evident because the attenuating effect of disorder is usually expressed as a multiplicative factor (sometimes called a characteristic function [135]) applied to each diffraction peak [136], regardless of whether the disorder is due to small displacements of the surface or due to defects and, in the intensity ratios appearing in Eq. (149) and (150), such factors cancel. Clearly in the growth spectra such as in Figs. 6 and 7 both disorder and changes in the electron-phonon interaction must play a role in the fact that the layer-by-layer peaks gradually become less pronounced. In some cases the specular intensity reaches a non-zero saturation value, such as for Li (110) in Fig. 6 or Na (110) in Fig. 7 a), while in other cases the specular intensity appears to continue decreasing with large coverage such as for Rb at $T = 90$ K in Fig. 7. For the systems which exhibit this saturation behavior with coverage it appears reasonable to assume that disorder attenuation is less important and the gradual disappearance of the layer-by-layer peaks is indicative of the influence of the electron-phonon interaction. For the systems that do not exhibit such saturation with coverage the disorder due to defects in the growing overlayer is surely playing a much larger role, but these systems are still amenable to analysis using Eq. (149) and (150) because, as mentioned above, the effects of disorder tend to cancel out of the ratios of the specular intensity for the same n taken at two different temperatures.

The comparatively simple physics concerning the electron-phonon interaction in alkali ultrathin films cannot be straightforwardly extended to other metals such as, for example, lead. The evolution of the HAS specular peak intensity of Pb(111) ultrathin films has been extensively studied as a function of thickness in the layer-by-layer growth regime at different temperatures [75,137,138]. Pb films grown on Cu(111) have, in common with the alkali films discussed above, the property of being considerably softer than the substrate, which practically restricts the phonon spectrum involved in electron-phonon interactions to that of the film on a rigid substrate [35]. However the HAS normalized specular intensity of Pb films measured during growth as a function of thickness at three different temperatures shown in Fig. 8a) exhibits, over a range up to about 30 Pb layers, rapid oscillations indicating a bilayer-like growth. These growth peaks are further modulated by an envelope of longer-period oscillations, having a length of about 8 layers, which has been convincingly interpreted as due to quantum size effects [75]. The comparatively large interlayer distance contraction affecting the topmost bilayer [139,140] causes the split-off of a surface phonon branch above the bulk phonon spectrum. This explains the bilayer growth mode and suggests that the oscillations of the HAS D-W exponent essentially depend on those of the top bilayer 2-D electron gas as induced by phonons of the entire film. In this case, an examination of the logarithmic D-W plots, similar to Figs. 3 and 5 above, using the three available temperatures of Fig. 8a) indicates that $n_{sat} = 9$ is a reasonable approximation.

The choice of $n_{sat} = 9$ is more clearly shown by examining the temperature dependence of the specular intensity as a function of ML number n as in Fig. 9. Shown in Fig. 9a) is the logarithmic tem-

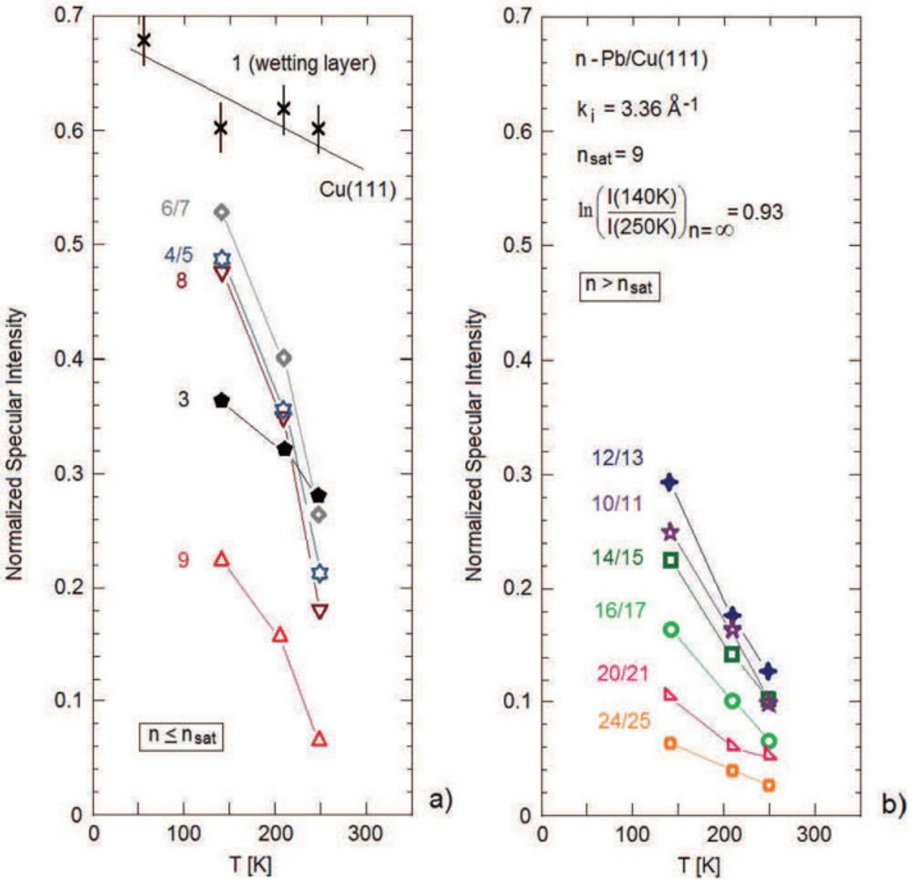

Fig. 9. Logarithmic temperature dependence (D-W plots) of the specular intensity for bilayer growth of Pb deposited on Cu(111). The three temperature points for each layer are 140, 210 and 250 K as shown in Fig. 8a) and are connected with lines. Each is labeled by the monolayer number, but distinct bilayers are labeled by two ML numbers, e.g., 4/5. a) Plots for ML numbers less than 10. Also shown is a straight line passing through the experimental points for the $n = 1$ wetting layer, and this line is the D-W thermal attenuation from measurements on clean Cu(111) [72,73]. b) Plots for large ML numbers. Only even numbers are given corresponding to the bilayer structure.

perature dependence of the specular intensity of each monolayer (or bilayer) through ML number $n = 9$. The ML number is shown in the case of identifiable monolayers, otherwise a bilayer peak is identified by two ML numbers, such as 4/5. The straight line that appears to pass through the points associated with the much less distinct wetting monolayer at $n = 1$ is taken from independent measurements of the D-W factor for clean Cu(111). ML numbers greater than $n = 9$ are shown in Fig. 9b). Clearly there is a distinct difference in the D-W behavior of those peaks with monolayer number $n \leq 9$ and those with larger ML numbers. The data for $n < 10$ ML are not linear in T, but show a downward curvature indicative that at higher temperatures the stiffer substrate phonons start contributing, thus increasing the slope. For $n \geq 10$ the intensities decrease nearly linearly with T indicating that the substrate is no longer having an appreciable effect. This alone would suggest $n_{sat} = 9$, although further support for this value comes from an examination of the incident energy dependence of the D-W behavior discussed below in connection with Fig. 10.

The values of λ_{HAS} derived from Eq. (149) for the three temperatures of Fig. 8a) are plotted, as a function of the nominal thickness layer number n, as filled diamond points connected by solid lines in Fig. 8b). Values of the work function are taken from measurements of ϕ as a function of Pb layer thickness n on a Si(111) substrate [141]. Meaningful values start from $n = 3$, because the first monolayer of Pb on Cu(111) actually plays the role of a wetting layer, and the second ML film is disordered [75,137]. However, the value of λ_{HAS} extracted from the $n = 1$ wetting layer is shown as an isolated diamond marked as "wl". The vertical bar represents the standard deviation uncertainty, and the short horizontal bars indicate the uncertainty in positions of the bilayer peaks at the three measured temperatures.

6.3. Determination of λ for Pb overlayers on Cu(111) using dependence of intensity on incident energy

The form of Eq. (135) above makes it clear that λ_{HAS} can also be obtained from measurements of the D-W exponent $2W^{eff}(\mathbf{k}_f, \mathbf{k}_i, T)$ at fixed temperature, but for two different incident energies. However, such measurements involve varying the temperature of the beam source chamber, which requires a correction for the change in intensity of the incident beam as a function of energy. For such a measurement at two different energies the e-ph coupling constant λ_{HAS} is again given by Eq. (148) with the modification that the intensity must be corrected by a factor of k_i^γ and α is replaced by

$$\alpha = \frac{\phi}{a_c k_B T} \frac{\Delta \ln\left[k_i^\gamma I(E_{iz}, T)\right]}{\Delta[k_{iz}^2]}, \tag{151}$$

where $\Delta \ln[k_i^\gamma I(E_{iz}, T)]$ and $\Delta[k_{iz}^2]$ are the differences between the respective quantities at the two incident energies.

The standard theoretical treatment of a jet beam nozzle expansion flow shows that the beam energy varies inversely as the square root of the stagnation temperature, implying that the correction factor is simply k_i, or $\gamma = 1$ [142]. In a series of measurements of He atom scattering from Pb overlayers made independently from the temperature-dependent data shown in Fig. 9 the question of the energy dependence of the incident beam was experimentally

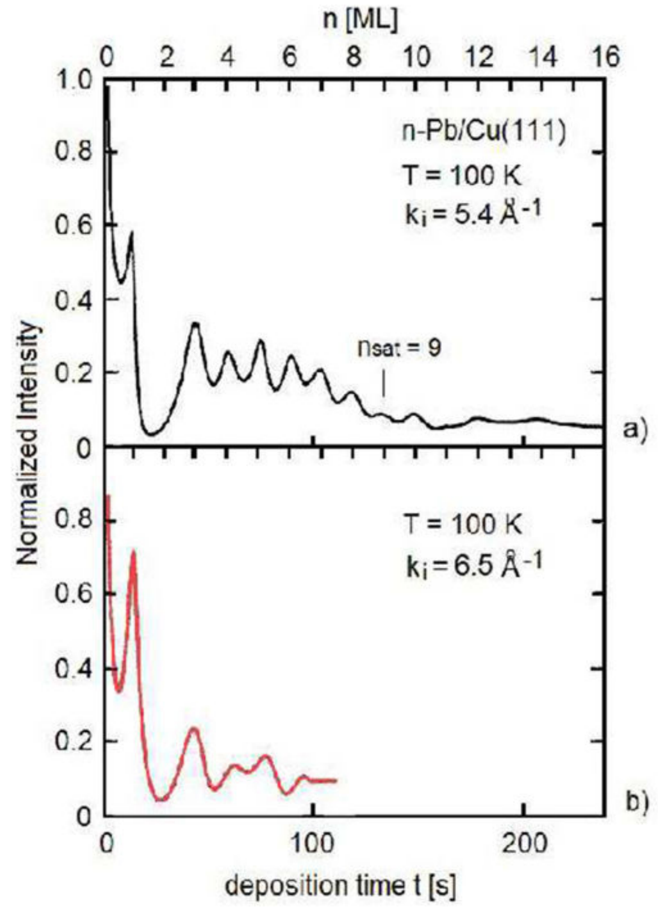

Fig. 10. Specular intensity growth curves for Pb deposited on Cu(111) taken at the same temperature of 100 K and two incident energies. a) Incident wave vector $k_i = 5.4$ Å^{-1}, and b) $k_i = 6.5$ Å^{-1}. The lower abcissa gives deposition time and the upper abscissa gives ML number. (Reprinted with permission from Ref. [115]. Copyright [2018] American Chemical Society).

addressed by changing the source temperature at constant pressure [138]. In this case, which was for low energies, the supersonic beam flux to a good approximation varied inversely in proportion to k_i, in agreement with the theoretical result. Further discussion on the dependence of the incident beam on stagnation temperature and pressure has been presented by Palau et al. [143].

Measurements presented in Fig. 10 of growth curves of Pb on Cu(111) were made at $T = 100$ K and two incident energies with wavevectors of 5.4 and 6.5 Å^{-1}. These show bilayer growth for ML numbers significantly greater than 10 for the lower energy and $n = 7$ for the larger energy [138]. The lower energy data in Fig. 10a) clearly show that saturation occurs at the ML coverage $n_{sat} = 9$. Plotted in Fig. 8b) as downward-pointing triangles are the values of λ_{HAS} extracted from this data using Eq. (151) with the incident beam energy correction given by $\gamma = 1$. However, because the energy difference between the two sets of data in Fig. 10 is not large, this energy correction is small. The values of λ_{HAS} are found to be in excellent agreement with those obtained from the temperature dependence at fixed incident energy. In Fig. 8b) the isolated point at $n = 5$ marked with a cross (+sign) is from the single measurement of the incident energy dependence of the D-W exponent taken during the same experiment in which the temperature-dependent data were obtained [137]. The agreement with the temperature-dependent measurements is quite good. These extracted λ_{HAS} values are compared in Fig. 8b) with previous measured values for thick films of 15–24 layers using angle resolved photoemission spectroscopy (ARPES) which lie in the range 0.7–1.05 [97] as shown as upward-pointed triangles connected by dash-dotted lines. Also shown as filled circle points are values for thin films calculated using density functional perturbation theory [35]. Older bulk values in the literature, which range from 1.12 to 1.68 [36,99], are shown as filled circles on the right vertical axis of Fig. 8b).

6.4. Chalcogenides and topological surfaces

A number of chalcogenide crystal surfaces, as well as other topological surfaces, have been investigated with He atom scattering. Those chalcogenides for which the temperature dependence of the Debye-Waller thermal attenuation has been measured are listed in Table 5. In most of these systems it was the specular thermal attenuation that was measured. Chalcogenides share the characteristic that they are layered compounds, and often their electronic properties are altered by doping to form degenerate semiconductors. The layered nature of these surfaces suggests that an approach similar to that used above for multiple layers of alkali metals or Pb can be adapted.

A discussion on the determination of the e-ph coupling constant for these systems starts from the expression for λ_{HAS} that is obtained from Eqs. (130) and (131) above, namely

$$\begin{aligned}\lambda_{HAS} &= \frac{m_e^*}{2\hbar^2 \mathcal{N}(E_F)} \frac{\phi \ \ln\left\{I(T_1)/I(T_2)\right\}}{k_{iz}^2 k_B (T_1 - T_2)} \\ &= \frac{\pi}{2n_s} \frac{\phi \ \ln\left\{I(T_1)/I(T_2)\right\}}{a_c k_{iz}^2 k_B (T_1 - T_2)} = \frac{\pi}{2n_s} \alpha \ .\end{aligned} \qquad (152)$$

The final form on the RHS of Eq. (152) is suggested by the discussion of layered surfaces in Sec. 6.2 and α is identical in form to that of Eq. (148), while

$$n_s = \frac{\pi\hbar^2 \mathcal{N}(E_F)}{m_e^* a_c} \ ; \ \alpha = \frac{\phi \ \ln\left\{I(T_1)/I(T_2)\right\}}{a_c k_{iz}^2 k_B (T_1 - T_2)} \ . \qquad (153)$$

The rather simple-looking expression in the second line of the above Eq. (152) nicely separates the surface electronic properties from the quantities actually measured in an experiment. The electronic properties expressed in the ratio $\mathcal{N}(E_F)/m_e^*$ are contained in the dimensionless n_s while the usually well-known work function and the experimentally measured slope of the D-W exponent are contained in α. The physical interpretation of n_s becomes that of the number of layers that are contributing to the e-ph coupling constant at the surface. The problem of determining the correct DOS $\mathcal{N}(E_F)$ appropriate for a particular surface becomes one of determining the number of layers n_s.

6.4.1. 1D example, topological surface with charge density wave: Bi(114)

Considered here is the case of the strongly corrugated Bi(114) surface, which acts in a specific symmetry direction approximately as a 1D electron gas and exhibits a charge density wave (CDW) below its critical temperature of $T_c \approx 290°$. Because of the large corrugation the non-specular diffraction peaks are large, and this example shows that it is possible to obtain useful information on λ_{HAS} from multiple diffraction peaks and from a CDW peak as observed in the He atom scattering spectra. The values of λ_{HAS} that are obtained from the diffraction peaks are nearly identical, and that produced by the CDW peak is only slightly smaller.

Low-dimensional free electron gases are often characterized by a CDW instability below a critical temperature T_c, generally induced by e-ph interaction via the Fröhlich-Peierls [186,187] or the Kelly-Falicov multivalley mechanisms [188–190]; with the former typically applying to metal surfaces with a CDW wavevector corresponding to some nesting wavevector at the Fermi contours, and the latter more appropriate to semimetal surfaces with pocket states at the

Table 5

The e-ph coupling constant λ_{HAS} for several chalcogenides and pnictogen chalcogenides as determined from the temperature dependence of the thermal attenuation of elastic specular He atom diffraction. The entries for $PtTe_2$ was evaluated from the dependence on incident angle of the diffuse elastic peak intensity at a constant temperature of 100 K. Values of λ_{HAS} in parenthesis are calculations without the Beeby correction. The value of the Beeby correction D used for MoS_2 is 13.6 meV [144,145], for $Bi_2Se_3(111)$ it is 6.54 [146], for $Bi_2Te_3(111)$ it is 6.22 [147], and for $Bi_2Te_2Se(111)$ it is 6.4 [148].

Surface	T range [K]	k_i^2 [Å^{-2}]	ϕ [eV]	λ_{TF} [Å]	λ_{HAS}	λ (other sources)
n-$Bi_2Se_3(111)$ [149]	120–300	20.7	4.9 [158]	≈60 [163]	0.23 (0.51)	0.15 [169], 0.42 [174] 0.25 [171], 0.077 [172] 0.17 [170], 0.26 [173]
n-$Bi_2Te_3(111)$ [150] (^{3}He atoms)	110–355	15.2	4.9 [158]	≈100 [164]	0.19 (0.35)	0.05 [168] 0.05 [169], 0.19 [170]
$Bi_2Te_2Se(111)$ [149]	120–300	22.0	4.9 [158]	≈100 [165]	0.08 (0.14)	0.12 [175]
2H–$MoS_2(001)$ [151]	95–450	121	5.2 [159]	≈11.0 [166]	0.41 (0.67)	∼0.1 [176,177] 0.12–0.20 [178]
1T-$TaS_2(001)$ [152,153]	180-280 [155,156] 350-380 [157]	29.2	5.2 [160]	≈10.2 [167]	1.0 [156] ∼0.4 [157]	1.0 [179] 0.69–2.09 [180] 0.38 [181]
2H–$TaSe_2$ [152,153]	50–120	137	5.5 [161]	≈10 [153]	0.58	0.49 [179] 0.39 [182]
1T-$PdTe_2(001)$ [154]	50–300	121	4.6 [162]	10.6 [154]	0.60	0.59 [183] 0.53 [184]
1T-$PtTe_2$ [154]	100	159	4.52 [162]	8.64 [154]	0.46 ± 0.01	0.92 [185]

Fermi level [191]. The phonon-induced transitions between narrow pockets (nests) realize what is meant as perfect nesting. Since He atoms scattered from a conducting surface probe the surface charge density directly, the occurrence of a CDW below T_c yields additional T-dependent diffraction peaks in the elastic scattering angular distribution at parallel wavevector transfers $\Delta K = |\Delta\mathbf{K}|$ equal or close to the nesting vectors Q_c. Recall that for the elementary 1D Peierls mechanism the nesting vector is $Q_c = 2k_F$. The high sensitivity of HAS permits the detection of weak surface CDWs that would be difficult to detect with other methods. Thus the comparison of diffraction intensities with that of the CDW can help answer the interesting question of whether the temperature dependence of the CDW diffraction peaks carries additional information on the e-ph interaction which sustains the CDW transition.

When considering the temperature dependence of a diffraction peak intensity for a wavevector transfer $\Delta\mathbf{K}$ equal to either a $\mathbf{G}$-vector of the unreconstructed surface lattice ($\Delta\mathbf{K} = \mathbf{G}$), or to a CDW wavevector Q_c, the D-W exponent also involves the longitudinal mean-square phonon displacement. For an isotropic mean-square displacement, Eqs. (140) and (143) also can be applied to diffraction peaks other than specular by replacing $4k_{iz}^2$ with $\Delta k_z^2 + \Delta\mathbf{K}^2$, calculated at the actual scattering geometry at which the diffraction peak is observed. In most HAS experiments the condition $\Delta\mathbf{K}^2 \ll \Delta k_z^2$ holds, so little difference is expected between the T-dependence of the diffraction and specular peaks, provided λ_{HAS} is independent, as it should be, of the scattering channel chosen in the experiment.

There is, however, a caveat for the use of a CDW diffraction intensity $I_{CDW}(T)$. It has been assumed implicitly that the D-W exponent $2W(T)$ includes all the temperature dependence of $I(T)$ and that this originates exclusively from thermal vibrations. This is clearly not true for the diffraction from a surface CDW which forms below T_c from a Fermi surface instability and has the temperature-dependent population of electron states near the Fermi level obeying Fermi statistics. In this case I_0 has an implicit dependence on T, which generally is negligible with respect to that of $2W(T)$, except near T_c; there its square root $\sqrt{I_0}$ behaves as an order parameter [192,193], and vanishes for increasing $T \to T_c$ as $(1 - T/T_c)^\beta$, where β is the order-parameter critical exponent. Typically $\beta = 1/3$ [61,180,194], and $T_c \approx 280$ K in the present case [61].

Bi(114) provides a good 1DEG example showing that a CDW diffraction peak also may be used to extract λ_{HAS}, provided that the temperature is away from the critical region. The ideal (114) truncation of bismuth as shown in Fig. 11a) is characterized by parallel atomic rows along the $x \equiv [1\bar{1}0]$ direction, separated by 7.1 Å in the normal direction $y \equiv [22\bar{1}]$, with a unit cell including two rows ($b = 14.2$ Å) and one atom per row (the atom spacing along the rows is $a = 4.54$ Å). At room temperature, the Bi(114) surface is reconstructed in a (1 × 2) fashion with 3 missing rows out of 4, so as to have one row per unit cell ($b = 28.4$ Å) and one atom per row as shown in Fig. 11a) and b). The electronic structure, calculated by Wells et al. [195] for the (1 × 1) phase [Fig. 11c), far left panel], shows cones centered at the $\overline{X}$ and $\overline{Y}$ points [Fig. 11c) and d)] at the Fermi level. Those at $\overline{Y}$ are folded into $\overline{\Gamma}$ in the (1 × 2) reconstructed phase. Both electronic structures allow for a multivalley CDW via e-ph interaction, the former with a 2-D character, the latter with a pure 1D character due to the cone alignment along $\overline{\Gamma}\,\overline{X}$ with a $G/2$ spacing. HAS angular distributions along $\overline{\Gamma}\,\overline{X}$ [61] in Fig. 12a) show the growth of additional peaks at $\pm G/2$ and $\pm 3G/2$ below $T \approx 280$ K, indicating the formation of a surface commensurate CDW [61]. The associated (2 × 2) reconstruction consists of a dimerization along the rows. The portion of the Bi(114)-(2 × 2) STM image reproduced in Fig. 11a) from Hofmann et al. [61,86] suggests a phase correlation between rows, giving an oblique (2 × 2) unit cell and a corresponding elongated hexagonal Brillouin zone (BZ) as illustrated in Fig. 11d).

The HAS D-W exponents for the specular $\mathbf{G} = (0,0)$, diffraction $\mathbf{G} = (\bar{1},0)$, and CDW $(\overline{3/2},0)$ peaks measured as a function of temperature below T_c are plotted in Fig. 12b). The specular and diffraction D-W exponents have almost the same slopes, the small difference being compensated by the ratio $(\Delta k_{iz}^2)_{(0,0)}/[\Delta k_z^2 + \Delta\mathbf{K}^2]_{(\bar{1},0)}$, resulting in the same values of λ_{HAS}^{1D} within less than 1%. The input data in Eq. (140) for dimension $d = 1$ are $\phi = 4.23$ eV [78], $2k_F = G/2 = 0.7$ Å^{-1}, $r_0(2 \times 2) = 9.08$ Å, incident energy $E_i = 14.5$ meV, and a fixed scattering angle of 91.5°, so that $(\Delta k_{iz}^2)_{(0,0)} = 54.3$ Å^{-2}. The $(\bar{1},0)$ diffraction occurs at the incident angle of 51.2°, which gives $(\Delta k_{iz}^2)_{(\bar{1},0)} = 53.8$ Å^{-2}, and the resulting e-ph coupling constant is $\lambda_{HAS}^{(1D)} = 0.45 \pm 0.03$. Within the margin of error, the value is the same for both specular and diffractive channels.

The CDW $(\overline{3/2},0)$ peak intensity exhibited in Fig. 12b) shows the expected critical behavior with $\beta \cong 1/3$, but a value of $\lambda_{HAS}^{(1D)}$ can be estimated from the nearly linear slope at the lowest temperatures measured far from the critical point. This value is smaller

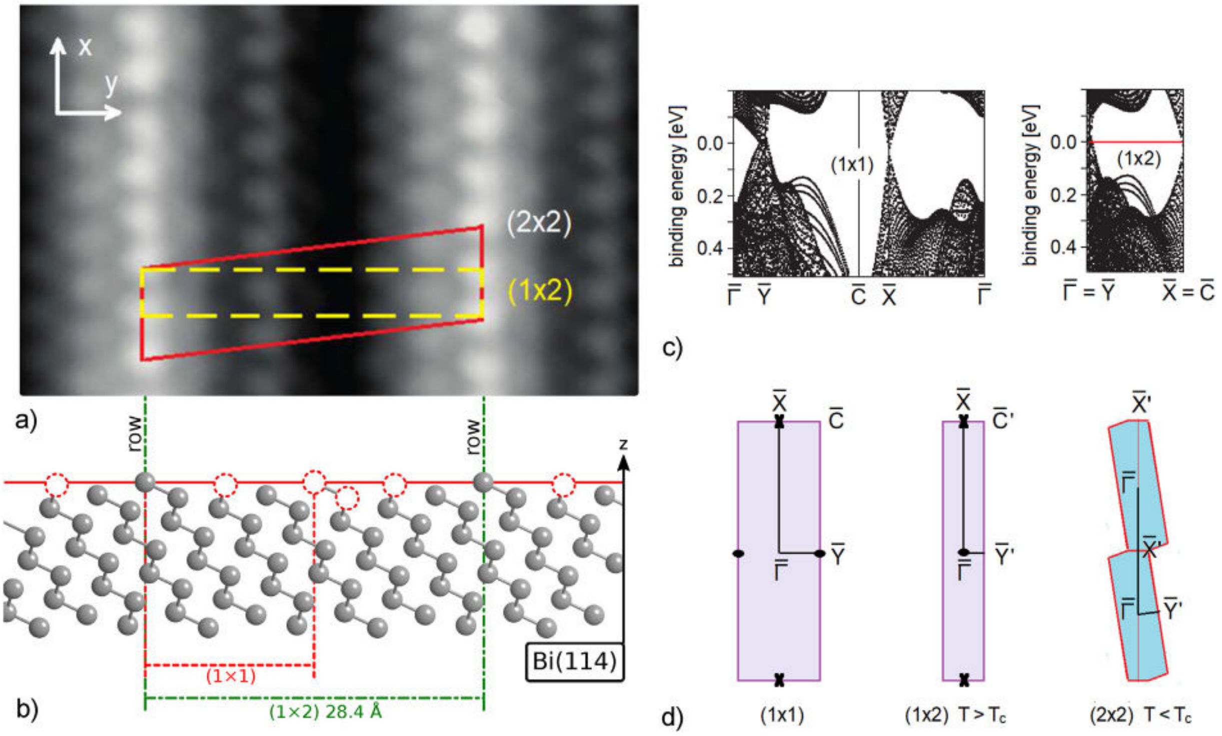

Fig. 11. a) The Bi(114) surface is characterized by parallel atomic rows due to a (1 × 2) surface reconstruction as visualised in STM images [153,195]. b) A side view of the ideal (114) truncation of bismuth (including the red dashed circles) and the actual (1 × 2) surface reconstruction (circles removed), giving rise to the parallel atomic rows with an inter-row distance of 28.4 Å and an interatomic distance of 4.54 Å. The corresponding (1 × 2) electronic structure c) is schematically represented as a folding of the calculated electronic structure [195] for the truncated Bi(114) (1 × 1) surface, with the corresponding surface BZ shown in d). In particular, the cones of electronic states occurring at the Fermi level at the $\overline{X}$ and $\overline{Y}$ symmetry points turn out to be aligned in the $\overline{\Gamma X}$ direction after the (1 × 2) folding [panel d)]. It allows for a multivalley 1D CDW instability along the rows leading to a (2 × 2) dimerization below ≈280 K and a corresponding CDW observed with HAS [61]. The (2 × 2) surface portion reproduced in a) [195] shows a π-dephasing of two adjacent rows so as to give a rhombohedric cell, with the corresponding BZ shown in d) [153]. (For interpretation of the references to colour in this figure legend, the reader is referred to the Web version of this article.)

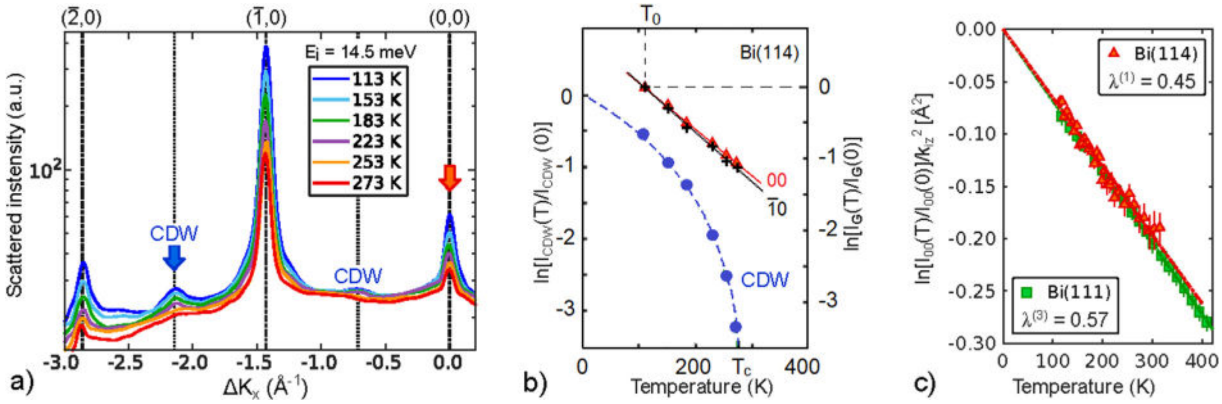

Fig. 12. Helium atom scattering data from Bi(114): a) HAS angular distributions for several different temperatures, ranging from 113 to 273 K as marked, showing both diffraction peaks of the (2 × 1) reconstruction and the appearance of the CDW feature according to a (2 × 2) superstructure [61]. b) The temperature dependence of the $(\overline{3/2},0)$ CDW peak (left ordinate scale) and of the (0, 0) (specular) and $(\overline{1},0)$ (diffraction) peak D-W exponents referred to the lowest temperature measured, T = 113 K. c) The D-W exponents of the Bi(114) and Bi(111) specular peaks, when divided by the respective squared perpendicular wavevector transfers, show similar slopes but lead to different e-ph coupling strengths.

than that obtained from the specular peak by ∼5% and is compensated for approximately the same amount by the correcting factor $(\Delta k_{iz}^2)_{(0,0)}/[\Delta k_z^2 + \Delta \mathbf{K}^2]_{(\overline{3/2},0)} = 1.047$, the incident angle for the CDW peak at $(\overline{3/2},0)$ being 62.75°. Thus it is reasonable to conclude that consistent values of $\lambda_{HAS}^{(1D)}$ can be extracted from the T-dependence of the CDW peaks.

It is interesting to compare the value $\lambda_{HAS}^{(1D)} = 0.45$ for Bi(114) to that previously derived for Bi(111), either treated as a 3-D system or as a 2-D bilayer. The 3-D result is $\lambda_{HAS}^{(3D)} = 0.57$ [46], in agreement with the value of $\lambda = 0.60$ in Hofmann's review [86]. Treated as a 2-D system with $n_s = 2$ (a single bilayer) it is found that $\lambda_{HAS}^{(2D)} = 0.40$, in fair agreement with a recent ab-initio calculation by Ortigzoa et al. for Bi(111) [94] which yielded $\lambda = 0.45$, the same value found here for Bi(114). As seen in Fig. 12c), the D-W exponent has about the same slope for Bi(111) and Bi(114), when the slopes are normalized by k_{iz}^2, in order to account for the different incident energies used in HAS experiments. The fact that $\lambda_{HAS}^{(1D)}$ [Bi(114)] < $\lambda_{HAS}^{(3D)}$[Bi(111)] reflects the dimensionality effect of γ_d, in the prefactor of Eq. (140). Incidentally, we note that treating Bi(114) as a 2-D system would yield a five times smaller, and surely unphysical, value for λ_{HAS} due to the large surface unit cell area.

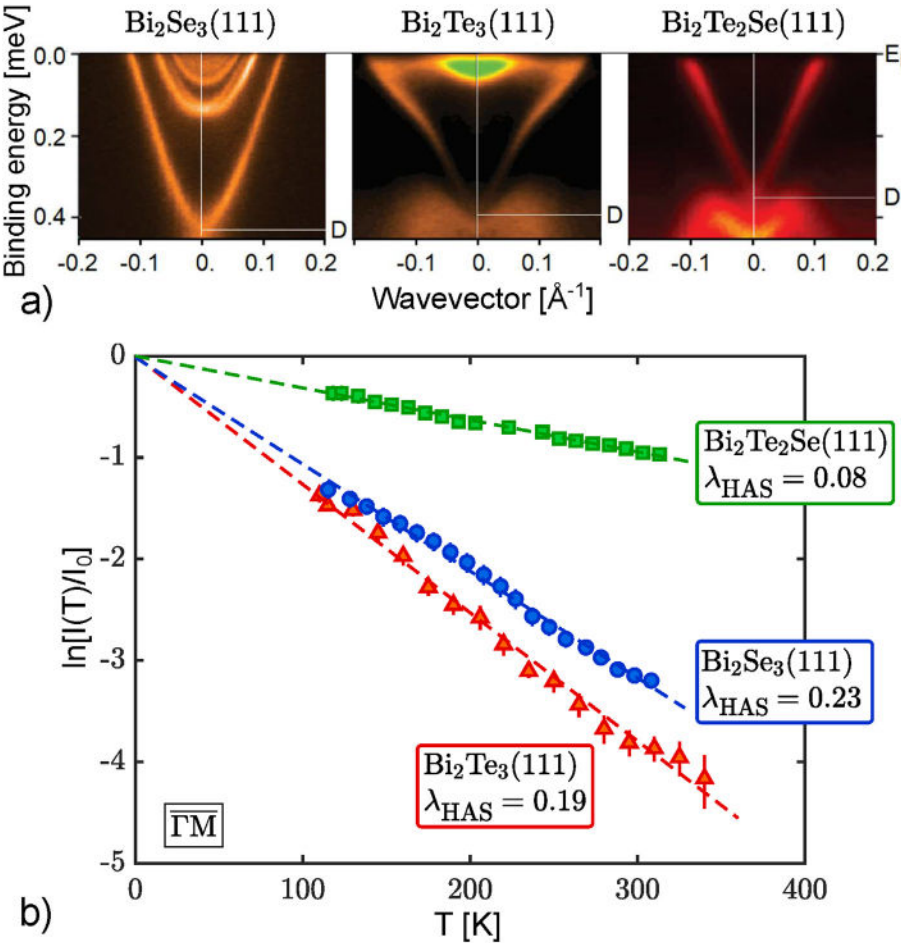

Fig. 13. Three different Bi chalcogenides Bi_2Se_3, Bi_2Te_3 and Bi_2Te_2Se: a) ARPES data for the (111) surface of three Bi chalcogenides with decreasing binding energy of the Dirac point (D) and of the surface conduction-band minimum (from 0.15 eV in Bi_2Se_3 [208] to 0.08 eV in Bi_2Te_3 [209] and ≈0 in Bi_2Te_2Se [210]. b) The D-W exponent slopes from HAS specular intensity measured as functions of temperature with the scattering plane in the $\overline{\Gamma M}$ direction for the same samples. The corresponding e-ph coupling constants λ_{HAS} decrease from $Bi_2Se_3(111)$ to $Bi_2Te_2Se(111)$, suggesting a dominant role in the e-ph interaction of the conduction band quantum-well electronic states over the Dirac electrons [153].

6.4.2. Pnictogen chalcogenides

Layered chalcogenides, such as 2-D topological materials, with strong intralayer and weak interlayer forces form a wide class of quasi-2D materials with a conducting surface. Some transition-metal dichalcogenides (TMDC) have been investigated with HAS since the late eighties in connection with CDW transitions, related Kohn anomalies in the bulk, and surface phonon dispersion curves [196–200]. More recently, HAS studies have been extended to the surface of other TMDCs such as 2H-$MoS_2(0001)$ [151] and 1T-$PtTe_2$ [201], as well as to pnictogen chalcogenides with surface topological electronic bands at the Fermi level, such as Bi_2Te_3 [150,202,203], Bi_2Se_3 [204,205] and Bi_2Te_2Se. These latter three will be considered in more detail here. The 2-D expression for the e-ph coupling constant $\lambda_{HAS}^{(2D)}$ in Eq. (143) is the one to be used for these systems. When dealing with the e-ph coupling constant λ_{HAS} expressed as an average over the whole phonon spectrum and over all electronic transitions across the Fermi level, natural questions are: a) which phonons contribute most, and b) which electronic states at the Fermi level are more important, and these questions are addressed here.

The theoretical analysis by Heid et al. [169] of the mode-selected e-ph coupling constants $\lambda_{\mathbf{Q},\nu}$ shows that in pnictogen chalcogenides, optical phonons give the major contribution to e-ph interaction, and consequently also to the D-W exponent. Both $Bi_2Se_3(111)$ [205] and $Bi_2Te_3(111)$ [203] exhibit two highly dispersed optical branches with deep minima at $\overline{\Gamma}$ for 3rd-layer longitudinal polarization and at $\approx\overline{\Gamma}\,\overline{M}/2$ for (mostly) 3rd-layer shear-vertical (SV3) polarization. Their optical character and largest amplitude at the central chalcogen layer of the quintuple layer endow these modes with a dipolar character and therefore a large e-ph interaction, consistent with the Heid et al. theoretical analysis [169]. Spin-echo ^{3}He scattering data from $Bi_2Te_3(111)$ [203] suggest a Kohn anomaly also in the longitudinal acoustic branch corresponding to a nesting across the Dirac cone above the surface conduction-band minimum. As discussed in Ref. [169], the interband e-ph coupling occurring when the Fermi level is above the surface conduction-band minimum is enhanced largely by the involvement of surface quantum-well states. This conclusion is confirmed by the following analysis of $\lambda_{HAS}^{(2D)}$ in Bi chalcogenides as a function of the Fermi level position.

The temperature dependence of HAS specular reflectivity from the three Bi chalcogenide surfaces $Bi_2Se_3(111)$, $Bi_2Te_3(111)$, and $Bi_2Te_{3-x}Se_x(111)$ (phase II with $x \approx 1$ [206,207]), hereafter approximated by $Bi_2Te_2Se(111)$) has been measured for three samples whose surface electronic states near the Fermi level, in particular the topological Dirac states and the quantum-well states above the surface conduction-band minimum, are known from ARPES data [163,208–210]. As seen in Fig. 13 (top panel), the binding energy of the Dirac point (D) with respect to the Fermi energy E_F decreases in the sequence $Bi_2Se_3(111)$, $Bi_2Te_3(111)$, $Bi_2Te_2Se(111)$, as does the surface conduction-band minimum (from 0.15 eV, to 0.08 eV and ≈0, respectively). Correspondingly, the D-W exponent slope derived from the HAS specular intensity as a function of temperature also decreases. Similar behavior is expected for the e-ph coupling constant $\lambda_{HAS}^{(2D)}$, which is shown in Table 5. These values are derived from Eq. (143) and (152) by setting $n_s = 2\lambda_{TF}/c_0$, where c_0 is the quintuple layer (QL) thickness and λ_{TF} is the Thomas-Fermi screening length, accounting for the surface band-bending extension in degenerate semiconductors and semimetals [211]. The factor 2 in the expression for n_s accounts for the fact that each QL contains two metal (Bi) layers. Note that the Fermi-level density of states includes the factor 2 for spin multiplicity, and this is appropriate for the quantum-well states above the surface conduction-band minimum that mostly contribute to $\lambda_{HAS}^{(2D)}$. No factor of 2 in n_s is necessary when only the Dirac states are involved, due to their multiplicity of 1. The error uncertainties given for λ_{HAS} in the following are based on the confidence bounds of the D-W slope. Other sources in terms of the uncertainty are a_c, ϕ and λ_{TF} with the largest contribution likely to be due to λ_{TF}. Taken together it is safe to assume a relative uncertainty of about 10% for λ_{HAS} as shown in Table 5.

With the input data collected in Table 5 and the D-W exponent slopes displayed in the bottom panel of Fig. 13 values evaluated are $\lambda_{HAS}^{(2D)} = 0.23 \pm 0.01$ for $Bi_2Se_3(111)$, 0.19 ± 0.01 for $Bi_2Te_3(111)$, and 0.080 ± 0.004 for $Bi_2Te_2Se(111)$, in good agreement with selected results from other sources shown in the last column of Table 5. This clearly indicates the dominant role of surface quantum well (QW) states over the modest contribution of Dirac electrons. The enhancement effect of QW states and related interband transitions has been investigated experimentally by Chen et al. [175] with high resolution ARPES for the family $Bi_2Te_{3-x}Se_x(111)$ $(0 \le x \le 3)$, including n-type $Bi_2Te_3(111)$, and theoretically for $Bi_2Se_3(111)$ and $Bi_2Te_3(111)$ by Heid et al. [169] As shown by Pan et al. [172] in accurate ARPES studies on bulk $Bi_2Se_3(111)$ samples, where only Dirac topological states are involved because the Fermi level is less than 0.3 eV above the Dirac point, the e-ph coupling constant turns out to be quite small, ranging from 0.076 ± 0.007 to 0.088 ± 0.009, similar to that found with HAS in $Bi_2Te_2Se(111)$ under similar conditions.

Since the surface QW states extend into the bulk on the order of λ_{TF}, i.e., much farther than the penetration of surface Dirac states, it is interesting to compare the above results for $\lambda_{HAS}^{(2D)}$ with the corresponding values of $\lambda_{HAS}^{(3D)}$ when these materials are treated as 3-D materials. The ratio $\lambda_{HAS}^{(3D)}/\lambda_{HAS}^{(2D)} = \pi/(k_F\lambda_{TF})$, with $k_F \simeq 0.1$Å^{-1} as seen in Fig. 13 (top), and λ_{TF} representing the 3DEG thickness, turns out to be $\simeq 1$.

Unlike Bi(114), where the quasi-1D character of the electron gas is quite evident, in layered pnictogen chalcogenides the considerable penetration of the QW states gives $\lambda_{HAS}^{(2D)} \simeq \lambda_{HAS}^{(3D)}$. This is consistent with the fact that the QW states are the surface states which provide the major contribution to the e-ph interaction. Information about which phonons contribute most to λ can also be obtained from inelastic HAS intensities, as suggested above. The Kohn anomalies reported in the lower part of the phonon spectrum [202–204] are indicative of a strong e-ph coupling for specific wavevectors and frequencies, though it has been predicted that the major contribution in these materials comes from polar optical modes [169]. Indeed this is in agreement with recent HAS measurements of the phonon dispersion curves in $Bi_2Se_3(111)$ [205], which indicate the longitudinal optical branch L3 (with the largest displacement on the 3rd (Se) atomic plane) as the one having the largest mode-selective e-ph coupling.

A number of additional chalcogenide surfaces have been investigated and those for which the thermal attenuation measurements yield an estimate of the e-ph coupling constant are listed in Table 5 together with the relevant experimental parameters and references. The entry for $PtTe_2$ differs from the others in that the elastic peak that was measured was not the specular, but was the off-specular diffuse elastic peak measured at a constant temperature of 100 K. The experimental parameter that was varied was the incident angle, keeping the source-to-detector angle fixed. Thus in this case the value of α in Eq. (152) must be modified to account for the correct wave vector difference, i.e., $k_{iz}^2 \rightarrow \Delta\mathbf{k}^2/4 = (\mathbf{k_f} - \mathbf{k_i})^2/4$. The details of using the angular dependence to determine λ_{HAS} are explained below in Sec. 6.5. In each case shown in Table 5, with reasonable choices for n_s determined using parameters taken from the literature, results for λ_{HAS} compare quite acceptably with values of λ for the bulk crystals determined from other sources, which may be either measurements or calculations.

6.5. Determining λ from incident angle dependence of elastic intensities

It is clear from the discussion of the elastic scattering intensity in Eqs. (10) and (31) that the elastic contribution to the differential reflection coefficient (angular distribution) for given incident and final angles can be expressed in terms of the transition matrix and effective Debye-Waller factor according to

$$\frac{d^2R^{elas}(\mathbf{k}_f,\mathbf{k}_i,T)}{d\Omega_f} \propto \frac{m^2|\mathbf{k}_i|}{k_{iz}} \left|T^0_{\mathbf{k}_f,\mathbf{k}_i}\right|^2 e^{-2W^{eff}(\mathbf{k}_f,\mathbf{k}_i,T)} , \tag{154}$$

where the squared transition matrix $\left|T^0_{\mathbf{k}_f,\mathbf{k}_i}\right|^2$ describes the scattered intensity from the corresponding frozen surface and the factor $k_{iz} = k_i \cos\theta_i$ arises from normalizing to the incident flux. This expression is valid for the entire elastic contribution to the angular distribution, e.g., it describes the intensity observed at the diffraction peak positions as well as the diffuse elastic scattering between diffraction peaks. For determining the coefficient λ from experimental data for elastic scattering in which the incident energy and temperature are held fixed but the incident and final angles may be varied, it is of interest to consider the following quantity, which is the intensity with the flux normalization removed, i.e.,

$$\mathcal{I}(\mathbf{k}_f,\mathbf{k}_i,T) = \cos\theta_i \frac{d^2R^{elas}(\mathbf{k}_f,\mathbf{k}_i,T)}{d\Omega_f} . \tag{155}$$

The ratio of $\mathcal{I}(\mathbf{k}_f,\mathbf{k}_i,T)$ at two different sets of angles (θ_i,θ_f) and (θ_i', θ_f') is

$$\frac{\mathcal{I}(\mathbf{k}_f',\mathbf{k}_i',T)}{\mathcal{I}(\mathbf{k}_f,\mathbf{k}_i,T)} = \frac{\left|T^0_{\mathbf{k}_f',\mathbf{k}_i'}\right|^2}{\left|T^0_{\mathbf{k}_f,\mathbf{k}_i}\right|^2} e^{-2W^{eff}(\mathbf{k}_f',\mathbf{k}_i',T) + 2W^{eff}(\mathbf{k}_f,\mathbf{k}_i,T)} , \tag{156}$$

where elastic scattering implies $|\mathbf{k}_f'| = |\mathbf{k}_i'| = |\mathbf{k}_f| = |\mathbf{k}_i| = k_i$. Taking the logarithm of both sides of Eq. (135) leads to

$$\ln\left\{\frac{\mathcal{I}(\mathbf{k}_f',\mathbf{k}_i',T)}{\mathcal{I}(\mathbf{k}_f,\mathbf{k}_i,T)}\right\} = 2\ln\left\{\frac{\left|T^0_{\mathbf{k}_f',\mathbf{k}_i'}\right|}{\left|T^0_{\mathbf{k}_f,\mathbf{k}_i}\right|}\right\} + 2W^{eff}(\mathbf{k}_f,\mathbf{k}_i,T) - 2W^{eff}(\mathbf{k}_f',\mathbf{k}_i',T). \tag{157}$$

From Eqs. (130) and (132) and the discussion in Subsection 6.4 the effective Debye-Waller exponent $2W^{eff}$ can be written, if the temperature T is comparable to or larger than the Debye temperature Θ_D, as

$$2W^{eff}(\mathbf{k}_f,\mathbf{k}_i,T) = n_s \frac{a_c}{2\pi\phi}\Delta\mathbf{k}^2 k_B T\lambda , \tag{158}$$

where, as before in Eq. (153), $n_s = \pi\hbar^2\mathcal{N}(E_F)/m_e^* a_c$ is the relevant saturation layer number. The logarithmic ratio of Eq. (157) thus

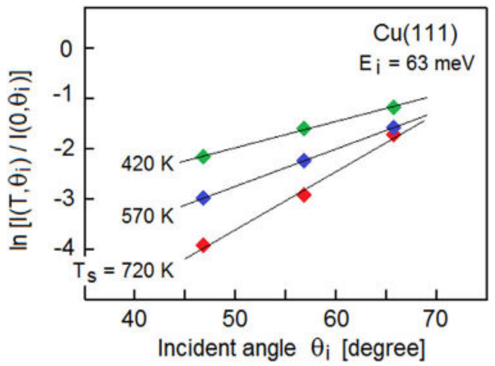

Fig. 14. Logarithmic plot of the specular intensity as a function of incident angle for He atom scattering from Cu(111) at three different temperatures as marked. The incident energy is 63 meV. Data from Ref. [73].

becomes an expression from which λ can be extracted

$$\ln\left\{\frac{\mathcal{I}(\mathbf{k}_f',\mathbf{k}_i',T)}{\mathcal{I}(\mathbf{k}_f,\mathbf{k}_i,T)}\right\} = 2\ln\left\{\frac{\left|T^0_{\mathbf{k}_f',\mathbf{k}_i'}\right|}{\left|T^0_{\mathbf{k}_f,\mathbf{k}_i}\right|}\right\} + n_s\frac{a_c}{2\pi\phi}\left[\Delta\mathbf{k}^2 - \Delta\mathbf{k}'^2\right]k_BT\lambda. \tag{159}$$

Under many circumstances, particularly if the two sets of angles are not too widely separated, the first term on the right hand side of Eq. (159) is small and can be neglected compared to the second term.

A case in point is the set of measurements for the specular intensity of He atom scattering from Cu(111) shown in Fig. 14 [73]. The logarithmic specular intensity is shown as a function of incident angle for the three different temperatures of 420, 570 and 720 K over a range of nearly 20° from $\theta_i = 47°–66°$. For the specular peak the squared momentum difference is simply $\Delta\mathbf{k}^2 = (2k_{iz})^2 = 4k_i^2\cos^2\theta_i$. A plot of $\cos^2\theta_i$ over the 20° range of Fig. 14 is very nearly linear, thus the linearity of all three sets of data shown there implies that the first term on the RHS of Eq. (159) is small, i.e., the scattering form factor or squared transition matrix is nearly constant, thus this term may be ignored. Eq. (159) now becomes simply

$$\ln\left\{\frac{\mathcal{I}(\mathbf{k}_f',\mathbf{k}_i',T)}{\mathcal{I}(\mathbf{k}_f,\mathbf{k}_i,T)}\right\} \approx 2n_s\frac{a_c}{2\pi\phi}\left[\cos^2\theta_i - \cos^2\theta_i'\right]k_i^2k_BT\lambda. \tag{160}$$

Using the 2-D formula $n_s = 2\pi/a_ck_F^2$ with $k_F = 0.25$ Å^{-1} [82] the data in Fig. 14 gives a value of $\lambda_{HAS} = 0.085$ at 720 K and $\lambda_{HAS} = 0.090$ at 420 K. This compares favorably with the value of $\lambda_{HAS} = 0.083$ obtained from other independent measurements of the temperature dependence shown in Table 2 and a recent measurement for bulk crystalline Cu of 0.093 [98].

A second interesting system for which experimental data has become available is the chalcogenide 1T-PtTe$_2$(0001 [154]. In this case the data consists of the diffuse elastic peak intensity as a function of incident angle from $\theta_i = 36.5°–34.5°$ in a configuration with a fixed angle of 90° between source and detector making for the specular position at $\theta_i = 45°$. The temperature was 100 K and incident energy was 83 meV ($k_i = 12.62$ Å^{-1}). For PtTe$_2$(0001) the work function is $\phi = 4.52$ eV [162] and with $n_s = 2$ these data, using Eq. (159) and ignoring the first term on the RHS, gives a value $\lambda_{HAS} = 0.46$, as shown in Table 5. This value is to be compared with a recent measurement of 0.92 [185].

6.6. *More on metals using energy-dependent specular intensities*

In addition to the system of Pb layers on a Cu(111) substrate discussed above in Sec. 6.3 there are three other systems for which λ_{HAS} can be determined from available measurements of the specular intensity as a function of incident energy. These are Mo (001), Nb(001) and small numbers of layers of fcc-Fe grown on a Cu(001) substrate. These, along with the relevant references to the source of experimental data are listed in Table 6. Following the approach used in Sections 6.3 and 6.4 the mass correction factor is determined from $\lambda_{HAS} = \pi\alpha/(2n_s)$ where $n_s = \pi\hbar^2\mathcal{N}(E_F)/(m_e^*a_c)$ and similar to Eq. (148) above

$$\alpha = \frac{\phi}{a_ck_BT}\frac{\Delta\ln[k_i^\gamma I(E_{iz},T)]}{\Delta[k_{iz}^2]}, \tag{161}$$

recalling that $\Delta\ln[k_i^\gamma I(E_{iz},T)]$ and $\Delta[k_{iz}^2]$ are the differences in the respective quantitatives at two different energies and k_i^γ is the factor that accounts for the energy-dependent correction for the incident beam flux.

The data for Mo (001) were taken at two distinct temperatures, 100 and 200 K, and for each case the incident beam energy range was from about 10 to 70 meV [212]. An evaluation of the effective layer number using parameters from the literature suggests that the optimum value is $n_s = 6$ which leads to $\lambda_{HAS} = 0.44$ at the lower temperature and $\lambda_{HAS} = 0.40$ at the higher temperature. This is to be compared with the accepted bulk value of 0.42 [99].

For Nb(001) [213] the temperature was 300 K and measurements over an energy range of 22–36 meV, and an analysis similar to that for Mo, lead to $n_s = 2$ and $\lambda_{HAS} = 0.89$. The standard bulk value for Nb is 1.12 [99].

A much more extensive set of data is available for multiple monolayers of iron deposited on a Cu(001) substrate [214]. Measurements were made only at ambient temperature ($T = 300$ K), but over an incident energy range from 25 to 57 meV and the monolayer number ranged from 1 to 16. Fe is known to initially deposit on Cu(001) with fcc ordering, while somewhere at or above 16 ML there is a transition to the native bcc structure. From this data, calculations of both α and λ_{HAS} using Eq. (161) with $n_s = 3$ are shown in Fig. 15 over the

Table 6
The e-ph coupling constant λ_{HAS} as determined from energy-dependent attenuation of He atom scattering intensities for some metal systems.

Surface	T [K]	E_i range [meV]	ϕ [eV]	n_s	λ_{HAS}	λ (other sources)
Mo (001) [212]	100	10–70	4.53 [78]	6	0.44	0.42 [99]
	200	23–73			0.40	
Nb(001) [213]	300	22–36	4.02 [78]	2	0.89	1.12 [99]
fcc-Fe/Cu(001) [214] 3–8 ML	300	25–57	4.67 [78]	3	0.35	0.34 [110]
Ru (0001) [128]	200	10–97	4.71 [78]	2	0.33	0.4 ± 0.1 [36] 0.45 [99]

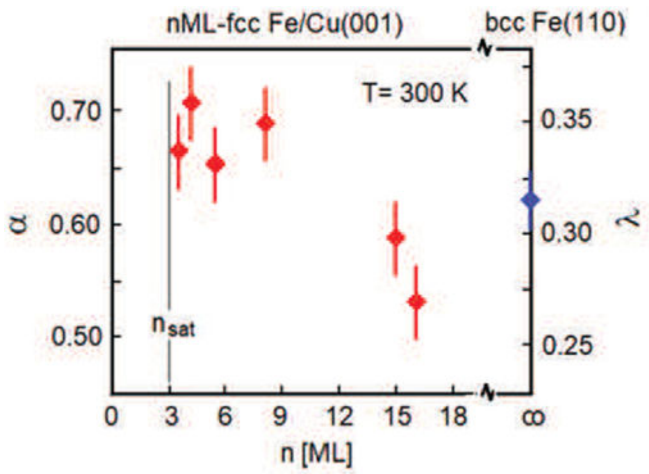

Fig. 15. Graph of λ (right scale) and α (left scale) as a function of monolayer number n for multiple layers of Fe on a Cu(001) substrate. The saturation layer number $n_s = 3$ is denoted by a vertical line. The phase transition from fcc structure at small layer number to bcc occurs at or just after $n = 16$. Data from Ref. [214].

range of 3–16 monolayers. For ML number less than 3 the data, as a function of deposition rate, does not give clearly distinct features from which α can be extracted, but for ML numbers of 3 or larger, a clear and distinct pattern emerges indicating that the saturation to the fcc structure occurs at $n_s = 3$. In Fig. 15 the calculations taking $n_s = n_{sat} = 3$ for both α (left scale) and λ_{HAS} (right scale) are shown for the measured data with ML numbers 3–8 as well as 15 and 16. The average of λ_{HAS} values over 3–8 ML is about 0.35 which favorably compares to the accepted calculated bulk value of 0.34 as determined from electrical resistivity [110]. At ML numbers of 15 and 16 there is a significant drop in the value of λ_{HAS} exhibited in Fig. 15 and this is surely the result of approaching the known phase transition from fcc to native bcc structure that occurs somewhere at or above ML number 16.

6.7. Graphite and graphene on metal substrates

There are three independent measurements of the temperature dependence of the specular peak for He atom scattering from graphite, and it is useful to compare these with a substantial number of measurements of single-layer graphene supported on various metal substrates. References to the measurements and values of λ_{HAS} extracted from these measurements appear in Table 7. Two different models have been used to calculate the values of λ_{HAS} appearing in Table 7. The first model is the form found in Eq. (153) and used for the systems discussed up to now, using the dimensionless number $n_s = 6$ as explained in the paragraph below. The second model is motivated by the fact that high energy optical phonon modes are known to contribute an important role in the value of the e-ph coupling constant for graphite and graphene. This second model is based on using an Einstein phonon distribution to represent the optical modes and is explained below.

In the case of graphene supported on metals there is a certain amount of charge transfer to and from the Dirac cones, depending on the relative difference between the work function of graphene and that of the substrate. The work function of self-standing graphene is 4.5 eV, smaller than those of the metal surfaces considered here [226]. Therefore they should all act as acceptors. ARPES data show, however, that Ir (111) (H. Vita et al.) [227], Pt (111) (P. Sutter et al.) [228], and Ni(111) (A. Alattis et al.) [229], act as acceptors with respect to graphene, whereas Ru (0001) (Katsiev et al.) [230], and Cu(111) (Walter et al.) [231] act as donors. Previous HAS studies have provided evidence that the tail of the substrate electron charge density, at least on Gr/Ru (0001), actually extends beyond the graphene [232]. Thus the substrate surface work function is adopted for use in Eq. (153), its role is to account for the steepness of the He-surface repulsive potential within the Wentzel-Karmers-Brillouin (WKB) approximation [46]. In either electron or hole doping each Dirac cone contributes a DOS at the Fermi level, $\mathcal{N}(E_F) = a_c k_F / \pi \hbar v_F$ [233], with k_F the Fermi wavevector referred to a K-point of the surface Brillouin zone (SBZ), and v_F the Fermi velocity. Identifying m_e^* with the cyclotron effective mass for doped graphene $m_e^* = \hbar k_F / v_F$ [234], gives $n_s = 1$ for a single Dirac cone. Only one third of a given cone is within the SBZ, but diametric electron transitions at the Fermi level connect points in neighboring SBZs, these are equivalent to umklapp transitions with **G** vectors in the ΓM directions between dif-

Table 7
The e-ph coupling constants λ_{HAS} obtained from atom scattering data for HOPG and single-layer graphene adsorbed on metal crystal substrates are shown in the columns marked as λ_{HAS} for the two calculational models. All measurements were done with ordinary HAS, except where otherwise noted in the first column. All values of λ_{HAS} for Gr/metals were derived using $n_s = 6$, and are calculated using the unit cell area a_c of the metal substrate. The column marked as "λ_{HAS}/substrate" gives the values determined for the clean metal substrate surface. (Values of other parameters showing no error indication are taken from the literature, where possible error sources are discussed [36,78,98,99,110,113].) A theoretical calculation by Park et al. produces a value of up to $\lambda = 0.21$ for single-layer free-standing graphene, depending on doping level [215].

Surface	T [K]	E_i [meV]	ϕ [eV]	α	λ_{HAS} Eq. (153)	λ_{HAS} Eq. (162)	λ_{HAS} substrate	λ (substrate bulk values)
C (0001)	150-400 [129,216]	63	4.5 [223]	1.70	0.41	0.12		0.70 ± 0.08 [224]
	250-360 [217]	69		1.41	0.37	0.12		0.034–0.28 [215]
	400-500 [217]	69		0.76	0.20	0.09		$\leq$0.20 [225]
	300-360 [220]	63		1.76	0.46	0.16		
Gr/Ni(111)	200-400 [129,218]	66	5.35 [78]	0.71	0.19	0.06	0.56	0.3, 0.7 [110]
(^{3}He atoms)	200-700 [219]	8		0.69	0.16	0.08	0.36	
(Neon atoms)	100-200 [218]	66		0.58	0.16	(0.3)		
Gr/Ru (0001)	300-400 [220]	67	4.71 [78]	0.44	0.14	0.05	0.44	0.45 [99]
	200-600 [221]	32		0.38	0.15	0.06	0.33	0.4 [36]
(Neon atoms)	90-150 [128]	43		0.58	0.18	(0.02)	0.39	
Gr/Ir (111)	100-500 [129]	17.5	5.76 [78]	1.88	0.54	0.17	0.30	0.41 [110], 0.34 [113] 0.50 [99]
Gr/Rh (111)	150-450 [222]	19.3	4.98 [78]	1.65	0.43	0.14		0.41, 0.51 [110]
		63		1.16	0.31	0.10		
Gr/Pt (111)	300-400 [220]	67	5.70 [78]	1.53	0.54	0.20		0.66 [110]
Gr/Cu(111)	100-300 [129]	28	4.98 [78]	2.56	0.69	0.22	0.083	0.093 [98],0.13 [99] 0.1 [36]

ferent cone thirds inside the SBZ (umklapp intervalley transitions). With the inclusion of such transitions, $n_s = 6$ is the appropriate value.

Note that these transitions couple to phonons near the zone center and give a rather small contribution to λ. A thorough ARPES study by Fedorov et al. of graphene on Au (111), doped with alkali and Ca donor impurities, and electron concentrations ranging from $2 \cdot 10^{14}$ (for Cs) to $5 \cdot 10^{14}$ electrons/cm^2 (for Ca), shows that the largest contribution to λ is due to phonons near the zone boundaries KMK' [235]. The derived Eliashberg function, which gives the e-ph-weighed phonon DOS projected onto the impurity coordinates exhibits resonances with graphene phonons whose wavevectors arguably correspond to good Fermi surface nestings. The fact that the separation between the ZA and the optical phonon peaks increases with doping from that for Cs, near the K-point, to the one at smaller wavevectors for the largest Ca doping suggests that the e-ph coupling is mostly due to KK' intervalley transitions, either direct along the six edges (thus counting 3) or umklapp along the three long diagonals. First principle calculations by Park et al. appear to confirm the role of these transitions [215]. This is the intervalley e-ph coupling mechanism introduced by Kelly and Falicov in the 1970s for charge density wave transitions in semiconductor surface inversion layers [188–190]. In this case $n_s = 6$ enumerates the different nesting conditions that contribute to the e-ph coupling strength λ, and is adopted here for both graphene and graphite, independently of whether they are electron- or hole-doped.

In addition to the work of Federof et al. discussed above [235], Calandra and Mauri have shown that three optical branches with relatively large energy of around 160 meV, located at the **Q** points of the Dirac cones, make the major contributions to the total e-ph interaction in supported graphene [236]. This agrees with the Eliashberg function for quasi-free standing K-doped graphene on Au reported by Haberer et al. from an ARPES analysis [237], which is concentrated in the optical region between 150 and 200 meV in both the $\overline{\Gamma}\,\overline{K}$ and $\overline{K}\,\overline{M}$ directions (in the latter case with minor contributions from the acoustic modes). Since all available HAS measurements have been carried out with values of k_BT well beneath the optical phonon energies, Eq. (153) should be rewritten in a form that includes full temperature dependence, which can be done upon assuming that all the optical modes are of the same frequency ω_0. Starting from Eq. (128) the result is expressed in a form quite similar to Eq. (153), but with a different definition for α

$$\lambda_{HAS} = \frac{\pi}{2n_s}\alpha\,; \quad \alpha \equiv \frac{\phi\ \ln[I_0/I(T)]}{a_c k_{iz}^2 \hbar\omega_0 \left\{ n_{BE}(\omega_0, T) + \frac{1}{2} \right\}}\,. \tag{162}$$

In the high temperature limit Eq. (162) coincides with Eq. (153), while in the low temperature limit $k_BT \ll \hbar\omega_0$ it is again independent of T and given by

$$\lambda_{HAS} = \frac{\pi}{n_s} \frac{\phi\ \ln[I_0/I(0)]}{a_c k_{iz}^2 \hbar\omega_0}\,. \tag{163}$$

Since $k_BT < \hbar\omega_0$ the above will give values of λ_{HAS} that are smaller than that of Eq. (153). Note, however, that the density of states $\mathcal{N}(E_F)$ is unaffected by this Einstein mode approximation, thus the appropriate choice remains $n_s = 6$.

The high temperature harmonic approximation for λ_{HAS} of Eq. (153) is valid when the average phonon energy sampled by the e-ph interaction is smaller than k_BT over the temperatures at which the D-W exponent is measured. In general this condition is met for soft materials such as simple metals. On the other hand, one could call hard materials those for which high energy optical phonons are the dominant contributors to the e-ph interaction. Representative of such hard materials are the supported graphene systems considered here, and the single optical frequency approximation of Eqs. (162) and (163) is more appropriate.

A value of 160 meV will be used for ω_0, as calculated by Calandra and Mauri for the optical modes of supported graphene around the K-point of the surface Brillouin zone, i.e., the ones which mostly sustain multivalley coupling [236]. The high-T approximation of Eq. (153), currently used in the analysis of soft materials, probably implies a substantial overestimation of λ_{HAS}, whereas the Einstein approximation of Eq. (163) for hard materials at comparatively low temperature should produce better agreement with the existing estimations of λ from various other methods.

6.7.1. Graphite

First graphite will be discussed and afterwards we compare with single-layer graphene supported on ordered metal substrates. Clean graphite C (0001) presents a weakly corrugated surface potential to He atom scattering which means that the specular peak is the dominant elastic scattering feature. The thermal attenuation of C (0001) has been measured by three independent groups over temperatures ranging from below 150 K–500 K [129,216,217,220]. As is apparent from the graphs of the D-W exponent in Fig. 16a), measured for graphite as a function of T by Oh et al. [216] and by Vollmer [217], the slope is essentially linear at lower temperature up to about 350 K. The slopes of the different measurements, and using $n_s = 6$, provide the values of λ_{HAS} listed in Table 7 together with the input parameters and the respective references. The average over the available data for graphite calculated from the high temperature formula of Eq. (153) is $\lambda_{HAS} = 0.36 \pm 0.09$ (0.41 ± 0.04 below 400 K) or, from Eq. (162) (Einstein model at the average experimental temperature) $\lambda_{HAS} = 0.12 \pm 0.03$ (0.13 ± 0.02 below 400 K). In general, the experimental error indicated comes from the slopes of the D-W plots, because uncertainties in other parameters extracted from the literature are not always given. Our estimation is that the overall uncertainty on λ_{HAS} is around 15% or less.

As is evident in Fig. 16a), for graphite above 400 K the slope of $2W(T)$ clearly decreases, apparently tending to a value about a factor of roughly 2 smaller at high temperature, and λ_{HAS} takes the values 0.20 from Eqs. (153) and (0.09) from Eq. (162). With the high-T formula the reduction with respect to data below 400 K is by a factor 2, while with the Einstein model the reduction is about 40%. Thus the slope reduction at higher temperature is not due entirely

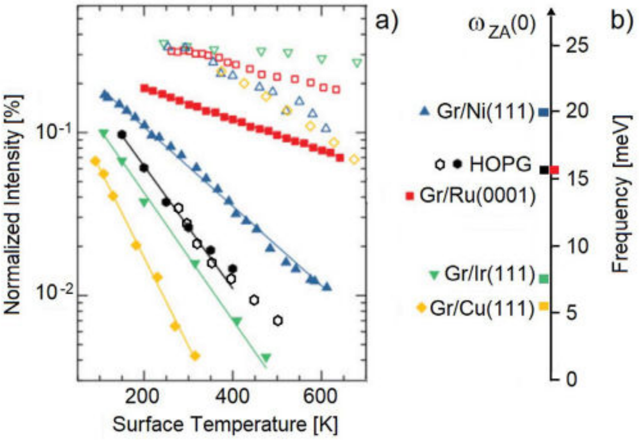

Fig. 16. a) The normalized specular HAS intensity in log scale (proportional to the D-W exponent) as a function of temperature for several systems of single-layer graphene supported on metal substrates (full symbols, defined in panel b)), together with similar data for the clean metals (open symbols). Also shown are the data for highly oriented pyrolytic graphite (HOPG) at low (full hexagons [129]) and high temperature (open hexagons [217]). b) The ZA mode frequency at $\mathbf{Q} = 0$ for HOPG and all the Gr/metal systems shown in panel b). The data are from Ref. [129] with some adjustment as explained in the text.

to the different approximations, but is to a large extent an intrinsic effect. This behavior is probably the consequence of the gradual transition of graphite from negative to positive in-plane thermal expansion, occurring at ∼500 K [238,239]. A bond contraction, such as that produced by an external pressure, generally yields a larger λ, while a dilation implies a smaller λ. This may explain the transition with temperature from a larger to a smaller λ_{HAS} observed in graphite. Interestingly, this is not observed in graphene, where the in-plane thermal expansion is predicted to remain negative up to a considerably larger temperature, well above the temperature range considered up to the present in HAS experiments [240].

This behavior of two different slopes of the D-W exponent observed in graphite, i.e., a steep slope at low temperatures and a less steep slope at high temperatures, is not seen in any of the supported graphene systems discussed below in the next Section. It is also seen from the last column in Table 7 that there is a rather large range of reported values of λ for bulk graphite, so that the values of λ_{HAS} at the surface as measured by He atom scattering are well within the range of reported bulk values.

6.7.2. Graphene supported on ordered metals

Shown in Table 7 are all of the systems of single layer graphene supported on close-packed metal surfaces for which D-W plots of the specular diffraction peak have been measured. For two of these systems, Gr/Ni(111) and Gr/Ru (0001), measurements were made with both He and Ne atom scattering. For Gr/Ni(111), in addition to experiments done with He and Ne atoms, measurements were taken at very low incident energy using the ^{3}He isotope in spin-echo spectrometry.

For all these experiments, atom diffraction and diffuse elastic scattering measurements were also carried out and these provide accurate control of the surface long-range order and defect concentrations which ensures the high quality of the graphene-substrate interface. The input parameters needed for evaluating λ_{HAS} are given in Table 7 together with the relevant references. For several of the clean metals the bulk value of λ_{HAS} has also been independently determined and those values appear in the next-to-last column. As stated previously for the case of graphite, the final column gives values from other sources for the e-ph constant λ of the pure bulk metal.

Two different calculations for each of the Gr/metal systems for λ_{HAS} are shown in Table 7. These are the two columns marked λ_{HAS}/Eq. (153) and λ_{HAS}/Eq. (162). As denoted by the equation numbers, these calculations were carried out similarly to those explained above in Sec. 6.7.1, using $n_s = 6$ and, for Eq. (162) with $\hbar\omega_0 = 160$ meV as suggested by the Calandra and Mauri work [236]. The values for the Einstein optical mode model of Eq. (162) are smaller, around one-third to one-half those of the corresponding calculation using the high temperature limit of Eq. (153).

There is a significant amount of spread in the reported values for the bulk metals, but the values of λ_{HAS} derived here for Gr/metals compare favorably, particularly for values calculated with the high temperature limit equation. It should also be noted that those values of λ_{HAS} are quite similar regardless of whether the projectile is He or Ne. The value 0.16 obtained for Gr/Ni(111) using Ne atoms or very low energy (8 meV) ^{3}He atoms with the spin-echo detection technique is close to that of ^{4}He at the much larger energy of 66 meV which is 0.19. In the two cases where data is available for Ne scattering, namely Gr/Ni(111) and Gr/Ru (0001), the calculated values using the Einstein model are placed in parenthesis. This is because the Einstein model is probably not as valid because the heavy Ne projectiles are expected to excite a larger range of phonons than the lighter He atom projectiles.

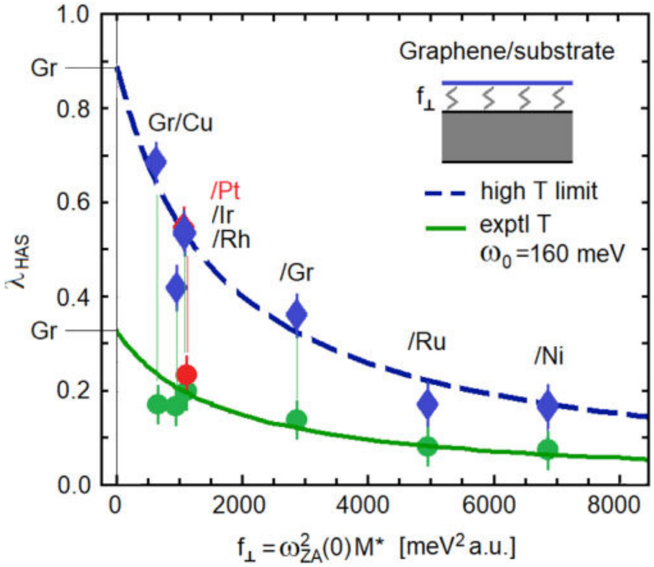

Fig. 17. The electron-phonon coupling constant λ_{HAS} plotted as a function of the ZA mode spring constant $f_\perp$ coupling graphene to the substrate. The data are from Ref. [241], with some adjustment; see discussion in the text. The upper dashed-line fitting curve with diamond-shaped data points, as explained in the text, allows the extrapolation of the value $\lambda = 0.89 \pm 0.04$ using the high temperature limit of Eq. (153) for ideally flat free-standing graphene (error bar calculated from the mean-square relative deviation from the fitting curve). Similarly, the lower solid-line curve with circular data points is the result of the Einstein mode approximation of Eq. (162) with $\omega_0 = 160$ meV using the average experimental temperatures and which predicts the value of $\lambda = 0.32 \pm 0.09$ for free standing graphene.

It is of interest to compare the values of λ_{HAS} calculated here with the bonding strength of the graphene to these metals. The Gr/metal bonding strength is usually judged by the Gr-metal separation distance, and the systems that have been investigated fall into two different categories, strongly bonded whose separation distance is 2.5 Å or less, and weakly bonded with a separation distance greater than 3 Å. Among the latter are the close packed surfaces of Ag, Au, Cu, Pt and Ir, while the former examples include Pd, Rh, Ru, Ni, Co and Re [241]. Another way of evaluating bonding strengths is by comparing the frequencies $\omega_{ZA}(0)$ of the shear vertical ZA mode at the zone center where the parallel wavevector is $\mathbf{Q} = 0$. At long wavelengths the ZA mode is nearly dispersionless as a function of $\mathbf{Q}$ for small $\mathbf{Q}$ and acts like an Einstein mode with a spring constant $f_\perp = M^*\omega^2_{ZA}(0)$ where $M^* = 2M_CM_S/(2M_C + M_S)$ is the effective mass, M_C the carbon mass and M_S is the mass of the substrate atom. For graphite M_S coincides with the planar unit cell mass $2M_C$ and therefore $M^* = M_C$. Fig. 17 shows λ_{HAS} plotted as a function of the interplanar force constant $f_\perp$ for both of the two different λ_{HAS} calculations. Values of $\omega_{ZA}(0)$ measured by HAS are taken from Refs. [129,241], except for that of Gr/Pt (111) which is extrapolated from the Politano et al. high resolution electron energy loss spectroscopy (HREELS) data [242].

Fig. 17 shows a clear and intriguing correlation between λ_{HAS} and the graphene-substrate interaction: the weaker the bonding, the stronger is the e-ph coupling in graphene. This may be qualitatively understood by considering that a stronger interaction with the substrate implies a substantial reduction of the vertical mean square displacement, and possibly also some localization of graphene free electrons.

Some reservations are called for concerning two of the values of $\omega_{ZA}(0)$ for the ZA mode that have been reported in the literature. In the case of Gr/Ru (0001) two widely different values of 16 and 27 meV have been reported [232,241,243]. The value of 27 meV measured with HREELS [243] appears to be incorrectly assigned and corresponds to the optical mode S_2 seen on the clean Ru (0001) surface

[244,245]. A more detailed discussion appears in Ref. [246]. In Fig. 17 the value $\omega_{ZA}(0) = 16$ meV is the one that is used.

The second reported value of $\omega_{ZA}(0)$ that needs to be discussed is that of Gr/Rh (111) for which a value of 7 meV has been reported [222]. This would appear to be too small when compared with the other strongly bound Gr/metal systems such as Gr/Ni and Gr/Ru where the value is rather in the range of 16–20 meV. Other systems that have been measured with HAS, for example for Gr/Ru (0001) and Gr/Ni(111), show that there are a variety of other modes and features that can produce peaks in the energy-resolved spectra at energies below 10 meV, including backfolding of the Rayleigh mode due to the super-periodicity of the moiré patterns induced on these strong binding graphene layers [221,232]. Regardless of this caveat about $\omega_{ZA}(0)$ for Gr/Rh (111), the value of 7 meV has been used, and the corresponding value for $f_{\perp} = 954\,\mathrm{meV}^2 a.u.$ is not far from fitting into the observed λ_{HAS} vs. $f_{\perp}$ correlations in the two curves shown in Fig. 17.

The largest contributions to the charge density oscillations detected by HAS come from the phonon shear-vertical (SV) mean square displacements of surface atoms, and these are inversely proportional in self-standing graphene to an effective shear-vertical force constant F (equal to 1908 meV^2 a. u. from the analysis of Gr/Ru (0001) HAS data [232]). Thus it is reasonable to suggest that λ for the supported graphene is inversely proportional to $F + f_{\perp}$ and scales as $\lambda_{Gr}/(1 + f_{\perp}/F)$, with λ_{Gr} (which is the value of λ_{HAS} for self-standing graphene) and F as fitting parameters. The best fit is obtained with $F = 1650\,\mathrm{meV}^2$ a. u., which is indeed quite close to the above value from the previous HAS study on Gr/Ru (0001), and $\lambda_{Gr} = 0.32$ and 0.89 from the experimental temperature with the Einstein model of Eq. (162) and in the high-T limit of Eq. (153), respectively (see Fig. 17). Since graphene is a diatomic lattice with two equal masses in the unit cell, the dispersion curve of the SV modes (as well as the shear-horizontal (SH) ones) has a gapless folding point at the K-point of the acoustic into the optic branch with a single effective SV force constant. Thus the change from F to $F + f_{\perp}$ caused by the substrate equally affects both the acoustic and optical branches, producing a sizeable effect on λ_{HAS}.

Although the two different approximations of Eqs. (153) and (162) produce different values for λ_{HAS} when projected to the limit of unsupported graphene, the similar nature of the two curves exhibited in Fig. 17 shows that such calculations produce predictions of the behavior of λ_{HAS} as a function of experimentally controllable parameters. In this case the controllable parameter is the bonding strength to the metal substrate. Predicting the behavior of the e-ph constant as a function of experimentally variable parameters is important and demonstrates the usefulness of the type of HAS experimental observations discussed here.

Thus determinations of λ such as those discussed here would be useful for comparing different systems and, within a given Gr-substrate system, comparing the effects of doping or other ways to alter the surface electron density. Another class of experiments would be to measure double and multiple layer supported graphene, and in particular it would be important to measure λ for twisted bilayer graphene (tBLG) which can be superconducting for specific twist angles [247–250], as well as measurements on the class of layered transition-metal chalcogenides which exhibit 2-D superconductivity (see, e.g., the recent work by Trainer et al. [251] and the HAS study of 2H–MoS_2 [151]). Also of interest would be to verify the prediction for free-standing graphene by carrying out He atom scattering experiments on unsupported graphene.

7. Inelastic close coupling formalism

In the electron-phonon approach developed here, the effective vibrational displacements encountered by a colliding atomic projectile are expressed in terms of the vibrational amplitudes of the target core atoms, and an explicit form is presented in Eq. (105). The classical limit of this effective displacement function is discussed in connection with Eq. (C.6) of Appendix C. Having expressions for the displacement experienced by the colliding projectile is very useful for many applications in surface physics, and one important application is the close coupling formalism for calculating elastic and inelastic scattering. The close coupling formalism was originally developed for gas phase molecular scattering problems [252], but shortly afterwards was extended to the case of elastic (diffractive) scattering of atoms from ordered periodic surfaces [253], and has received wide acceptance as a method of choice for obtaining exact results [254,254c]. More recently it has been extended to include inelastic scattering via phonons and is called the inelastic close coupling formalism (ICC) [255]. An advantage of the coupled channels formalism is that it leads to numerically exact results for a specified interaction potential. In this section we show how the classical form of the phonon displacement vector developed here is particularly suited to inelastic coupled channels calculations.

7.1. Basic principles

The starting point for the coupled channels formalism is the time-dependent Schrödinger equation for a particle scattering from a crystal surface, which is generated from the Hamiltonian of Eq. (37)

$$i\hbar\frac{\partial\Psi(\mathbf{r},t)}{\partial t} = \frac{-\hbar^2}{2m}\nabla^2\Psi(\mathbf{r},t) + V(\mathbf{r},t)\Psi(\mathbf{r},t). \tag{164}$$

The gas-surface interaction potential is assumed to have the form $V(\mathbf{r},t) = V(\mathbf{r} + \mathbf{u}(\mathbf{R},t))$ and is dependent on time through the instantaneous displacement from equilibrium $\mathbf{u}(\mathbf{R},t)$. In the present electron-phonon interaction formalism, $\mathbf{u}(\mathbf{R},t)$ is given by the effective vibrational displacement as for example discussed in Appendix C in connection with Eq. (C.6). The displacements are small compared to the lattice constant and the potential can be expanded in a Taylor series as

$$V(\mathbf{r},t) \approx V(\mathbf{r}) + \mathbf{u}(\mathbf{R},t)\cdot\nabla V(\mathbf{r}) + \dots . \tag{165}$$

It is of interest to note that Eq. (165) is sometimes called a single-phonon approximation because when coupled with a lowest-order quantum mechanical Born approximation the first order expansion term gives rise to inelastic exchanges of a single phonon while the next order expansion of Eq. (165), which is quadratic in the displacement, contributes to two-phonon inelastic transfers. However, it was shown long ago that in the Born approximation the two-phonon contribution to the intensity produced by the quatratic term in Eq. (165) is negligible in comparison to that of the single phonon [256,257]. In fact, the dominant two-phonon contributions come from the second order Born approximation to the perturbation series, using only the first order expansion of the potential shown in Eq. (165) [258–260]. This is an important distinction because it means that using only the first order expansion of Eq. (165) the inelastic coupled channels formalism can be accurately extended to the evaluation of multiple phonon transfers.

Due to the periodicity of the surface lattice, $V(\mathbf{r})$, can be expanded in a Fourier series as

$$V(\mathbf{r}) = \sum_{\mathbf{G}} V_{\mathbf{G}}(z)\, e^{i\mathbf{G}.\mathbf{R}}. \tag{166}$$

In order to obtain a tractable numerical solution to the Schrödinger equation the surface vibrational displacement must be expressed classically, and as mentioned above for a continuous surface evaluated within the electron-phonon coupling approach its α-th cartesian component is given by Eq. (C.7)

$$u_\alpha^{eff}(t) = 4\sqrt{\frac{k_B T}{\hbar\omega(\mathbf{Q},\nu)}}\sum_{\mathbf{Q},\nu}\left[\sum_{\mathbf{K},n}|C_\alpha(\mathbf{K},n,\mathbf{Q})|^2\right]^{1/2} \times\ e^{i\mathbf{Q}\cdot\mathbf{R}}\cos(\omega(\mathbf{Q},\nu)t)\ , \tag{167}$$

where the electron-phonon function $C_\alpha(\mathbf{K},n,\mathbf{Q})$ is defined in Eq. (102). We write the displacement in shortened notation as

$$\mathbf{u}^{eff}(\mathbf{R},t;T) = \sum_{\mathbf{Q},\nu}\mathbf{A}^{eff}(\mathbf{Q},\nu;T)\,e^{i\mathbf{Q}\cdot\mathbf{R}}\cos\left[\omega(\mathbf{Q},\nu)\ t\right], \tag{168}$$

where the effective vector amplitude $\mathbf{A}^{eff}$ collects all the prefactors involving the electron-phonon coupling.

As expressed in the Bloch and Floquet theorems, the periodicity of the interaction potential allows the wave function to be expanded as

$$\Psi(\mathbf{r},t) = e^{-iE_i t/\hbar}\sum_{\mathbf{G},\mathbf{Q},\nu,n_{\mathbf{Q},\nu}}\Psi_{\mathbf{G}+\mathbf{Q},n_{\mathbf{Q},\nu}}(z)\,e^{i(\mathbf{K}_i+\mathbf{G}+\mathbf{Q})\cdot\mathbf{R}}\,e^{-in_{\mathbf{Q},\nu}\omega(\mathbf{Q},\nu)t}, \tag{169}$$

where E_i is the incident energy of the projectile and $n_{\mathbf{Q},\nu}$ stands for the number of phonons of the phonon mode $(\mathbf{Q},\nu)$.

Substituting Eq. (169) into the Schrödinger equation of Eq. (164), together with subsequent Fourier transformation in both space and time leads to the following set of coupled differential equations for the scattered waves

$$\begin{aligned}&\left[\frac{\hbar^2}{2\ m}\frac{d^2}{dz^2} + \frac{\hbar^2}{2\ m}\mathbf{k}^2_{\mathbf{G}+\mathbf{Q},n_{\mathbf{Q},\nu},z} - V_\mathbf{0}(z)\right]\Psi_{\mathbf{G}+\mathbf{Q},n_{\mathbf{Q},\nu}}(z)\\ &= \sum_{\nu'}\sum_{\mathbf{Q}'}\sum_{n_{\mathbf{Q}',\nu'}}\sum_{\mathbf{G}'\neq\mathbf{G}}V_{\mathbf{G}-\mathbf{G}'}(z)\,\Psi_{\mathbf{G}'+\mathbf{Q}',n_{\mathbf{Q}',\nu'}}(z)\\ &\quad+\frac{1}{2}\sum_{\nu'}\sum_{\mathbf{Q}'}\sum_{n_{\mathbf{Q}',\nu'}}\mathbf{A}^{eff}(\mathbf{Q}',\nu';T)\\ &\quad\cdot\sum_{\mathbf{G}'}\left[\mathbf{D}_{\mathbf{G}-\mathbf{G}'-\mathbf{Q}'}(z)+\mathbf{D}_{\mathbf{G}-\mathbf{G}'+\mathbf{Q}'}(z)\right]\\ &\quad\times\left[\Psi_{\mathbf{G}+\mathbf{Q}',n_{\mathbf{Q}',\nu'}+1}(z)+\Psi_{\mathbf{G}+\mathbf{Q}',n_{\mathbf{Q}',\nu'}-1}(z)\right],\end{aligned} \tag{170}$$

and

$$\begin{aligned}&\left[\frac{\hbar^2}{2\ m}\frac{d^2}{dz^2} + \frac{\hbar^2}{2\ m}\mathbf{k}^2_{\mathbf{G}+\mathbf{Q},n_{\mathbf{Q},\nu}+1,z} - V_\mathbf{0}(z)\right]\Psi_{\mathbf{G}+\mathbf{Q},n_{\mathbf{Q},\nu}+1}(z)\\ &= \sum_{\nu'}\sum_{\mathbf{Q}'}\sum_{n_{\mathbf{Q}',\nu'}}\sum_{\mathbf{G}'\neq\mathbf{G}}V_{\mathbf{G}-\mathbf{G}'}(z)\,\Psi_{\mathbf{G}'+\mathbf{Q}',n_{\mathbf{Q}',\nu'}+1}(z)\\ &\quad+\frac{1}{2}\sum_{\nu'}\sum_{\mathbf{Q}'}\sum_{n_{\mathbf{Q}',\nu'}}\mathbf{A}^{eff}(\mathbf{Q}',\nu';T)\\ &\quad\cdot\sum_{\mathbf{G}'}\left[\mathbf{D}_{\mathbf{G}-\mathbf{G}'-\mathbf{Q}'}(z)+\mathbf{D}_{\mathbf{G}-\mathbf{G}'+\mathbf{Q}'}(z)\right]\\ &\quad\times\left[\Psi_{\mathbf{G}+\mathbf{Q}',n_{\mathbf{Q}',\nu'}+2}(z)+\Psi_{\mathbf{G}+\mathbf{Q}',n_{\mathbf{Q}',\nu'}}(z)\right],\end{aligned} \tag{171}$$

where the perpendicular wave vector is determined from

$$\mathbf{k}^2_{\mathbf{G}+\mathbf{Q},n_{\mathbf{Q},\nu},z} = \mathbf{k}_i^2 - (\mathbf{K}_i+\mathbf{G}+\mathbf{Q})^2 - \frac{2\ m}{\hbar}n_{\mathbf{Q},\nu}\omega(\mathbf{Q},\nu)\ , \tag{172}$$

and $\hbar^2\mathbf{k}^2_{\mathbf{G}+\mathbf{Q},n_{\mathbf{Q},\nu},z}/2m$ is the kinetic energy associated with motion in the z-direction for the $\Psi_{\mathbf{G}+\mathbf{Q},n_{\mathbf{Q},\nu}}(z)$ scattered wave. The vector

$$\mathbf{D}_{\mathbf{G}-\mathbf{G}'\pm\mathbf{Q}'}(z) \equiv \left[i(\mathbf{G}-\mathbf{G}'\pm\mathbf{Q}')V_{\mathbf{G}-\mathbf{G}'\pm\mathbf{Q}'}(z), V'_{\mathbf{G}-\mathbf{G}'\pm\mathbf{Q}'}(z)\right]\ , \tag{173}$$

shown here in cartesian components is the contribution of the gradient of the interaction potential.

The coupled channels formalism gets its name from the set of staircase coupled differential equations of Eqs. (170) and (171). Within this scheme, each inelastic diffraction channel is represented by an equation with an effective potential consisting of $V_\mathbf{0}(z)$ plus the asymptotic energy, given by $\hbar^2(\mathbf{K}_i+\mathbf{G}+\mathbf{Q})^2/2m - n_{\mathbf{Q},\nu}\hbar\omega(\mathbf{Q},\nu)$. Each inelastic excitation, either annihilation or creation, is represented by one of these channels. It is usual to describe these as channels dressed by the phonon field. The number of channels dressed by a given number of phonons forms a block, called a Floquet block. Double phonon excitation and higher order multiple phonon contributions of the same active mode are taken into account by including more Floquet blocks, i.e., those dressed by two or three or more phonons, by creating a staircase structure of Eqs. (170) and (171) through terms of order $n_{\mathbf{Q}_\nu} \pm 1$. Furthermore, two coupling terms of very different nature are now present: $V_{\mathbf{G}-\mathbf{G}'}(z)$ is responsible for the intrablock coupling, and the scalar contraction $\mathbf{A}^{eff}(\mathbf{Q},\nu;T)\cdot\mathbf{D}_{\mathbf{G}-\mathbf{G}'\mp\mathbf{Q}'}(z)$ for the interblock coupling. It is the latter which is responsible for the thermal attenuation of the elastic diffraction intensities. In many other approaches, as for example presented in Sec. 3 above, the thermal attenuation is expressed by a Debye-Waller factor. However, this coupled channels approach, which is approximate in the sense that the continuous variables $\mathbf{Q}$ and $\omega(\mathbf{Q},\nu)$ are discretized and the number of phonons excited is limited, gives a unitary result that is numerically exact. This means that, within the constraint of the finite number of phonons allowed, it automatically calculates the thermal attenuation due to those phonons.

The coupled channels equations are solved by invoking the usual boundary conditions for the diffracted beams, i.e., the wave function must vanish deep inside the surface, while in the asymptotic region outside the surface it must act as a linear combination of plane waves:

$$\begin{aligned}&\text{for}\quad z\to-\infty\\ &\psi_{\mathbf{G}+\mathbf{Q},n_{\mathbf{Q},\nu}}(z)\to 0\\ &\text{for}\quad z\to+\infty\\ &\psi_{\mathbf{G}+\mathbf{Q},n_{\mathbf{Q},\nu}}(z)\to\begin{cases}k_z^{-1/2}e^{-ik_z z}\,\delta_{\mathbf{G},\mathbf{0}} + k^{-1/2}_{\mathbf{G}+\mathbf{Q},n_{\mathbf{Q},\nu},z}\,S_{\mathbf{G}+\mathbf{Q},n_{\mathbf{Q},\nu}}\,e^{ik_{\mathbf{G}+\mathbf{Q},n_{\mathbf{Q},\nu},z}z} & \text{if } \mathbf{K}^2_{\mathbf{G}+\mathbf{Q},n_{\mathbf{Q},\nu},z}>0,\\ \kappa^{-1/2}_{\mathbf{G}+\mathbf{Q},n_{\mathbf{Q},\nu},z}\,S_{\mathbf{G}+\mathbf{Q},n_{\mathbf{Q},\nu}}\,e^{-\kappa_{\mathbf{G}+\mathbf{Q},n_{\mathbf{Q},\nu},z}z} & \text{if } \mathbf{K}^2_{\mathbf{G}+\mathbf{Q},n_{\mathbf{Q},\nu},z}<0,\end{cases}\end{aligned} \tag{174}$$

where to handle the case of evanescent waves for which $\mathbf{k}^2_{\mathbf{G}+\mathbf{Q},n_{\mathbf{Q},\nu},z} < 0$ we use the notation $\kappa_{\mathbf{G}+\mathbf{Q},n_{\mathbf{Q},\nu},z} = +\sqrt{-\mathbf{k}^2_{\mathbf{G}+\mathbf{Q},n_{\mathbf{Q},\nu},z}}$ and must choose the positive value of the square root.

There is one equation for each channel considered, and each channel is labeled by its value of reciprocal lattice vectdor $\mathbf{G}$, phonon parallel wave vector $\mathbf{Q}$, phonon frequency value ν and number of multiple phonon excitations $n_{\mathbf{Q},\nu}$. This means that the total number $\mathcal{N}$ of channels to be considered is the product of the numbers of each of these four categories.

The coupled channels formalism is not an initial value solution to the Schrödinger equation, such as the case for the distorted wave Born approximation discussed above in Sec. 3. Instead, it is a complete boundary value solution, meaning that when it is completely solved it can produce solutions corresponding to all possible physical boundary conditions. The implication of this is that the whole set of Eqs. (170) and (171) typically must be solved $\mathcal{N}$ times, each with slightly different initial conditions, where $\mathcal{N}$ includes a number of evanescent channels sufficient to assure numerical convergence. Then, from these $\mathcal{N}^2$ solutions a linear combination is formed to match the desired boundary conditions, which for the typical experiment requires that in the asymptotic region the solution must consist of a single incoming plane wave and all other waves are outgoing. For this reason the computation time normally scales as $\mathcal{N}^3$, although for the purely elastic case involving only diffraction some numerical schemes have been reported that scale at a somewhat slower rate with $\mathcal{N}$ [261]. In spite of the seemingly unfavorable scaling rate with $\mathcal{N}$, nowadays CC calculations with large $\mathcal{N}$ are not computationally prohibitive due to the fact that computer power has increased immensely.

It is also of interest to note that the coupled channel method determines far more information than any typical experiment ever measures. For example, most experiments that measure energy resolved spectra are limited to a geometry in which the detector direction lies within the scattering plane, i.e., the plane defined by the incident beam and the surface normal. Furthermore, most such experimental set-ups are restrained to geometry in which the incident beam and detector direction are at fixed angles with respect to each other, this angle being called the source-detector angle θ_{SD}. For such experiments, the energy and parallel momentum conservation laws for single phonon excitation are

$$\Delta E = E_f - E_i = \hbar\omega(Q, \nu) \ , \tag{175}$$

and

$$K_f - K_i = Q + G \ . \tag{176}$$

Combining these two conservation equations leads to a parabolic relationship between $\omega(Q, \nu)$ and Q called the scan curve, given by

$$\Delta E = \hbar\omega(Q, \nu) \ = \ E_i \left\{ \frac{\left[\sin(\theta_i) + \frac{Q+G}{k_i}\right]^2}{\sin^2(\theta_f)} - 1 \right\} \ . \tag{177}$$

This shows that for a given incident angle $\theta_i \ = \ \theta_{SD} \ - \ \theta_f$ the experiment measures only those single phonon excitations with frequencies and wave vectors related by the scan curve parabola. This is only a small subset of the complete spectrum generated by a coupled channels calculation for the same given incident angle.

7.2. Decoupling of phonon modes

Because of the large number $\mathcal{N}$ of channels, and particularly because of the high scaling rate of computer time with $\mathcal{N}$, the solution of the complete inelastic coupled channels problem of Eqs. (170) and (171), even with a coarsely discretized set of frequencies and **Q** values risks becoming computationally prohibitive. An approximation that has been carried out computationally, and that produces physically reasonable results is to ignore quantum interference between multiple phonon excitations by considering only one single phonon excitation at a time, i.e., consider only a single phonon frequency and wave vector $\omega(\mathbf{Q}, \nu)$ with each set of solutions, and this phonon is called the active mode. This decoupling approximation is justified by the fact that in a harmonic crystal there is no interference between different phonon modes. For calculations that have been carried out thus far, only a single given **Q**-vector value is assumed to occur [255]. In this active mode approximation the set of Eqs. (170) and (171) reduce to the following:

$$\begin{aligned}
&\left[\frac{\hbar^2}{2\ m}\frac{d^2}{dz^2} \ + \ \frac{\hbar^2}{2\ m}\mathbf{k}^2_{\mathbf{G}+\mathbf{Q},n_{\mathbf{Q},\nu},z} - V_{\mathbf{0}}(z)\right]\Psi_{\mathbf{G}+\mathbf{Q},n_{\mathbf{Q},\nu}}(z)\\
&= \sum_{\mathbf{G}'\neq\mathbf{G}} V_{\mathbf{G}-\mathbf{G}'}(z)\,\Psi_{\mathbf{G}'+\mathbf{Q},n_{\mathbf{Q},\nu}}(z)\\
&\quad+\frac{1}{2}\,\mathbf{A}^{eff}(\mathbf{Q},\nu;T)\cdot\sum_{\mathbf{G}'}\left[\mathbf{D}_{\mathbf{G}-\mathbf{G}'-\mathbf{Q}}(z)+\mathbf{D}_{\mathbf{G}-\mathbf{G}'+\mathbf{Q}}(z)\right]\\
&\quad\times\left[\Psi_{\mathbf{G}+\mathbf{Q},n_{\mathbf{Q},\nu}+1}(z)+\Psi_{\mathbf{G}+\mathbf{Q},n_{\mathbf{Q},\nu}-1}(z)\right],
\end{aligned} \tag{178}$$

and

$$\begin{aligned}
&\left[\frac{\hbar^2}{2\ m}\frac{d^2}{dz^2} \ + \ \frac{\hbar^2}{2\ m}\mathbf{k}^2_{\mathbf{G}+\mathbf{Q},n_{\mathbf{Q},\nu}+1,z} - V_{\mathbf{0}}(z)\right]\Psi_{\mathbf{G}+\mathbf{Q},n_{\mathbf{Q},\nu}+1}(z)\\
&= \sum_{\mathbf{G}'\neq\mathbf{G}} V_{\mathbf{G}-\mathbf{G}'}(z)\,\Psi_{\mathbf{G}'+\mathbf{Q},n_{\mathbf{Q},\nu}+1}(z)\\
&\quad+\frac{1}{2}\,\mathbf{A}^{eff}(\mathbf{Q},\nu;T)\cdot\sum_{\mathbf{G}'}\left[\mathbf{D}_{\mathbf{G}-\mathbf{G}'-\mathbf{Q}}(z)+\mathbf{D}_{\mathbf{G}-\mathbf{G}'+\mathbf{Q}}(z)\right]\\
&\quad\times\left[\Psi_{\mathbf{G}+\mathbf{Q},n_{\mathbf{Q},\nu}+2}(z)+\Psi_{\mathbf{G}+\mathbf{Q},n_{\mathbf{Q},\nu}}(z)\right].
\end{aligned} \tag{179}$$

Within the active mode approximation multiple quantum excitation of the phonon is treated by the method of Floquet blocks [255]. As mentioned above, the number of Floquet blocks dressing each channel $\Psi_{\mathbf{G}+\mathbf{Q},n_{\mathbf{Q},\nu}}(z)$ is given by the total number of phonon creations and annihilations retained for convergence of the calculation.

As a special case, for situations in which one is interested in calculating the thermal attenuation of elastic diffraction intensities it is useful to ignore the momentum and consider excitations of phonons of energy $\hbar\omega$ with no dependence on **Q**. This is accomplished by restricting Eqs. (178) and (179) to the special case of $\mathbf{Q} \ = \ 0$, i. e.

$$\begin{aligned}
&\left[\frac{\hbar^2}{2\ m}\frac{d^2}{dz^2} + \frac{\hbar^2}{2\ m}\mathbf{k}^2_{\mathbf{G},n,z} - V_{\mathbf{0}}(z)\right]\Psi_{\mathbf{G},n}(z)\\
&= \sum_{\mathbf{G}'\neq\mathbf{G}} V_{\mathbf{G}-\mathbf{G}'}(z)\Psi_{\mathbf{G}',n}(z) + \frac{1}{2}\mathbf{A}^{eff}\cdot\sum_{\mathbf{G}'}\left[\mathbf{D}_{\mathbf{G}-\mathbf{G}'}(z)+\mathbf{D}_{\mathbf{G}-\mathbf{G}'}(z)\right]\\
&\quad\times\ \left[\Psi_{\mathbf{G},n+1}(z)+\Psi_{\mathbf{G},n-1}(z)\right] ,
\end{aligned} \tag{180}$$

and

$$\begin{aligned}
&\left[\frac{\hbar^2}{2\ m}\frac{d^2}{dz^2} \ + \ \frac{\hbar^2}{2\ m}\mathbf{k}^2_{\mathbf{G},n+1,z} - V_{\mathbf{0}}(z)\right]\Psi_{\mathbf{G},n+1}(z)\\
&= \sum_{\mathbf{G}'\neq\mathbf{G}} V_{\mathbf{G}-\mathbf{G}'}(z)\,\Psi_{\mathbf{G}',n+1}(z) + \frac{1}{2}\,\mathbf{A}^{eff}\cdot\sum_{\mathbf{G}'}\left[\mathbf{D}_{\mathbf{G}-\mathbf{G}'}(z)+\mathbf{D}_{\mathbf{G}-\mathbf{G}'}(z)\right]\\
&\quad\times\ \left[\Psi_{\mathbf{G},n+2}(z)+\Psi_{\mathbf{G},n}(z)\right] ,
\end{aligned} \tag{181}$$

where $n_{\mathbf{Q},\nu}$ has been replaced by n in order to simplify the notation.

7.3. Calculating observable intensities

The general scattering matrix $S_{\mathbf{G}+\mathbf{Q},n_{\mathbf{Q},\nu}}$ resulting from the solution of the set of Eqs. (180) and (181) as well as Eqs. (178) and (179) is unitary and the mode-specific scattering probabilities are expressed as

$$I_{\mathbf{G}+\mathbf{Q},n_{\mathbf{Q},\nu}} = |S_{\mathbf{G}+\mathbf{Q},n_{\mathbf{Q},\nu}}|^2, \tag{182}$$

although this quantity is not, in general, observable experimentally. In order to obtain the observable elastic diffraction and inelastic intensities it is necessary to average over the phonon spectral density $\rho(\omega(\mathbf{Q},\nu))$ and the initial number of phonons $n^{(i)}_{\mathbf{Q},\nu}$, and sum over the final number of phonons of the active mode, $n^{(f)}_{\mathbf{Q},\nu}$. Note that, as opposed to purely elastic diffractive scattering from a rigid periodic surface, because there are multiple phonons transferred with different values of parallel momentum transfer $\mathbf{Q}$, there will in general be non-zero elastic scattering intensity between the diffraction peaks. This is diffuse elastic background due to multiple phonon excitations whose total energy transfer to the surface is zero, but whose total wave vector exchange is non-zero. If we define $\Delta n_{\mathbf{Q},\nu} = n^{(f)}_{\mathbf{Q},\nu} - n^{(i)}_{\mathbf{Q},\nu}$ as the net number of phonons exchanged in the scattering process, then the observable elastic scattering intensity at parallel wave vector $\mathbf{G}+\mathbf{Q}$ is

$$\langle I_{\mathbf{G}+\mathbf{Q}} \rangle = \langle I^{el}_{\mathbf{G}+\mathbf{Q}} \rangle + \langle I^{inel}_{\mathbf{G}+\mathbf{Q}} \rangle, \tag{183}$$

where the elastic contribution (corresponding to $\Delta n_{\mathbf{Q},\nu} = 0$, i.e., no net exchange of phonons) is given by

$$\langle I^{el}_{\mathbf{G}+\mathbf{Q}} \rangle = \int_0^{\omega_c} \left| S_{\mathbf{G}+\mathbf{Q},\mathbf{0}} \left(\Delta n_{\mathbf{Q},\nu}\omega(\mathbf{Q},\nu)) = 0 \right) \right|^2 \rho(\omega(\mathbf{Q},\nu))\, d\omega(\mathbf{Q},\nu), \tag{184}$$

and the actual diffraction peak intensity is obtained by setting $\mathbf{Q} = 0$. The inelastic contribution coming from terms with $\Delta n_{\mathbf{Q},\nu} \neq 0$ is given by

$$\langle I^{inel}_{\mathbf{G}+\mathbf{Q}} \rangle = \sum_{\Delta n_{\mathbf{Q},\nu}=1}^{\infty} \int_0^{\omega_c} \left[e^{-\Delta n_{\mathbf{Q},\nu}\beta\hbar\omega(\mathbf{Q},\nu)} \left| S_{\mathbf{G}+\mathbf{Q},\mathbf{0}}(-\Delta n_{\mathbf{Q},\nu}\omega(\mathbf{Q},\nu)) \right|^2 + \left| S_{\mathbf{G}+\mathbf{Q},\mathbf{0}}(+\Delta n_{\mathbf{Q},\nu}\omega(\mathbf{Q},\nu)) \right|^2 \right] \rho(\omega(\mathbf{Q},\nu))\, d\omega(\mathbf{Q},\nu). \tag{185}$$

In these expressions $\beta = 1/k_B T$, and ω_c is a cutoff frequency defined by the maximum allowed frequency in the phonon spectral density $\rho(\omega(\mathbf{Q},\nu))$.

The scattering amplitude elements are calculated for a number of phonons of the active mode that are exchanged given by $\Delta n_{\mathbf{Q},\nu}$. One effect of an increasing surface temperature is to enlarge the number of phonons involved in the scattering process. This leads also to an increase of the number of Floquet blocks necessary to obtain numerical convergence. Therefore, the thermal attenuation in this formalism is dependent on the number of Floquet blocks. As the number of inelastic channels increases, since the theory is unitary, the diffraction intensities associated with the elastic channels decrease due to a redistribution of the total flux into more and more open elastic and inelastic scattering channels. An additional advantage of this formalism is that it makes it possible to calculate the percentages of the total intensity due to the elastic and inelastic contributions and to have an idea of the multiphonon background. Moreover, this analysis also makes clear the importance of the contributions of small phonon frequencies since this implies that their Floquet blocks are densely packed and the resulting effective coupling is stronger. As a final comment, it should be noted that since this method is numerically exact it automatically includes the contributions due to coupling with the bound states in the adsorption potential well. This means that bound state resonances, regardless of whether they are elastic or inelastic (phonon assisted) are correctly calculated.

An example of the application of this inelastic close coupling formalism is provided by a recent analysis of the structure and dynamics of the Bi(111) surface [262] using He atom scattering measurements [70]. The interaction potential $V(\mathbf{r})$ was taken to be a corrugated Morse potential of the form

$$V(\mathbf{r}) \;=\; D\left(e^{-2\kappa(z-\xi(\mathbf{R}))} - e^{-\kappa z} \right) , \tag{186}$$

where D is the well depth and κ is the stiffness parameter. The corrugation function of the BCC Bi(111) surface was represented by a summation of sinusoidal functions

$$\xi(\mathbf{R}) = \xi(x,y) = \xi_0 \left(\cos\left[\frac{2\pi}{a}\left(x - \frac{y}{\sqrt{3}} \right) \right] + \cos\left[\frac{2\pi}{a}\left(x + \frac{y}{\sqrt{3}} \right) \right] + \cos\left[\frac{2\pi}{a}\frac{2y}{\sqrt{3}} \right] \right), \tag{187}$$

with ξ_0 as the corrugation amplitude and a is the lattice constant which for Bi is 4.538 Å. With the above corrugation function the Fourier components $V_{\mathbf{G}}(z)$ of the potential become

$$V_{\mathbf{G}-\mathbf{G}'}(z) \;=\; D\,\frac{v_{n,m}}{v_{0,0}}\, e^{-2\kappa z} , \tag{188}$$

where the integers n and m are those needed to specify the surface reciprocal lattice vectors, i.e., $\mathbf{G} = \mathbf{G}(n,m)$. The coefficients are expressed in terms of the modified Bessel functions of the first kind $I_n(\alpha)$ with $\alpha = 2\kappa\xi_0$ as

$$v_{n,m} \;=\; \frac{\sqrt{3}a^2}{4\pi} \sum_{k=-\infty}^{+\infty} I_k(\alpha) \left[I_{k+n}(\alpha) I_{k-m}(\alpha) + I_{k-n}(\alpha) I_{k+m}(\alpha) \right] . \tag{189}$$

Results of calculations of the diffraction peak intensities at several temperatures spanning a rather large range are shown in Fig. 18. The potential parameters used were a well depth $D = 7.898$ meV, a stiffness parameter $\kappa = 0.884$ Å^{-1}, and a corrugation amplitude of $\xi_0 = 0.07$ Å^{-1}. The phonon spectrum was a Debye distribution with a Debye temperature of 85 K. It is seen that the relative intensities of the specular and observable diffraction peaks are well reproduced by the calculations, and even the apparent asymmetries between the intensities of corresponding negative and positive index diffraction peaks, introduced by the increasing inelastic background at higher temperatures, are also reproduced.

Further illustration of the usefulness of this ICC formalism is seen in the thermal attenuation in Fig. 19 which shows Debye-Waller plots of the specular and diffraction intensities. The left panel shows the natural logarithm of the specular intensity as a function of surface temperature and the points are ICC calculations taken in both high symmetry directions as indicated in the figure caption. The line passing through the points is the result of a standard neutron scattering Debye-Waller function of the type shown in Eq. (2) with a Debye temperature of 85.9 K (assuming for M_S the mass of a single Bi atom), which is also in agreement with the experimental measurements of the thermal attenuation. The right panel of Fig. 19 shows similar good agreement for the first order diffraction peaks in the two high symmetry directions. The dashed line shows a standard Debye-Waller plot the type shown in Eq. (2) with a Debye temperature of 85.9 K and momenta adjusted for the diffraction peak, while the displaced solid line shows a similar calculation with a Debye temperature of 85 K.

An important remark to make at this point is that the Debye temperature obtained here is an independent evaluation, which is obtained from fitting the ICC calculations to the diffraction peak intensities as shown in Fig. 18. This value is independent of the Debye temperature appearing in the neutron scattering approximation of, e.g., Eq. (2) or Eq. (135), which is typically evaluated by fitting the Debye-Waller factor to the thermal attenuation of the specular or another diffraction peak. Thus, the determination of Θ_D from Fig. 18

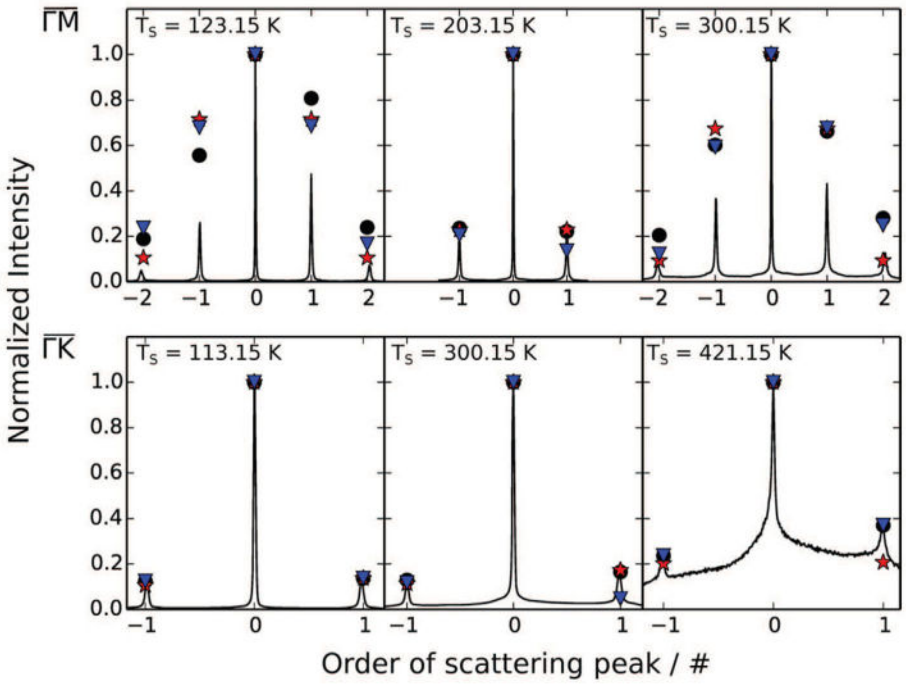

Fig. 18. He atom scattering from Bi(111): measured and calculated diffraction peak intensities in both high symmetry lattice directions at several surface temperatures and an incident beam energy of 17 meV [262]. Black dots signify measured peak areas, red stars signify calculated peak intensities using elastic close-coupling with a Debye-Waller attenuation, and blue downward triangles signify calculated peak intensities using the inelastic close-coupling approach. The "order" of the scattering peak refers to the number of reciprocal lattice vectors needed when fulfilling the Bragg condition. Upper panel: Angular scans in the ΓM direction at three different surface temperatures. Lower panel: Angular scans in the ΓK direction at three different surface temperatures. (For interpretation of the references to colour in this figure legend, the reader is referred to the Web version of this article.)

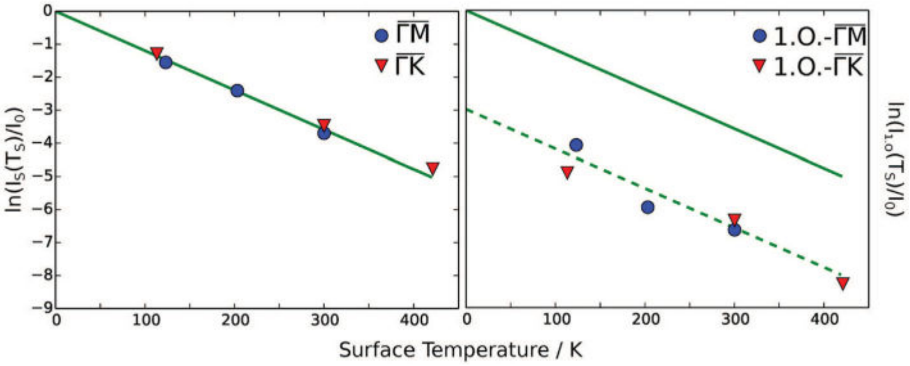

Fig. 19. He atom scattering from Bi(111): natural logarithm of the calculated intensities divided by the elastic (unattenuated) specular intensity [262]. Left panel: Attenuation of the specular contribution in both high-symmetry directions. The green line corresponds to a fit of a simple D-W-like attenuation with a Debye temperature of $\Theta_D = 85.9$ K. Right panel: Attenuation of the calculated first-order diffraction peaks in both high-symmetry directions. The parallel but shifted behavior confirms a D-W-like attenuation of the diffraction peaks with the same Debye temperature as for the specular. (For interpretation of the references to colour in this figure legend, the reader is referred to the Web version of this article.)

provides an independent evaluation of the e-ph coupling constant λ_{HAS} via Eq. (136). Using the mass of a single Bi atom and the present value of $\Theta_D = 85$ K, the Debye force constant appearing in Eq. (136) is $f_{Ds} = M_S \Theta_D^2 k_B^2 / \hbar^2 = 4.2 \times 10^4$ erg/cm^2. Using the 3-D free electron DOS obtained in Subsection 5.5 related to the unit cell volume v_c, i.e., $N(E_F) = v_c m_e^* k_F / \pi^2 \hbar^2$ where $v_c = c a_c$ and a_c is the surface unit cell area and c the cell depth, Eq. (136) becomes

$$\lambda_{HAS} = \frac{6\pi^2 \phi}{v_c k_F f_{Ds}} . \qquad (190)$$

In bismuth $a_c = 17.8$ Å^2 and $c = 11.823$ Å. With ϕ and k_F taken from Table 2 one obtains $\lambda_{HAS} = 0.62$, which compares favorably with the value of 0.57 derived by fitting the thermal attenuation of the specular peak and the calculated value of 0.60 [86].

8. Conclusions

This paper begins with a review of formal scattering theory as it applies to the collisions of atoms with surfaces at kinetic energies in the range where no penetration into the target is expected, which in the case of He atoms or other rare gas atoms usually means incident energies not much greater than approximately 10 eV. In fact, the most interesting regime, and the one that is capable of producing the most detailed information about the surface structure and dynamics, is when quantum effects such as diffraction and single phonon transfer predominate and this implies projectile energies less than 100 meV. Under such conditions, the incoming atoms are reflected by the rapidly decreasing electronic distribution as it extends outward from the surface away from the core atoms making up the crystal target. Thus the collision takes place not with the cores, but with the electronic distribution a significant distance in front of the first layer of cores. In particular, the static corrugation and the vibrational displacements sensed by the colliding atom are those of the electron distribution, and these electron density vibrational displacement vectors may be significantly different from those of the cores. Most theoretical treatments in the past have treated this difficulty by approximating the projectile-surface interaction with an effective potential. In this treatment we utilize electron-phonon coupling theory to determine the corrugation and vibrational displacements of the electronic density and these are related directly to the positions and displacements of the cores through the e-ph coupling constants.

In Sec. 2 we show, starting from a rather general form of the interaction potential, how to develop the elastic and inelastic transition rates (and hence the scattering spectra) and it is shown how a Debye-Waller factor must arise. However, unlike typical bulk scattering probes such as neutrons or X-rays, atomic projectiles scatter from the surface electron density and their scattering spectra and Debye-Waller factor are expressed in terms of the effective vibrational displacement operators of the electron cloud, which are only indirectly related to the vibrational displacements of the cores.

Since most treatments of inelastic scattering, and many methods for calculating weak diffraction intensities such as is often the case for metal targets, use the distorted wave Born approximation, Sec. 3 shows how the DWBA can be extracted from the general theory. This approach has two advantages, first it gives a well defined prescription for determining the appropriate transition matrix operator for use in the DWBA, and secondly it clearly shows that the Debye-Waller factor must appear in the DWBA. This latter point is important because in earlier theoretical treatments using the DWBA the Debye-Waller factor either did not appear, was incorrectly evaluated, or had to be factored into the intensity spectra in an ad hoc fashion. The present treatment explains the failure of these earlier treatments, which was usually due to applying approximations or expansions of the interaction potential too early in the theoretical development.

The approach developed in Secs. 2 and 3 provides a theoretical framework in which the vibrational displacements of the surface electron density are calculated using electron-phonon coupling. The effective vibrational displacements of the electron density are related directly to those of the cores, i.e., they are directly related to the phonon displacements that can be readily calculated for a semi-infinite crystal lattice. The approach depends on the well established fact that the repulsive part of the potential experienced by an incoming atomic projectile is due to Pauli exchange forces, and is proportional to the surface electron density. With the effective displacements of the electron distribution it is then a straightforward matter to evaluate the displacement correlation functions necessary for calculating the elastic and inelastic scattering spectra and the Debye-Waller factor. The formal treatment of the electron-phonon coupling appears in Sec. 4 where the transition rates for elastic and single phonon inelastic scattering are presented. From these transition rates explicit expressions for the effective displacement operators of the electron distribution that scatters the atoms are obtained. In the process, electron-phonon coupling theory identifies the thin, essentially two-dimensional region of the surface at which the atomic projectile is both reflected and energy transfer takes place, i.e., essentially the region containing the locus of classical turning points.

In order to relate experimental atom-surface scattering spectra to quantities typically measured for bulk electron-phonon interactions a series of standard e-ph coupling approximations are applied in Sec. 5. It is found that the scattered spectra can be related to the electron-phonon coupling constant λ familiar to superconductivity theory, or more specifically to its mode specific components $\lambda_{\mathbf{Q},\nu}$.

Previously, it has been shown that the intensity of single phonon peaks in energy resolved scattering spectra are proportional to $\lambda_{\mathbf{Q},\nu}$. This result shows that relative values of the $\lambda_{\mathbf{Q},\nu}$ can be obtained through measurements of the intensities of single phonon peaks. In this work we obtain in a more general way the same result for the inelastic intensities and show that the $\lambda_{\mathbf{Q},\nu}$ associated with atom-surface scattering contain a dependence on surface temperature, a dependence that is relatively weak, but increases in importance as the scattering becomes stronger. The ability of using inelastic scattering to extract the mode components $\lambda_{\mathbf{Q},\nu}$ shows that sampling different segments of the phonon spectrum should serve to pinpoint which phonons are most important for electron pairing in superconductors, and particularly for low-dimensional superconductors. This is in contrast with the information extracted from the D-W factor, which is able to obtain only the averaged value of λ for a given system.

This approach also produces the elastic diffraction spectrum arising from scattering from the corrugation of the electron density caused by the electron-phonon coupling. The standard e-ph approximations show that diffraction peak intensities can be expressed in terms of a weighted summation over the electron-phonon matrix elements. Thus, this shows that even measurements of elastic diffraction provide information on the electron-phonon interaction and its contribution to the interaction potential.

It is through examination of the single phonon transition rates that it is possible to identify the effective vibrational displacement vector operators of the surface electron density, i.e., the displacement operators that cause the creation or annihilation of phonons in the scattering collision. With these displacement operators, it is then straightforward to evaluate the time and position dependent displacement correlation functions and the mean square displacement needed to evaluate the Debye-Waller factor. These quantities are directly related to the displacement operators of the crystal cores through the electron-phonon coupling. As a result of the e-ph coupling these quantities are also found to have additional dependence on the temperature, i.e., dependence on temperature beyond that arising from the usual Bose-Einstein factors found in the well known correlation functions for the core displacements.

An important result is that the evaluation of the mean square displacement allows a precise definition of the Debye-Waller factor, and specifically this means that all components of its argument $2W^{eff}(\mathbf{k}_f, \mathbf{k}_i)$ are defined in terms of the corresponding correlation function for the crystal cores. This is an important property that is lacking in virtually all previous treatments. For example, the simplest treatment of $2W^{eff}(\mathbf{k}_f, \mathbf{k}_i)$ assigns it a value similar to that used for neutron scattering as shown in Eq. (1), or the simpler reduction of Eq. (2) where a Debye phonon model has been used to express it in terms of projectile atom energy, a surface mass and a Debye temperature. However, as discussed in the Introduction, the only part of Eq. (2) that is well defined is its linear dependence on the temperature. The surface mass, the energy dependence, and the Debye temperature all must be regarded as effective quantities that may or may not bear a simple relationship to the corresponding quantities of the surface cores. In the present treatment based on electron-phonon coupling, the surface mass that appears in $2W^{eff}(\mathbf{k}_f, \mathbf{k}_i)$ is that of the crystal cores. The energy dependence found in this approach is considerably more complicated than that appearing in Eq. (1). It involves not only the momentum vector $\Delta\mathbf{k} = \mathbf{k}_f - \mathbf{k}_i$, but also has energy dependence arising from the projectile distorted wave functions and the electron-projectile overlap. This energy dependence automatically includes effects of the attractive van der Waals force and its associated adsorption well in the interaction potential because these are built into the distorted wave functions appearing in the overlap integrals.

As examples of the application of the theory presented here, and its potential for obtaining information from the analysis of experimental data, in Sec. 6 we discuss extracting the values of the electron-phonon coupling constant λ from measurements of the Debye-Waller thermal attenuation of He atom scattering. Most often the type of scattering data analyzed was the thermal attenuation of the specular diffraction peak or a non-specular diffraction peak. However, other examples show that values of λ can be extracted from analysis of the energy or angular dependence of the D-W factor, or even from the temperature dependence of the diffuse elastic intensity measured between diffraction peaks, or from diffraction features arising from charge density waves at the surface. Starting with the available data for the D-W thermal attenuation of the He atom scattering specular peak from simple metals, over 50 different systems have been analyzed. In addition to simple metals, metallic overlayers on various substrates have been examined as well as chalcogenides, other topological surfaces and single-layer graphene adsorbed on metal substrates. For all of these systems the values of λ measured at the surface via scattering of rare gas atoms are in reasonable agreement with known values from other sources such as measured bulk values or calculated values. This work demonstrates that all aspects of the observable scattering in atom-surface systems, such as elastic and inelastic spectra as well as the Debye-Waller factor, can be expressed in terms of the electron-phonon interaction parameters. This implies that experimental measurements will be capable of providing extensive information on the nature of the electron-phonon coupling interaction near the surface.

In addition to presenting expressions for the scattering transition rates, we use the displacement operators developed here to evaluate the classical form of the displacement vectors at the locus of classical turning points. These are useful quantities needed, for example in applications such as classical molecular dynamics simulations of surface scattering, or for computationally intensive calculations of elastic and inelastic scattering such as inelastic coupled channels computations discussed in Section 7. An important result arising from the ICC calculation is that it provides for an alternative method of determining λ_{HAS}. This is because a comparison of the ICC calculation with the HAS diffraction peak intensities at any given temperature produces a value of the Debye temperature, a value which is independent of that derived from a comparison with experimental data for the Debye-Waller factor of Eq. (2). This is discussed in Subsection 5.4 with a specific example of Bi(111) evaluated with Eq. (190) in Subsection 7.3.

The formal theoretical development presented in the first four sections of this review assumes a perfectly ordered surface, and consequently does not contain a diffuse elastic scattering component, it is nevertheless easy to understand that the D-W factor also applies to diffuse elastic scattering. The diffuse elastic scattering signal is usually a rather sharp peak in the energy-resolved atom-surface scattering spectra appearing at zero energy transfer in the region between the coherent diffraction peaks. It is due to symmetry breaking defects in and on the surface such as steps and other disorder or adsorbates. To include diffuse elastic scattering in the present theory it is only a question of including in the transition matrix additional terms corresponding to a small distribution of defects or adsorbates. For example, this could be accomplished by adding into the transition matrix of Eq. (62) a contribution due to a random distribution of defects or adsorbates. If the distribution is sufficiently dilute the D-W factor is negligibly different in form, but is seen to apply to the diffuse elastic intensity in a manner similar to that of the diffraction peaks. We have used this fact implicitly in several of the systems analyzed for values of λ in Sec. 6. The diffuse elastic intensity in He atom scattering has been used to determine the nature and shape of dilute distributions of adsorbates on metal surfaces [263] and it would be of interest to look into this further, for example one could investigate the effects on the value of λ due to various densities of adsorbates on metal surfaces.

The large variety of systems already analyzed and presented in Sec. 6 make it easy to think of other systems that would be of interest to investigate for determination of λ. Examples that immediately suggest themselves are the various classes of high $- T_C$ superconductors such as cuprates, perovskites, etc. Measuring λ should be relevant for many surface phenomena related to low-energy collective excitations on metal surfaces such as phasons, amplitons and acoustic surface plasmons. For many such systems the variations of strength of λ can be measured as a function of film thickness on a layer-by-layer basis. The examples discussed above in Subsections 6.4 and 6.7 of topological surfaces and supported graphene also provide ample numbers of new systems that could be analyzed for λ and in particular for how λ varies under the influence of various experimentally controllable parameters such as dopants. Knowledge of the e-ph coupling is also relevant to 2-D and quasi-1D superconductivity in nanotechnology as well as to other transport properties such as thermo-electricity, etc. It is also able to discriminate in topological insulators contributions of the quantum well states over the Dirac electrons and this interaction acts as the driving mechanism for the observed CDW transition. Thus, HAS spectroscopy can help to elucidate whether and where the coexistence of CDWs and superconductivity is competitive or cooperative. Pnictogen chalcogenides where topological superconductivity can be induced by pressure, intercalation or proximity to superconductors offer possible scenarios of coexistence with CDWs. The values of λ obtained from HAS allows to stress the role of surface quantum well and conduction-band states with respect to that of Dirac states. In particular the study in Subsection 6.7 of graphene supported on metal substrates, showing how λ varies with the binding strength, make it obvious that He scattering investigations should be carried out on double and multiple layer supported graphene. Of particular interest would be investigations of twisted bilayer graphene and other systems in the burgeoning field of twintronics.

Declaration of competing interest

The authors declare that they have no known competing financial interests or personal relationships that could have appeared to influence the work reported in this paper.

Acknowledgment

We would like to thank the referees for valuable and useful comments and suggestions. One of us (GB) would like to thank Prof. Marco Bernasconi for helpful discussions. SMA would like to acknowledge support from Ministerio de Ciencia e Innovación through a grant with reference PID2021-125735NB-I00 and also support from the Fundación Humanismo y Ciencia.

Appendix A. Expansion of the Displacement Vector and Correlation Functions in Normal Modes

Reproduced here are some useful expressions that result from the theory of crystal vibrations in the harmonic approximation [264] as they apply to a semi-infinite surface. For simplicity the case of a Bravais lattice is considered. Following the standard treatments of bulk crystal vibrations which are expanded in terms of normal modes, the α-th cartesian component of the displacement vector of the surface atomic core sitting at the ℓ-th surface lattice site $\mathbf{u}_\ell(t)$ can be expanded as [264].

$$u_{\alpha,\ell}(t) = \sum_{\mathbf{Q},\nu} \left[\frac{\hbar}{2NM\omega(\mathbf{Q},\nu)}\right]^{1/2} e_\alpha(\mathbf{Q},\nu) e^{i\mathbf{Q}\cdot\mathbf{R}_\ell} \left[\widehat{a}^\dagger(\mathbf{Q},\nu)e^{-i\omega(\mathbf{Q},\nu)t} + \widehat{a}(\mathbf{Q},\nu)e^{i\omega(\mathbf{Q},\nu)t}\right], \tag{A.1}$$

where $\sum_{\mathbf{Q},\nu}$ is a summation over the parallel wave vector $\mathbf{Q}$ and branch number ν of the mode, M is the surface atomic mass, $\omega(\mathbf{Q},\nu)$ is the mode frequency, and $e_\alpha(\mathbf{Q},\nu)$ is the α-th cartesian component of the mode polarization vector. The operators $\widehat{a}^\dagger(\mathbf{Q},\nu)$ and $\widehat{a}(\mathbf{Q},\nu)$ are, respectively, creation and annihilation operators, whose average is given by

$$\left\langle \widehat{a}^\dagger(\mathbf{Q},\nu)\,\widehat{a}(\mathbf{Q}',\nu')\right\rangle = n_{BE}(\omega(\mathbf{Q},\nu))\ \delta_{\mathbf{Q},\mathbf{Q}'}\ \delta_{\nu,\nu'}\ , \tag{A.2}$$

with $n_{BE}(\omega(\mathbf{Q},\nu))$ the Bose-Einstein distribution function given by

$$n_{BE}(\omega(\mathbf{Q},\nu)) = \left[\exp\left(\frac{\hbar\omega(\mathbf{Q},\nu)}{k_BT}\right) - 1\right]^{-1}. \tag{A.3}$$

Making use of Eq (A.2) the average displacement correlation function can be evaluated with the result

$$\langle \Delta\mathbf{k}\cdot\mathbf{u}_\ell(0)\Delta\mathbf{k}\cdot\mathbf{u}_{\ell'}(t)\rangle = \sum_{\alpha,\alpha'=1}^{3} \Delta k_\alpha \Delta k_{\alpha'} \sum_{\mathbf{Q},\nu}\left[\frac{\hbar}{2NM\omega(\mathbf{Q},\nu)}\right] e_\alpha(\mathbf{Q},\nu)\, e^*_{\alpha'}(\mathbf{Q},\nu)$$
$$\times e^{-i\mathbf{Q}\cdot(\mathbf{R}_{\ell'}-\mathbf{R}_\ell)}\left\{\left[n_{BE}(\omega(\mathbf{Q},\nu))+1\right]e^{-i\omega(\mathbf{Q},\nu)t} + n_{BE}(\omega(\mathbf{Q},\nu))\,e^{i\omega(\mathbf{Q},\nu)t}\right\}. \tag{A.4}$$

Expressed more simply as the tensor of vibrational amplitudes, the correlation function is

$$\left\langle u_{\alpha,\ell}(0)u_{\alpha',\ell'}(t)\right\rangle = \sum_{\mathbf{Q},\nu}\left[\frac{\hbar}{2NM\omega(\mathbf{Q},\nu)}\right] e_\alpha(\mathbf{Q},\nu)e^*_{\alpha'}(\mathbf{Q},\nu)$$
$$\times\, e^{i\mathbf{Q}\cdot(\mathbf{R}_{\ell'}-\mathbf{R}_\ell)}\left\{\left[n_{BE}(\omega(\mathbf{Q},\nu))+1\right]e^{-i\omega(\mathbf{Q},\nu)t} + n_{BE}(\omega(\mathbf{Q},\nu))e^{i\omega(\mathbf{Q},\nu)t}\right\}. \tag{A.5}$$

For completeness we write also the average mean-square displacement, which is independent of lattice site ℓ and time t and is readily obtained by evaluating Eq. (A.5) at equal times and positions.

$$\left\langle u_{\alpha,\ell}u_{\alpha',\ell}\right\rangle = \sum_{\mathbf{Q},\nu}\left[\frac{\hbar}{NM\omega(\mathbf{Q},\nu)}\right] e_\alpha(\mathbf{Q},\nu)e^*_{\alpha'}(\mathbf{Q},\nu)\left[n_{BE}(\omega(\mathbf{Q},\nu)) + \frac{1}{2}\right]. \tag{A.6}$$

The argument of the Debye-Waller factor is expressed in terms of the mean-square displacement

$$2W(\mathbf{k}_f,\mathbf{k}_i) = \left\langle\left(\Delta\mathbf{k}\cdot\mathbf{u}_\ell(t)\right)^2\right\rangle$$
$$= \sum_{\alpha,\alpha'=1}^{3}\Delta k_\alpha\Delta k_{\alpha'}\sum_{\mathbf{Q},\nu}\left[\frac{\hbar}{NM\omega(\mathbf{Q},\nu)}\right] e_\alpha(\mathbf{Q},\nu)e^*_{\alpha'}(\mathbf{Q},\nu)\left[n_{BE}(\omega(\mathbf{Q},\nu)) + \frac{1}{2}\right]. \tag{A.7}$$

Note that for atom-surface scattering the displacements and correlation functions considered in this appendix are not those of the atomic cores in the crystal target. They are the effective displacements and correlations at the position at which the scattering takes place, i.e., those of the electron density in the region of the locus of classical turning points of the potential. In this case the mass M becomes an effective mass and not necessarily that of the crystal lattice. However the mathematical forms of the displacement and correlation functions remain similar.

Appendix B. Examples of Effective Temperature-dependent Atom-Surface Potentials

In several instances we have arrived at the need to evaluate an effective, temperature-dependent atom-surface interaction potential such as that first seen in Eq. (59), reproduced here as Eq. (B.1) below. It is of interest to examine example cases in order to see how introduction of the Debye-Waller-like factor into the Fourier transform of this potential affects the character of the original interaction potential with a rigid surface.

$$v^{eff}_{\Delta\mathbf{K}}(T,z) = \frac{1}{2\pi}\int_{-\infty}^{+\infty} dq e^{iqz} v_{\Delta\mathbf{K},q} e^{-\widetilde{W}(\Delta\mathbf{K},q)}$$
$$= \frac{1}{2\pi}\int_{-\infty}^{+\infty} dq e^{iqz} v_{\Delta\mathbf{K},q} e^{[-q^2\langle u_z^2\rangle - 2q\Delta K_x\langle u_z u_x\rangle - 2q\Delta K_y\langle u_z u_y\rangle]/2}. \tag{B.1}$$

For now, it is assumed the averaged displacement cross terms vanish, leaving a relatively simple looking Fourier transform to evaluate

$$v(T,z) \;=\; \frac{1}{2\pi}\int_{-\infty}^{+\infty} dq\; e^{iqz}\; v_q\; e^{-q^2\langle u_z^2\rangle/2}\;. \tag{B.2}$$

Two examples will be considered here. One is the physically obvious case of an exponentially repulsive potential. The other is the somewhat less physical step-function, but one that gives an illustrative example of how the temperature alters features of the potential.

Appendix B.1. Step-Function Potential

An interesting case to start with is that of considering the atom-surface interaction potential to be a step function repulsive barrier of height V_0. Of course this implies that the energy of the incoming particle is less than V_0.

$$v(z) \;=\; \begin{cases} 0\,, & z>0 \\ V_0\,, & z<0 \end{cases}\;. \tag{B.3}$$

For simplicity, take $V_0 \;=\; 1$ and recognize that the Fourier transform of the step function is

$$S_q \;=\; \frac{1}{i}\lim_{\delta\to 0^+}\frac{1}{q-i\delta}\;. \tag{B.4}$$

This choice is readily checked by evaluating the integral as a countour integral on the complex q-plane

$$\begin{aligned} v(z) &= 1-\frac{1}{2\pi i}\lim_{\delta\to 0^+}\int_{-\infty}^{+\infty} dq e^{iqz}\frac{1}{q-i\delta} \\ &= 1-\frac{1}{2\pi i}\lim_{\delta\to o^+}\oint dq e^{iqz}\frac{1}{q-i\delta} \\ &= \begin{cases} 0, & z>0 \\ 1, & z<0 \end{cases}, \end{aligned} \tag{B.5}$$

where the contour is chosen to be closed by a semicircle in the upper half-plane if $z \;>\; 0$ and in the lower half-plane if $z \;<\; 0$.

Now, consider the Debye-Waller modified effective step function potential

$$S_q^{eff} \;=\; \frac{1}{i}\lim_{\delta\to o^+}\frac{1}{q-i\delta}\; e^{-q^2u^2}\;, \tag{B.6}$$

where $u=\sqrt{\langle u_z^2\rangle/2}$. The Fourier transform is less obviously carried out via countour integration in the complex plane

$$v^{eff}(z) \;=\; 1-\frac{1}{2\pi i}\lim_{\delta\to o^+}\int_{-\infty}^{+\infty} dq\; e^{iqz}\;\frac{1}{q-i\delta}\; e^{-q^2u^2}\;, \tag{B.7}$$

but is readily evaluated using another approach. Consider the derivative

$$\begin{aligned} \frac{dv^{eff}(z)}{dz} &= \frac{-1}{2\pi i}\lim_{\delta\to o^+}\int_{-\infty}^{+\infty} dq\; iq\; e^{iqz}\frac{1}{q-i\delta}e^{-q^2u^2} \\ &= \frac{-1}{2\pi}\int_{-\infty}^{+\infty} dq e^{iqz}e^{-q^2u^2} \\ &= \frac{-1}{2\pi}e^{-z^2/4u^2}\int_{-\infty}^{+\infty} dq e^{-(qu-iz/2u)^2} = \frac{-1}{2\sqrt{\pi}u}e^{-z^2/4u^2}. \end{aligned} \tag{B.8}$$

Integrating the above result gives $v^{eff}(z)$ in terms of the error function.

$$v^{eff}(z) == 1-\frac{1}{2\sqrt{\pi}u}\int_{-\infty}^{z} dz'\;\; e^{-z'^2/4u^2} = \frac{1}{2}\left[1-\mathrm{erf}\left(\frac{z}{2u}\right)\right]\;, \tag{B.9}$$

where the error function is defined by [265]

$$\mathrm{erf}(z) \;=\; \frac{2}{\sqrt{\pi}}\int_0^z dt\; e^{-t^2}\;. \tag{B.10}$$

Thus it becomes apparent that the effect of including the Debye-Waller-like factor into the effective, temperature-dependent potential is to round off the sharp corners of the step potential. An example is shown in Fig. B.20 where the effective potential is compared with the step function in which the parameter $u = \sqrt{\langle u_z^2 \rangle /2} = 0.2$ Å, which is a quite large value, approximately what one would expect for an average crystal displacement in the neighborhood of the melting temperature.

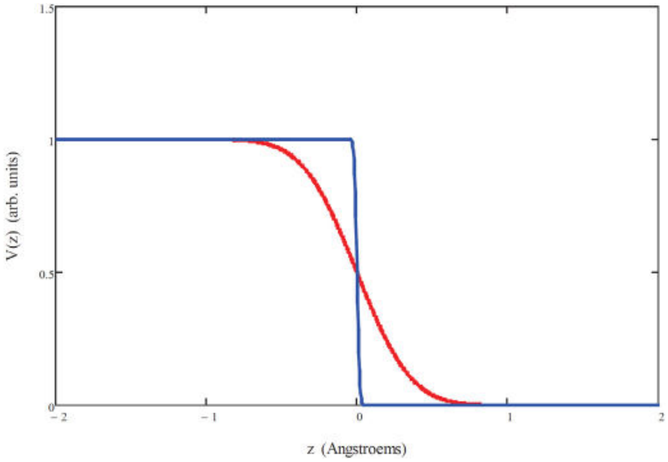

Fig. B.20 Effective potential derived from a step-function potential, compared to the original step function. The value of the root mean square displacement is taken as $u = 0.2$ Å.

Appendix B.2. Repulsive Exponential Potential

The second potential to consider is the physically interesting repulsive exponential potential, which is the approximate form expected for a potential which is proportional to the shape of the electronic density as it spills out of the crystal surface.

$$v(z) = e^{-2\kappa z} . \tag{B.11}$$

The Fourier transform of the exponential potential, at least within the condition $z > 0$ is given by

$$v_q = \frac{1}{i} \frac{1}{q - i2\kappa} , \tag{B.12}$$

as can be seen by the following contour integral carried out in the complex q-plane

$$v(z) = \frac{1}{2\pi i} \int_{-\infty}^{+\infty} dq e^{iqz} \frac{1}{q - i2\kappa} = \frac{1}{2\pi i} \oint dq e^{iqz} \frac{1}{q - i2\kappa} = \begin{cases} e^{-2\kappa z} & z > 0 \\ 0, & z < 0 \end{cases} , \tag{B.13}$$

where the contour is taken to be an infinite semicircle in the upper half plane if $z > 0$, and a semicircle in the lower half plane if $z < 0$, and it is assumed that $\kappa > 0$ and real. It becomes clear that Eq. (B.11) is, in the strictest sense, a mathematically improper Fourier transform for representing the exponential function, with clear limitations of validity indicating $z > 0$, but as long as we stay within this condition it should work quite well for physical illustration.

Using Eq. (B.11), the effective potential including the Debye-Waller-like factor into the Fourier transform becomes, again using as above $u = \sqrt{\langle u^2 \rangle /2}$

$$\begin{aligned} v^{eff}(z) &= \frac{1}{2\pi i} \int_{-\infty}^{+\infty} dq \; e^{iqz} \; \frac{1}{q - i2\kappa} \; e^{-q^2 u^2} \\ &= \frac{1}{2\pi i} \; e^{-z^2/4u^2} \int_{-\infty}^{+\infty} dq \; \frac{1}{q - i2\kappa} e^{-(qu - iz/2u)^2} \\ &= \frac{1}{2\pi i} \; e^{-z^2/4u^2} \int_{-\infty - iz/2u}^{+\infty - iz/2u} dy \; \frac{1}{y - i2\kappa u + iz/2u} e^{-y^2} . \end{aligned} \tag{B.14}$$

Subject to the condition $z > 4\kappa u^2$ the above integral can be converted to a contour integral in the complex y-plane

$$v^{eff}(z) = \frac{1}{2\pi i} e^{-z^2/4u^2} \left\{ \oint dy \; \frac{1}{y - i2\kappa u + iz/2u} \; e^{-y^2} + \int_{-\infty}^{+\infty} dy \; \frac{1}{y - i2\kappa u + iz/2u} e^{-y^2} \right\} . \tag{B.15}$$

The first integral on the right hand side of Eq. (B.15) can be carried out using the calculus of residues on a contour that consists of a long rectangle with one long side on the straight line at $y = -iz/2u$ and the return long side along the $y = 0$ axis, noting that the vertical ends at $y \to \pm\infty$ give a vanishing contribution. The second integral on the right hand side of Eq. (B.15) can be related to an auxiliary function to the error function, the function $w(z)$ whose integral representation is given by [265].

$$w(z) = \frac{i}{\pi} \int_{-\infty}^{+\infty} dt\, e^{-t^2} \frac{1}{t+z} = e^{-z^2} \left[1 - \text{erf}(-iz)\right] . \tag{B.16}$$

With the above, Eq. (B.15) is cast into the form

$$\begin{aligned} v^{eff}(z) &= \frac{1}{2\pi i} e^{-z^2/4u^2} \left\{ 2\pi i e^{-y^2}|_{y=i2\kappa u - iz/2u} + \frac{\pi}{i} w(iz/2u - i2\kappa u) \right\} \\ &= e^{-2\kappa(z-2\kappa u^2)} \left\{ 1 - \frac{1}{2}\left[1 - \text{erf}\left(\frac{z}{2u} - 2\kappa u\right)\right]\right\} . \end{aligned} \tag{B.17}$$

The effective potential is seen to be a shifted exponential with the origin translated by $2\kappa u^2$, multiplied by a correction factor involving the error function. We recall that the above analysis has two conditions, the first $z > 0$ is superseded by the second which is $z > 4\kappa u^2$ since we are working under the assumption that $\kappa > 0$. At the position $z = 4\kappa u^2$ the correction factor is $-1/2$ and rapidly diminishes as z increases positively away from the surface.

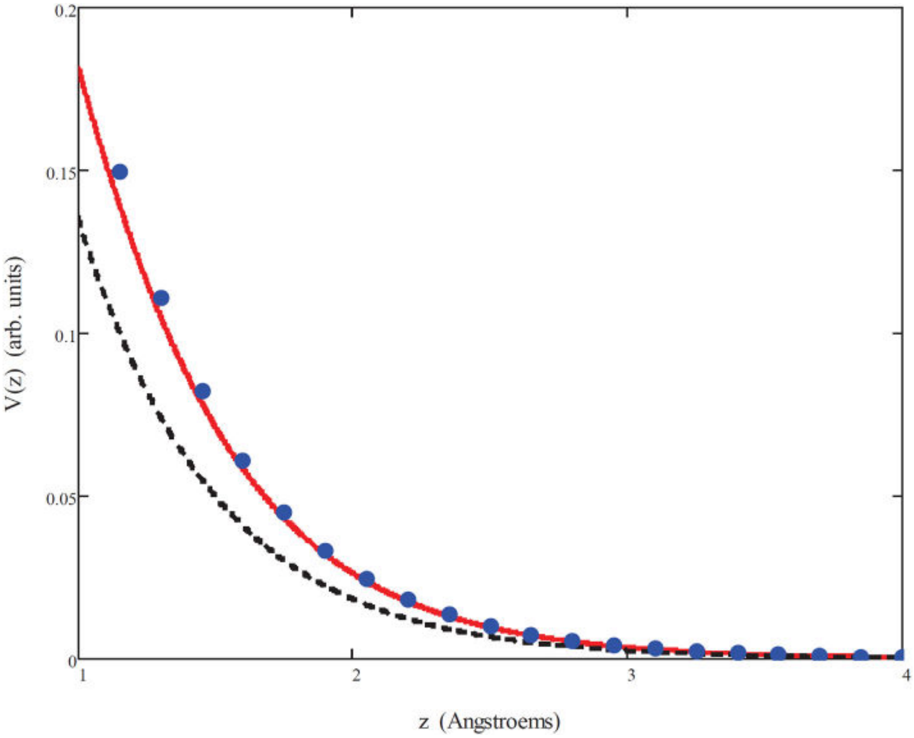

Fig. B.21 Effective potential derived from an exponential potential, compared to the original exponential and to a shifted exponential. Solid curve: effective potential; dashed curve: exponential from which the effective potential was derived; and circles: exponential potential shifted by $z \to z - 2\kappa u^2 = z -$ 0.18 Å., with $\kappa = 1$ Å^{-1}, and $u = 0.3$ Å.

An example calculation for $v^{eff}(z)$ is shown in Fig. B.21 for a typical interaction of He atoms with metal surfaces in which we choose $\kappa = 1$ Å^{-1} and $u = 0.3$ Å (a large value). This shows as a solid curve the effective potential $v^{eff}(z)$, the dashed curve is the original exponential $\exp\{-2\kappa z\}$, and the points are the original exponential shifted by $z \to z - 2\kappa u^2 = z - 0.18$ Å. The agreement between the shifted exponential and the effective potential is quite good (at least in the region $z \gtrsim 1$ Å), implying that the effect of the Debye-Waller-like correction to the effective potential is merely to shift the origin outward from the surface by about a distance given by $\Delta z = \kappa < u_z^2 >$. This may, at first glance, appear like a trivial shift, however, a shift in position of the surface of that magnitude might become of importance when considering the temperature-dependence of the shape of a corrugated surface.

It should also be noted that the numerical calculation shown in Fig. B.21 fails (i.e., it fails to look like an exponential), using the given parameters, for $z \lesssim 0.5$ Å. This is in part because the whole treatment depends on the condition $z \gg 4\kappa u^2 = 0.36$ Å arising from the validity of the (improper) Fourier transform used for an exponential. However, for this choice of the parameters κ and u, which is quite reasonable for He atom scattering from metal surfaces, the classical turning point of He atoms with thermal energies of incidence would be substantially larger than 1 Å from the outermost layer of crystal cores, so the above conclusions hold rather well.

Appendix C. Classical Limit of the Phonon Displacement

In Subsection 4.4 an expression was presented in Eq. (105) for the effective displacement operator describing vibrations of the atom-surface potential at the classical turning point, due to the electron-phonon coupling with the vibrations of the core atoms of the crystal. This is obtained from the time and position dependent correlation function of Eq. (103), which for convenience is repeated here

$$\left\langle u^{eff}_{\alpha,j}(0)u^{eff}_{\alpha',j'}(t)\right\rangle = 2\hbar\sum_{\mathbf{Q},\nu}\sum_{\mathbf{K},n} C_\alpha(\mathbf{K},n,\mathbf{Q})C^*_{\alpha'}(\mathbf{K},n,\mathbf{Q})e^{i\mathbf{Q}\cdot\left(\mathbf{R}_j-\mathbf{R}_{j'}\right)}$$
$$\times\left\{\left[n_{BE}(\omega(\mathbf{Q},\nu))+1\right]e^{-i\omega(\mathbf{Q},\nu)t} + n_{BE}(\omega(\mathbf{Q},\nu))e^{i\omega(\mathbf{Q},\nu)t}\right\}, \tag{C.1}$$

where the α cartesian component of the vector $\mathbf{C}(\mathbf{K},n,\Delta\mathbf{K})$ is

$$C_\alpha(\mathbf{K},n,\mathbf{Q}) = \sqrt{\frac{1}{NM\omega(\mathbf{Q},\nu)}}\frac{e_\alpha(\mathbf{Q},\nu)\ B_\alpha(\mathbf{K},n,\mathbf{Q})}{\left(\chi_{k_{iz}}(z)\left|\ \hat{q}_\alpha\ n^{eff}_{\Delta\mathbf{K}}(T,z)\right|\chi_{k_{fz}}(z)\right)}\ . \tag{C.2}$$

Eq. (C.1) above implies that the time-dependent displacement operator can be written in the following form:

$$u^{eff}_{\alpha,j}(t) = \sqrt{2\hbar}\sum_{\mathbf{Q},\nu}\left[\sum_{\mathbf{K},n}\left|C_\alpha(\mathbf{K},n,\mathbf{Q})\right|^2\right]^{1/2} e^{i\mathbf{Q}\cdot\mathbf{R}_j}\left[\hat{a}^\dagger(\mathbf{Q},\nu)e^{-i\omega(\mathbf{Q},\nu)t}+\hat{a}(\mathbf{Q},\nu)e^{i\omega(\mathbf{Q},\nu)t}\right]. \tag{C.3}$$

Eq. (C.3) is identical with the standard form exhibited in Eq. (A.1) of Appendix A, but with several important differences: (1) there is a summation over all occupied electronic states, (2) the polarization vector $e_\alpha(\mathbf{Q},\nu)$ appearing in Eq. (A.1) now appears embedded in the more complicated effective vector $C_\alpha(\mathbf{K},n,\mathbf{Q})$, and (3) those mode polarization vectors $e_\alpha(\mathbf{Q},\nu)$ and mass M contained in $C_\alpha(\mathbf{K},n,\mathbf{Q})$ are specifically identified as those of the core atoms.

It is of interest, e.g., for purposes of classical dynamics simulations, or inelastic close coupling calculations, to have a purely classical form of the displacement. This is obtained from Eq. (C.3) by eliminating the quantum mechanical creation and annihilation operators using the semi-classical transition

$$\hat{a}^\dagger(\mathbf{Q},\nu) \longrightarrow \sqrt{n_{BE}(\omega(\mathbf{Q},\nu))+1}\ ,$$
$$\hat{a}(\mathbf{Q},\nu) \longrightarrow \sqrt{n_{BE}(\omega(\mathbf{Q},\nu))}\ , \tag{C.4}$$

which gives

$$u^{eff}_{\alpha,j}(t) = \sqrt{2\hbar}\sum_{\mathbf{Q},\nu}\left[\sum_{\mathbf{K},n}\left|C_\alpha(\mathbf{K},n,\mathbf{Q})\right|^2\right]^{1/2} e^{i\mathbf{Q}\cdot\mathbf{R}_j}\left[\sqrt{n_{BE}(\omega(\mathbf{Q},\nu))+1}e^{-i\omega(\mathbf{Q},\nu)t}+\sqrt{n_{BE}(\omega(\mathbf{Q},\nu))}e^{i\omega(\mathbf{Q},\nu)t}\right]. \tag{C.5}$$

Finally the last remnant of quantum mechanics disappears upon taking the high temperature limit

$$u^{eff}_{\alpha,j}(t) = 4\sqrt{\frac{k_BT}{2\omega(\mathbf{Q},\nu)}}\sum_{\mathbf{Q},\nu}\left[\sum_{\mathbf{K},n}\left|C_\alpha(\mathbf{K},n,\mathbf{Q})\right|^2\right]^{1/2} e^{i\mathbf{Q}\cdot\mathbf{R}_j}\cos(\omega(\mathbf{Q},\nu)t). \tag{C.6}$$

The above evaluates the displacement operator in terms of the mode specific electron-phonon coupling components $C_\alpha(\mathbf{K},n,\mathbf{Q})$. This, in principle can be evaluated numerically from Eq. (102) and some of the approximations used in evaluating the correlation functions in Sec. 5 can be applied in order to obtain simpler expressions.

The final step is to write the classical phonon displacement vector as a function of the continuous variable $\mathbf{R}$ as, for example, is needed for the coupled channels approach as in Eq. (167). This end result is simply to change the discrete position variable $\mathbf{R}_j$ in Eq. (C.6) by the continuous variable, i.e.,

$$u^{eff}_{\alpha}(t) = 4\sqrt{\frac{k_BT}{2\omega(\mathbf{Q},\nu)}}\sum_{\mathbf{Q},\nu}\left[\sum_{\mathbf{K},n}\left|C_\alpha(\mathbf{K},n,\mathbf{Q})\right|^2\right]^{1/2} e^{i\mathbf{Q}\cdot\mathbf{R}}\cos(\omega(\mathbf{Q},\nu)t). \tag{C.7}$$

The justification for such a simple change comes from considerations of non-Bravais unit cells with a basis, briefly mentioned above in connection with Eq. (17). Although for simplicity, we have not considered non-Bravais unit cells in this review, it is possible to do so by introducing into the general form of the displacement operator a second discrete variable that counts elements of the basis within the unit cell, and this is the integer κ that appears in Eq. (17) [264]. One can then consider the limit of a surface unit cell whose basis consists of a large number of small units [52], and in this limit the discrete variable $\mathbf{R}_j$ in Eq. (C.6) is replaced by the continuous variable $\mathbf{R}$ appearing in Eq. (C.7).

References

[1] F.O. Goodman, H.Y. Wachman, Dynamics of Gas–Surface Scattering, Academic Press, New York, 1976.

[2] H. Hoinkes, The physical interaction potential of gas atoms with single-crystal surfaces, determined from gas-surface diffraction experiments, Rev. Mod. Phys. 52 (1980) 933.

[3] G. Benedek, J.P. Toennies, Atomic Scale Dynamics at Surfaces: Theory and Experimental Studies with Helium Atom Scattering, Springer Series in Surface Sciences, 63, Springer Press, Heidelberg, 2018, ISBN: 978-3-662-56443-1.

[4] E. Hulpke (Ed.), Helium Atom Scattering from Surfaces, Springer Series in Surface Sciences, 27, Springer Press, Heidelberg, 1992.

[5] T. Engel, K.H. Rieder, Structural Studies of Surfaces with Atomic and Molecular Beam Diffraction, Springer Tracts Mod. Phys. 19, 1982, p. 55.

[6] D. Farias, K.H. Rieder, Atomic beam diffraction from solid surfaces, Reports on Progress in Physics, 61, 1998, p. 1575.

[7] B. Gumhalter, Single- and multiphonon atom–surface scattering in the quantum regime, Phys. Rep. 351 (2001) 1.

[8] A.W. Kleyn, T.C.M. Horn, Rainbow scattering from solid-surfaces, Phys. Rep. 199 (1991) 192.

[9] S. Miret-Artés, E. Pollak, Classical theory of atom-surface scattering: the rainbow effect, Surf. Sci. Rep. 67 (2012) 161.

[10] J.R. Manson, Energy transfer to phonons in atom and molecule collisions with surfaces, in: E. Hasselbrink, B.I. Lundqvist (Eds.), Handb. Surf. Sci. 3 (2008) 54.

[11] B. Poelsema, G. Comsa, Scattering of Thermal Energy Atoms from Disordered Surfaces, Springer Tracts in Modern Physics, 115, Springer, Berlin, 1989.

[12] A.P. Jardine, H. Hedgeland, G. Alexandrowicz, W. Allison, J. Ellis, Helium-3 spin-echo: principles and application to dynamics at surfaces, Prog. Surf. Phys. 84 (2009) 323.

[13] A.P. Graham, The low energy dynamics of adsorbates on metal surfaces investigated with helium atom scattering, Surf. Sci. Rep. 49 (2003) 115.

[14] For a perspective and extensive references see: Geert-Jan Kroes, Toward a database of chemically accurate barrier heights for reactions of molecules with metal surfaces, J. Phys. Chem. Lett. 6 (2015) 4106.

[15] O. Bünermann, H. Jiang, Y. Dorenkamp, A. Kandratsenka, S.M. Janke, D.J. Auerbach, A.M. Wodtke, Electron-hole pair excitation determines the mechanism of hydrogen atom adsorption, Science 350 (2015) 1346.

[16] [16a] O. Stern, Eine direkte Messung der thermischen Molekulargeschwindigkeit, Z. Phys. 2 (1920) 49.
[16b] O. Stern, Nachtrag zu meine Arbeit “Eine direkte Messung der thermischen Molekulargeschwindigkeit”, Z. Phys. 2 (1920) 417.

[17] [17a] F. Knauer, O. Stern, Über die Reflexion von Molekularstahlen, Z. Phys. 53 (1929) 779.
[17b] O. Stern, Beugung von Molekularstrahlen am Gitter einer Krystallspaltfläche, Naturwissenschaften 17 (1929) 391.

[18] [18a] I. Estermann, O. Stern, Beugung von Molekularstrahlen, Z. Phys 61 (1930) 95.
[18b] I. Estermann, R. Frisch, O. Stern, Monochromasierung der de Broglie-Wellen von Molekularstrahlen, Z. Phys. 73 (1932) 348[18c] O.R. Frisch, What Little I Remember, Cambridge University Press, Cambridge, 1979.

[19] [19a] R. Frisch, O. Stern, Anomalien bei der spiegelnden Reflexion und Beugung von Molekularstrahlen an Kristallspaltflächen. I, Z. Phys. 84 (1933) 430.
[19b] R. Frisch, Anomalien bei der spiegelnden Reflexion und Beugung von Molekularstrahlen an Kristallspaltflächen. II, Z. Phys. 84 (1933) 443.

[20] [20a] J.E. Lennard-Jones, A.F. Devonshire, Diffraction and selective adsorption of atoms at crystal surfaces, Nature 137 (1936) 1069.
[20b] A.F. Devonshire, The interaction of atoms and molecules with solid surfaces v - the diffraction and reflexion of molecular rays, Proc. Roy. Soc. (London) Ser. A 156 (1936) 37.
[20c] J.E. Lennard-Jones, A.F. Devonshire, The interaction of atoms and molecules with solid surfaces vi - the behavior of adsorbed helium at low temperatures, Proc. Roy. Soc. (London) Ser. A 158 (1936) 242.

[21] R. Campargue, High intensity supersonic molecular beam apparatus, Rev. Sci. Instrum. 35 (1964) 111.

[22] J.P. Toennies, Molekularstrahlmessungen von Stossquerschnitten für Übergange Zwischen Definierten Rotationszustanden Zwei-atomiger Molekule .I. Experimentelle Methode, Z. Phys. 182 (1965) 257.

[23] G. Scoles (Ed.), Atomic and Molecular Beam Methods, Oxford University Press, Oxford, 1988.

[24] W. Pauli, Über den Zusammenhang des Abschlusses der Elektronengruppen im Atom mit der Komplexstruktur der Spektren, Z. Phys. 31 (1925) 765.

[25] E. Zaremba, W. Kohn, Theory of helium adsorption on simple and noble-metal surfaces, Phys. Rev. B 15 (1977) 1769.

[26] [26a] J.M. Jackson, N.F. Mott, Energy exchange between inert gas atoms and a solid surface, Proc. Roy. Soc. (London) Ser. A 137 (1932) 703. [26b] J.M. Jackson, A quantum mechanical theory of energy exchanges between inert gas atoms and a solid surface, Proc. Cambridge Phil. Soc. 28 (1932) 136.

[27] N. Esbjerg, J.K. Nørskov, Dependence of the He-scattering potential at surfaces on the surface-electron-density profile, Phys. Rev. Lett. 45 (1980) 807.

[28] P. Senet, J.P. Toennies, G. Benedek, Theory of the He-phonon forces at a metal surface, Europhys. Lett. 57 (2002) 430.

[29] A. Chizmeshya, E. Zaremba, The interaction of rare-gas atoms with metal-surfaces - a scattering-theory approach, Surf. Sci. 268 (1992) 432.

[30] O. Gunnarsson, K. Schönhammer, Inelastic scattering of rare-gas atoms from metal surfaces. Excitation of electron-hole pairs, Phys. Rev. B 25 (1982) 2514.

[31] G. Benedek, J. Ellis, N.S. Luo, A. Reichmuth, P. Ruggerone, J.P. Toennies, Enhanced helium-atom scattering from longitudinal surface phonons in Cu(001), Phys. Rev. B 48 (1993) 4917.

[32] E. Hulpke, J. Lüdecke, Hydrogen-induced phonon anomaly on ohe W(110) surface, Phys. Rev. Lett. 68 (1992) 2846.

[33] G. Benedek, J.P. Toennies, Helium atom scattering spectroscopy of surface phonons - genesis and achievements, Surf. Sci. 299/300 (1994) 587.

[34] U. Harten, J.P. Toennies, Ch Wöll, Helium time-of-flight spectroscopy of surface-phonon dispersion-curves of the noble-metals, Faraday Discuss. Chem. Soc. 80 (1985) 137.

[35] I. Yu Sklyadneva, G. Benedek, E.V. Chulkov, P.M. Echenique, R. Heid, K.-P. Bohnen, J.P. Toennies, Mode-selected electron-phonon coupling in superconducting Pb nanofilms determined from He atom scattering, Phys. Rev. Lett. 107 (2011) 095502.

[36] G. Grimvall, The Electron-Phonon Interaction in Metals, North-Holland, New York, 1981.

[37] This approximation is usually called the Grimvall approximation and is typically valid for simple metals. In the case of semiconductors the Grimvall approximation is not valid, and a simple and appropriate approximation is to replace the energy denominator by the gap energy E_{gap}.

[38] [38a] G.M. Eliashberg, Interactions between electrons and lattice vibrations in a superconductor, Zh. Eksp. Teor. Fiz. 38 (1960) 966 [Soviet Phys.-JETP 11 696 (1960)]. [38b] G.M. Eliashberg, The low temperature specific heat of metals, Zh. Eksp. Teor. Fiz. 43 (1962) 1005 [Soviet Phys.-JETP **16** 780 1963].

[39] G. Benedek, M. Bernasconi, K.-P. Bohnen, D. Campi, E.V. Chulkov, P.M. Echenique, R. Heid, I. Yu Sklyadneva, J.P. Toennies, Unveiling mode-selected electron-phonon interactions in metal films by helium atom scattering, Phys. Chem. Chem. Phys. 16 (2014) 7159.

[40] W.H. Weinberg, Application of Debye-Waller theory to atomic and molecular scattering from solid surfaces, J. Chem. Phys. 57 (1972) 5463.

[41] P.B. Allen, Neutron spectroscopy of superconductors, Phys. Rev. B 6 (1972) 2577.

[42] P.B. Allen, Effect of soft phonons on superconductivity: A re-evaluation and a positive case for Nb_3Sn, Solid State Commun. 14 (1974) 937.

[43] I. Yu Sklyadneva, A. Leonardo, P.M. Echenique, S.V. Eremeev, E.V. Chulkov, Electron-phonon contribution to the phonon and excited electron (hole) linewidths in bulk Pd, J. Phys. Condens. Matter 18 (2006) 7923.

[44] Xuetao Zhu, L. Santos, C. Howard, R. Sankar, F.C. Chou, C. Chamon, M. El-Batanouny, Electron-phonon coupling on the surface of the topological insulator Bi2Se3 determined from surface-phonon dispersion measurements, Phys. Rev. Lett. 108 (2012) 185501.

[45] A. Tamtögl, P. Kraus, M. Mayrhofer-Reinhartshuber, D. Campi, M. Bernasconi, G. Benedek, W.E. Ernst, Surface and subsurface phonons of Bi(111) measured with helium atom scattering, Phys. Rev. B 87 (2013) 035410.

[46] J.R. Manson, G. Benedek, S. Miret-Artés, Electron-phonon coupling strength at metal surfaces directly determined from the helium atom scattering Debye-Waller factor, J. Phys. Chem. Lett. 7 (2016) 1016; ibid (2016) 1691.

[47] L.S. Rodberg, R.M. Thaler, Introduction to the Quantum Theory of Scattering, Academic Press, New York, 1967.

[48] R.G. Newton, Scattering Theory of Waves and Particles, Springer Verlag, New York, 1982.

[49] L. van Hove, Correlations in space and time and Born approximation scattering in systems of interacting particles, Phys. Rev. 95 (1954) 249.

[50] [50a] R. Glauber, The scattering of neutrons by systems of nuclei, in: Minutes of the 1952 Washington Meeting of the American Physical Society, May 1–3, 1952, See P. 189 of Phys. Rev, 87, 1952, p. 179. [50b] R. Glauber, Time-dependent displacement correlations and inelastic scattering by crystals, Phys. Rev. 98 (1955) 1692.

[51] R. Weinstock, Inelastic scattering of slow neutrons, Phys. Rev. 65 (1944) 1.

[52] J.R. Manson, Inelastic scattering from surfaces, Phys. Rev. B 43 (1991) 6924.

[53] J.R. Manson, Multiphonon atom-surface scattering, Comput. Phys. Commun. 80 (1994) 145.

[54] N. Cabrera, V. Celli, R. Manson, Theory of surface scattering and detection of surface phonons, Phys. Rev. Lett. 22 (1969) 346.

[55] J.R. Manson, V. Celli, Inelastic surface scattering of non-penetrating particles, Surf. Sci. 24 (1971) 495.

[56] M. Gell-Mann, M.L. Goldberger, The formal theory of scattering, Phys. Rev. 91 (1953) 398.

[57] R.P. Feynman, Statistical Physics, A Set of Lectures, Benjamin/Cummings, Reading, MA, 1972.

[58] J. Lindhard, On the properties of a gas of charged particles, Danske Matematisk-fysiske Meddeleiser, Det Kongelige Danske Videnskabernes Selskab 28 (8) (1954) 1–57.

[59] See Ref. [3], (Chapter 13).

[60] J.L. Beeby, Scattering of helium atoms from surfaces, J. Phys. Chem. 4 (1971) L359.

[61] P. Hofmann, M.M. Ugeda, A. Tamtögl, A. Ruckhofer, W.E. Ernst, G. Benedek, A.J. Martínez-Galera, A. Stróżecka, J.M. Gómez-Rodríguez, E. Rienks, M.F. Jensen, J.I. Pascual, J.W. Wells, Strong-coupling charge density wave in a one-dimensional topological metal, Phys. Rev. B 99 (2019) 035438.

[62] J.W. Wells, J.H. Dil, F. Meier, J. Lobo-Checa, V.N. Petrov, J. Osterwalder, M.M. Ugeda, I. Fernandez-Torrente, J.I. Pascual, E.D.L. Rienks, M.F. Jensen, P. Hofmann, Nondegenerate metallic states on Bi(114): a one-dimensional topological metal, Phys. Rev. Lett. 102 (2009) 096802.

[63] G. Benedek, S. Miret-Artés, J.R. Manson, A. Ruckhofer, W.E. Ernst, A. Tamtögl, Origin of the electron-phonon interaction of topological semimetal surfaces measured with helium atom scattering, J. Phys. Chem. Lett. 11 (2020) 1927.

[64] J.-F. Sadoc, R. Mosseri, A new method to generate quasi-crystalline structures - examples in 2D tilings, J. Phys. France 51 (1990) 205.
[65] H.S.M. Coxeter, Introduction to Geometry, second ed., John Wiley and Sons Inc., New York, 1969.
[66] G. Benedek, J.R. Manson, S. Miret-Artés, The Electron–Phonon Interaction of Low-Dimensional and Multi-Dimensional Materials From He Atom Scattering, Adv. Mat. 32 (2020) 2002072.
[67] N.D. Lang, w. Kohn, Theory of metal surfaces - charge density and surface energy, Phys. Rev. B 1 (1970) 4555.
[68] J.M. Li, J. Wang, Q. Sun, Y. Jia, First-principles study of Friedel oscillations normal to the low index surfaces of Al, Phys. B Condens. Matter 406 (2011) 2767.
[69] A. Tamtögl, M. Mayrhofer-Reinhartshuber, P. Kraus, W.E. Ernst, Surface Debye temperature and vibrational dynamics of Antimony(111) from helium atom scattering measurements, Surf. Sci. 617 (2013) 225.
[70] M. Mayrhofer-Reinhartshuber, A. Tamtögl, P. Kraus, K.H. Rieder, W.E. Ernst, Vibrational dynamics and surface structure of Bi(111) from helium atom scattering measurements, J. Phys. Condens. Matter 24 (2012) 104008.
[71] Ph.D. Dissertation G. Zhang, University of Göttingen, Max-Planck- Institut für Strömungsforschung, 1990. Report No. 102 (1991).
[72] J. Lapujoulade, Y. Lejay, G. Armand, The thermal attenuation of coherent elastic-scattering of noble-gas from metal-surfaces, Surf. Sci. 95 (1980) 107.
[73] J. Lapujoulade, J. Perreau, A. Kara, The thermal attenuation of elastic-scattering of helium from copper single-crystal surfaces, Surf. Sci. 129 (1983) 59.
[74] H.-J. Ernst, E. Hulpke, J.P. Toennies, Helium-atom-scattering study of the structure and phonon dynamics of the W(001) surfaec between 200 K and 1900 K, Phys. Rev. B 46 (1992) 16081.
[75] B.J. Hinch, C. Koziol, J.P. Toennies, G. Zhang, Evidence for quantum size effects observed by helium atom scattering during the growth of Pb on Cu(111), Europhys. Lett. 10 (1989) 341.
[76] Ch Bronner, P. Tegeder, Unoccupied electronic band structure of the semi-metallic Bi(111) surface probed with two-photon photoemission, Phys. Rev. B 87 (2013) 035123.
[77] P.O. Gartland, S. Berge, B.J. Slagsvold, Photoelectric work function of a copper single-crystal for (100), (110), (111) and (112) faces, Phys. Rev. Lett. 28 (1972) 738.
[78] H.B. Michaelson, Work function of elements and its periodicity, J. Appl. Phys. 48 (1977) 4729.
[79] J. Speight, sixteenth ed., Lange's Handbook of Chemistry, vol. 1, McGraw Hill, Boston, 2004, p. 132.
[80] E. Wimmer, A.J. Freeman, M. Weinert, H. Krakauer, J.R. Hiskes, A.M. Karo, Cesiation of W(001) - work function lowering by multiple dipole formation, Phys. Rev. Lett. 48 (1982) 1128.
[81] Y. Ohtsubo, L. Perfetti, M.O. Goerbig, P. Le Fèvre, F. Bertran, A. Taleb-Ibrahimi, Non-trivial surface-band dispersion on Bi(111), New J. Phys. 15 (2013) 033041.
[82] S.S. Tsirkin, S.V. Eremeev, E.V. Chulkov, Inelastic electron-electron scattering for surface states on Cu(110) and Ag(110), Phys. Rev. B 84 (2011) 115451.
[83] K. Sugawara, T. Sato, S. Souma, T. Takahashi, M. Arai, T. Sasaki, Anisotropic spin-orbit interaction in Sb(111) surface studied by high-resolution angle-resolved photoemission spectroscopy, J. Magn. Magn Mater. 310 (2007) 2177.
[84] K.E. Smith, G.S. Elliott, S.D. Kevan, Reconstruction and fermi-surface of W(001), Phys. Rev. B 42 (1990) 5385.
[85] In Ref. [46] this was erronously reported as 1.09 Å^{-1}.
[86] P. Hofmann, The surfaces of bismuth: structural and electronic properties, Prog. Surf. Sci. 81 (2006) 191.
[87] J. Jiang, S.S. Tsirkin, K. Shimada, H. Iwasawa, M. Arita, H. Anzai, H. Namatame, M. Taniguchi, I. Yu Sklyadneva, R. Heid, K.-P. Bohnen, P.M. Echenique, E.V. Chulkov, Many-body interactions and Rashba splitting of the surface state on Cu(110), Phys. Rev. B 89 (2014) 085404.
[88] D. Campi, M. Bernasconi, G. Benedek, Phonons and electron-phonon interaction at the Sb(111) surface, Phys. Rev. B 86 (2012) 075446.
[89] C.P. Poole, J.F. Zasadinsky, R.K. Zasadinsky, P.B. Allen, Electron-phonon coupling constants, in: C.P. Poole Jr. (Ed.), Handbook of Superconductivity, Academic Press, New York, 1999, pp. 478–483. Ch. 9, Sec. G.
[90] M. Aldén, S. Mirbt, H.L. Skriver, N.M. Rosengaaard, B. Johansson, Surface magnetism in iron, cobalt, and nickel, Phys. Rev. B 46 (1992) 6303.
[91] D.A. Papaconstantopoulos, L.L. Boyer, B.M. Klein, A.R. Williams, V.L. Morruzzi, J.F. Janak, Calculations of superconducting properties of 32 metals with z less-than-or-equal-to 49, Phys. Rev. B 15 (1977) 4221.
[92] A. Arranz, R.F. Sanchez-Rojo, J. Aliva, V. Pérez-Dieste, P. Dumas, M.C. Asensior, Electronic properties and Fermi surface of Ag(111) films deposited onto H-passivated Si(111)-(1 X 1) surfaces, Phys. Rev. B 65 (2002) 075405.
[93] P. Aebi, J. Osterwalder, R. Fasel, D. Naumovič, L. Schlapbach, Fermi-surface mapping with photoelectrons at uv energies, Surf. Sci. 307 (1994) 917.
[94] M. Alcántara-Ortigoza, I. Yu Sklyadneva, R. Heid, E.V. Chulkov, T.S. Rahman, K.-P. Bohnen, P.M. Echenique, Ab initio lattice dynamics and electron-phonon coupling of Bi(111), Phys. Rev. B 90 (2014) 195438.
[95] P. Straube, F. Pforte, T. Michalke, K. Berge, A. Gerlach, A. Goldmann, Photoemission study of the surface state at Y on Cu(110): band structure, electron dynamics, and surface optical properties, Phys. Rev. B 61 (2000) 14072.
[96] E.W. Plummer, J. Shi, S.-J. Tang, E. Rotenberg, S.D. Kevan, Enhanced electron-phonon coupling at metal surfaces, Prog. Surf. Sci. 74 (2003) 251.
[97] Y.F. Zhang, J.F. Jia, T.Z. Han, Z. Tang, Q.T. Shen, Y. Guo, Z.Q. Qiu, Q.K. Xue, Band structure and oscillatory electron-phonon coupling of Pb thin films determined by atomic-layer-resolved quantum-well states, Phys. Rev. Lett. 95 (2005) 096802. Note: this reference reports values of λ that range from 0.7 to 0.9 for 15 to 21 monolayers, respectively, of Pb(111) on a Si(111)-7X7 substrate.
[98] X. Shen, Y.P. Timalsina, T.-M. Lu, M. Yamaguchi, Experimental study of electron-phonon coupling and electron internal thermalization in epitaxially grown ultrathin copper films, Phys. Rev. B 91 (2015) 045129.
[99] P. B. Allen, in Ref. [89].
[100] E. Hulpke, J. Lower, A. Reichmuth, Strain and confined resonances in ultrathin alkali-metal films, Phys. Rev. B 53 (1996) 13901.
[101] Calculated from $k_F = \sqrt{3\pi/a_c n_s}$.
[102] C. Kittel, Introduction to Solid State Physics, eighth ed., John WIley and Sons, Inc, New York, 2005.
[103] L. Petersen, B. Schaefer, E. Laegsgaard, I. Stensgaard, F. Besenbacher, Imaging the surface Fermi contour on Cu(110) with scanning tunneling microscopy, Surf. Sci. 457 (2000) 319.
[104] O. Zeybek, A.M. Dvarpanah, S.D. Barrett, Electronic surface states of Cu(110) surface, Surf. Sci. 600 (2006) 5176.
[105] A.R. Canario, T. Kravchuk, V.A. Esaulov, Bandgaps, surface states and the anomalous neutralization of Li$^+$ on (111) surfaces of noble metals, New J. Phys. 8 (2006) 227.
[106] I.R. Collins, A.D. Laine, P.T. Andrews, Unoccupied surface-states of W(001) studied by angle-resolved untraviolet inverse photoemission, J. Phys. Condens. Matter 4 (1992) 2891.
[107] G. Leschik, R. Courths, H. Wern, S. Hufner, H. Eckardt, J. Noffke, Band-structure of platinum from angle resolved photoemission experiments, Solid State Commun. 52 (1984) 221.
[108] M. Heinrichsmeier, F. Fleszar, A.G. Eguiluz, LDA calculation of the surface-states on the (001), (110) and (111) surfaces of aluminum, Surf. Sci. 285 (1993) 129.
[109] C. Baldacchini, L. Choido, F. Allegretti, C. Mariani, M.G. Betti, P. Monachesi, R. Sole, Cu(100) surface: high-resolution experimental and theoretical band mapping, Phys. Rev. B 68 (2003) 195109.
[110] P.B. Allen, Empirical electron-phonon-gamma values from resistivity of cubic metallic elements, Phys. Rev. 36 (1987) 2920.
[111] A. Gester, A. Lock, J. P. Toennies, (unpublished).
[112] A.D. Corso, Clean Ir(111) and Pt(111) electronic surface states: a first-principle fully relativistic investigation, Surf. Sci. 637–638 (2015) 106.
[113] W.L. McMillan, Transition temperature of strong-coupled superconductors, Phys. Rev. 167 (1968) 331.
[114] B. Weitzel, H. Micklitz, Superconductivity in granular systems built from well-defined rhombohedral Bi clusters: evidence for Bi-surface superconductivity, Phys. Rev. Lett. 66 (1991) 385.
[115] G. Benedek, S. Miret-Artés, J.P. Toennies, J.R. Manson, The electron-phonon coupling constant of metallic overlayers from specular He-atom scattering, J. Phys. Chem. Lett. 9 (2018) 76.
[116] D. Campi, M. Bernasconi, G. Benedek, A.P. Graham, J.P. Toennies, Surface lattice dynamics and electron-phonon interaction in cesium ultra-thin films, Phys. Chem. Chem. Phys. 19 (2017) 16358.
[117] B. Flach, Thesis, University of Göttingen, unpublished, 2000.
[118] A.P. Ovchinnikov, B.M. Tsarev, Field emission of lithium films on faces of tungsten and rhenium single crystals, Fiz. Tverd. Tela **9**, Sov. Phys. Solid State 9 (1967) 3512 2766 (1968)].
[119] A. Carlsson, B. Hellsing, S.A. Lindgren, L. Walldén, High-resolution photoemission from a tunable quantum well: Cu(111)/Na, Phys. Rev. B 56 (1997) 1593 (Note: this is a calculated value of λ for the surface).
[120] H. Schief, J.P. Toennies, Observation of valence-band structure in the LVV-auger spectra of thin epitaxial sodium layers, Phys. Rev. B 12 (1994) 8773.
[121] P.B. Allen, M.L. Cohen, Pseudopotential calculation of the mass enhancement and superconducting transition temperature of simple metals, Phys. Rev. 187 (1969) 525.
[122] G. Benedek, P. Toennies, G. Zhang, Effects of surface magnetization on the surface phonons of Fe(110) by helium atom scattering, Phys. Rev. Lett. 68 (1992) 2644.
[123] M.J. Verstraete, Ab initio calculation of spin-dependent electron-phonon coupling in iron and cobalt, J. Phys. Condens. Matter 25 (2013) 136001.
[124] S. Bartholmei, P. Fouquet, G. Witte, Growth and dynamics of ultrathin barium films on Cu(100), Surf. Sci. 473 (2001) 227.
[125] A.O.E. Animalu, Total electronic band structure energy for 29 elements, Proc. Roy. Soc. Lond. Math. Phys. Sci. 294 (1966) 376.
[126] K.A. McEwen, Fermi surface of barium, Proc. Roy. Soc. Lond. Math. Phys. Sci. 322 (1971) 509.
[127] A. Politano, B. Borca, M. Minniti, J.J. Hinarejos, A.L. Vázquez de Parga, D. Farías, R. Miranda, Helium reflectivity and Debye temperature of graphene grown epitaxially on Ru(0001), Phys. Rev. B Condens. Matter 84 (2011) 35450.
[128] G. Anemone, A. Al Taleb, W.W. Hayes, J.R. Manson, D. Farías, Quantum decoherence behavior in neon scattering from Ru(0001) and graphene/Ru(0001) surfaces: experiment and comparison with calculations, J. Phys. Chem. C 121 (2017) 22815.
[129] A. Al Taleb, G. Anemone, R. Miranda, D. Farías, Characterization of interlayer forces in 2D heterostructures using neutral atom scattering, 2D Mater. 5 (2018) 045002.
[130] G. Bracco, L. Bruschi, L. Pedemonte, R. Tatarek, Temperature dependence of the Ag(llO) surface phonons, Surf. Sci. 377–379 (1997) 325.
[131] A. Tamtögl, E. Bahn, J. Zhu, P. Fouquet, J. Ellis, W. Allison, Graphene on Ni(111): electronic corrugation and dynamics from helium atom scattering, J. Phys. Chem. C 119 (2015) 25983.
[132] G. Benedek, M. Bernasconi, D. Campi, I.V. Silkin, I.P. Chernov, V.M. Silkin, E.V. Chulkov, P.M. Echenique, J.P. Toennies, G. Anemone, A. Al Taleb, R. Miranda, D. Farías, Evidence for a spin acoustic surface plasmon from inelastic atom scattering, Sci. Rep. 11 (2021) 1506.

[133] K. Wurde, A. Mazur, J. Pollmann, Surface electronic-structure of PB(001), Pb(110), and Pb(111), Phys. Rev. 49 (1994) 7679.

[134] B. Flach, E. Hulpke, Sternhögle, Characterization of epitaxial rubidium films with helium-atom scattering, Surf. Sci. 412 (1998) 12.

[135] P. Beckmann, A. Spizzichino, The Scattering of Electromagnetic Waves from Rough Surfaces, The Macmillan Company, New York, 1963, p. 70. Ch. 5.

[136] G.J. Kroes, M. Wijzenbroek, J.R. Manson, Possible effect of static surface disorder on diffractive scattering of H_2 from Ru(0001): Comparison between theory and experiment, J. Chem. Phys. 147 (2017) 244705.

[137] G. Zhang, PhD. Dissertation, University of Göttingen, MaxPlanck-Institut für Strömungsforschung Report, 1991.

[138] J. Braun, University of Göttingen, Ph. D. Thesis, 1997. [Max-Planck-Institut für Strömungsforschung, Göttingen, Germany Bericht 11.

[139] I. Yu Sklyadneva, R. Heid, K.-P. Bohnen, P.M. Echenique, E.V. Chulkov, Surface phonons on Pb(111), J. Phys. Condens. Matter 24 (2012) 104004.

[140] F. Calleja, A.L. Vázquez de Parga, E. Anglada, J.J. Hinarejos, R. Miranda, F. Yndurain, Crystallographic and electronic contribution to the apparent step height in nanometer-thin Pb(111) films grown on Cu(111), New J. Phys. 11 (2009) 123003.

[141] Y. Qi, X. Ma, P. Jiang, S. Ji, Y. Fu, J.F. Jia, Q.-K. Xue, S.B. Zhang, Atomic-layer-resolved local work functions of Pb thin films and their dependence on quantum well states, Appl. Phys. Lett. 90 (2007) 013109.

[142] H.C.W. Beijerinck, N.F. Verster, Absolute intensities and perpendicular temperatures of supersonic beams of polyatomic gases, Physica C 111 (1981) 327.

[143] A.S. Palau, S.D. Eder, T. Andersen, A. Komár Ravn, G. Bracco, B. Holst, Centre line intensity of a supersonic helium beam, Phys. Rev. 98 (2018) 063611.

[144] H. Qiu, T. Xu, Z. Wang, W. Ren, H. Nan, Z. Ni, Q. Chen, S. Yuan, F. Miao, F. Song, G. Long, Y. Shi, L. Sun, J. Wang, X. Wang, Hopping transport through defect-induced localized states in molybdenum disulphide, Nat. Commun. 4 (2013) 2642, https://doi.org/10.1038/ncomms3642.

[145] H. Peelaers, C.G. Van de Walle, Effects of strain on band structure and effective masses in MoS_2, Phys. Rev. B 86 (2012) 241401.

[146] A. Ruckhofer, A. Tamtögl, M. Pusterhofer, M. Bremholm, W.E. Ernst, Helium-surface Interaction and electronic Corrugation of Bi_2Se_3(111), J. Phys. Chem. C 123 (2019) 17829.

[147] A. Tamtögl, M. Pusterhofer, M. Bremholm, E.M. Hedegaard, B.B. Iversen, P. Hofmann, J. Ellis, W. Allison, S. Miret-Artés, W.E. Ernst, A helium-surface interaction Potential of Bi_2Te_3(111) from ultrahigh-resolution spin-echo measurements, Surf. Sci. 678 (2018) 25.

[148] Average over Bi_2Se_3(111) and Bi_2Te_3(111). [63].

[149] A. Tamtögl et al., (unpublished).

[150] A. Tamtögl, P. Kraus, N. Avidor, M. Bremholm, E.M.J. Hedegaard, B.B. Iversen, M. Bianchi, P. Hofmann, J. Ellis, W. Allison, G. Benedek, W.E. Ernst, Electron-phonon Coupling and surface Debye Temperature of Bi_2Te_3(111) from helium atom scattering, Phys. Rev. B 95 (2017) 195401.

[151] G. Anemone, A. Al Taleb, G. Benedek, A. Castellanos-Gomez, D. Farías, Electron-phonon coupling Constant of 2H-MoS_2(0001) from helium-atom scattering, J. Phys. Chem. C 123 (2019) 3682 ; sample with surface carrier concentration estimated in the 10^{12}cm^{-2} (0.1-1%) range.

[152] C. Heimlich, Georg August University of Göttingen, 1987. Ph. D. Thesis.

[153] G. Benedek, J.R. Manson, S. Miret-Artés, A. Ruckhofer, W.E. Ernst, A. Tamtögl, J.P. Toennies, Measuring the electron-phonon interaction in two-dimensional superconductors with He atom scattering, Condens. Matter 5 (2020) 79.

[154] G. Anemone, P. Casado Aguilar, M. Garnica, F. Calleja, A. Al Taleb, C.-N. Kuo, C.S. Lue, A. Politano, A.L. Vàzquez de Parga, G. Benedek, D. Farìas, R. Miranda, Electron-phonon coupling in superconducting 1T-$PdTe_2$, 2D Mater. Appl. 5 (2021) 25, https://doi.org/10.1038/s41699-021-00204-5.

[155] Y. Yu, F. Yang, X.F. Lu, Y.J. Yan, Y.H. Cho, L. Ma, X. Niu, S. Kim, Y.-W. Son, D. Feng, S. Li, S.-W. Cheong, X.H. Chen, Y. Zhang, Gate-tunable phase transitions in thin flakes of 1T-TaS2, Nat. Nanotechnol. 10 (2015) 270.

[156] Textured nearly commensurate CDW (NCCDW), see Ref. [155].

[157] Metallic incommensurate CDW (ICCDW), see Ref. [155].

[158] J. Suh, D. Fu, X. Lin, J.K. Furdyna, K.M. Yu, W. Walukiewicz, J. Wu, Fermi-level stabilization in the topological insulators Bi2Se3 and Bi2Te3: origin of the surface electron gas, Phys. Rev. B 89 (2014) 115307.

[159] S. Choi, Z. Shaolin, W. Yang, Layer-number dependent work function of MoS_2, J. Kor. Phys. Soc. 64 (2014) 1550.

[160] T. Shimada, F.S. Ohuchi, B.A. Parkinson, Work function and photothreshold of layered metal dichalcogenides, Jpn. J. Appl. Phys. 33 (1994) 2696.

[161] D. Tsoutsou, K.E. Aretouli, P. Tsipas, J. Marquez-Velasco, E. Xenogiannopoulou, N. Kelaidis, S.A. Giamini, D. Dimoulas, Epitaxial 2D $MoSe_2$ ($HfSe_2$) semiconductor/2D $TaSe_2$ Metal van der Waals heterostructures, ACS Appl. Mater. Interfaces 8 (2016) 1836.

[162] F.A. Rasmussen, K.S. Thygesen, Computational 2D materials database: electronic structure of transition-metal dichalcogenides and oxides, J. Phys. Chem. C 119 (2015) 13169.

[163] M. Bianchi, D. Guan, S. Bao, J. Mi, B. Brummerstedt Iversen, P.D.C. King, P. Hofmann, Coexistence of the topological state and a two-dimensional electron gas on the surface of Bi_2Se_3, Nat. Commun. 1 (2010) 128, https://doi.org/10.1038/ncomms1131; from the effective mass components given in this paper the total effective mass is $m^e_* = \sqrt[3]{m_x m_y m_z} = 0.146 m_e$.

[164] M.T. Pettes, J. Maassen, I. Jo, M.S. Lundstrom, L. Shi, Effects of surface band bending and scattering on thermoelectric transport in suspended bismuth telluride nanoplates, Nano Lett. 13 (2013) 5316.

[165] P. Gehring, B.F. Gao, M. Burghard, K. Kern, Growth of high-mobility Bi_2Te_2Se nanoplatelets on hBN sheets by van der Waals epitaxy, Nano Lett. 12 (2012) 5137.

[166] Derived from a screening length of 1.1 nm as given in Ref. [144] for a carrier density close to that of HAS measurements. This is consistent with a carrier effective mass of 0.45 me. [145].

[167] From an estimated electrostatic screening length of < 1nm, see Ref. [155].

[168] G.Q. Huang, Surface lattice vibration and electron-phonon interaction in topological insulator Bi_2Te_3(111) films from first principles, Europhys. Lett. 100 (2012) 17001.

[169] R. Heid, I. Yu Sklyadneva, E.V. Chulkov, Electron-phonon coupling in topological surface states: the role of polar optical modes, Sci. Rep. 7 (2017) 1095.

[170] Y.L. Chen, J.G. Analytis, J.-H. Chu, Z.K. Liu, S.-K. Mo, X.L. Qi, H.J. Zhang, D.H. Lu, X. Dai, Z. Fang, S.C. Zhang, I.R. Fisher, Z. Hussain, Z.-X. Shen, Experimental realization of a three-dimensional topological insulator, Bi_2Te_3 , Science 325 (2009) 178.

[171] R.C. Hatch, M. Bianchi, D. Guan, S. Bao, J. Mi, B.B. Iversen, L. Nilsson, L. Hornekær, P. Hofmann, Stability of the Bi_2Se_3(111) topological state: electron-phonon and electron-defect scattering, Phys. Rev. B 83 (2011) 241303.

[172] Z.-H. Pan, A.V. Fedorov, D. Gardner, Y.S. Lee, S. Chu, T. Valla, Measurement of an exceptionally weak electron-phonon coupling on the surface of the topological insulator Bi_2Se_3 using angle-resolved photoemission spectroscopy, Phys. Rev. Lett. 108 (2012) 187001.

[173] I. Zeljkovic, K.L. Scipioni, D. Walkup, Y. Okada, W. Zhou, R. Sankar, G. Chang, Y.J. Wang, H. Lin, A. Bansil, F. Chou, Z. Wang, V. Madhavan, Nanoscale determination of the mass enhancement factor in the lightly doped bulk insulator lead selenide, Nat. Commun. 6 (2015) 6559.

[174] S. Giraud, A. Kundu, R. Egger, Electron-phonon scattering in topological insulator thin films, Phys. Rev. B 85 (2012) 035441.

[175] C. Chen, Z. Xie, Y. Feng, H. Yi, A. Liang, S. He, D. Mou, J. He, Y. Peng, X. Liu, et al., Tunable Dirac fermion dynamics in topological insulators, Sci. Rep. 3 (2013) 2411.

[176] Z. Li, J.P. Carbotte, Impact of electron-phonon interaction on dynamic conductivity of gapped Dirac fermions: application to single layer MoS_2, Physica B 421 (2013) 97.

[177] Y. Ge, A.Y. Liu, Phonon-mediated superconductivity in electron-doped single-layer MoS_2: a first-principles prediction, Phys. Rev. B 87 (2013) 241408(R).

[178] N. Nayyar, D. Le, V. Turkowski, T.S. Rahman, Electron-phonon Interaction Excitations and Ultrafast Photoemission from Doped Monolayer MoS_2, arXiv:1501.07908, 2015. surface carrier concentration from 1% ($\lambda = 0.12$) to 3% ($\lambda = 0.20$).

[179] K. Rossnagel, On the origin of charge-density waves in select layered transition-metal dichalcogenides, J. Phys. Condens. Matter 23 (2011) 213001.

[180] A.Y. Liu, Electron-phonon coupling in compressed 1T-TaS_2: Stability and superconductivity from first principles, Phys. Rev. B 79 (R) (2009) 220515; calculated for 1T-TaS_2 under pressure from 5 GPa ($\lambda = 2.09$) to 30 GPa ($\lambda = 0.69$).

[181] N.F. Hinsche, K.S. Thygesen, Electron–phonon interaction and transport properties of metallic bulk and monolayer transition metal dichalcogenide TaS_2, 2D Mater. 5 (2018) 015009 ; for the 2H-TaS_2 polytype.

[182] D. Bhoi, S. Khim, W. Nam, B.S. Lee, Chanhee Kim, B.-G. Jeon, B.H. Min, S. Park, Kee Hoon Kim, Interplay of charge density wave and multiband superconductivity in 2H-Pd_xTaSe_2, Sci. Rep. 6 (2016) 24068.

[183] M.K. Hooda, C.S. Yadav, Electronic transport properties of intermediately coupled superconductors: $PdTe_2$ and $Cu_{0.04}PdTe_2$, Europhys. Lett. 121 (2018) 17001.

[184] K. Kim, S. Kim, J.S. Kim, H. Kim, J.-H. Park, B.I. Min, Importance of the van Hove singularity in superconducting $PdTe_2$, Phys. Rev. B 97 (2018) 165102.

[185] M. Yan, H. Huang, K. Zhang, E. Wang, W. Yao, K. Deng, G. Wan, H. Zhang, M. Arita, H. Yang, Z. Sun, H. Yao, Y. Wu, S. Fan, W. Duan, S. Zhou1, Lorentz-violating type-II Dirac fermions in transition metal dichalcogenide $PtTe_2$, Nat. Commun. 8 (2017) 257.

[186] R.E. Peierls, Quantum Theory of Solids, Oxford University Press, Oxford, 1955.

[187] H. Fröhlich, On the theory of superconductivity: the one-dimensional case, Proc. Roy. Soc. Lond. 223 (1954) 296.

[188] M.J. Kelly, L.M. Falicov, Electronic ground-state of inversion layers in many-valley semiconductors, Phys. Rev. B 15 (1977) 1974.

[189] M.J. Kelly, L.M. Falicov, Optical-properties of charge-density-wave ground-states for inversion layers in many-valley semiconductors, Phys. Rev. B 15 (1977) 1983.

[190] M.J. Kelly, L.M. Falicov, Electronic structure of inversion layers in many-valley semiconductors, Phys. Rev. Lett. 37 (1976) 1021.

[191] A. Tamtögl, P. Kraus, M. Mayrhofer-Reinhartshuber, G. Benedek, M. Bernasconi, D. Dragoni, D. Campi, W.E. Ernst, Statics and dynamics of multivalley charge density waves in Sb(111), Quant. Mater. 4 (2019) 18.

[192] R. Liu, T. Ma, S. Wang, J. Yang, Thermodynamical potentials of classical and quantum systems, Discrete Contin. Dyn. Syst. Ser. B 24 (2019) 1411.

[193] T. Ma, S. Wang, Cahn-Hilliard equations and phase transition dynamics for binary systems, Discrete Continuous Dyn. Syst. - Ser. B (DCDS-B) 11 (2019) 741.

[194] G. Benedek, F. Hofmann, P. Ruggerone, G. Onida, L. Miglio, Surface phonons in layered crystals - theoretical aspects, Surf. Sci. Rep. 20 (1994) 3.

[195] J.W. Wells, J.H. Dil, F. Meier, J. Lobo-Checa, V.N. Petrov, J. Osterwalder, M.M. Ugeda, I. Fernandez-Torrente, J.I. Pascual, E.D.L. Rienks, et al., Nondegenerate metallic states on Bi(114): a one-dimensional topological metal, Phys. Rev. Lett. 102 (2009) 096802.

[196] G. Benedek, L. Miglio, J.G. Skofronick, G. Brusdeylins, C. Heimlich, J.P. Toennies, Surface phonon dynamics in 2H-TaSe$_2$*(001)*, J. Vac. Sci. Technol. 5 (1987) 1093.

[197] G. Benedek, G. Brusdeylins, C. Heimlich, L. Miglio, J.G. Skofronick, J.P. Toennies, Shifted surface phonon anomaly in 2H-TaSe$_2$*(001)*, Phys. Rev. Lett. 60 (1988) 1037.

[198] G. Brusdeylins, C. Heimlich, J.G. Skofronick, J.P. Toennies, R. Vollmer, G. Benedek, Determination of the critical exponents for a charge density wave transition in 2H-TaSe$_2$ by helium atom scattering, Europhys. Lett. 9 (1989) 563.

[199] G. Benedek, L. Miglio, G. Seriani, in: E. Hulpke (Ed.), Helium Atom Scattering from Surfaces, Springer Press, Heidelberg, 1992.

[200] G. Benedek, G. Brusdeylins, F. Hofmann, P. Ruggerone, J.P. Toennies, R. Vollmer, J.G. Skofronick, Strong coupling of Rayleigh phonons to charge density waves in 1T-TaS$_2$, Surf. Sci. 304 (1994) 185.

[201] G. Anemone, M. Garnica, M. Zappia, P.C. Aguilar, A. Al Taleb, C.N. Kuo, C.S. Lue, A. Politano, G. Benedek, A.L.V. de Parga, R. Miranda, D. Farías, Experimental determination of surface thermal expansion and electron-phonon coupling constant of 1T-PtTe$_2$, 2D Mater. 7 (2020) 025007.

[202] C. Howard, M. El-Batanouny, R. Sankar, F.C. Chou, Anomalous behavior in the phonon dispersion of the (001) surface of Bi$_2$Te$_3$ determined from helium atom-surface scattering measurements, Phys. Rev. B 88 (2013) 035402.

[203] A. Tamtögl, D. Campi, M. Bremholm, E.M.J. Hedegaard, B.B. Iversen, M. Bianchi, P. Hofmann, N. Marzari, G. Benedek, J. Ellis, et al., Nanoscale surface dynamics of Bi$_2$Te$_3$(111): Observation of a prominent surface acoustic wave and the role of van der Waals interactions, Nanoscale 10 (2018) 14627.

[204] X. Zhu, L. Santos, R. Sankar, S. Chikara, C. Howard, F.C. Chou, C. Chamon, M. El-Batanouny, Interaction of phonons and Dirac fermions on the surface of Bi$_2$Se$_3$: a strong Kohn anomaly, Phys. Rev. Lett. 107 (2011) 186102.

[205] A. Ruckhofer, D. Campi, M. Bremholm, P. Hofmann, G. Benedek, M. Bernasconi, W.E. Ernst, A. Tamtögl, THz surface modes and electron-phonon coupling in Bi$_2$Se$_3$(111), Phys. Rev. Res. 2 (2020) 023186.

[206] J.L. Mi, M. Bremholm, M. Bianchi, K. Borup, S. Johnsen, M. Søndergaard, D. Guan, R.C. Hatch, P. Hofmann, B.B. Iversen, Phase separation and bulk p-n transition in single crystals of Bi$_2$Te$_2$Se topological insulator, Adv. Mater. 25 (2013) 889.

[207] According to the surface lattice constant $a = 4.31$ Å as determined by HAS and Fig. 1(b) of [206], $X \approx 1$ for the present sample.

[208] M. Bianchi, R.C. Hatch, D. Guan, T. Planke, J. Mi, B.B. Iversen, P. Hofmann, The electronic structure of clean and adsorbate-covered Bi$_2$Se$_3$: an angle-resolved photoemission study, Semicond. Sci. Technol. 27 (2012) 124001.

[209] M. Michiardi, I. Aguilera, M. Bianchi, V.E. de Carvalho, L.O. Ladeira, N.G. Teixeira, E.A. Soares, C. Friedrich, S. Blügel, P. Hofmann, Bulk band structure of Bi2Te3, Phys. Rev. B 90 (2014) 075105.

[210] L. Barreto, L. Kühnemund, F. Edler, C. Tegenkamp, J. Mi, M. Bremholm, B.B. Iversen, C. Frydendahl, M. Bianchi, P. Hofmann, Surface-dominated transport on a bulk topological insulator, Nano Lett. 14 (2014) 3755.

[211] B.I. Shklovskii, A.E. Efros, Electronic Properties of Doped Semiconductors, Springer Series in Solid State Sciences, vol. 45, Springer Press, Heidelberg, 1984.

[212] D.-M. Smilgies, Goerg August University of Göttingen, Ph. D. Thesis, 1991. Bericht 6/1991 MPI-SF ISSN 0436-1199.

[213] M.W. Hüppauf, Universität Göttingen, Diplom Thesis, 1989.

[214] W. Steinhögl, Georg August University of Göttingen, Ph. D. thesis, 1998.

[215] C.H. Park, F. Giustino, M.L. Cohen, S.G. Louie, Electron-phonon interactions in graphene, bilayer graphene, and graphite, Nano Lett. 8 (2008) 4229.

[216] J.P. Oh, T. Kondo, D. Hatake, J. Nakamura, Elastic and inelastic scattering components in the angular intensity distribution of He scattered from graphite, Surf. Sci. 603 (2009) 895.

[217] R. Vollmer, University of Göttingen, 1992, p. 140. Ph. D. Thesis.

[218] A. Al Taleb, G. Anemone, W.W. Hayes, J.R. Manson, D. Farías, Multiphonon excitation and quantum decoherence in neon scattering from solid surfaces, Phys. Rev. B 95 (2017) 075414.

[219] A. Tamtögl, E. Bahn, J. Zhu, P. Fouquet, J. Ellis, W. Allison, Graphene on Ni(111): electronic corrugation and dynamics from helium atom scattering, J. Phys. Chem. C 119 (2015) 25983.

[220] H. Shichibe, Y. Satake, K. Watanabe, A. Kinjyo, A. Kunihara, Y. Yamada, M. Sasaki, W.W. Hayes, J.R. Manson, Probing interlayer interactions between graphene and metal substrates by supersonic rare-gas atom scattering, Phys. Rev. B 91 (2015) 155403.

[221] A. Al Taleb, G. Anemone, D. Farías, R. Miranda, Acoustic surface phonons of graphene on Ni(111), Carbon 99 (2016) 416.

[222] K.D. Gibson, S.J. Sibener, Growth, structure, and vibrational properties of few layer graphene grown on Rh(111), J. Phys. Chem. C 120 (2016) 24158.

[223] G. Moos, C. Gahl, R. Fasel, M. Wolf, T. Hertel, Anisotropy of quasiparticle lifetimes and the role of disorder in graphite from ultrafast time-resolved photoemission spectroscopy, Phys. Rev. Lett. 87 (2002) 267402.

[224] K. Sugawara, T. Sato, S. Souma, T. Takahashi, H. Suematsu, Anomalous quasiparticle lifetime and strong electron-phonon coupling in graphite, Phys. Rev. Lett. 98 (2007) 036801 (ARPES measurements in K-K direction).

[225] C.S. Leem, B.J. Kim, Chul Kim, S.R. Park, T. Ohta, A. Bostwick, E. Rotenberg, H.-D. Kim, M.K. Kim, H.J. Choi, C. Kim, Effect of linear density of states on the quasiparticle dynamics and small electron-phonon coupling in graphite, Phys. Rev. Lett. 100 (2008) 016802.

[226] G. Giovannetti, P.A. Khomyakov, G. Brocks, V.M. Karpan, J. van den Brink, P.J. Kelly, Doping graphene with metal contacts, Phys. Rev. Lett. 101 (2008) 026803.

[227] H. Vita, S. Bottcher, K. Horn, E.N. Voloshina, R.E. Ovcharenko, T. Kampen, A. Thissen, Y.S. Dedkov, Understanding the origin of band gap formation in graphene on metals: graphene on Cu/Ir(111), Sci. Rep. 4 (2014) 5704.

[228] P. Sutter, J.T. Sadowsky, E. Sutter, Graphene on Pt(111): growth and substrate interaction, Phys. Rev. B 80 (2009) 245411.

[229] M. Alattas, U. Schwingenschlögl, Quasi-freestanding graphene on Ni(111) by Cs intercalation, Sci. Rep. 6 (2016) 26753.

[230] K. Katsiev, Y. Losovyj, Z.H. Zhou, E. Vescovo, L. Liu, P.A. Dowben, D.W. Goodman, Graphene on Ru(0001): evidence for two graphene band structures, Phys. Rev. B 85 (2012) 195405.

[231] A.L. Walter, S. Nie, A. Bostwick, K.S. Kim, L. Moreschini, Y.J. Chang, D. Innocenti, K. Horn, K.F. McCarty, E. Rotenberg, Electronic structure of graphene on single-crystal copper substrates, Phys. Rev. B 84 (2011) 195443.

[232] D. Maccariello, D. Campi, A. Al Taleb, G. Benedek, D. Farías, M. Bernasconi, R. Miranda, Low-energy excitations of graphene on Ru(0001), Carbon 93 (2015) 1.

[233] This equation appears in Ref. [246], but with an error. There the denominator contains an erroneous extra factor of $\hbar k_F$.

[234] V. Ariel, N. Natan, Electron effective mass in graphene, arXiv: 1206.6100v2 [physics.gen-ph] 12 Aug 2012, in: Int. Conf. On Electromagnetics in Advanced Applications (ICEAA), 2013, pp. 696–698, https://doi.org/10.1109/ICEAA.2013.663234.

[235] A.V. Fedorov, N.I. Verbitskiy, D. Haberer, C. Struzzi, L. Petaccia, D. Usachov, O.Y. Vilkov, D.V. Vyalikh, J. Fink, M. Knupfer, B. Büchner, A. Grüneis, Observation of a universal donor-dependent vibrational mode in graphene, Nat. Commun. 5 (2014) 3257.

[236] M. Calandra, F. Mauri, Electron-phonon coupling and electron self-energy in electron-doped graphene: calculation of angular-resolved photoemission spectra, Phys. Rev. B 76 (2007) 205411.

[237] D. Haberer, L. Petaccia, A.V. Fedorov, C.S. Praveen, S. Fabris, S. Piccinin, O. Vilkov, D.V. Vyalikh, A. Preobrajenski, N.I. Verbits, H. Shiozawa, J. Fink, M. Knupfer, B. Buchner, A. Gruneis, Anisotropic Eliashberg function and electron-phonon coupling in doped graphene, Phys. Rev. B 88 (2013) 081401.

[238] A.C. Bailey, B. Yates, Anisotropic thermal expansion of pyrolytic graphite at low temperature, J. Appl. Phys. 41 (1970) 5088.

[239] B. Marsden, A. Mummery, P. Mummery, Modelling the coefficient of thermal expansion in graphite crystals: implications of lattice strain due to irradiation and pressure, Proc. Roy. Soc. A 474 (2018) 0075 (and references therein).

[240] N. Mounet, N. Marzari, First-principles determination of the structural, vibrational and thermodynamic properties of diamond, graphite, and derivatives, Phys. Rev. B 71 (2005) 205214.

[241] A. Al Taleb, D. Farías, Phonon dynamics of graphene on metals, J. Phys. Condens. Matter 28 (2016) 103005.

[242] A. Politano, A.R. Marino, G. Chiarello, Phonon dispersion of quasi-freestanding graphene on Pt(111), J. Phys. Condens. Matter 24 (2012) 104025.

[243] M-Ch Wu, Q. Xu, D.W. Goodman, Investigations of graphitic overlayers formed from methane decomposition on Ru(0001) and Ru(1120) catalysts with scanning tunneling microscopy and high-resolution electron energy loss spectroscopy, J. Phys. Chem. 98 (1994) 5104.

[244] J. Braun, K.L. Kostov, G. Witte, L. Surnev, J.G. Skofronick, S.A. Safron, Ch Wöll, Surface phonon dispersion curves for a hexagonally close packed metal surface: Ru(0001), Surf. Sci. 372 (1997) 132.

[245] R. Heid, K.-P. Bohnen, T. Moritz, K.L. Kostov, D. Menzel, W. Widdra, Anomalous surface lattice dynamics of a simple hexagonal close-packed surface, Phys. Rev. B 66 (2002) 161406.

[246] G. Benedek, J.R. Manson, S. Miret-Artés, The electron-phonon coupling constant for single-layer graphene on metal substrates determined from He atom scattering, Phys. Chem. Chem. Phys. 23 (2021) 7575.

[247] R. Bistritzer, A.H. MacDonald, Moiré bands in twisted double-layer graphene, Proc. Natl. Acad. Sci. Unit. States Am. 108 (2011) 12233.

[248] Y. Cao, V. Fatemi, S. Fang, K. Watanabe, T. Taniguchi, E. Kaxiras, P. Jarillo-Herrero, Unconventional superconductivity in magic-angle graphene superlattices, Nature 556 (2018) 43.

[249] Y. Cao, V. Fatemi, A. Demir, S. Fang, S.L. Tomarken, J.Y. Luo, J.D. Sanchez-Yamagishi, K. Watanabe, T. Taniguchi, E. Kaxiras, R.C. Ashoori, P. Jarillo-Herrero, Correlated insulator behaviour at half-filling in magic-angle graphene superlattices, Nature 556 (2018) 80.

[250] U. Mogera, G.U. Kulkarni, A new twist in graphene research: twisted graphene, Carbon 156 (2020) 470.

[251] D.J. Trainer, B. Wang, F. Bobba, N. Samuelson, X. Xi, J. Zasadzinski, J. Nieminen, A. Bansil, M. Iavarone, Proximity-induced superconductivity in monolayer MoS$_2$, ACS Nano 14 (2020) 2718.

[252] [252a] R.G. Gordon, New method for constructing wavefunctions for bound states and scattering, J. Chem. Phys. 51 (1969) 14. [252b] R.G. Gordon, Quantum scattering using piecewise analytic solutions, Methods Comput. Phys. 10 (1971) 81.

[253] G. Wolken Jr., Theoretical studies of atom-solid elastic scattering: He+LiF, J. Chem. Phys. 58 (1973) 3047.

[254] [254a] A. Liebsch, J. Harris, Interaction of helium with a metal-surface .2. coupled channels method and effect of out-of-plane scattering for Cu(110), Surf. Sci. 123 (1982) 355.

[254b] R.B. Laughlin, Helium Diffraction from the GaAs(110) surface and the Generation of Helium-surface Potentials, Phys. Rev. B 25 (1982) 2222.
[254c] G. Drolshagen, A. Kaufhold, J.P. Toennies, Energy-dependence of diffraction intensities - He-4+LiF(001), Isr. J. Chem. 22 (1982) 283.

[255] A.S. Sanz, S. Miret-Artés, Selective adsorption resonances: quantum and stochastic approaches, Phys. Rep. 451 (2007) 37.

[256] J.E. Lennard-Jones, C. Strachan, The interaction of atoms and molecules with solid surfaces I - the activation of adsorbed atoms to higher vibrational states, Proc. Roy. Soc. (London) Ser. A 150 (1935) 442.

[257] [257a] C. Strachan, The interaction of atoms and molecules with solid surfaces II - the evaporation of adsorbed atoms, Proc. Roy. Soc. (London) Ser. A 150 (1935) 456. [257b] C. Strachan, The interaction of atoms and molecules with solid surfaces IX - the emission and absorption of energy by a solid, Proc. Roy. Soc. (London) Ser. A 158 (1937) 591.

[258] J.R. Manson, G. Armand, Simple approximation to thermal attenuation in low energy atom-surface scattering: multiple phonon processes, Surf. Sci. 195 (1988) 513.

[259] G. Armand, J.R. Manson, C.S. Jayanthi, Thermal attenuation in atom-surface scattering: the two phonon contribution, J. Phys. 47 (1986) 1357.

[260] G. Armand, J.R. Manson, C.S. Jayanthi, Thermal attenuation in atom-surface scattering: the multiphonon contribution, Phys. Rev. B 34 (1986) 6627.

[261] [261a] D.E. Manolopoulos, R.E. Wyatt, Quantum scattering via the log derivative version of the Kohn variational principle, Chem. Phys. Lett. 152 (1988) 23. [261b] D.E. Manolopoulos, R.E. Wyatt, D.C. Clary, Iterative solution in quantum scattering-theory - the log derivative Kohn approach, J. Chem. Soc. Faraday Trans. 86 (1990) 1641.

[262] P. Kraus, A. Tamtögl, M. Mayrhofer-Reinhartshuber, F. Apolloner, Ch. Gösweiner, S. Miret-Artés, W.E. Ernst, Surface structure of Bi(111) from helium atom scattering measurements. Inelastic close-coupling formalism, J. Phys. Chem. C 119 (2015) 17235.

[263] A.M. Lahee, J.R. Manson, J.P. Toennies, C. Wöll, Helium atom differential cross-sections for scattering from single adsorbed CO molecules on a Pt(111) surface, J. Chem. Phys. 86 (1987) 7194.

[264] A.A. Maradudin, E.W. Montroll, G.H. Weiss, In Solid State Physics: Theory of Lattice Dynamics in the Harmonic Approximation, Academic Press, New York, 1963. Suppl. 3.

[265] M. Abramowitz, L.A. Stegun, In Handbook of Mathematical Functions, U.S. Department of Commerce, Washington, DC, 1964, p. 297.